# Unsteady Aerodynamic Models for Agile Flight at Low Reynolds Numbers

Steven L. Brunton

A Dissertation
Presented to the Faculty
of Princeton University
in Candidacy for the Degree
of Doctor of Philosophy

Recommended for Acceptance
by the Department of
Mechanical and Aerospace Engineering
Adviser: Clarence W. Rowley

April 2012

# Abstract

This work develops low-order models for the unsteady aerodynamic forces on a wing in response to agile maneuvers at low Reynolds number. Model performance is assessed on the basis of accuracy across a range of parameters and frequencies as well as of computational efficiency and compatibility with existing control techniques and flight dynamic models. The result is a flexible modeling procedure that yields accurate, low-dimensional, state-space models. The modeling procedures are developed and tested on direct numerical simulations of a two-dimensional flat plate airfoil in motion at low Reynolds number, $\mathrm{Re} = 100$, and in a wind tunnel experiment at the Illinois Institute of Technology involving a NACA 0006 airfoil pitching and plunging at Reynolds number $\mathrm{Re} = 65,000$. In both instances, low-order models are obtained that accurately capture the unsteady aerodynamic forces at all frequencies. These cases demonstrate the utility of the modeling procedure developed in this thesis for obtaining accurate models for different geometries and Reynolds numbers.

Linear reduced-order models are constructed from either the indicial response (step response) or realistic input/output maneuvers using a flexible modeling procedure. The method is based on identifying stability derivatives and modeling the remaining dynamics with the eigensystem realization algorithm. A hierarchy of models is developed, based on linearizing the flow at various operating conditions. These models are shown to be accurate and efficient for plunging, pitching about various points, and combined pitch and plunge maneuvers, at various angle of attack and Reynolds number. Models are compared against the classical unsteady aerodynamic models of Wagner and Theodorsen over a large range of Strouhal number and reduced frequency for a baseline comparison. Additionally, state-space representations are developed for Wagner's and Theodorsen's models, making them compatible with modern control-system analysis.

A number of computational tools are developed throughout this work. Highly unsteady maneuvers are visualized using finite-time Lyapunov exponent fields, which highlight separated flows and wake structures. A new fast method of computing these fields is presented. In addition, we generalize the immersed boundary projection method computations to use a moving base flow, which allows for the simulation of complex geometries undergoing large motions with up to an order of magnitude speed-up.

The methods developed in this thesis provide a systematic approach to identify unsteady aerodynamic models from analytical, numerical, or experimental data. The resulting models are shown to be reduced-order models of the linearized Navier-Stokes equations that are expressed in state-space form, and they are, therefore, both efficient and accurate. The specific form of the model, which separates added-mass forces, quasi-steady lift, and transient forces, guarantees that the resulting models are accurate over the entire range of frequencies. Finally, the models are low-dimensional linear systems of ordinary differential equations, so that they are compatible with existing flight dynamic models as well as a wealth of modern control techniques.

# Acknowledgements

My greatest thanks are to my advisor, Clancy Rowley, who has been both a role model and a source of encouragement and guidance throughout my time at Princeton. Clancy has provided a supportive environment that has allowed me to explore my interests, and I am grateful for his patience and optimism about my work.

I am thankful for Rob Stengel and Lex Smits, my thesis readers, for generously providing me with constructive comments that improved the quality of this work. I also thank Phil Holmes and Naomi Leonard for being on my thesis committee and for advice along the way. I am grateful for the many road trips and conversations that I shared with Gigi Martinelli. My undergraduate advisors, Jerry Marsden and Wang Sang Koon, deserve thanks for providing me with powerful tools and guiding me on my path. I would also like to thank Jessica O'Leary and Jill Ray for all of their advice and hard work to help make things go smoothly.

Toward the end of my studies, I was very fortunate to visit the Illinois Institute of Technology and work with Dave Williams in his wind tunnel. Learning about experiments from Dave was a highlight of my graduate work. I would also like to thank Wes Kerstens for his help with the experiments and for helping me to beat a hurricane home.

Working in Professor Rowley's group has truly been a pleasure. I especially enjoyed the time spent with current and former lab mates, who have taught me a great deal: Juan Melli, Melissa Green, Sunil Ahuja, Zhanhua Ma, Milos Ilak, Peter Norgaard, Sam Taira, Dirk Luchtenberg, Lauren Padilla, Jonathan Tu, Brandt Belson, Kevin Chen, Imene Goumiri, and Carla Bahri. I also enjoyed our semi-regular beer and wings at the Ivy. Mort has been a good lab dog, through thick and thin.

All of my love and thanks go to my wife Bing; her love and support have not wavered. And to our son James, who has been a blessing to his parents. Thanks to my loving parents and my sister, who were my first and greatest teachers. I would not be where I am without the love and support of my family.

I gratefully acknowledge the support of this work by the Princeton MAE second year fellowship, the Air Force Office of Scientific Research Grant FA9550-07-1-0127, and the FAA Joint University Program for Air Transportation.

This dissertation carries the number T-3236 in the records of the Department of Mechanical and Aerospace Engineering.

# Contents

# List of Tables

# List of Figures

# Nomenclature

| | |
|---|---|
| $a$ | Pitch axis location with respect to $1/2-$chord ($a=-1$ leading edge, $a=1$ trailing edge), |
| $(A_r, B_r, C_r)$ | Reduced order state-space realization of order $r$ for strictly proper transfer function $G(s)$, |
| $b$ | Half-chord length of airfoil, |
| $c$ | Chord length of airfoil, |
| $C(k)$ | Theodorsen's transfer function, |
| $\tilde{C}(s)$ | Empirically determined Theodorsen transfer function |
| $C_L$ | Lift coefficient [$C_L \triangleq L/\bar{q}S$], |
| $C_{L_\alpha}$ | Lift coefficient slope in $\alpha$ [$C_{L_\alpha} \triangleq \partial C_L/\partial\alpha$], |
| $C_L^{\mathrm{AM}}$ | Added-mass portion of lift coefficient, |
| $C_L^{\mathrm{circ}}$ | Circulatory lift attenuated by wake, |
| $C_L^{\mathrm{QS}}$ | Quasi-steady portion of lift coefficient, |
| $C_1$ | Empirically determined added-mass coefficient, |
| $C_2$ | Empirically determined lift coefficient slope, |
| ERA | Eigensystem Realization Algorithm, |
| $f$ | Frequency of pitch or plunge motion, |
| FTLE | Finite-Time Lyapunov Exponent, |
| $g$ | Horizontal position of pitch axis (positive left), |
| $h$ | Vertical position of pitch axis (positive down), |
| IBPM | Immersed Boundary Projection Method, |
| $k$ | Reduced frequency [$k \triangleq \omega c/2U_\infty$], |
| $L$ | Dimensional lift force, |
| $\mathcal{L}$ | Laplace transform, |
| nLCS | Negative-time Lagrangian coherent structure, |
| OKID | Observer/Kalman Filter Identification |
| $p$ | Pitch axis location in chords from leading edge, |
| pLCS | Positive-time Lagrangian coherent structure, |
| $\bar{q}$ | Dynamic pressure [$\bar{q} \triangleq 1/2\rho\|\mathbf{V}\|^2$], |
| Re | Reynolds number [Re $\triangleq cU_\infty/\nu$], |
| $S$ | Wing surface area in 3D, or chord in 2D, |
| $s$ | Laplace variable (alternatively, non-dimensional time $s = 2U_\infty t/c$) |
| $SE(2)$ | Special Euclidean group on $\mathbb{R}^2$, |
| $St$ | Strouhal number [$St \triangleq fM/U_\infty$] |
| $T_pSE(2)$ | Tangent space to $SE(2)$ at point $p \in SE(2)$, |
| $TSE(2)$ | Tangent bundle of $SE(2)$, |

| | |
|---|---|
| $U_\infty$ | Free-stream velocity, |
| $\mathbf{u_B}$ | Velocity of immersed body, |
| $\mathbf{V}$ | Flight path vector, |
| $\mathbf{x}$ | Unsteady aerodynamic state, |
| $X_0$ | Discrete particle grid [$X_0 \subset \mathbb{R}^n$], |
| $\tilde{y}(t)$ | Output in response to step input (indicial response), |
| $\alpha$ | Angle-of-attack of airfoil (degrees) [$\alpha \triangleq \theta - \gamma$], |
| $\alpha_e$ | Effective angle of attack, |
| $\alpha_0$ | Base angle about which flow is linearized, |
| $\gamma$ | Flight path angle (degrees), |
| $\Delta$ | The Cauchy-Green deformation tensor, |
| $\Delta\alpha$ | Amplitude of pitch or plunge maneuver, |
| $\Delta t_f$ | Fine time step, |
| $\Delta t_c$ | Coarse time step, |
| $\eta$ | Normal displacement of pitch axis, |
| $\theta$ | Pitch angle (degrees), |
| $\theta_r$ | Pitch angle in right handed coordinates, |
| $\xi$ | Parallel displacement of pitch axis, |
| $\sigma(\Phi; \mathbf{x})$ | FTLE for flow $\Phi$ at the point $\mathbf{x}$, |
| $\Sigma_a(\Phi)$ | Set of particles with FTLE above a given threshold $a$; for $a$ sufficiently large, this set represents a neighborhood of the dominant LCS ridges. [$\Sigma_a(\Phi) \triangleq \{\mathbf{x} \mid \sigma(\Phi; \mathbf{x}) > a\}$] |
| $\phi(s)$ | Wagner's indicial response function, |
| $\tilde{\Phi}$ | Approximation to the particle flow map $\Phi$, |
| $\Phi_a^b$ | Particle flow map from time $t = a$ to time $t = b$, |
| $\Phi\|_{X_0}$ | Flow map restricted to a discrete grid $X_0$, |
| $\mathbf{D}\Phi$ | The Jacobian of the flow map $\Phi$, |
| $\mathcal{I}\Phi$ | Shorthand for interpolation [$\mathcal{I}\Phi \triangleq \mathcal{I}(\Phi\|_{X_0})$], |
| $\mathcal{I}(\Phi\|_{X_0})$ | Interpolant of the flow map $\Phi\|_{X_0}$, defined on a discrete grid $X_0$, |
| $\omega$ | Frequency of pitch or plunge maneuver. |

"Stall also sometimes appears to occur to birds. One can make a bird stall if one has some knowledge of aerodynamics. I often tried to do this with seagulls on the shore of Lake Constance. I had bread in my hand and as the birds tried to get it, I slowly withdrew my hand. Then the birds tried to decrease their speed to get it, which required an increased lift coefficient. Several times, apparently, the birds exceeded the critical angle of their wings and stalled. The difference between the bird and an airplane is that the bird can easily produce additional lift by vigorously flapping its wings. The phenomenon of flow separation depends largely on viscous effects, which are neglected in the circulation theory of lift."

–**Theodore Von Karman,** ***Aerodynamics***, 1964

# Chapter 1

# Introduction

## 1.1 Motivation for improved aerodynamic models

The unsteady aerodynamic forces and moments associated with time-varying fluid flows are ubiquitous in modern engineering. The design of cars, boats, and planes all involve careful optimization to streamline the body, improving efficiency by minimizing the amount of flow separation and drag. Modern sky-scrapers and bridges are also susceptible to unsteady aerodynamic forcing from gusting wind, and they must be designed to avoid aeroelastic resonance. Perhaps the most striking illustration of the potential of unsteady aerodynamics for engineering design comes from biological propulsion. It is observed that birds, bats, insects and fish routinely harness unsteady fluid dynamics to improve their propulsive efficiency, maximize thrust and lift, and increase maneuverability. As unmanned aerial vehicles (UAVs) become smaller and lighter, unsteady aerodynamic forces become increasingly important during agile maneuvers and gust disturbances. The most important parameter for quantifying this trend is the dimensionless Reynolds number, $\mathrm{Re} = cU_\infty/\nu$, where $c$ is the chord length of the wing, $U_\infty$ is the free-stream velocity, and $\nu$ is the kinematic viscosity. An example of the unsteady separated flow behind a flat plate at low Reynolds number ($\mathrm{Re} = 100$) is shown in Figure 1.1. This system is characterized by strong leading and trailing edge separation and a complex wake.

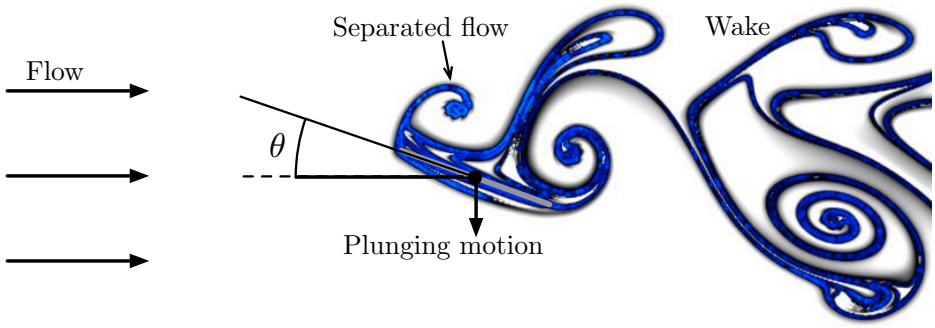


Figure 1.1: Unsteady flow field for airfoil in downward stroke of sinusoidal plunge at fixed inclination $\theta = 20^\circ$ and Reynolds number $\mathrm{Re} = 100$. (finite-time Lyapunov exponent flow visualization is discussed in Chapter 4)

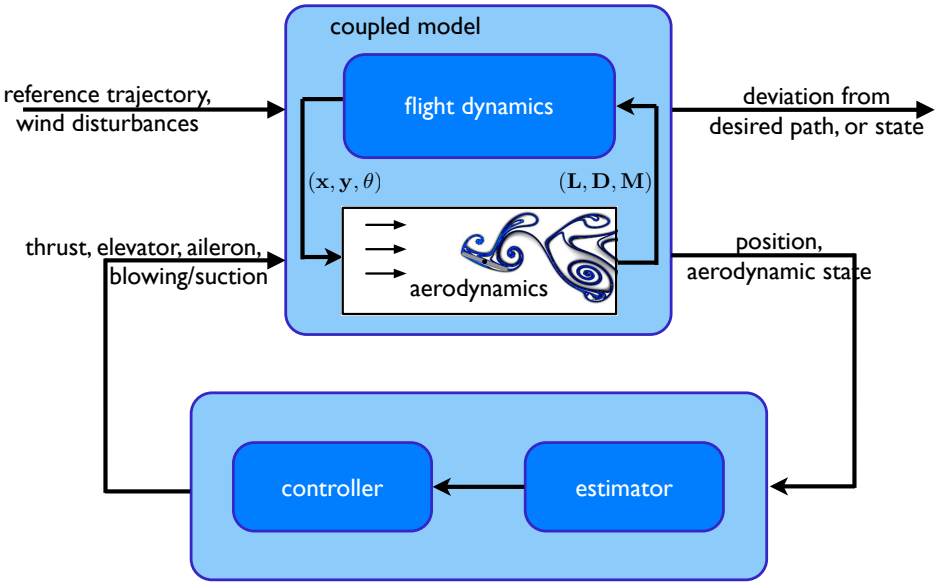


Figure 1.2: Schematic showing unsteady aerodynamic model in the context of flight dynamics and flight control.

The need for accurate, efficient aerodynamic models has been a key motivation in research efforts over the past century. Aerodynamic models are necessary tools in the design of aircraft as well as the evaluation of aeroelastic and flight dynamic stability. Many studies indicate that the enhanced performance in bio-locomotion [5, 123] is due to utilization of unsteady aerodynamic mechanisms. These biological observations coupled with advances in small-scale manufacturing techniques and feedback control design have opened up new and interesting problems in unsteady aerodynamic research.

This thesis develops low-dimensional models for the unsteady aerodynamic forces on a small-scale wing in agile motion. It is critical that the reduced-order models obtained are both accurate and efficient. Moreover, models must be expressed in state-space form for compatibility with the standard framework for feedback control design. Figure 1.2 is a schematic illustrating how an unsteady aerodynamic model coupled with a flight dynamic model fits into the modern control framework.

Accurate state-space aerodynamic models are particularly important when the flight dynamic and aerodynamic time scales are comparable. In this case, modern control techniques such as $\mathcal{H}_\infty$ synthesis are necessary for robust performance. Because small, lightweight aircraft have shorter flight dynamic time-scales, we seek models for small vehicles and bio-flyers at low Reynolds number, between $10^2 - 10^5$.

## 1.2 Previous work on unsteady aerodynamics

Historically, the development of aerodynamic theory has been closely related to advances in technology. Currently, the rapid miniaturization of unmanned aircraft is driving research into unsteady aerodynamics. At the same time, improved compu-

tational resources have made it possible to analyze complex fluid dynamical systems using direct numerical simulations and model reduction. Finally, advances in state-space control theory techniques are making it possible to extend the unsteady flight envelop using coupled unsteady aerodynamic and flight dynamic models.

### 1.2.1 Aerodynamic models for flight control

Most aerodynamic models used for flight control rely on the quasi-steady assumption that forces and moments depend in a static manner on such parameters as relative velocity and angle of attack. While these models work well for conventional aircraft [110, 100, 27], they do not describe the unsteady aerodynamic forces that are important for small, agile aircraft to avoid obstacles, respond to gusts, and track potentially elusive targets. Small, light weight aircraft have a lower stall velocity, and therefore, gusts and rapid motions excite large reduced frequencies, $k = \pi f c/U_\infty$, where $f$ is the frequency of motion, which results in an unsteady flow field.

There is, however, a wide range of unsteady aerodynamic models in the literature [60]. The classical unsteady models of Wagner [125] and Theodorsen [114] remain widely used and provide a benchmark for the linear models that follow them. Wagner's model constructs the lift in response to arbitrary input motion by convolving the time derivative of the motion with the analytically computed step response. Theodorsen developed an equivalent model in the frequency domain using the same model assumptions of an incompressible, inviscid, planar wake. Although Theodorsen's model applies only to sinusoidal input motion, it was suitable for the analysis of flutter instability with the tools available at the time. However, with modern tools, it is possible to construct a state-space realization based on Theodorsen's model that is useful for time domain analysis, as will be demonstrated in Chapter 6. Even so, both models are limited by the inviscid assumption that allow for them to be solved in closed form with analytic techniques.

Sophisticated models for the unsteady fluid dynamics, and resulting aerodynamic forces, may be obtained using direct numerical simulations (DNS) [29, 112, 113], computational fluid dynamics (CFD) [107, 108, 74, 3, 93], wind tunnel experiments [82, 129], and water channel experiments [77, 54, 15, 39]. Each of these methods may provide accurate estimates of the viscous fluid dynamic interactions that lead to transient unsteady aerodynamics. However, these methods are extremely expensive, both in time and equipment. It is important, therefore, to obtain low-dimensional models from these complex model systems [24, 106, 73, 33].

Linear indicial response models are a general class of aerodynamic models, which may be constructed based on analytical, experimental, or numerical step response information [65, 92, 118]. Indicial response models are a mainstay of the unsteady aerodynamics [57, 60] and aeroelasticity communities [71, 90, 70, 81, 89]. They have been used for a wide range of problems ranging from understanding the effect of control surfaces [58], to the modeling of gusts [59], and the suppression of shedding on bridges and buildings [98, 21, 20, 16, 119]. Because these models may be formed from CFD or wind tunnel data, they are able to capture limited viscous effects, such as stable laminar boundary layer separation. Wagner's model is an indicial response model based on an analytically computed step response. A fundamental limitation of indicial response models is their formulation based on the convolution integral, which does not fit into the modern framework for feedback control design.

The application of feedback control design to problems in unsteady fluid dynamics has been both challenging and rewarding. Because of the wealth of powerful linear control techniques, one generally applies flow control using a linear model of the Navier-Stokes equations around a given fixed point or attractor; a review of the work in this field is found in Kim & Bewley [55]. However, complex fluid systems are typically high dimensional, making them computationally expensive to simulate and intractable for many control techniques. This motivates the need for accurate reduced-order models. One method for obtaining reduced-order models that accurately represent the input/output dynamics is balanced proper orthogonal decomposition (BPOD) [94]. BPOD has been successfully applied to a number of systems including channel flow [46], the Blasius boundary layer [4], and the periodically shedding flat plate [1]. It has recently been shown that the eigensystem realization algorithm (ERA) [52, 51] produces the same reduced-order models as BPOD, but without the need for adjoint simulations [68].

### 1.2.2 Models based on nonlinear flow physics

The unsteady aerodynamics of small-scale wings at a high angle of attack is at the focus of efforts to study bird and insect flight as well as to develop advanced controllers for high-performance micro air vehicles (MAVs). The short time scales involved in gusts and agile maneuvering make small wings susceptible to unsteady laminar separation, which can either enhance or destroy the lift depending on the specific maneuver. For example, certain insects [5, 99, 131] and birds [123] use the shape and motion of their wings to maintain the high transient lift from a rapid pitch-up, while avoiding stall and the substantially decreased lift that follows. Moreover, at smaller sizes, added-mass forces become increasingly important. The enhanced performance observed in bio-locomotion relies on unsteady mechanisms that will be important for model-based control of MAVs [2]. The effect of Reynolds number and aspect ratio on small wings is discussed in Ol *et al.* [77, 54]. Nonlinear separated flow effects, such as dynamic stall [34, 69, 72, 109, 56] and vortex shedding [76, 9] are important for larger amplitude maneuvers at high angle of attack. Figure 4.1 shows a large amplitude maneuver with leading edge vortex and periodic vortex shedding.

Figure 1.3 shows the lift coefficient versus angle of attack for a flat plate at low Reynolds number (Re = 100) [12]. At a critical angle, $\alpha_{\text{crit}} = 28^\circ$, the flow undergoes a supercritical Hopf bifurcation, after which the flow is characterized by laminar, periodic vortex shedding [1]. A hierarchy of models including linear reduced order models at various angle of attack and extended to include nonlinear separated flow effects, such as dynamic stall [34, 69, 109] and vortex shedding [76, 9], is ideal for capturing the effects of agile maneuvers and gusts on small-scale wings. In this thesis, a common framework is developed for this hierarchy of models, and model identification techniques and maneuvers are used to develop linear unsteady models for sub-critical angle of attack.

Additionally, unsteady separated flows are investigated using finite-time Lyapunov exponent (FTLE) fields [41, 102]. For an unsteady flow field, it is not possible to identify separated regions with streamlines alone [41]. However, ridges in the FTLE field identify regions of separated flow and wake structures. FTLE fields have also been useful for understanding nonlinear flow mechanisms underlying the breakdown of classical linear unsteady models [9].

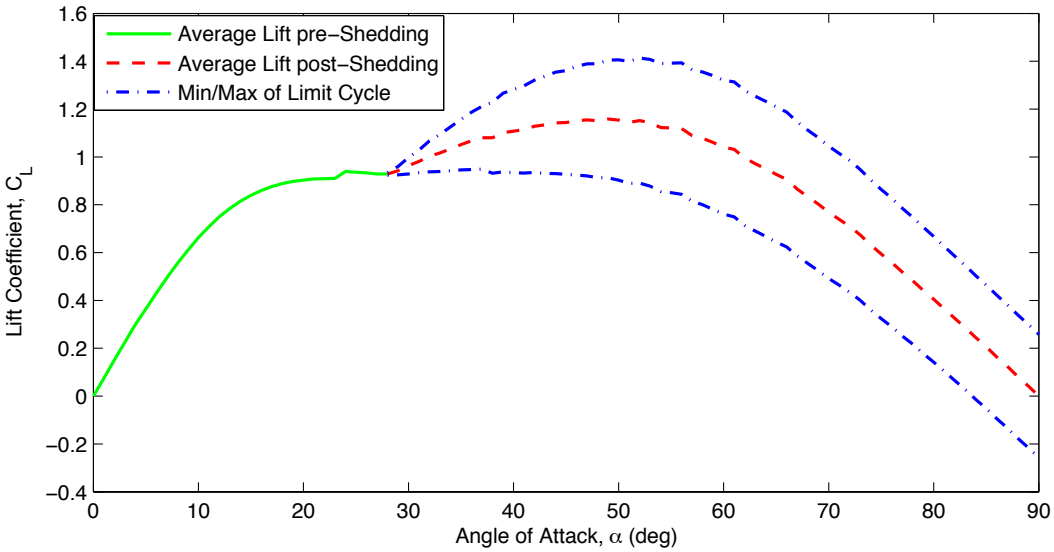


Figure 1.3: Lift coefficient vs. static angle of attack for flat plate at Re = 100. Hopf bifurcation occurs at $\alpha_{\text{crit}} = 28°$, after which the flow is characterized by laminar, periodic vortex shedding.

## 1.3 Organization and contribution

A principal contribution of this work is to provide a number of methods to obtain accurate low-dimensional models linearized about various angle of attack. In particular, we develop low-dimensional models that combine the best attributes of indicial response (accurate, flexible, time-domain) and Theodorsen's model (physically motivated, parameterized by pitch axis location) in a state-space realization. Models are obtained for angle of attack up to the Hopf bifurcation angle.

Chapter 2 provides a brief review of background material. This includes classical unsteady aerodynamic models 2.1, model reduction and system identification techniques 2.2, and dynamical systems tools for visualizing unsteady separated flows 2.4. Additionally, Galerkin projection is reviewed 2.3, and the added-mass forces arising from unsteady potential flow are discussed 2.5. A canonical pitch maneuver is presented in Section 2.6.

Chapters 3 and 4 describe computational tools developed during this thesis to simulate and visualize unsteady fluid dynamics. Chapter 3 involves a modification of the immersed boundary projection method to solve the two-dimensional incompressible Navier-Stokes equations in the body-fixed frame, yielding better accuracy and computational efficiency for moving-wing simulations. Chapter 4 develops a number of algorithms for fast computation of finite-time Lyapunov exponent fields in unsteady flows based on particle flow map approximations. The finite-time Lyapunov exponent (FTLE) field is useful for visualizing unsteady fluid coherent structures. In particular, we have used the FTLE field to show how the classical unsteady model of Theodorsen breaks down at large reduced frequency and Strouhal number [9].

Chapter 5 provides the theoretical foundation and algorithms for developing unsteady aerodynamic models that are used extensively in later chapters. In this

chapter, aerodynamic models are seen as a nonlinear dynamical system related to the unsteady Navier-Stokes equations with body motion as an input, and forces and moments are the nonlinear outputs (as computed from either the velocity or vorticity field state). It is then shown that under certain assumptions and linearization about various operating conditions, one recovers a very general linear unsteady aerodynamic model.

Chapters 6, 7, and 8 provide specific instances of how the modeling techniques from Chapter 5 may be used in practice. Chapter 6 shows that the classical models of Wagner and Theodorsen may be cast into the general state-space form, and may be modified to reflect empirically determined dynamics. Chapter 7 provides results for models of a flat plate airfoil at Reynolds number $\mathrm{Re} = 100$ at various angle of attack. Chapter 8 provides models based on wind tunnel measurements at Reynolds number $\mathrm{Re} = 65,000$.

## 1.4 Assumptions, conventions, and notation

A number of coordinate systems and notations are used in this thesis. Aerodynamic forces and moments are fluid dynamic in nature, but they are referenced to a coordinate system that is relevant to flight dynamic considerations. In particular, lift and drag are the forces perpendicular and parallel to the flight path vector, which is the velocity vector of the aircraft center of mass. However, throughout this work, and indeed in many previous works, we are interested in the aerodynamics of the wing isolated from the flight dynamic body, and there is no uniquely defined flight path vector. Therefore, there is a choice of the *aircraft center of mass*, or other relevant, *special* aerodynamic point, such as pitch axis, aerodynamic center, center of gravity, etc. There is also a choice of whether to use lift and drag coefficients, referred to the velocity vector, or to use the force coefficient components normal and tangential to the wing (body axes), or to use the force coefficients in the earth-relative $z$ and $x$ directions, the former being the force counteracting gravity. There are advantages and disadvantages to each choice, and each is valid for different problems of interest.

Lift and drag are measured in reference to the free stream velocity. Flight dynamic coordinates are used when applicable, but in general, models are formulated using *aerodynamic* coordinates consistent with Theodorsen, as discussed in Section 5.1.1. In particular, unless specifically stated, translational motion of the airfoil is measured in reference to the center of rotation. On occasion, models will be derived with translational motion referred to the mid-chord of the wing, since this simplifies the added-mass forces. Finally, this work concentrates on modeling the two-dimensional, longitudinal lift aerodynamics, although the methods are sufficiently general for the development of models for the drag and moment coefficients for more complicated motions.

Unless otherwise stated, lengths are nondimensionalized by the chord $c$, and velocities are nondimensionalized by the free-stream velocity $U_\infty$. This results in dimensionless time $t' = tc/U_\infty$ and frequency $f' = fU_\infty/c$. Note that the early work of Theodorsen and Wagner nondimensionalize lengths using the half-chord $b = c/2$. However, nondimensionalizing by the full chord $c$ is more common in current literature [126, 79, 18].

# Chapter 2

# Background

This chapter provides an overview of tools that are used in this thesis. We discuss quasi-steady aerodynamics, the classical unsteady aerodynamic models of Wagner and Theodorsen, and linear indicial theory in Section 2.1. These models are the inspiration for the more general class of models derived in Chapter 5. In Section 2.2 we present two system identification tools, the eigensystem realization algorithm (ERA) and observer Kalman/filter identification (OKID). Both methods are used extensively in Chapters 7 and 8 to identify models of the form derived in Chapter 5. Section 2.3 illustrates the Galerkin projection of the Navier-Stokes equations onto a set of basis modes. Next, Section 2.4 introduces the finite-time Lyapunov exponent and its use in visualizing separated flows. Section 2.5 addresses added-mass forces, which arise from the theory of unsteady potential flow. Finally, a canonical pitch-up, hold, pitch-down maneuver is introduced in Section 2.6.

## 2.1 Linear unsteady aerodynamic models

This section provides a brief review of the most frequently used linear unsteady aerodynamic models in the literature. First, we begin with the simplest steady and quasi-steady models in Section 2.1.1. Next, the linear indicial theory is discussed in Section 2.1.2. Finally, the classical unsteady models of Wagner and Theodorsen are presented in Section 2.1.3. These models are the basis for the improved models in Chapter 5, and they provide a benchmark for comparison.

In all of the models that follow, the goal is to predict the lift force on an airfoil that may be rapidly pitching or plunging vertically in addition to its forward motion. It is convenient to use the non-dimensional lift coefficient,

$$C_L = \frac{2L}{\rho U_\infty^2 S} \tag{2.1}$$

where $L$ is the dimensional lift force, $\rho$ is the fluid density, $U_\infty$ is the free-stream velocity, and $S$ is the wing surface area for a three-dimensional airfoil or chord length $c$ for a two-dimensional airfoil. The lift coefficient depends on the geometry, configuration, and motion of the wing. The wing configuration is given by the angle of attack, $\alpha$, which is the angle of inclination of the airfoil with respect to the free-stream velocity, and the vertical position of the pitch axis, $h$. The dependence of $C_L$ on $\alpha$ and $h$ will be elaborated on in the following sections.

### 2.1.1 Quasi-steady lift models

The simplest steady model of the lift coefficient for a two-dimensional airfoil in an inviscid fluid is linear in $\alpha$:

$$C_L = 2\pi\alpha \tag{2.2}$$

Angle of attack and plunge motion, given by $\dot{\alpha}$ and $\dot{h}$, respectively, may be included in a quasi-steady model by introducing the *effective angle of attack*, $\alpha_e$. A small downward plunge velocity results in a change in angle of attack equal to $\Delta\alpha = \tan^{-1}(\dot{h}/U_\infty) \approx \dot{h}/U_\infty$. Similarly, angle of attack motion, $\dot{\alpha}$, results in local vertical velocities along the airfoil, and hence a distribution of local angle of attack that may be modeled as an *effective camber*. This contributes to a change in angle of attack equal to $\Delta\alpha = c\dot{\alpha}(1-2a)/4U_\infty$, where $a$ is the pitch axis location with respect to the 1/2-chord[1]. This yields the quasi-steady model:

$$C_L = 2\pi\left(\alpha + \frac{\dot{h}}{U_\infty} + \frac{c}{2}\frac{\dot{\alpha}}{U_\infty}\left(\frac{1}{2} - a\right)\right) = 2\pi\alpha_e \tag{2.3}$$

### 2.1.2 Linear indicial theory

Linear indicial response models are mainstays of the unsteady aerodynamics [115, 57, 58, 59, 65, 92] and aeroelasticity [81, 70, 90, 71, 89, 119, 20] communities. The indicial response is defined as the output response to a step control input.

Linear indicial models are orders of magnitude more computationally efficient than direct numerical simulations (DNS) or computational fluid dynamic (CFD) solutions, and they are flexible in that they may be constructed from analytic numerical or experimental step response data. However, the convolution integral approach to indicial response models does not fit into the linear system framework required for feedback control.

The method of linear indicial response is based on the assumption that the flow can be linearized with respect to a given boundary condition or forcing function. The method is used to reconstruct an output measurement $y$ (aerodynamic forces and moments) given an arbitrary input $u$ (wing motion or control surface deflection). In general, the flow field is a smooth nonlinear function of boundary conditions and forcing functions away from bifurcation points. For example, the lift coefficient $C_L$ depends smoothly on angle of attack $\alpha$ until a bifurcation occurs at a critical angle $\alpha_{\text{crit}}$, after which the flow is characterized by periodic vortex shedding. Away from the critical point, it is possible to linearize the flow field about some input $u_0$:

$$y(t) = y(u_0, t_0) + \left.\frac{\partial y}{\partial u}\right|_{u_0} \Delta u + \mathcal{O}(\Delta u^2) \tag{2.4}$$

The function $\partial y/\partial u$ is the impulse response, and it does not depend on $u$, but only on the time $t$ after the step. It is then possible to write the linearized equation as

$$y(t) = y(t_0) + \frac{dy}{du}(t)\Delta u = y(t_0) + \tilde{y}(t)\Delta u \tag{2.5}$$

[1]Pitching about the leading edge corresponds to $a = -1$, whereas the trailing edge is $a = 1$.

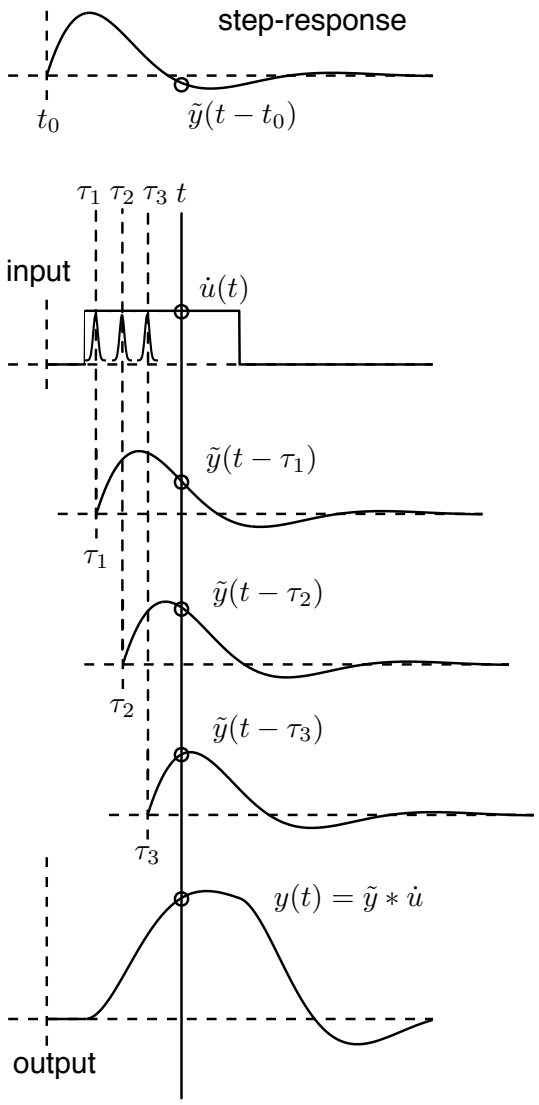


Figure 2.1: Schematic of linear indicial response model obtained by convolution.

The indicial response $\tilde{y}(t)$ is the output in response to a step input, $\dot{u} = \delta(t)$, where $\delta(t)$ is the Dirac delta function. An indicial response model reconstructs the output response $y(t)$ to an arbitrary input, $u(t)$ by linear superposition (convolution):

$$y(t) = \tilde{y}(t)u(0^-) + \int_0^t \tilde{y}(t-\tau)\dot{u}(\tau)d\tau \tag{2.6}$$

Often, the indicial response is broken up as $\tilde{y}(t) = dy/du \cdot \phi(t)$, where $dy/du$ is a generalization of the lift slope (when $y = C_L$ and $u = \alpha$), and $\phi(t)$ is a normalized indicial response with $\lim_{t\to\infty} \phi(t) = 1$. Figure 2.1 illustrates the convolution integral in Eq. (2.6), where time-shifted copies of the indicial response $\tilde{y}$ are integrated to obtain the response to a general input.

The indicial response may be obtained analytically or empirically from experiments or simulations. The only assumption is that of linear time invariance. A more general approach based on functionals has been developed to extend this theory for nonlinear indicial response [115, 117, 116, 118, 91]. More examples of indicial response are found in Reisenthel [91] and Leishman [60].

### 2.1.3 Classical models of Wagner and Theodorsen

Among the wide range of unsteady aerodynamic models in the literature [60], the classical models of Wagner [125] and Theodorsen [114] remain widely used and provide a benchmark for the linear models that proceed them. Indeed, these models have been remarkably successful for over three-quarters of a century, in part because they are derived from first principles using clear assumptions. Wagner's and Theodorsen's theories are derived analytically for an idealized two-dimensional flat plate airfoil moving through an inviscid, incompressible fluid. The motion of the flat plate is assumed to be infinitesimal, leaving an idealized planar wake. Both theories refine the quasi-steady theory in Eq. (2.3) by including the effect of the wake history on the induced circulation around the airfoil.

The same simplifying assumptions that make Wagner's and Theodorsen's models analytically tractable also limit the ability of these models to capture the viscous effects that become increasingly important for lower Reynolds number flows. In addition, the models were formulated before the widespread use of control theory, and are not in state-space form. The first issue motivates the more general models developed in Chapter 5. Additionally, Chapter 6 addresses the problem of casting Wagner's and Theodorsen's models into a modern state-space framework. Because both models are discussed in considerably more detail in Chapter 6, this section only provides the basic model formulations, along with some relevant historical details.

#### Wagner's model

In 1925, Wagner [125] developed a model by computing analytically the effect of idealized planar wake vorticity on the circulation around the airfoil in response to a step in angle of attack. Therefore, Wagner's model is an indicial response model, and his expression for the circulatory lift $C_L^c$ is of the form of Eq. (2.6):

$$C_L^c(t) = 2\pi \left( \alpha(0)\phi_w(s) + \int_0^s \dot{\alpha}(\sigma)\phi_w(s-\sigma)d\sigma \right) \tag{2.7}$$

$s = 2U_\infty t/c$ is time normalized by half-chord convection time, $\phi_w$ is Wagner's indicial response function, and the inviscid lift slope $C_{L_\alpha} = 2\pi$ has been factored out.

A distinct advantage of Wagner's model is that it is formulated in the time domain, making it useful for arbitrary input maneuvers. However, the convolution integral model is not in a form that is easily incorporated into state-space models for use with modern control theory.

#### Theodorsen's model

Ten years later, in 1935, Theodorsen [114] derived a related model to study the aeroelastic problem of flutter instability. Theodorsen's model consists of added-mass

terms that account for the reaction force due to the mass of fluid directly accelerated by the airfoil, and circulatory terms that account for lift due to viscous forces. The circulatory terms consist of the effective angle of attack from the quasi-steady theory above, Eq. (2.3), multiplied by Theodorsen's transfer function $C(k)$, which relates sinusoidal inputs of reduced frequency $k = \omega c/2U_\infty$ to their aerodynamic response.

$$C_L = \underbrace{\frac{\pi}{2}\left[\ddot{h} + \dot{\alpha} - \frac{a}{2}\ddot{\alpha}\right]}_{\text{Added-Mass}} + \underbrace{2\pi\left[\alpha + \dot{h} + \frac{1}{2}\dot{\alpha}\left(\frac{1}{2} - a\right)\right]C(k)}_{\text{Circulatory}} \tag{2.8}$$

Lengths have been nondimensionalized by chord length $c$, and time is nondimensionalized by $c/U_\infty$, where $U_\infty$ is the free stream velocity. $C(k)$ is expressed in terms of Hankel functions $H_\nu^{(2)} = J_\nu - iY_\nu$ in the following way:

$$C(k) = \frac{H_1^{(2)}(k)}{H_1^{(2)}(k) + iH_0^{(2)}(k)} \tag{2.9}$$

where $J_\nu$ and $Y_\nu$ are Bessel functions of the first and second kind, respectively.

Theodorsen's model is particularly attractive since the various forces are isolated. With the exception of Theodorsen's function $C(k)$, which is expressed in the frequency domain, the model is an ordinary differential equation. However, this hybrid notation limits Theodorsen's model to sinusoidal input motions, which are sufficient for flutter analysis but not for use with modern control techniques. This model is extended to a state-space formulation in Chapter 6.

It is important to note that Theodorsen's original paper [114] addresses more than just the unsteady lift coefficient in response to angle of attack and vertical plunge motion. In particular, Theodorsen also computes the moment coefficient, includes the effect of an aileron, and analyses aeroelastic stability. The related problem of a sinusoidal gust is explored by von Kármán and Sears [124].

## 2.2 System identification with ERA/OKID

The eigensystem realization algorithm (ERA) was developed by Juang and Pappa [52, 51] to extend the minimal realization theory of Ho and Kalman [43] to systems with noisy data. The ERA produces reduced order models of a linear time-invariant system based on its Markov parameters $\mathcal{H}_i$, which are the output history from impulse-response experiments. When these parameters decay slowly, as in lightly damped systems, the ERA involves the inversion of a large input matrix. For this reason, the ERA is often used in conjunction with Observer/Kalman Filter Identification (OKID) [53, 88, 17, 87, 51] that constructs an asymptotically stable observer to identify the system. A major benefit of OKID is that Markov parameters may be identified for a system using input/output data from realistic maneuvers, such as actual flight data, as in Valasek *et al.* [120].

Recently, Ma *et al.* [68] have shown that the ERA efficiently produces the same reduced order models as the method of snapshot-based balanced proper orthogonal decomposition (BPOD) [128, 94], without the need for adjoint simulations. Balanced models have been effectively used for feedback control on a number of physical applications including the flat-plate boundary layer [4], flat plate at high

incidence [1], cavity resonances and combustion oscillations [47], and the transitional channel flow [46]. The work of Silva *et al.* [106, 105] has used the ERA and OKID to obtain reduced-order models from CFD for the unsteady aerodynamics excited by aeroelastic modes. In many of the examples above, balanced models have better performance at lower model order, compared against models obtained by Galerkin projection onto POD modes.

### 2.2.1 The eigensystem realization algorithm (ERA)

The eigensystem realization algorithm (ERA) identifies a reduced-order, discrete-time, state-space realization for a physical system based on snapshots $\mathcal{H}_k = y(k\Delta t)$ from an impulse response. ERA is a powerful tool for obtaining reduced-order models for linear dynamical systems of high dimension.

Consider a stable, discrete-time system with state vector $\mathbf{x}(k) \in \mathbb{R}^n$ and multiple inputs $\mathbf{u}(k) \in \mathbb{R}^p$ and outputs $\mathbf{y}(k) \in \mathbb{R}^q$:

$$\begin{aligned} \mathbf{x}(k+1) &= A\mathbf{x}(k) + B\mathbf{u}(k) \\ \mathbf{y}(k) &= C\mathbf{x}(k) + D\mathbf{u}(k) \end{aligned} \tag{2.10}$$

The *order* of the system refers to $n$, the dimension of the state vector $\mathbf{x}$. For fluid systems, the system order may be in the millions or larger. High-dimensional systems are expensive to simulate and are intractable for use with modern control techniques, which motivates the the need for approximate models of lower order.

The goal of model reduction is to obtain an approximation to the model in Eq. (2.10), in terms of a low-dimensional state vector $\mathbf{x}_r \in \mathbb{R}^r$, where $r \ll n$. The resulting model, Eq. (2.11), approximates the original system in the sense that it is *close* with respect to a given operator norm.

$$\begin{aligned} \mathbf{x}_r(k+1) &= A_r\mathbf{x}_r(k) + B_r\mathbf{u}(k) \\ \mathbf{y}(k) &= C_r\mathbf{x}_r(k) + D_r\mathbf{u}(k) \end{aligned} \tag{2.11}$$

Typically, one measures the agreement of the models in Eqs. (2.10) and (2.11) using the infinity norm, $\|G - G_r\|_\infty$, where $G$ and $G_r$ are the transfer function representations of the models above: $G \triangleq C(sI - A)^{-1}B + D$.

ERA is a method of model reduction based on impulse-response parameters that may be collected from experimental data or from numerical simulations. Following closely to Ma *et al.* [68], we review the main steps. First, collect data from an impulse response, which is defined as the output in response to setting $\mathbf{u}(k) = 1$ for $k = 0$ and $\mathbf{u}(k) = 0$ for $k \in \mathbb{Z}^+$. The measured output of the impulse response are called Markov parameters, $\mathcal{H}_k$, and are readily obtained by substituting the impulsive $\mathbf{u}(k)$ into Eq. (2.10) above:

$$\mathbf{u}(k) = \begin{cases} 1, & k = 0 \\ 0, & k \in \mathbb{Z}^+ \end{cases} \quad \Longrightarrow \quad \mathcal{H}_k \triangleq \mathbf{y}(k) = \begin{cases} D, & k = 0 \\ CA^{k-1}B, & k \in \mathbb{Z}^+ \end{cases} . \tag{2.12}$$

1. The first term in the impulse response is the $D$ matrix, or feed-through term.

2. Gather the next $(m_c + m_o) + 2$ output measurements from the impulse response, where $m_c$ and $m_o$ are integers representing the number of snapshots for controllability and observability. The Markov parameters $\mathcal{H}_k = CA^{k-1}B$

are synthesized into generalized Hankel matrices, $H$ and $H'$, where the elements of $H'$ are shifted forward by one time step.

$$H = \begin{bmatrix} CB & CAB & \cdots & CA^{m_c}B \\ CAB & CA^2B & \cdots & CA^{m_c+1}B \\ \vdots & \vdots & \ddots & \vdots \\ CA^{m_o}B & CA^{m_o+1}B & \cdots & CA^{m_c+m_o}B \end{bmatrix} \tag{2.13}$$

$$H' = \begin{bmatrix} CAB & CA^2B & \cdots & CA^{m_c+1}B \\ CA^2B & CA^3B & \cdots & CA^{m_c+2}B \\ \vdots & \vdots & \ddots & \vdots \\ CA^{m_o+1}B & CA^{m_o+2}B & \cdots & CA^{m_c+m_o+1}B \end{bmatrix} \tag{2.14}$$

**3.** Compute the singular value decomposition of $H$ from Eq. (2.13):

$$H = U\Sigma V^* = \begin{bmatrix} U_1 & U_2 \end{bmatrix} \begin{bmatrix} \Sigma_1 & 0 \\ 0 & 0 \end{bmatrix} \begin{bmatrix} V_1^* \\ V_2^* \end{bmatrix} = U_1\Sigma_1 V_1^* \tag{2.15}$$

**4.** If $r$ is the desired model order, let $\Sigma_r$ be the first $r \times r$ block of $\Sigma_1$, and let $U_r, V_r$ be the first $r$ columns of $U_1, V_1$. The $A_r, B_r$, and $C_r$ matrices in the reduced-order model in Eq. (2.11) are then given as follows:

$$A_r = \Sigma_r^{-1/2} U_r^* H' V_r \Sigma_r^{-1/2} \tag{2.16}$$

$$B_r = \text{ first } p \text{ columns of } \Sigma_r^{1/2} V_1^* \tag{2.17}$$

$$C_r = \text{ first } q \text{ rows of } U_r \Sigma_r^{1/2} \tag{2.18}$$

It is important to note that ERA is not only useful for model reduction when Eq. (2.10) is known. ERA is also useful for system identification when only the Markov parameters from Eq. (2.12) are known. This observation relies on the fact that the algorithm, in particular steps 2 and 3, only require knowledge of the Hankel matrices $H$ and $H'$, which are based on output measurements only.

Since it is often difficult to obtain an impulse response in experiments, it is useful to construct an *estimate* of the Markov parameters from a more realistic set of input-output data. Thus, the ERA is often used in conjunction with the observer/Kalman filter identification (OKID) method, which estimates the system Markov parameters from noisy input-output measurements.

### 2.2.2 Observer/Kalman filter identification (OKID)

The observer/Kalman filter identification (OKID) method was developed in part to compliment the ERA for lightly damped experimental systems with noise [53, 88, 17, 87, 51, 35]. In this section, the general problem of identifying Markov parameters from arbitrary input-output data is posed. After identifying a number of numerical complications, the OKID method is introduced to address these issues.

Recall that the response of the discrete system in Eq. (2.10) to an arbitrary input signal, with zero initial condition $\mathbf{x}(0) = 0$, may be written in terms of the Markov parameters $\mathcal{H}_i$ from Eq. (2.12):

$$\begin{bmatrix}\mathbf{y}(0) & \mathbf{y}(1) & \cdots & \mathbf{y}(n)\end{bmatrix} = \begin{bmatrix}\mathcal{H}_0 & \mathcal{H}_1 & \cdots & \mathcal{H}_n\end{bmatrix} \underbrace{\begin{bmatrix}\mathbf{u}(0) & \mathbf{u}(1) & \cdots & \mathbf{u}(n) \\ 0 & \mathbf{u}(0) & \cdots & \mathbf{u}(n-1) \\ \vdots & \vdots & \ddots & \vdots \\ 0 & 0 & \cdots & \mathbf{u}(0)\end{bmatrix}}_{U} \tag{2.19}$$

It is often possible to invert the matrix of control inputs, $U$, to solve for the Markov parameters. However, $U$ may be sparsely populated, so that either it is un-invertible, or inversion is ill-conditioned. In addition, $U$ is large for lightly damped systems, making inversion computationally expensive. Finally, experimental noise is not optimally filtered by simply inverting $U$ to solve for the Markov parameters.

The OKID method addresses each of these issues. Markov parameters $\mathcal{H}_i$ are computed by the following algorithm based on the work of Juang *et al.* [53]:

**1.** Choose the the number of observer Markov parameters to identify $p$.

**2.** Construct the data matrices below:

$$\mathbf{y} = \begin{bmatrix}\mathbf{y}(0) & \mathbf{y}(1) & \mathbf{y}(2) & \cdots & \mathbf{y}(p) & \cdots \mathbf{y}(l-1)\end{bmatrix} \tag{2.20}$$

$$V = \begin{bmatrix}\mathbf{u}(0) & \mathbf{u}(1) & \mathbf{u}(2) & \cdots & \mathbf{u}(p) & \cdots & \mathbf{u}(l-1) \\ & \mathbf{v}(0) & \mathbf{v}(1) & \cdots & \mathbf{v}(p-1) & \cdots & \mathbf{v}(l-2) \\ & & \mathbf{v}(0) & \cdots & \mathbf{v}(p-2) & \cdots & \mathbf{v}(l-3) \\ & & & \ddots & \vdots & \ddots & \vdots \\ & & & & \mathbf{v}(0) & \cdots & \mathbf{v}(l-p-1)\end{bmatrix} \tag{2.21}$$

where $\mathbf{v}(i) = \begin{bmatrix}\mathbf{u}(i) & \mathbf{y}(i)\end{bmatrix}^T$.

The matrix $V$ resembles $U$, except that it has been augmented with the outputs $\mathbf{y}(i)$. In this way, we are working with a system that is augmented to include a Kalman filter. Analogous to Eq. (2.19), we are now identifying the Markov parameters of the *augmented* system, $\bar{\mathcal{H}}$, using the equation $\mathbf{y} = \bar{\mathcal{H}}V$.

**3.** Identify the matrix $\bar{\mathcal{H}}$ of observer Markov parameters by solving $\mathbf{y} = \bar{\mathcal{H}}V$ for $\bar{\mathcal{H}}$ using the right pseudo-inverse of $V$.

**4.** Recover system Markov parameters $\mathcal{H}_k$ from the observer Markov parameters.

$$\mathcal{H}_k = \bar{\mathcal{H}}_k^{(1)} + \bar{\mathcal{H}}_k^{(2)} D + \sum_{i=0}^{k-1} \bar{\mathcal{H}}_i^{(2)} \mathcal{H}_{k-i-1} \tag{2.22}$$

where $D = \bar{\mathcal{H}}_{-1}$. The formula in Eq. (2.22) is derived in Juang *et al.* [53].

Thus, the OKID method identifies the observer Markov parameters of a system augmented with an asymptotically stable Kalman filter. The system Markov parameters are then extracted from the observer Markov parameters using Eq. (2.22).

The ERA and OKID methods will both be used extensively to identify unsteady aerodynamic models of the form given in Chapter 5. In Chapter 7 models are obtained from direct numerical simulations using the ERA. In Chapter 8 models are obtained from wind tunnel measurements using the combined ERA/OKID methods.

## 2.3 Galerkin projection of Navier-Stokes equations

The two-dimensional incompressible Navier-Stokes equations with an immersed boundary that satisfies no penetration and no slip are given by:

$$\frac{\partial \mathbf{u}}{\partial t} + (\mathbf{u} \cdot \nabla)\,\mathbf{u} = -\nabla p + \frac{1}{\mathrm{Re}}\nabla^{\mathbf{2}}\mathbf{u} + \int_S \mathbf{f}\left(\xi(s,t)\right)\delta(\xi - \mathbf{x})ds \tag{2.23}$$

$$\nabla \cdot \mathbf{u} = 0 \tag{2.24}$$

$$\mathbf{u}(\xi(s,t)) = \int_{\mathbf{x}} \mathbf{u}(\mathbf{x})\delta(\mathbf{x} - \xi)d\mathbf{x} = \mathbf{u}_B(\xi(s,t)) \tag{2.25}$$

The output equation of interest is the vector of forces resulting from the velocity field $u$, which may be expressed using the surface stress, $S_i$:

$$\mathcal{F}_i = \oint_{\partial B} S_i \; d\xi = \oint_{\partial B} \left[-p\mathbf{n} + \mu\nabla\mathbf{u}\right] d\xi \tag{2.26}$$

$$= \oint_{\partial B} \left[\Delta^{-1}\left(\nabla\mathbf{u} : \nabla\mathbf{u}\right)\mathbf{n} + \mu\nabla\mathbf{u}\right] d\xi \tag{2.27}$$

The pressure is a quadratic function of velocity, which may be seen by taking the divergence of both sides of the NS equation and using the incompressibility of $\mathbf{u}$.

It is possible to write this in the following dynamical systems notation:

$$\dot{x} = L^1 x + Q^1(x,x) + \mathbf{f} \tag{2.28}$$

$$y = L^2 x + Q^2(x,x) \tag{2.29}$$

where $L^1, L^2$ are linear operators and $Q^1, Q^2$ are bilinear quadratic forms.

The dynamics near an equilibrium $\bar{x}$ may be approximated by expanding the velocity field as a sum of $\bar{x}$ and a number of orthonormal basis modes $\{\varphi_i\}_{i=1}^r$, as in Eq. (2.30). Typically $r$ is chosen to be large enough that the approximation is good, yet small enough that the resulting system is of a significantly lower order.

$$x \approx \bar{x} + a_i\varphi_i \tag{2.30}$$

Substituting this into the dynamical system in Eq. 2.28, we find:

$$\dot{a}_k\varphi_k = L^1\left(\bar{x} + a_i\varphi_i\right) + Q^1\left(\bar{x} + a_i\varphi_i, \bar{x} + a_j\varphi_j\right) \tag{2.31}$$

$$= L^1\bar{x} + a_i L^1\varphi_i + Q^1(\bar{x},\bar{x}) + a_j Q^1(\bar{x},\varphi_j) + a_i Q^1(\varphi_i,\bar{x}) + a_i a_j Q^1(\varphi_i,\varphi_j)$$

$$= \underbrace{L^1\bar{x} + Q^1(\bar{x},\bar{x})}_{=0} + a_i \underbrace{\left[L^1\varphi_i + Q^1(\bar{x},\varphi_i) + Q^1(\varphi_i,\bar{x})\right]}_{=\tilde{L}^1\varphi_i} + a_i a_j Q^1(\varphi_i,\varphi_j)$$

Finally, because the modes $\varphi_i$ are orthonormal, we take the inner product of both sides with $\varphi_k$:

$$\dot{a}_k = a_i\langle\tilde{L}^1\varphi_i,\varphi_k\rangle + a_i a_j\langle Q^1(\varphi_i,\varphi_j),\varphi_k\rangle \tag{2.32}$$

$$= \hat{L}^1_{ik}a_i + \hat{Q}^1_{ijk}a_i a_j \tag{2.33}$$

where $\hat{L}^1_{ij}$ and $\hat{Q}^1_{ijk}$ are new linear and bilinear operators on mode coefficients. Plugging Eq. 2.30 into the output equation, Eq. 2.29 results in:

$$y = L^2(\bar{x} + a_i\varphi_i) + Q^2(\bar{x} + a_i\varphi_i, \bar{x} + a_j\varphi_j) \tag{2.34}$$

$$= \underbrace{L^2\bar{x} + Q^2(\bar{x},\bar{x})}_{=\bar{y}} + a_i \underbrace{\left[L^2\varphi_i + Q^2(\bar{x},\varphi_i) + Q^2(\varphi_i,\bar{x})\right]}_{=\tilde{L}^2\varphi_i} + a_i a_j Q^2(\varphi_i,\varphi_j) \tag{2.35}$$

Finally, the output $y$ is given by:

$$y_k = \bar{y}_k + \hat{L}^2_{ik}a_i + \hat{Q}^2_{ijk}a_i a_j \tag{2.36}$$

The subscript $k$ represents the $k$-th coordinate of $y$, and has nothing to do with the time step in a discrete-time formulation.

## 2.4 Finite-time Lyapunov exponents

To characterize the unsteady fluid dynamics of airfoils at low Reynolds numbers, it is important to identify regions of separated flow and wake structures. For an unsteady flow field, it is not possible to identify separated regions with instantaneous streamlines alone [41]. Lagrangian coherent structures [40, 41, 102, 37] (LCS) are unsteady analogues of the stable and unstable manifolds from dynamical systems theory. LCS are ridges in the field of finite-time Lyapunov exponents (FTLE) that satisfy an additional hyperbolicity condition [41]. The FTLE indicates the amount of stretching between neighboring particles, and is typically computed by integrating a grid of particles through a time-resolved sequence of velocity snapshots from an unsteady flow. A strength of the method is that the LCS are robust to noisy data as might be obtained using PIV measurements [41, 38].

FTLE fields may be computed using either forward or backward time integration of particle grids, in which case the LCS represent repelling or attracting material

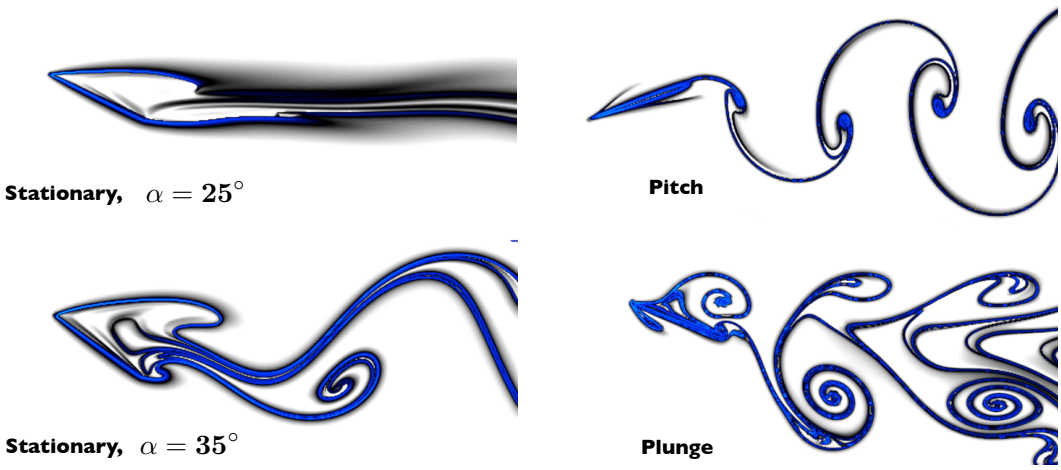


Figure 2.2: Canonical maneuvers of flat plate at Re = 100. (top left) Stationary $\alpha = 25°$, (bottom left) stationary $\alpha = 35°$, (top right) sinusoidal pitch (20° amplitude, $f = 0.4$ frequency), (bottom right) sinusoidal plunge (20° offset, $f = 0.4$ frequency).

lines, respectively. These material lines isolate regions of separated flow around the airfoil as well as the sluggish flow in the wake. Figure 2.2 shows the FTLE field for various configurations of a flat plate airfoil that are chosen to isolate individual motions and unsteady flow features [9]. The ridges, plotted in blue, indicate the separation bubble and wake regions. For the case of a stationary plate at $\alpha = 25°$ the velocity field is steady, and, therefore, the ridges are also steady and coincide with streamlines. However, each of the other three flows are unsteady, and the FTLE ridges do not coincide with streamlines.

Lagrangian coherent structures, and more generally ridges in the FTLE field, are transport barriers in forward and backward time. This fact is consistent with the view that LCS generalize the concepts of stable and unstable manifolds in finite-time to unsteady flow fields. Figure 2.3 shows a grid of particles advected with the flow, with the dominant FTLE ridge superimposed [13]. As time passes the particles on the exterior of the ridge rapidly flow by, from left to right, leaving the slow particles conglomerated on or in the interior of the ridge boundary. The bottom two flows do not have an *interior* region, and are qualitatively different than the first flow.

A detailed discussion of the standard computation of FTLE fields is given in Section 4.2.

## 2.5 Added-mass forces

Added-mass forces, which appear in Theodorsen's model in Eq. (6.2), are important unsteady fluid reaction forces in response to an accelerating body. Simply put, when a body is accelerated in a surrounding fluid, the fluid must accelerate out of the way of the body. This additional mass of fluid that is accelerated is referred to as the *apparent* or *added mass* due to the surrounding fluid. Figure 2.4 is a schematic depiction of the added mass of the fluid.

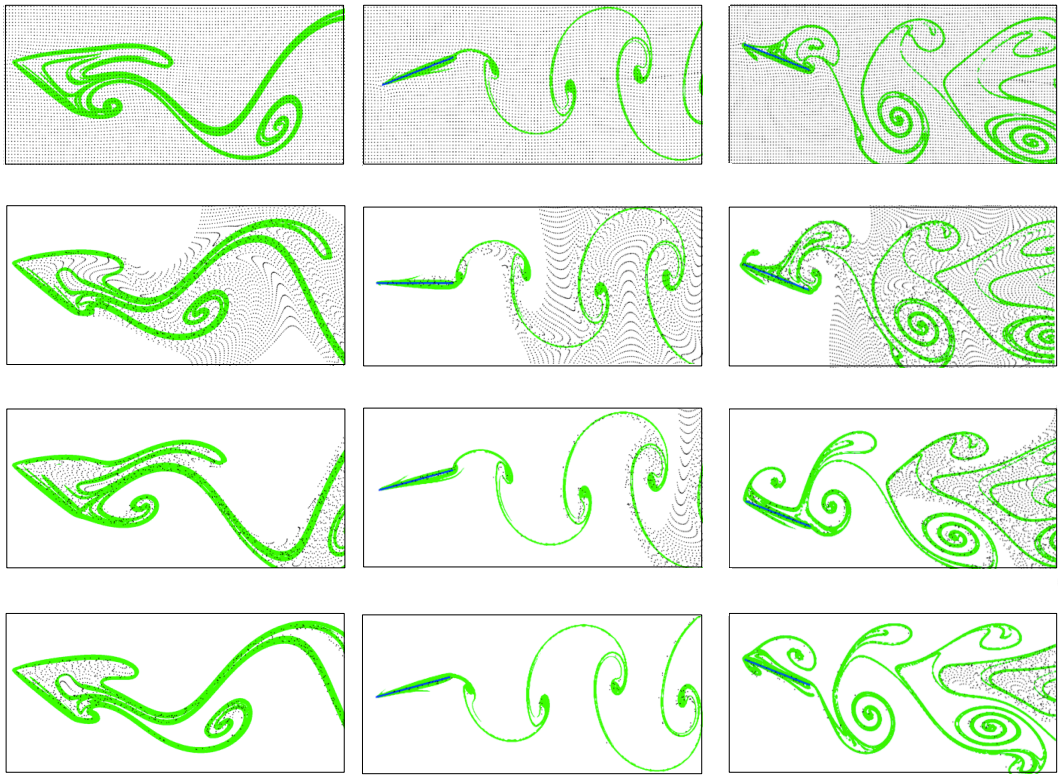

Figure 2.3: Validation of Lagrangian coherent structures as material lines with a grid of points integrated forward along velocity field snapshots. (left) Plate at $\alpha = 35°$, (middle) pitching plate, (right) plunging plate.

A simple and intuitive example of added mass arises in the physics of gas bubbles rising in a carbonated beverage. Based on the relative density of the displaced liquid and the gas bubble, we expect the buoyant force of the displaced liquid to cause a large acceleration of the gas bubble, on the order of hundreds of times the acceleration of gravity. However, because the bubble must accelerate liquid out of its way, equal to half of the volume of the bubble, the added-mass of the liquid greatly reduces the bubble's acceleration to about two times the acceleration due to gravity. There is a long and interesting history of the added-mass effect in rising bubbles [66].

Under certain assumptions, such as potential or Stokes flow, the added-mass formulation simplifies considerably. Consider the kinetic energy of a fluid accelerated by a body; for now, consider an ideal fluid that is inviscid and irrotational. Because of the linearity of the potential flow equations, it follows that the fluid velocity field induced by a moving body will be linearly proportional to the velocity of the body. Therefore, we may write the kinetic energy as

$$T_\phi = \rho \frac{I}{2} \|\mathbf{U}\|^2 \qquad \text{where} \qquad I = \int_V \frac{\mathbf{u}}{\|\mathbf{U}\|} \cdot \frac{\mathbf{u}}{\|\mathbf{U}\|} \, dV \tag{2.37}$$

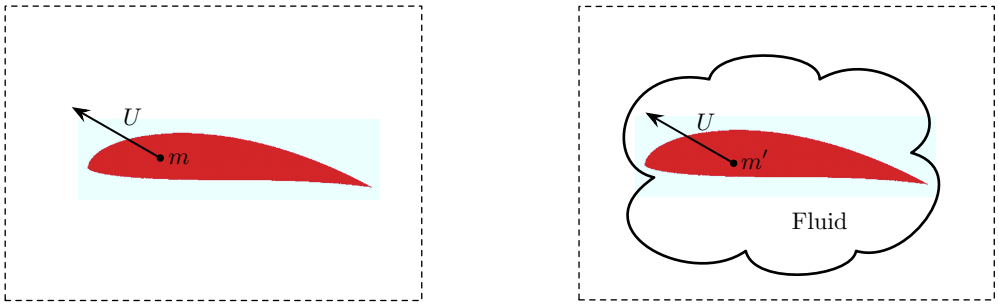


Figure 2.4: Schematic illustrating the added-mass effect. (left) Moving airfoil. (right) Moving airfoil and "added-mass".

Again, $\mathbf{u}$ is the fluid velocity field, and $\mathbf{U}$ is the velocity of the body. For a fixed motion, $I$ is constant.

$$\frac{dT_\phi}{dt} = -\mathbf{F}\cdot\mathbf{U} \quad \Longrightarrow \quad F_i = -\rho I_{ij}\dot{U}_j \tag{2.38}$$

The tensor $I_{ij}$ is not isotropic, since it depends on the direction of the flow. There are many detailed and thorough derivations of the theory of added-mass for potential flow [104, 75, 7].

## 2.6 Canonical pitch-up, hold, pitch-down maneuver

A canonical pitch-up, hold, pitch-down maneuver has been developed by the AIAA fluid dynamics technical committee (FDTC) on low-Reynolds number aerodynamics discussion group (2010-2011) [26, 79]. The purpose of this maneuver, given by Eq. (2.39), is to compare and study various experiments, simulations and models.

$$G_\alpha(t) = \log\left[\frac{\cosh(a(t-t_1))\cosh(a(t-t_4))}{\cosh(a(t-t_2))\cosh(a(t-t_3))}\right], \quad \alpha(t) = \alpha_{\max}\frac{G_\alpha(t)}{\max(G_\alpha(t))} \tag{2.39}$$

The time $t_1$ is the start of the pitch-up, $t_2$ is the end of the pitch-up and the beginning of the hold period, $t_3$ is the end of the hold and the beginning of the pitch-down, and $t_4$ is the end of the pitch-down, and consequently, the maneuver. $\alpha_{\max}$ is the angle of attack during the hold, and $a$ is a parameter that determines how gradual ($a$ small) or sharp ($a$ large) the corners are at $t_1, t_2, t_3$ and $t_4$.

Figure 2.5 shows a simulation of the maneuver for a flat plate at Re $= 100$ pitching about the leading edge. In this example, $t_1 = 1, t_2 = 3, t_3 = 4$, and $t_4 = 6$, $a = 11$ and $\alpha_{\max} = 45°$. There are a number of features in the flow field and lift measurement that make this an interesting maneuver. First, the sharp corners, linear ramps, and hold period separate the effects of $\ddot{\alpha}$, $\dot{\alpha}$ and $\alpha$ on the lift output. Additionally, a large leading edge vortex forms and sheds during the maneuver.

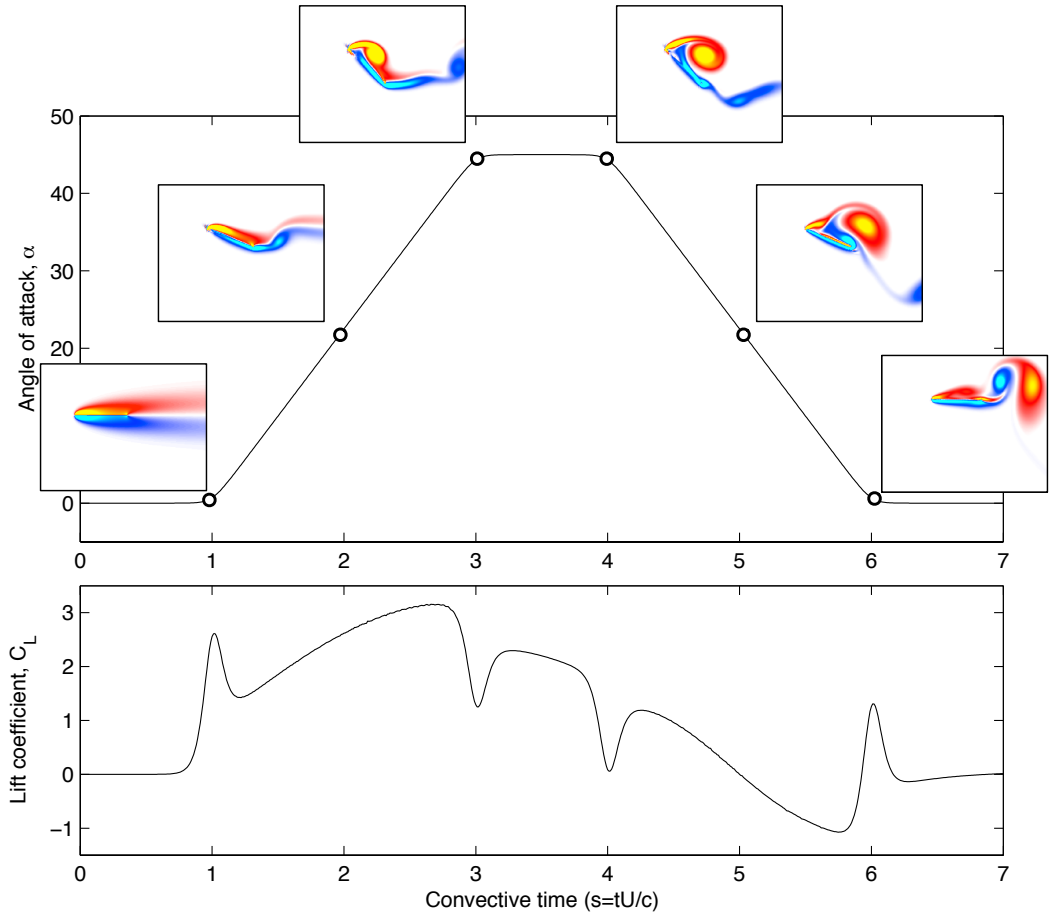


Figure 2.5: Canonical pitch-up, hold, pitch-down maneuver. (top) Angle of attack and (bottom) lift coefficient from simulation at Re = 100.

# Chapter 3

# Direct numerical simulations with unsteady base flow

The numerical results in this thesis are based on direct numerical simulations (DNS) of the incompressible 2D Navier-Stokes (NS) equations, using the multidomain immersed boundary projection method (IBPM) of Taira and Colonius [111, 19]. This chapter addresses a modification to the immersed boundary method to solve the NS equations in the body-fixed frame of a moving airfoil. In particular, the motion of the body is transferred to an unsteady base flow motion.

For a stationary body the boundary conditions are fixed, and it is possible to solve the projection equations in the IBPM by first computing a single Cholesky factorization at the beginning of the simulation [19], after which the equations may be solved rapidly for each subsequent timestep. When the body is in motion, the boundary conditions vary with time, and it is more efficient to use an iterative conjugate gradient method rather than to recompute the Cholesky factorization at each timestep. However, in the body-fixed frame of a moving airfoil, the boundary conditions are fixed, and it is possible to use a single Cholesky factorization, as in the case of the stationary body. This is more accurate than the iterative conjugate-gradient method and more efficient for a large number of timesteps. Additionally, it is possible to simulate large amplitude motions in the body-fixed frame that would otherwise leave the computational domain.

An overview of the immersed boundary projection method is presented in Section 3.1. Section 3.2 provides a description of the body-frame coordinate system and how the motion of the body may be transferred to an unsteady base flow. Section 3.3 describes the implementation, and in Section 3.4 the modified code (IBPM-UBF) is validated and benchmarked against the original code. This chapter is also intended to supplement the IBPM user manual.

## 3.1 Immersed boundary projection method

This section provides a brief overview of the immersed boundary projection method (IBPM) [111, 19]. The numerical method has been rigorously validated in two-dimensions on a number of example problems, as well as in three-dimensions against an oil tow tank experiment at $\mathrm{Re} = 100$ for a flat rectangular wing with low aspect ratio ($\mathrm{AR} = 2$) at $\alpha = 30^\circ$ [111, 19].

All of the numerical experiments presented here are based on the motion of a 2D flat plate at Reynolds number $\mathrm{Re} \equiv cU_\infty/\nu \in [100, 1000]$. The computational domain consists of five nested grids, the finest covering a domain of $4c \times 4c$ and the coarsest covering a domain of $64c \times 64c$, where $c$ is the chord length of the plate. Each grid has resolution $400 \times 400$, which is sufficiently fine for results to converge.

The 2D incompressible Navier-Stokes equations with an immersed boundary that satisfies no penetration and no slip are given in Eqs. (3.1−3.3):

$$\frac{\partial \mathbf{u}}{\partial t} + (\mathbf{u} \cdot \nabla)\,\mathbf{u} = -\nabla p + \frac{1}{\mathrm{Re}}\nabla^{\mathbf{2}}\mathbf{u} + \int_S \mathbf{f}\left(\xi(s,t)\right)\delta(\xi - \mathbf{x})ds \tag{3.1}$$

$$\nabla \cdot \mathbf{u} = 0 \tag{3.2}$$

$$\mathbf{u}(\xi(s,t)) = \int_{\mathbf{x}} \mathbf{u}(\mathbf{x})\delta(\mathbf{x} - \xi)d\mathbf{x} = \mathbf{u}_B(\xi(s,t)) \tag{3.3}$$

Here $\mathbf{u}$ is the fluid velocity field, $p$ is the pressure, $\mathbf{u}_B$ is the velocity of the immersed body, and $\mathbf{f}$ is the force on the body. Variables have been suitably nondimensionalized by the chord length $c$ and free-stream velocity $U_\infty$.

Figure 3.1 shows the vorticity contours and boundary layer profiles for a two-dimensional flat plate at various angle of attack. The flow is attached for $\alpha = 0°$ and $\alpha = 10°$. At $\alpha = 20°$, there is flow reversal and a stable separation bubble. For $\alpha = 30°$ and $\alpha = 40°$, the flow is fully separated and exhibits unsteady vortex shedding; the instantaneous vorticity field at a single phase is shown for these cases.

## 3.2 Body frame and flight dynamic coordinates

Consider a two-dimensional airfoil moving in a uniform flow field, as in Figure 3.2. The uniform base flow has magnitude $U_{\mathrm{BF}}$ at an angle $\alpha_{\mathrm{BF}}$ and the airfoil's position is specified as an element $g \in SE(2)$, where $SE(2) = \left\{(A, b) \,|\, A \in SO(2) \text{ and } b \in \mathbb{R}^2\right\}$ is the special Euclidean group of rotations and translations in $\mathbb{R}^2$. The motion of the airfoil is specified as an element $(g, \xi) \in TSE(2)$ with coordinates $(x, y, \theta, \dot{x}, \dot{y}, \dot{\theta})$. $TSE(2) = \{(g, \xi) \,|\, g \in SE(2) \text{ and } \xi \in T_gSE(2)\}$ is the tangent bundle of $SE(2)$, and $T_gSE(2)$ is the tangent space to $SE(2)$ at a point $g \in SE(2)$.

In flight dynamics, it is typical to represent the airfoil motion in a frame that is moving with the base flow, as shown in Figure 3.3. It is convenient to introduce the airfoil's velocity vector $\mathbf{V}$ and flight path angle $\gamma$, as well as the angle of attack $\alpha = -\theta - \gamma$, as in [110].

$$\mathbf{V} = \begin{bmatrix} \dot{x} - U_{\mathrm{BF}}\cos(\alpha_{\mathrm{BF}}) \\ \dot{y} - U_{\mathrm{BF}}\sin(\alpha_{\mathrm{BF}}) \end{bmatrix}, \qquad \gamma = \tan^{-1}\left(\frac{\dot{y} - U_{\mathrm{BF}}\sin(\alpha_{\mathrm{BF}})}{-\left(\dot{x} - U_{\mathrm{BF}}\cos(\alpha_{\mathrm{BF}})\right)}\right) \tag{3.4}$$

The flight path angle and the angle of attack are measured in the clockwise direction.

Figure 3.4 shows the airfoil in the body-fixed frame. The free stream velocity has magnitude $\|\mathbf{V}\|$ and angle $\alpha$, as well as a rotational component $-\dot{\theta}$ about the origin, which is the original center of rotation:

$$\mathbf{V}_{\mathrm{rot}}(x, y, t) = \begin{bmatrix} u_{\mathrm{rot}} \\ v_{\mathrm{rot}} \end{bmatrix} = \begin{bmatrix} \dot{\theta}(t) \cdot (y - y_C) \\ -\dot{\theta}(t) \cdot (x - x_C) \end{bmatrix} \tag{3.5}$$

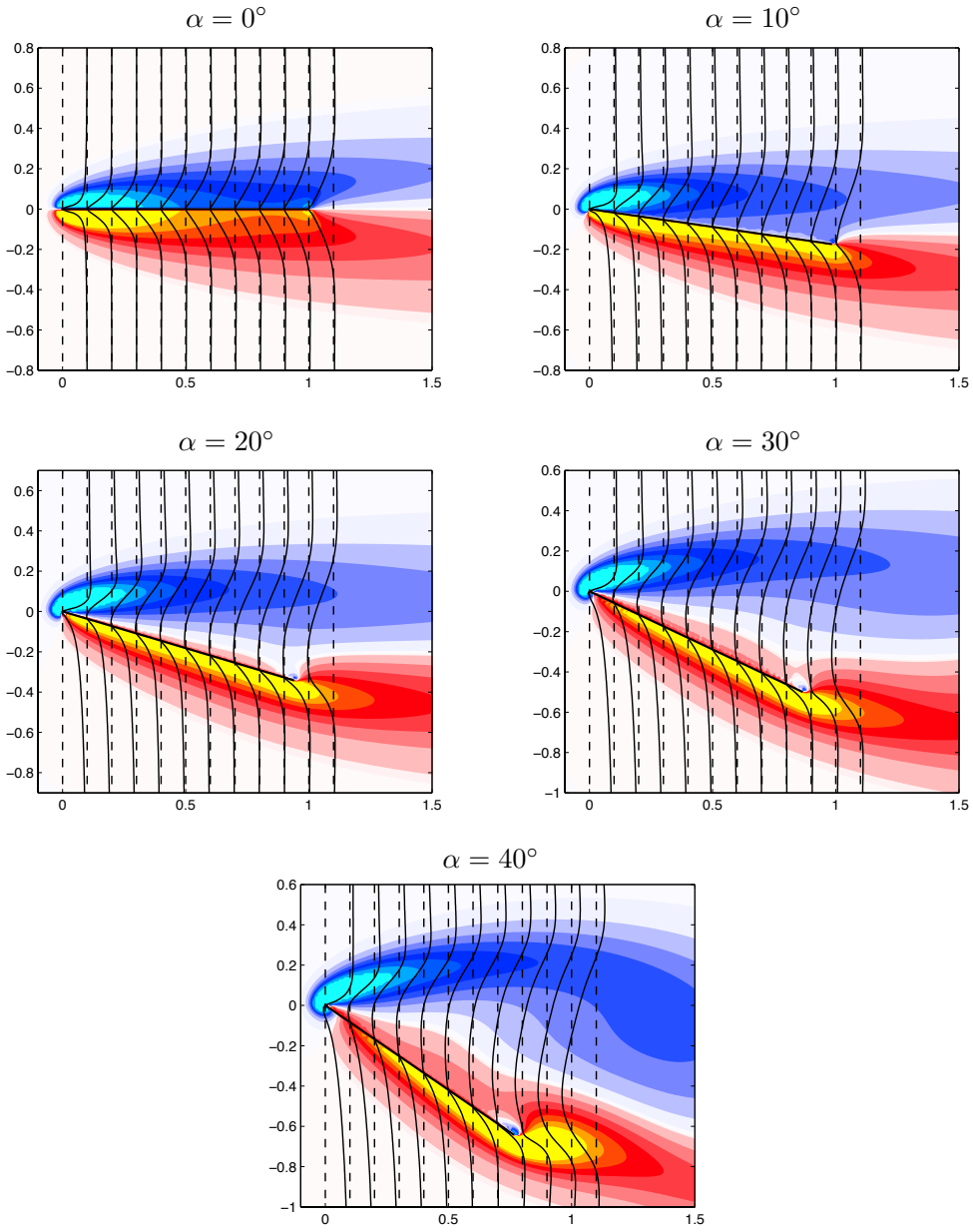


Figure 3.1: Vorticity contours and boundary layer profiles for a two-dimensional flat plate at various fixed angle of attack. Simulations are performed using the immersed boundary projection method at Re = 100. The flow is unsteady at $\alpha = 30°$ and $\alpha = 40°$, and an instantaneous vorticity field is shown for a particular phase of vortex shedding.

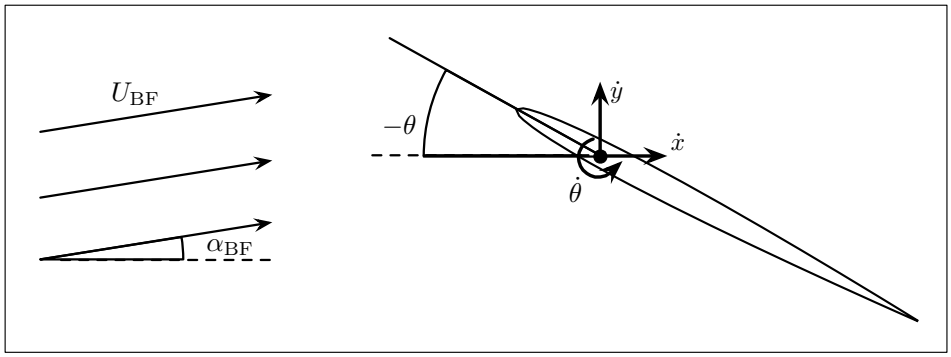


Figure 3.2: Moving airfoil in laboratory reference frame.

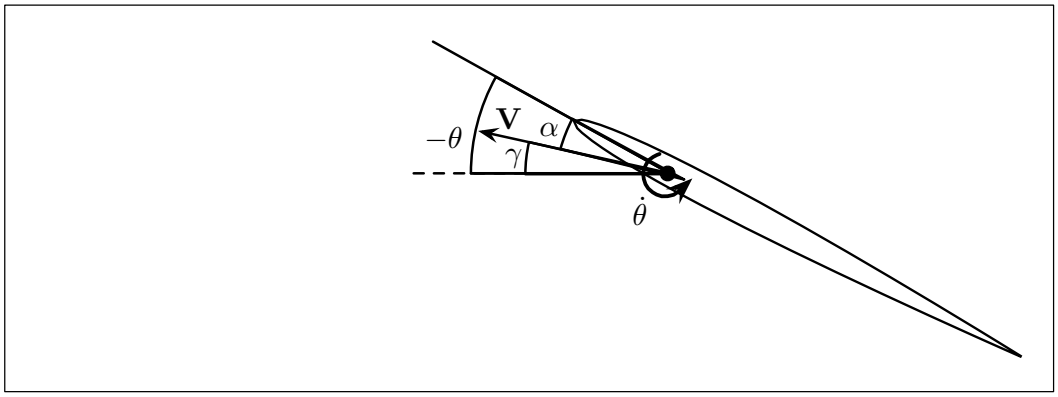


Figure 3.3: Moving airfoil in body center-of-mass frame.

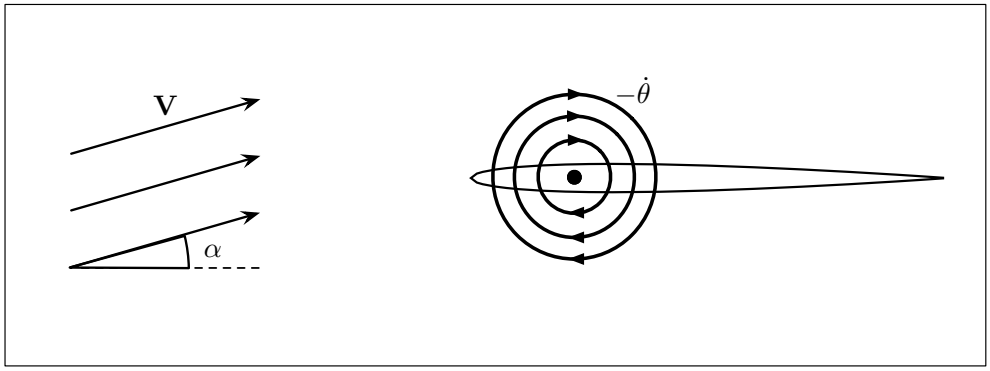


Figure 3.4: Moving airfoil in body-fixed frame.

$(x_C, y_C)$ is the center of rotation.

This yields the unsteady base flow velocity field:

$$u(x, y, t) = \|\mathbf{V}\| \cos(\alpha) + \dot{\theta}(y - y_C) \tag{3.6}$$

$$v(x, y, t) = \|\mathbf{V}\| \sin(\alpha) - \dot{\theta}(x - x_C) \tag{3.7}$$

with constant vorticity everywhere, given by

$$\omega = \nabla \times \begin{bmatrix} u & v \end{bmatrix}^T = v_x - u_y = -\dot{\theta} - \dot{\theta} = -2\dot{\theta} \tag{3.8}$$

Thus, an immersed body with motion given by $(g, \xi) \in TSE(2)$ may be viewed in the body-fixed reference frame with the induced unsteady base flow velocity field given by Eqs. (3.6) and (3.7). Note that the unsteady base flow at any instant is the superposition of a uniform flow and a solid body rotation, which have zero vorticity and constant vorticity everywhere, respectively. Using the immersed boundary method of Colonius and Taira [19], which is formulated with a nullspace approach and multi-domain far-field boundary conditions, it is possible to solve the NS equations (3.1−3.3) in the body-fixed frame by simply using Eqs. (3.6) and (3.7) in the place of a uniform base flow. This approach has been used in [18] for a flat plate plate accelerating in the $x$-direction. Demonstrating the validity of this approach rigorously using a symmetry reduction of $SE(2)$ to the body-fixed frame will be an interesting extension of this work.

## 3.3 Software implementation

The goal of this code is to solve the equations of motion in the body-fixed frame by transferring the motion of a given body to a motion of an unsteady base flow. In the IBPM code, an instance of the `Geometry` class may consist of multiple `RigidBody` objects, each with its own `Motion`, as in Figure 3.5, and the following pseudo-code:

```
Geometry:
    RigidBody1->Motion1  [Primary]
    RigidBody2->Motion2
    ...
    RigidBodyN->MotionN
```

The first element in the list, `RigidBody1`, is considered the *primary* rigid body; the body-frame coordinates are referenced to this body. There must be a method to transfer the motion from the *primary* rigid body to the base flow. Currently the unsteady base flow is only implemented for a single rigid body; however, if there are multiple rigid bodies, they must each be transformed into the body-fixed frame of the *primary* body.

The following pseudo-code describes the `transferMotion` method of the `Geometry` class. It is currently not possible to perform group operations on `Motion` elements, and so it is not trivial writing each of the other body motions in a frame fixed to the first body. This is the subject of ongoing work.

```
Motion* Geometry::transferMotion() {
    vector<RigidBody>::iterator body;
```

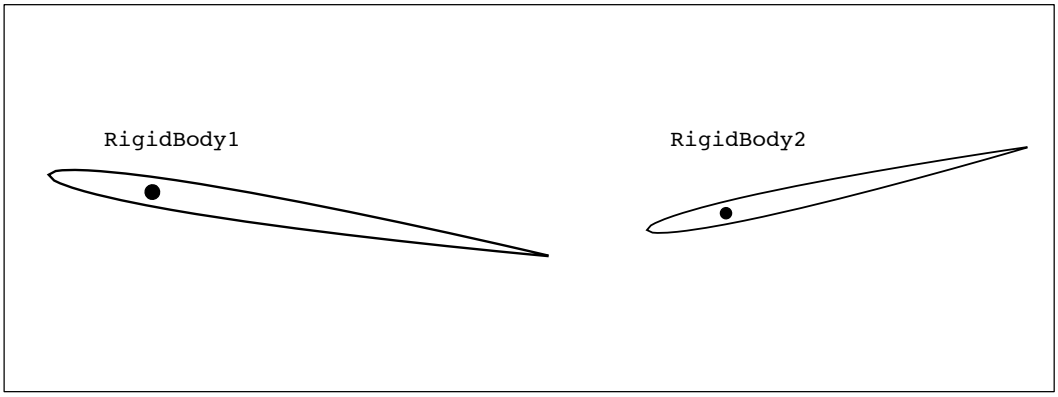


Figure 3.5: Schematic of multiple rigid bodies, as represented in code.

```
    Motion* _bfMotion = NULL;
    body = _bodies.begin();
    _bfMotion = body->getMotion();
    for(body=_bodies.begin();body!=_bodies.end();++body) {
       body->setMotion(body->getMotion() - _bfMotion)
    }
    return _bfMotion
}
```

### 3.3.1 Unsteady base flow usage

To use the unsteady base flow functionality, the user adds `-ubf True` to the `ibpm` command line call. This makes it possible to reuse existing scripts and geometry files with minimal modification, as in the following example:

```
>> ./build/ibpm -Re 100 -geom cylinder.geom -dt 1.e-2 -ubf True
```

```
# cylinder.geom
body Cylinder
  circle_n 0 0 0.5 314
  motion PitchPlunge 0, 0, 1, 1
end
```

### 3.3.2 Lift measured from flight path angle

In the new IBPM-UBF code, the lift force is the component of force perpendicular to the velocity vector $\mathbf{V}$ from Eq. (3.4), as in [110]. The original IBPM code does not correct for the change in $\mathbf{V}$ when the body is in motion, $(\dot{x}, \dot{y}) \neq (0, 0)$. Therefore, in the original IBPM code, the lift and drag forces are simply the force components in the vertical and horizontal directions in the lab frame.

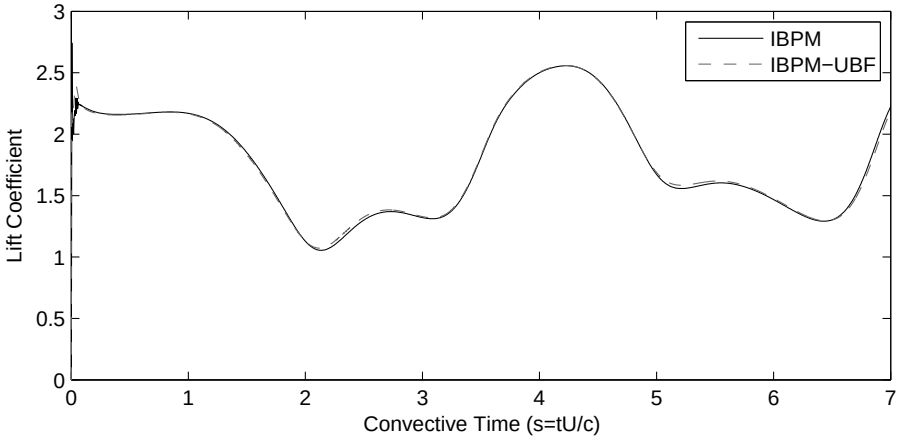


Figure 3.6: Comparison of lift coefficient for stationary plate at $\alpha = 45°$.

## 3.4 Validation and benchmarks

In this section, the IBPM-UBF code is validated against the IBPM code on a number of test cases. In Section 3.4.1, the codes are compared for an impulsively started flat plate at fixed angle of attack $\alpha = 45°$. In Section 3.4.2, the codes are compared for a large amplitude pitching maneuver at various pitch axis locations. Section 3.4.3 summarizes the computation time of both methods. In the psuedo-code that follows, `developedBL.bin` is a binary file containing the `State` (fluid state) for a flat plate with a fully developed boundary layer. The other command line options may be found in the IBPM manual.

### 3.4.1 Stationary, $\alpha = 45°$, Re $= 300$

The following code is used to simulate the flow past an impulsively started flat plate at 45° inclination:

```
>> ./build/ibpm -nx 200 -ny 200 -ngrid 5 -length 4 -xoffset 1.5
    -yoffset -2 -geom stationary_a45.geom -Re 300 -ic developedBL.bin
    -dt .01 -nsteps 700 -ubf True

# stationary_a45.geom
body Plate
    line 0 0 1 0 0.02   #  points on a line, spaced approximately 0.02
    center 0.25 0        #  center at quarter-chord
    motion FixedPosition 0 0 45. #  x, y, theta (deg)
end
```

Figure 3.6 shows the lift coefficient from the IBPM and IBPM-UBF simulations. The vorticity fields are plotted in Figure 3.7. The agreement of the IBPM and IBPM-UBF simulations in both the lift coefficient and the vorticity fields confirms the accuracy of the new IBPM-UBF method.

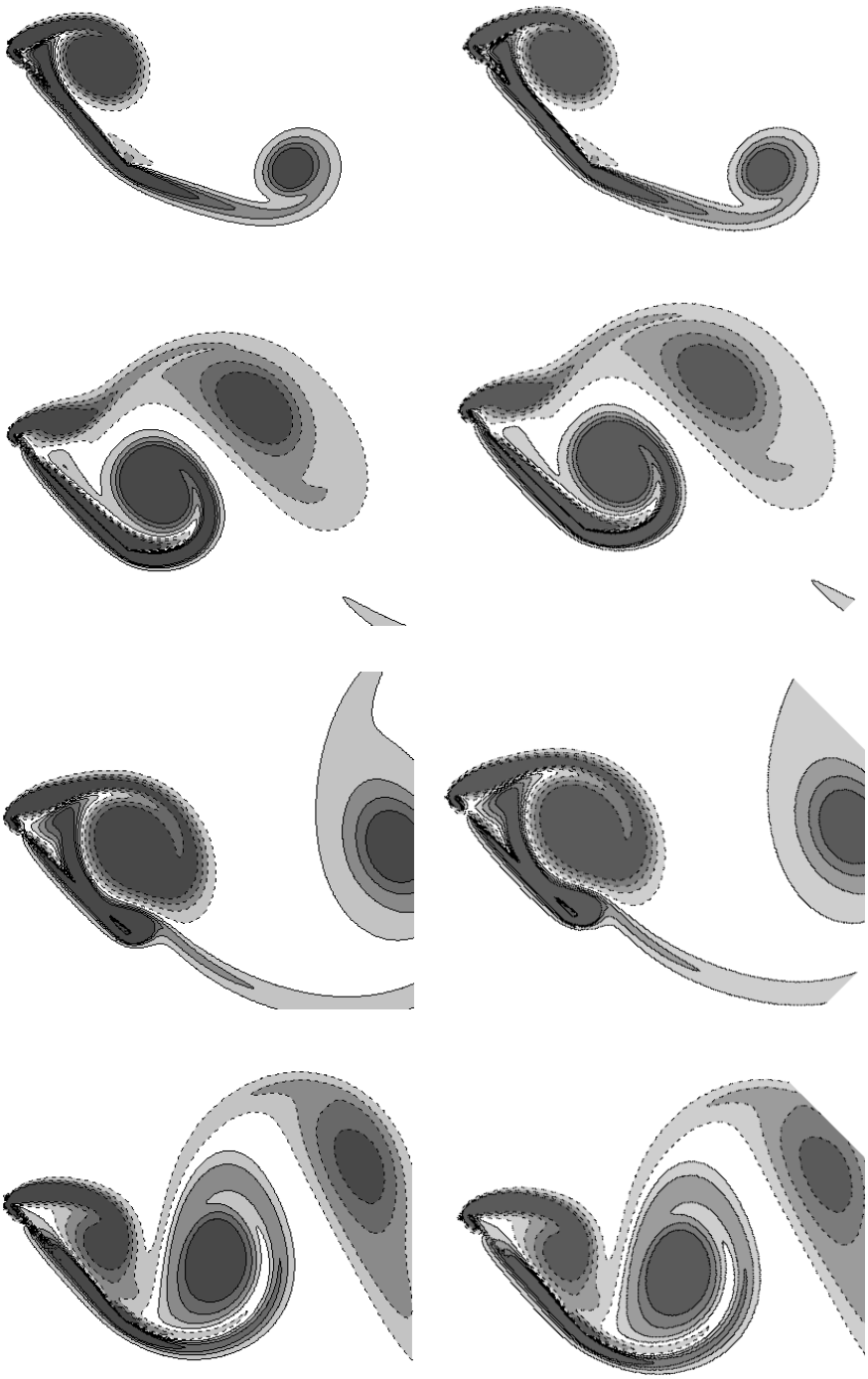

Figure 3.7: Comparison of IBPM (left) and IBPM-UBF (right) for a two-dimensional flat plate at $\alpha = 45°$ (Re = 300). From top to bottom: $t = 1.0$, $t = 3.0$, $t = 5.0$, and $t = 7.0$. Vorticity contours are plotted, and the IBPM-UBF solution is rotated by 45°.

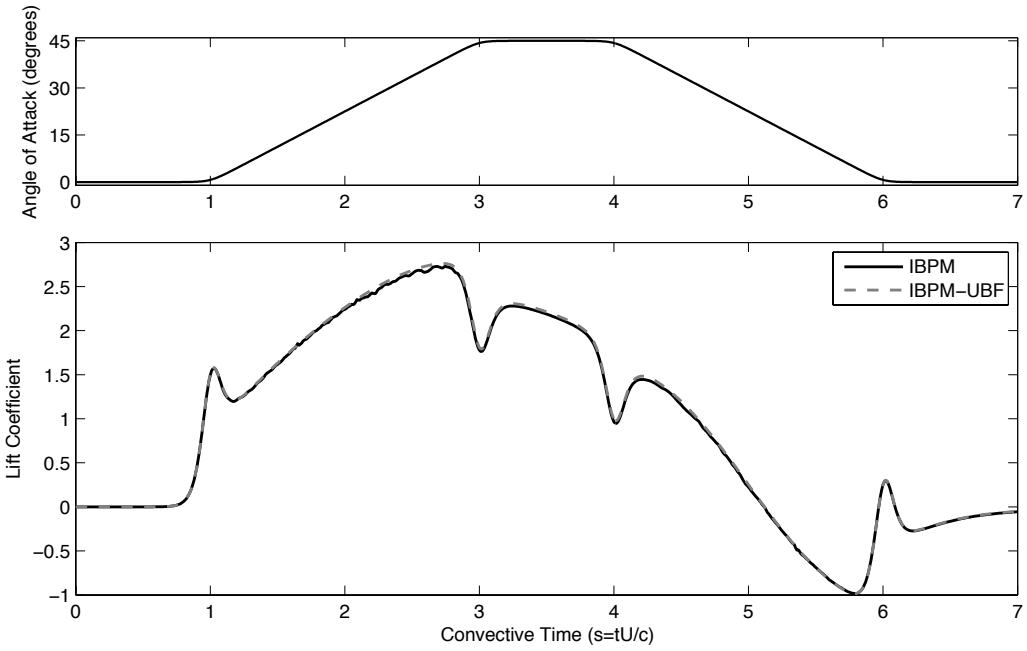


Figure 3.8: Canonical pitch-up, hold, pitch-down maneuver about quarter chord.

### 3.4.2 Pitching about various points

The following large amplitude pitching maneuvers are based on the canonical maneuver from Eq. (2.39) in Section 2.6. Figure 3.8 shows the lift coefficient from both codes for pitching about the quarter-chord, and Figure 3.9 is for pitching about the mid-chord.

**Pitching about quarter-chord, $\alpha_{\max} = 45°$**

```
>> ./build/ibpm -nx 200 -ny 200 -ngrid 5 -length 4 -xoffset -1.5
    -yoffset -2 -geom canonical_p25_a45.geom -Re 100 -ic developedBL.bin
    -dt .01 -nsteps 700 -ubf True

# canonical_p25_a45.geom
body Plate
    line 0 0 1 0 0.02   #  points on a line, spaced approximately 0.02
    center 0.25 0       #  center at quarter-chord
    motion Canonical 45 11 1. 3. 4. 6. #  AMP (deg), a, t1, t2, t3, t4
end
```

**Pitching about mid-chord, $\alpha_{\max} = 10°$**

```
>> ./build/ibpm -nx 400 -ny 400 -ngrid 5 -length 4 -xoffset -1.5
   -yoffset -2 -geom canonical_p50_a10.geom -Re 100 -ic developedBL.bin
   -dt .01 -nsteps 700 -ubf True
```

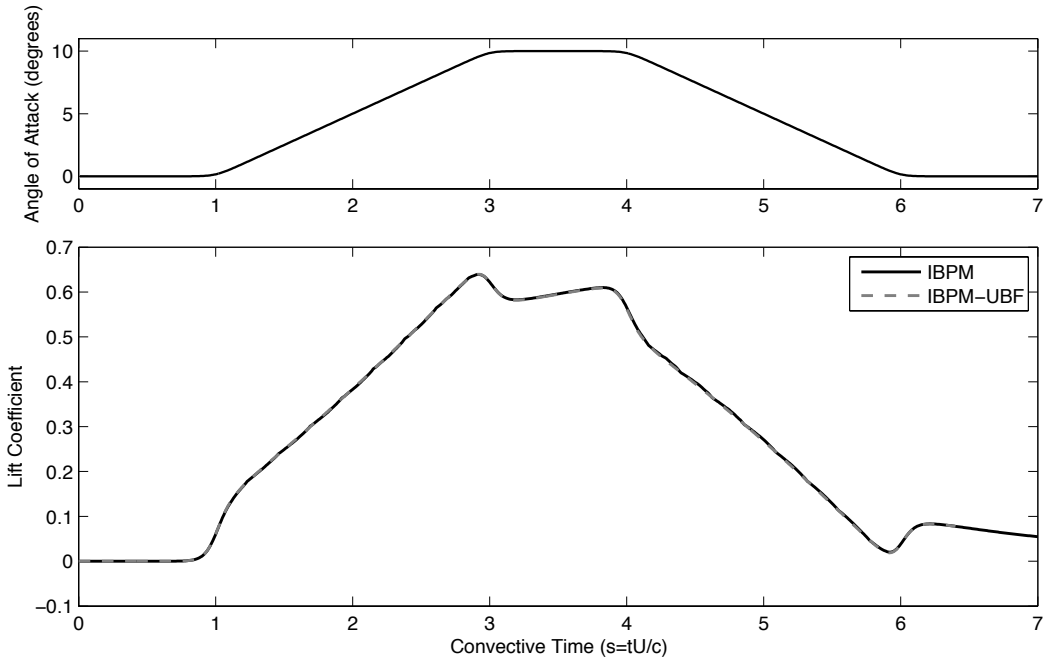


Figure 3.9: Canonical pitch-up, hold, pitch-down maneuver about mid chord.

```
# canonical_p50_a10.geom
body Plate
    line 0 0 1 0 0.01   #  points on a line, spaced approximately 0.01
    center 0.50 0       #  center at mid-chord
    motion Canonical 10 11 1. 3. 4. 6. #  AMP (deg), a, t1, t2, t3, t4
end
```

### 3.4.3 Computational speed-up

The IBPM-UBF code is 24X faster than the IBPM code for the canonical pitch-up, hold, pitch-down maneuver about the quarter-chord with grid resolution $200 \times 200$ and 700 timesteps with $\Delta t = 0.01$, shown in Figure 3.8. The IBPM-UBF code ran in 00:04:40, while the IBPM code ran in 01:51:20. For the canonical maneuver about the middle-chord with higher resolution $400 \times 400$, the IBPM-UBF code requires a smaller timestep, $\Delta t = .005$ for stability, while the IBPM code uses $\Delta t = .01$. In this case, the IBPM-UBF code is 12X faster.

The reason for this speed-up is that in the body-fixed frame the boundary conditions are fixed, and it is possible to use the same Cholesky factorization to efficiently solve the projection equations at each timestep. At a given timestep, computing the Cholesky factorization is more expensive than solving the projection equations using a conjugate-gradient iteration. However, if the body is stationary relative to the grid, a single Cholesky factorization may be computed at the beginning of the simulation, and each subsequent timestep is computed more rapidly than when using conjugate-gradient iteration.

## 3.5 Summary of numerical methods

This chapter extends the immersed boundary projection method to simulate unsteady flow fields in the body-frame of a moving wing. The modified code, based on an unsteady base flow formulation, is more accurate and an order of magnitude faster than the original code when solving for the fluid flow over a moving body. Additionally, the new IBPM-UBF code is able to solve for large amplitude wing motions that would have left the computational domain in the IBPM code.

# Chapter 4

# Fast computation of finite-time Lyapunov exponent fields for unsteady flows

Finite-time Lyapunov exponent (FTLE) fields are useful for visualizing unsteady aerodynamic flows, such as those studied in this thesis, since they identify regions of separated flow as well as wake structures. Figure 4.1 shows the lift and drag coefficients for a rapid pitch-up maneuver about the middle-chord to an angle of $\alpha = 32^\circ$ for a two-dimensional flat plate airfoil at low Reynolds number, Re = 300. The FTLE fields in this figure illustrate flow structures associated with the transient high and low lift configurations. Additionally, FTLE fields are useful for understanding the breakdown of classical unsteady aerodynamic models at large reduced frequency and Strouhal number, as shown in [9].

Lagrangian coherent structures (LCS) are hyperbolic material lines or surfaces that provide a useful analogue of invariant manifolds for unsteady flow fields. LCS are often determined as ridges of the field of FTLE that satisfy an additional hyperbolicity criterion. Since the FTLE field is computed using velocity field snapshots from the full nonlinear Navier-Stokes equations, the resulting LCS reveal the invariant manifold structure of the underlying nonlinear dynamical system. However, FTLE fields are expensive to compute due to the large number of particle trajectories that must be integrated to construct a particle flow map. Moreover, it is often necessary to compute a sequence of FTLE fields in time to visualize unsteady events. The methods presented here speed-up the computation of a sequence of FTLE fields by removing redundant trajectory integrations between neighboring particle flow maps. There are two categories of methods that approximate the particle flow map. The unidirectional method composes intermediate flow maps of the same time direction, and the bidirectional method composes intermediate flow maps of opposite time directions. It is shown that the unidirectional method is both fast and accurate, providing orders of magnitude computational savings over the standard method, when computing a sequence of FTLE fields in time to visualize the coherent structures of an unsteady flow. These methods have been published in [10].

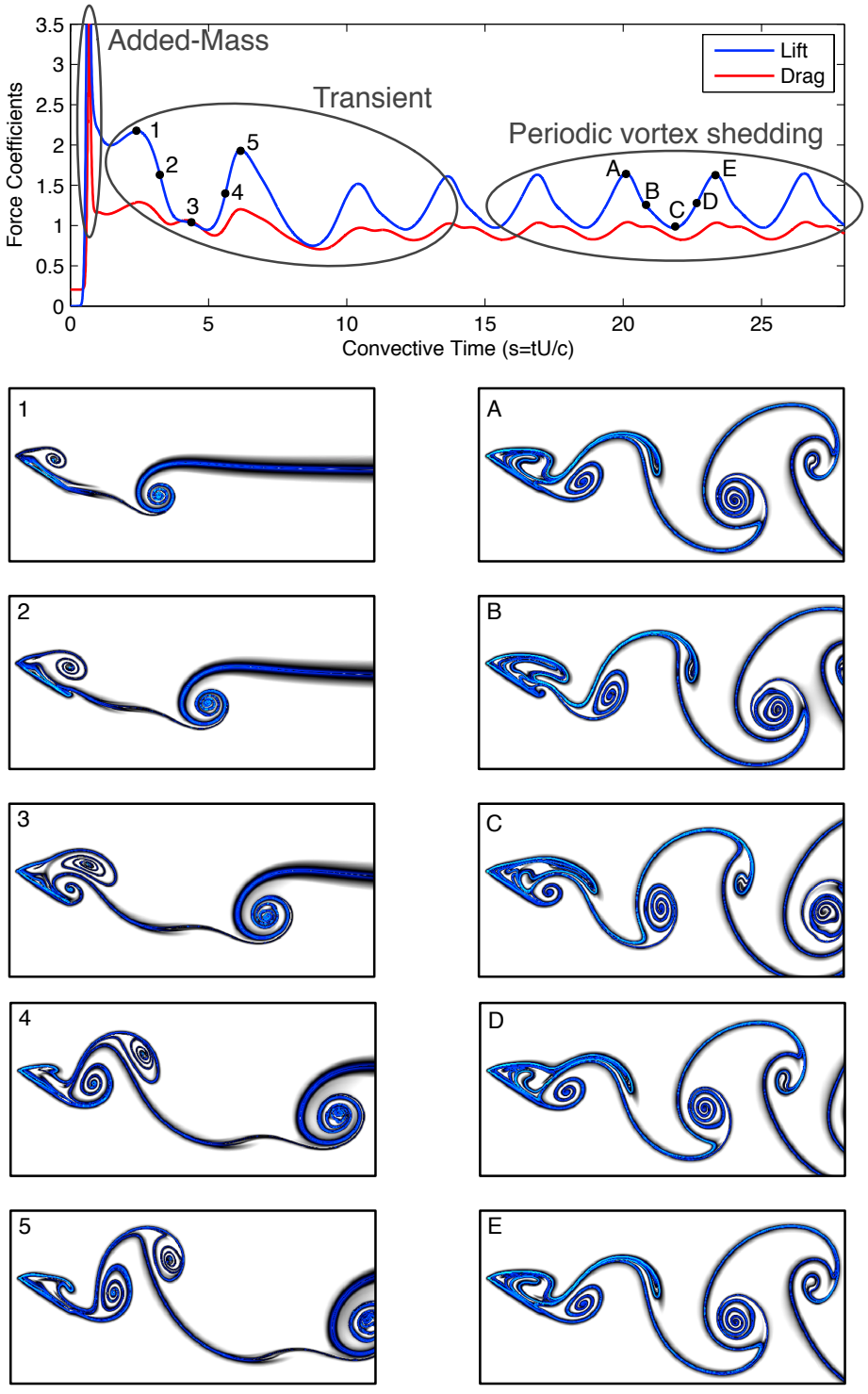


Figure 4.1: (top) Lift and drag coefficients for a two-dimensional flat plate undergoing a rapid pitch-up to 32° about the middle-chord at Re = 300. (left, right) FTLE fields for a single vortex shedding period.

## 4.1 Introduction

Coherent structures are important for understanding and modeling the underlying physical mechanisms of complex fluid flows [45]. In particular, Lagrangian coherent structures (LCS) are defined using particle trajectories and are Galilean-invariant, unlike Eulerian criteria [42]. LCS are hyperbolic material lines or surfaces [41] that extend the notion of invariant manifolds from dynamical systems theory to unsteady flows. Ridges of the finite-time Lyapunov exponent (FTLE) field provide candidate material lines that are LCS if and only if the Lagrangian rate of strain is nonzero along the ridge, distinguishing true hyperbolic material lines from regions of high shear [41]. A ridge of the FTLE field can refer to either a curvature or second derivative ridge, although the latter is more convenient for practical computation [102]. FTLE fields provide a measure of the stretching between nearby particles in a given flow and are important in determining transport mechanisms and separatrices in unsteady flows.

The theory and computation of finite-time Lyapunov exponents (FTLE), also known as direct Lyapunov exponents (DLE), is a relatively modern development [41, 102], with extensions to 3-dimensional [37, 40] and $n$-dimensional [64] flows. FTLE analysis has been widely applied in a number of branches of fluid mechanics, including fluid transport [97, 28, 101], bio-propulsion [83, 130, 36], flow over airfoils [67, 13, 9], plasmas [80], and geophysical flows [62, 63].

FTLE analysis is particularly useful for time-varying flows, where it becomes necessary to compute a sequence of FTLE fields in time. As flows become more complex, computations become increasingly expensive. In particular, FTLE calculations are expensive because a large number of particle trajectories must be integrated in order to obtain a particle flow map, often from stored velocity fields. When computing a sequence of FTLE fields in time, it is possible to speed up the computation considerably by eliminating redundant particle integrations. One approach that has been developed uses adaptive mesh refinement to reduce the number of integrations [31, 32, 96, 103].

The approach here is to construct an approximate flow map by composing intermediate flow maps from FTLE field calculations at neighboring times. The first class of flow map approximation, denoted bidirectional composition, constructs a flow map by composing intermediate flow maps that are aligned in both positive and negative-time. The second class, denoted unidirectional composition, composes intermediate flow maps that are all aligned in the same time direction. The methods are compared using analytic estimates for accumulated error and computation time as well as benchmarks on a number of example flows.

### 4.1.1 Main results

In this chapter we demonstrate that the unidirectional method is both fast and accurate, although it requires significantly more memory than the bidirectional method. Orders of magnitude speed-up may be achieved over the standard method, and computational improvement scales with the desired time resolution of the FTLE animation.

The bidirectional method suffers from significant error. In particular, the errors in the positive-time LCS (pLCS) align with the negative-time LCS (nLCS) and

vice versa. To understand this coherent error, we provide an error analysis for both methods, and uncover an important relationship between the pLCS and nLCS, which correspond to finite-time unstable and stable manifolds, respectively. In particular, in the neighborhood of a time-dependent saddle, particles near the pLCS flow into particles near the nLCS in positive time.

## 4.2 Standard computation of finite-time Lyapunov exponents

Consider a time-dependent velocity field $\mathbf{u}$ on $\mathbb{R}^n$ and a particle trajectory $\mathbf{x}(t)$ which satisfies

$$\dot{\mathbf{x}} = \mathbf{u}\left(\mathbf{x}(t), t\right). \tag{4.1}$$

The velocity field, $\mathbf{u}$, may be an unsteady solution of the Navier-Stokes equation, although it is only assumed that $\mathbf{u}$ is at least continuous, $C^0$, in time and continuously differentiable, $C^1$, in space. However, to extract Lagrangian coherent structures from the Hessian of the FTLE field, $\mathbf{u}$ must be twice continuously differentiable, $C^2$, in space [102]. The velocity field may be analytically defined, but is more often obtained from experiments or direct numerical simulation that produce velocity field data at discrete snapshots over a finite range of time. A method of computing finite-time Lyapunov exponents (FTLE) on a finite amount of discrete velocity field data was developed in [41, 102].

Computing an FTLE field typically involves four steps. First, a grid of particles $X_0 \subset \mathbb{R}^n$ is initialized over the domain of interest. The particles are advected (i.e., integrated) with the flow from initial time 0 to final time $T$, resulting in a time-$T$ particle flow map, $\Phi_0^T$, defined as:

$$\Phi_0^T : \mathbb{R}^n \to \mathbb{R}^n; \quad \mathbf{x}(0) \mapsto \mathbf{x}(0) + \int_0^T \mathbf{u}(\mathbf{x}(\tau), \tau) d\tau. \tag{4.2}$$

Next, the flow map Jacobian, $\mathbf{D}\Phi_0^T$ is computed, usually by finite-differencing, to obtain the Cauchy-Green deformation tensor,

$$\Delta = \left(\mathbf{D}\Phi_0^T\right)^* \mathbf{D}\Phi_0^T \tag{4.3}$$

where $^*$ denotes transpose. Finally, the largest eigenvalue, $\lambda_{\max}$, of this symmetric tensor is evaluated at each grid location, resulting in the FTLE field:

$$\sigma(\Phi_0^T; \mathbf{x_0}) = \frac{1}{|T|} \log \sqrt{\lambda_{\max}(\Delta(\mathbf{x_0}))}. \tag{4.4}$$

The bottleneck in this procedure is the large number of particle integrations required to obtain the particle flow map, $\Phi_0^T$. Moreover, if the velocity field is time-varying, it is necessary to compute a sequence of FTLE fields in time to visualize unsteady events, as shown schematically in Fig. 4.2.

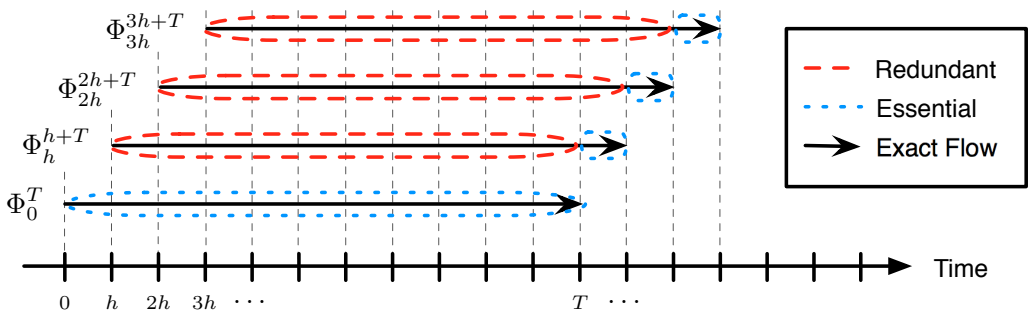


Figure 4.2: The standard method for computing a sequence of FTLE fields. Flow maps $\Phi_{kh}^{kh+T}$ for $k \in \{0, 1, 2, 3\}$ (solid black arrow) are broken into essential (blue dotted) and redundant (red dashed) particle integrations.

## 4.3 Flow map approximation

As seen in Fig. 4.2, the standard method of computing a sequence of FTLE fields involves inefficient re-integration of particles. The unidirectional and bidirectional methods outlined below streamline the computation of neighboring FTLE fields by approximating the time-$T$ flow map, $\Phi_{t_0}^{t_0+T}$, which can be written as:

$$\Phi_{t_0}^{t_0+T} \quad = \quad \Phi_{t_{N-1}}^{t_N} \circ \cdots \circ \Phi_{t_1}^{t_2} \circ \Phi_{t_0}^{t_1} \tag{4.5}$$

where $t_N = t_0 + T$.

Because the flow maps are obtained numerically on a discrete grid of points, $X_0 \subset \mathbb{R}^n$, it is necessary to interpolate the maps at points $\mathbf{x} \notin X_0$. Consider a flow map $\Phi : \mathbb{R}^n \to \mathbb{R}^n$, and the same flow map restricted to $X_0$, $\Phi|_{X_0} : X_0 \to \mathbb{R}^n$. The interpolation operator $\mathcal{I}$ takes the discrete map $\Phi|_{X_0}$ and returns the interpolated map, $\mathcal{I}\Phi : \mathbb{R}^n \to \mathbb{R}^n$, which approximates $\Phi$ on $\mathbb{R}^n$:

$$\mathcal{I} : \Phi|_{X_0} \mapsto \mathcal{I}\Phi. \tag{4.6}$$

Here we use the shorthand $\mathcal{I}\Phi \triangleq \mathcal{I}\left(\Phi|_{X_0}\right)$. We now obtain an approximation to the flow map in Eq. (4.5):

$$\begin{aligned} \tilde{\Phi}_{t_0}^{t_0+T}(X_0) &= \mathcal{I}\Phi_{t_{N-1}}^{t_N} \circ \cdots \circ \mathcal{I}\Phi_{t_1}^{t_2} \circ \Phi_{t_0}^{t_1}(X_0) \\ &\approx \Phi_{t_0}^{t_0+T}(X_0) \end{aligned} \tag{4.7}$$

The bidirectional method approximates the time-$T$ flow map $\Phi_{t_0}^{t_0+T}$ by first integrating backward to a reference time, $t = 0$, then interpolating forward through a previously computed time-$T$ map, $\Phi_0^T$, and finally integrating forward to time $t_0+T$. The unidirectional method approximates the time-$T$ flow map by composing a number of smaller time flow maps, $\Phi_{t_i}^{t_i+h}$, which all have the same time direction. Additionally, the chain rule may be applied to each of the methods, resulting in an approximation to the flow map Jacobian, $\mathbf{D}\Phi_{t_0}^{t_0+T}$.

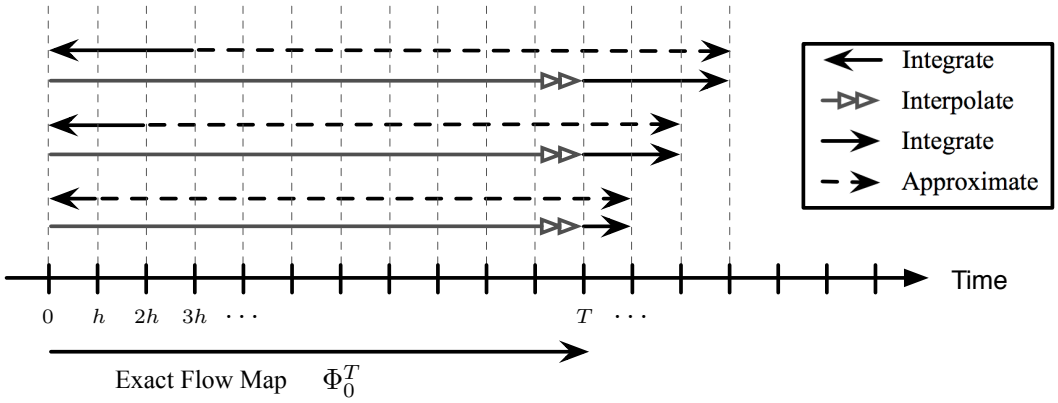


Figure 4.3: Schematic for bidirectional method (a). Given a known flow map $\Phi_0^T$ (solid black arrow), it is possible to approximate the flow map at later times $\tilde{\Phi}_{kh}^{kh+T}$ (dashed black arrow) by integrating backward in time to $t = 0$ (black left arrow), flowing forward through the interpolated map $\mathcal{I}\Phi_0^T$ that was already computed (gray double arrow), and integrating trajectories forward to the correct final time (black right arrow).

### 4.3.1 Bidirectional composition

Bidirectional approximation eliminates redundancy from neighboring FTLE field computations by using the information from a known flow map at a given time, $\Phi_0^T$, to calculate an approximation to the flow map at future times, $\Phi_{t_0}^{t_0+T}$. First, $X_0$ is integrated backward from $t_0$ to the reference time 0. The distorted grid $\Phi_{t_0}^0(X_0)$ is then flowed forward through the interpolated map, $\mathcal{I}\Phi_0^T$, and finally integrated forward an amount $t_0$ to the desired time $t_0 + T$:

$$\Phi_{t_0}^{t_0+T} \quad = \quad \Phi_T^{t_0+T} \circ \mathcal{I}\Phi_0^T \circ \Phi_{t_0}^0. \tag{4.8}$$

The flow $\Phi_0^T$ is stored as a reference solution to compute an approximation to the flow map at later times $\tilde{\Phi}_{kh}^{kh+T} \approx \Phi_{kh}^{kh+T}$ by

$$\tilde{\Phi}_{kh}^{kh+T} \quad = \Phi_T^{kh+T} \circ \mathcal{I}\Phi_0^T \circ \Phi_{kh}^0 \qquad k \in \mathbb{Z} \tag{4.9}$$

This is referred to as bidirectional method (a), and it is shown in Fig. 4.3.

Instead of using $\Phi_0^T$ as the reference solution for every future time, it is convenient to use the new approximate flow map $\tilde{\Phi}_{kh}^{kh+T}$ as the reference solution for the next iteration, $\tilde{\Phi}_{(k+1)h}^{(k+1)h+T}$:

$$\tilde{\Phi}_{(k+1)h}^{(k+1)h+T} \quad = \Phi_{kh+T}^{(k+1)h+T} \circ \mathcal{I}\tilde{\Phi}_{kh}^{kh+T} \circ \Phi_{(k+1)h}^{kh}. \tag{4.10}$$

Errors compound more quickly because approximate flow maps are used as the reference solutions for later approximations. However, fewer total integration steps are required, since the reference map advances with every iteration. This is referred to as bidirectional method (b), and is shown in Fig. 4.4.

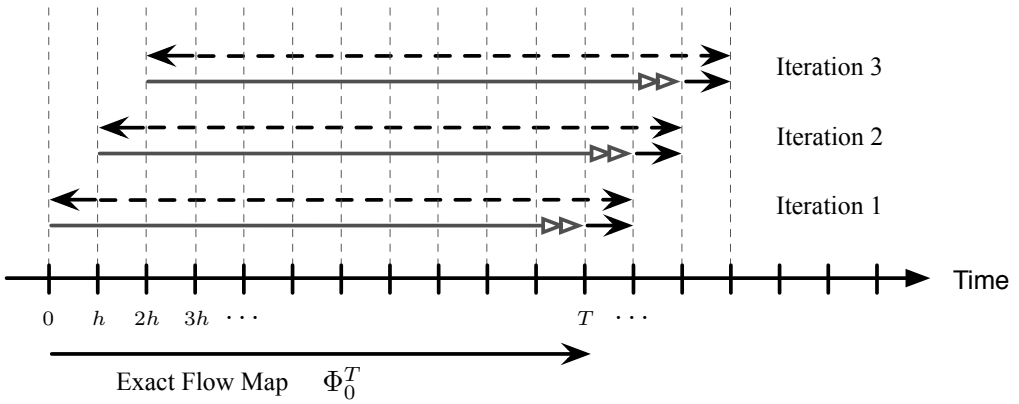


Figure 4.4: Schematic for bidirectional method (b). As in Fig. 4.3, a known flow map (solid black arrow) is used to approximate the flow map at a later time $\tilde{\Phi}_{kh}^{kh+T}$ (dashed black arrow). The approximate flow map (double gray arrow) is used as the known map for the next step.

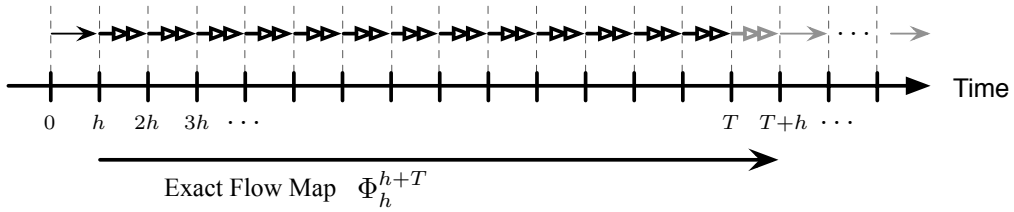


Figure 4.5: Schematic for unidirectional method. Time-$h$ flow maps (short double arrows) are stored and composed to approximate the time-$T$ flow map (long black arrow). The next flow map only requires integrating one new time-$h$ flow map (gray double arrow).

### 4.3.2 Unidirectional composition

The basis of the unidirectional method is to eliminate redundant particle integrations by only integrating particle trajectories through a given velocity field a single time. If a sequence of FTLE snapshots is desired at a time spacing of $h$, for example as frames in an animation, then it is convenient to break up the time-$T$ flow map into smaller time-$h$ flow maps, where $T = kh$:

$$\tilde{\Phi}_0^{kh} \quad = \quad \mathcal{I}\Phi_{(k-1)h}^{kh} \circ \cdots \circ \mathcal{I}\Phi_h^{2h} \circ \Phi_0^h \tag{4.11}$$

This method is called unidirectional because particle flow maps of the same time direction are used, as opposed to the bidirectional method that composes both positive-time and negative-time flow maps.

The simplest approach is to compute a number of time-$h$ flow maps and store them in memory. Then, to construct an approximate $\Phi_{t_0}^{t_0+T}$, it remains only to compose the sequence of interpolated time-$h$ flow maps. The next iteration in-

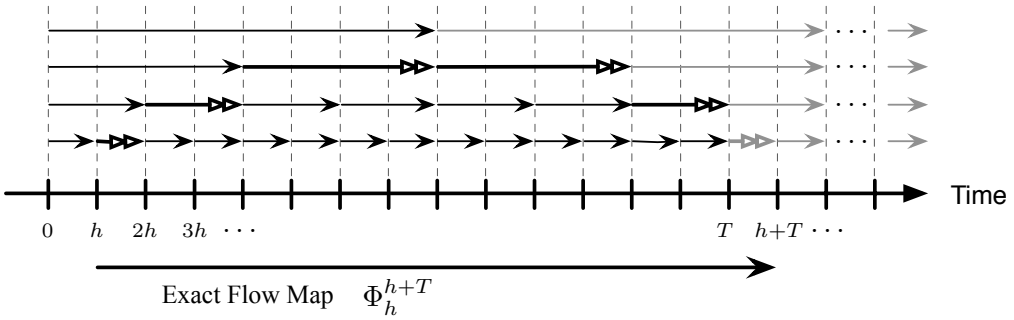


Figure 4.6: Schematic for unidirectional method with multiple tiers. The bottom tier of time-$h$ flow maps is computed as in Fig. 4.5. Pairs are composed to form the next tier of time-$2h$ flow maps, and so on. This method requires more storage, but fewer total compositions when computing a series of FTLE fields for an animation.

volves integrating one more time-$h$ flow map and composing the next sequence, as in Fig. 4.5.

To further improve efficiency by reducing the total number of flow map compositions, it is possible to construct a multi-tiered hierarchy of flow maps for reuse in neighboring flow map constructions. With enough memory, it is possible to reduce the number of interpolated compositions by increasing the number of tiers of flow maps, each tier being constructed as the composition of two of the flow maps in the next tier lower, as in Fig. 4.6.

### 4.3.3 Chain rule of compositions

As seen in Eq. (4.3), once the flow map $\Phi_{t_0}^{t_0+T}$ is obtained, it is necessary to compute the flow map Jacobian in order to extract the FTLE. Applying the chain rule to Eq. (4.5), it is possible to express the flow map Jacobian as a product of the Jacobians of intermediate flow maps:

$$\begin{aligned}\mathbf{D}(\Phi_{t_0}^{t_N})(\mathbf{x}) &= \mathbf{D}\left(\Phi_{t_{N-1}}^{t_N} \circ \cdots \circ \Phi_{t_1}^{t_2} \circ \Phi_{t_0}^{t_1}\right)(\mathbf{x}) \\ &= \mathbf{D}\Phi_{t_{N-1}}^{t_N}\left(\Phi_{t_0}^{t_{N-1}}(\mathbf{x})\right) \times \cdots \times \mathbf{D}\Phi_{t_0}^{t_1}(\mathbf{x})\end{aligned} \tag{4.12}$$

Applied to the bidirectional methods, this yields:

$$\begin{aligned}\Phi_h^{h+T} =& \Phi_T^{h+T} \circ \Phi_0^T \circ \Phi_h^0 \\ \implies \quad \mathbf{D}\Phi_h^{h+T}(\mathbf{x}) =& \mathbf{D}\Phi_T^{h+T}\left(\Phi_0^T \circ \Phi_h^0\right)(\mathbf{x}) \times \mathbf{D}\Phi_0^T\left(\Phi_h^0\right)(\mathbf{x}) \circ \mathbf{D}\Phi_h^0(\mathbf{x}),\end{aligned} \tag{4.13}$$

and applied to the unidirectional methods, this yields:

$$\begin{aligned}\Phi_0^T =& \Phi_{T-h}^T \circ \cdots \circ \Phi_h^{2h} \circ \Phi_0^h \\ \implies \quad \mathbf{D}\Phi_0^T(\mathbf{x}) =& \mathbf{D}\Phi_{T-h}^T\left(\Phi_0^{T-h}(\mathbf{x})\right) \times \cdots \times \mathbf{D}\Phi_h^{2h}\left(\Phi_0^h(\mathbf{x})\right) \times \mathbf{D}\Phi_0^h(\mathbf{x}).\end{aligned} \tag{4.14}$$

| Problem | Dim. | BCs | Velocity Field | Time Periodic |
|---|---|---|---|---|
| Double Gyre | 2D | Closed | Analytic | Yes |
| Pitching plate | 2D | Open | Data files (DNS) | Yes |
| ABC flow | 3D | Periodic | Analytic | No |

Table 4.1: Attributes of each example vector field.

This method adds significant complexity to the computation of the flow map Jacobian. However, it may be useful to compute the Jacobian of intermediate flow maps for a detailed stability analysis or to decide on an integration time, $T$.

## 4.4 Example velocity fields

A number of velocity fields are used in the following sections to test the fast methods. The attributes of each example velocity field is given in Table 4.1. Below is a description of how to compute the given velocity fields and an image of each corresponding FTLE field.

### Double gyre

The double gyre is an analytically defined velocity field that is time-periodic on the closed and bounded domain, $[0, 2] \times [0, 1]$. The stream-function is

$$\begin{aligned} \psi(x, y, t) &= A \sin\left(\pi f(x, t)\right) \sin(\pi y) \\ f(x, t) &= \epsilon \sin(\omega t) x^2 + x - 2\epsilon \sin(\omega t) x, \end{aligned} \tag{4.15}$$

which yields the following vector field

$$\begin{aligned} u &= -\frac{\partial \psi}{\partial y} = -\pi A \sin\left(\pi f(x)\right) \cos(\pi y) \\ v &= \frac{\partial \psi}{\partial x} = \pi A \cos\left(\pi f(x)\right) \sin(\pi y) \frac{df}{dx} \end{aligned} \tag{4.16}$$

The positive-time FTLE field for the double gyre is shown in Fig. 4.7. The light blue ridges are regions with high FTLE, and are candidates for repelling pLCS.

### Pitching flat plate

The second example is the unsteady velocity field of a flat plate pitching in a uniform flow at low Reynolds number, $Re = 100$. The plate pitches about its leading edge according to the following angle of attack motion:

$$\alpha(t) = \alpha_{\max} \sin(2\pi f t) \tag{4.17}$$

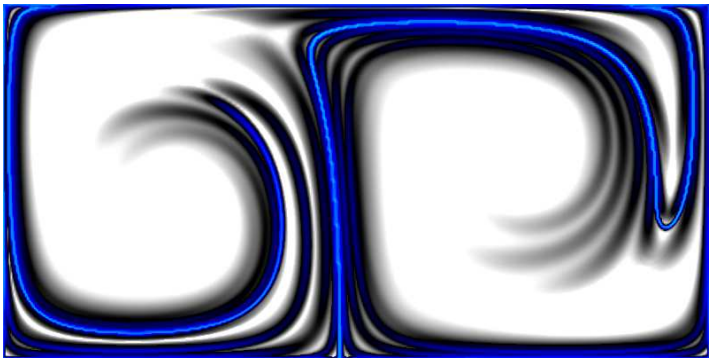

Figure 4.7: FTLE field for double gyre with $A = 0.1, \omega = 2\pi/10, \epsilon = 0.25, T = 15$.

Figure 4.8: FTLE field for pitching plate at $Re = 100$, $St = 0.274$, and $T = -15$.

with maximum angle of attack, $\alpha_{\max} = 20°$, and frequency $f = 0.4$. The Strouhal number, $St$, is a dimensionless pitching frequency given by:

$$St = \frac{fA}{U_\infty} = 0.274 \tag{4.18}$$

where $A = 2\sin(20°)$ is the amplitude of the plate's excursion, and $U_\infty = 1$ is the free stream velocity of the uniform flow.

The motion of the plate is simulated with the multi-domain immersed boundary method of Taira & Colonius [19], which uses a second-order Adams-Bashforth time-stepper. The output of the direct numerical simulation (DNS) is a time-sequence of velocity fields spaced 0.05 apart in non-dimensional time units. Each velocity field snapshot is defined on five nested grids. The finest grid covers a $4 \times 4$ domain and the coarsest grid covers a $64 \times 64$ domain, non-dimensionalized by chord length. Each grid has resolution $200 \times 200$. This provides a large computational domain for integrating particle trajectories. Velocity fields from the DNS are stored on disk and are loaded for use in FTLE field computations.

The negative-time FTLE field for the pitching plate is shown in Fig. 4.8. The regions with large FTLE are brightly colored to indicate that they are candidates for attracting nLCS. In this example, regions of large FTLE clearly outline the wake and separated flow around the plate.

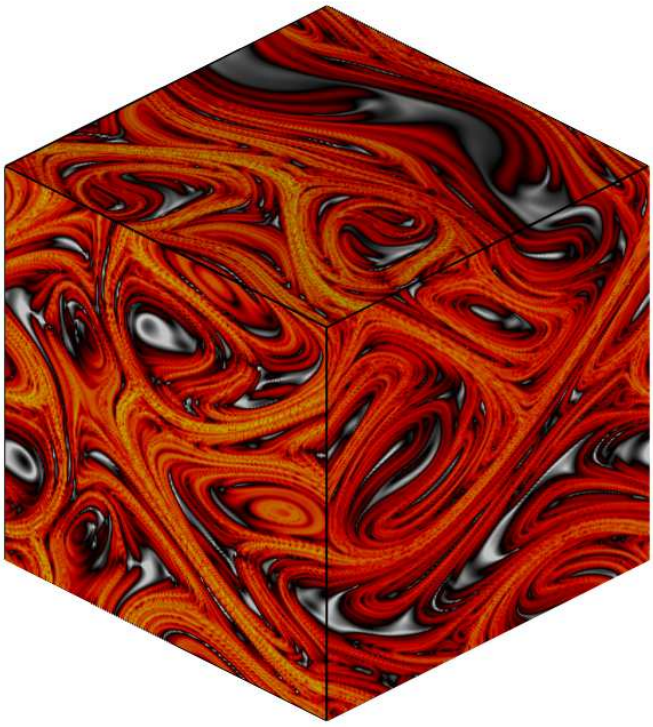

Figure 4.9: FTLE field for unsteady ABC flow ($A = \sqrt{3}$, $B = \sqrt{2}$, $C = 1$, $T = -8$).

### Unsteady ABC flow

The unsteady ABC flow is a 3D flow that is aperiodic in time, has spatially periodic boundary conditions, and whose velocity field is defined analytically as follows:

$$\begin{aligned} \dot{x} &= (A + \frac{1}{2} t \sin(\pi t)) \sin z + C \cos y \\ \dot{y} &= B \sin x + (A + \frac{1}{2} t \sin(\pi t)) \cos z \\ \dot{z} &= C \sin y + B \cos x \end{aligned} \tag{4.19}$$

All FTLE fields are computed on the periodic cube $X, Y, Z \in [0, 1)$, where $x = 2\pi X$, $y = 2\pi Y$, and $z = 2\pi Z$. The negative-time FTLE field for the unsteady ABC flow is shown in Fig. 4.9. Ridges of the FTLE field that are candidates for the attracting nLCS are colored in red and yellow.

## 4.5 Comparison of methods to compute approximate finite-time Lyapunov exponent fields

Each method from Section 4.3 is implemented and tested on three example problems: the periodic double gyre, 2D flow over a pitching flat plate at Reynolds number 100,

and 3D unsteady ABC flow. These examples are chosen because they cover a range of cases, including two-dimensional and three-dimensional vector fields. In addition, vector fields are either defined analytically or obtained from data files from DNS. Open, closed, and periodic domains are each investigated.

Each example problem is discussed more in Section 4.4, including details such as how the velocity field is defined, and on what domain. In the pitching plate example, velocity field snapshots are all loaded up-front before applying the methods.

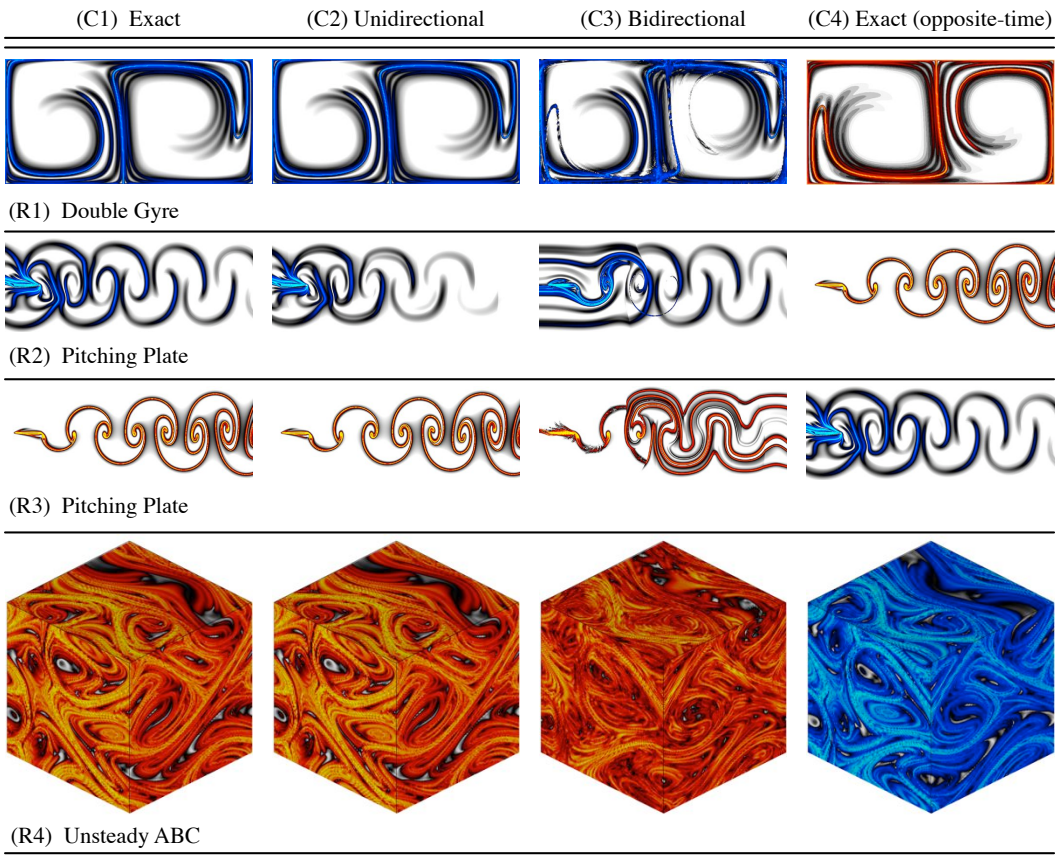


Figure 4.10: Graphical comparison of each method on four examples: (top row) positive-time FTLE of double gyre, (second row) positive-time FTLE of 2D pitching plate, (third row) negative-time FTLE of 2D pitching plate, (bottom row) negative-time FTLE of 3D ABC flow. Each figure shows the FTLE field after a number of iterations of the given method. The number of iterations $k$ was chosen so that $kh \approx T$ to magnify the effect of bidirectional error. The column of FTLE fields calculated using unidirectional composition, (C2), agree well with the exact FTLE fields computed using the standard method, (C1). The column of FTLE fields calculated using bidirectional composition, (C3) all have significant error that is aligned with the opposite-time coherent structures. The opposite-time FTLE fields are shown in the rightmost column, (C4), for comparison with the bidirectional method. FTLE fields computed for positive-time flow maps are blue and those computed for negative-time flow maps are red.

| Problem | Resolution | $T/h$ | Frames | Method | Memory (GB) | Speed-up | Accurate |
|---|---|---|---|---|---|---|---|
| Double Gyre | $1024 \times 512$ | 15 | 30 | Standard | 0.05 | 1 | Yes |
| | | | | Unidirectional | 0.36 | 10 | Yes |
| | | | | Bidirectional | 0.14 | 6.2 | No |
| Pitching plate | $1024 \times 512$ | 15 | 30 | Standard | 0.48 | 1 | Yes |
| | | | | Unidirectional | 0.70 | 8.2 | Yes |
| | | | | Bidirectional | 0.50 | 5.4 | No |
| Pitching plate | $600 \times 300$ | 150 | 192 | Standard | 0.48 | 1 | Yes |
| | | | | Unidirectional | 1.8 | 67 | Yes |
| | | | | Bidirectional | 0.48 | 54 | No |
| ABC flow | $128^3$ | 20 | 40 | Standard | 0.48 | 1 | Yes |
| | | | | Unidirectional | 2.6 | 6.8 | Yes |
| | | | | Bidirectional | 0.73 | 7.3 | No |

Table 4.2: Comparison of FTLE methods on example fluid flows. The unidirectional method is both fast and accurate, but requires more memory than the other methods, providing one or two orders of magnitude computational improvement over the standard method.

Table 4.2 summarizes the results comparing each method on the three example fluid flows. In each comparison, the standard, unidirectional and bidirectional methods are used to compute a sequence of FTLE fields, which are frames in an unsteady animation. The flow map duration used to compute an FTLE field is $T$, and the time-spacing between neighboring FTLE fields is $h$, so the number of animation frames per flow map duration is $T/h$. As demonstrated in Section 4.5.2, this is an upper bound on the speed-up of the unidirectional method.

In each comparison, the unidirectional method accurately reproduces the FTLE field and offers the greatest speed-up over the standard method. However, it also requires more memory than any other method. The bidirectional method is fast and uses less memory than the unidirectional method, but is prone to large errors in the approximate flow map and does not accurately reproduce the FTLE field. Accuracy is assessed both visually and with the $L_2$ error norm.

Contour plots of the FTLE fields computed after a number of iterations of each method are shown in Fig. 4.10. The FTLE fields computed with the unidirectional method agree with those computed using the standard method, as seen by comparing the first and second columns of Fig. 4.10. FTLE fields computed using the bidirectional method, shown in the third column, have large errors. It is interesting to note that these errors are aligned with coherent structures found in the opposite-time FTLE field, shown in the fourth column. An analysis of this coherent error is provided in Section 4.6.

### 4.5.1 Example - double gyre

Figure 4.11 shows the $L_2$ and $L_\infty$ error of the forward-time FTLE field for the double gyre computed using the standard method with $T = 16$, as time-step $\Delta t$ and grid spacing $\Delta x$ are varied. At a given grid spacing, a reference FTLE field is computed using a sufficiently small time-step, $\Delta t = 10^{-4}$, so that the FTLE field may be considered exact. For small enough time-step $\Delta t \approx .001$, the FTLE field error converges. All integrations are performed using a fixed time-step, fourth order Runge-Kutta scheme.

The flow map approximation methods are only faster than the standard method when used to compute a sequence of FTLE fields in time, as in the construction of frames for a movie. Figure 4.12 compares computation time and $L_2$ error vs. frame number (iteration #) for a sequence of FTLE fields of the double gyre, computed using the standard, unidirectional, and bidirectional methods. Each iteration produces an FTLE field that is a single frame in an animation of the unsteady FTLE field. In this example, the flow map duration is $T = 16$, the time spacing between each FTLE field is $h = 1$, and the time-step of integration is $\Delta t = 0.01$. The multi-tier unidirectional method uses four tiers.

The first FTLE field takes roughly the same time to compute using each of the methods. However, for subsequent iterations, the unidirectional and bidirectional methods are significantly faster. The computation time of bidirectional method (a) increases with the number of iterations, $k$, because integrating back from $t = kh$ to the reference time $t = 0$ becomes more costly as $k$ increases, as seen in Fig. 4.4. After $T/2h = 8$ iterations of bidirectional method (a), it is advantageous to compute a new reference flow map using the standard method. This explains the breaks in the solid red curve in part (b) of Fig. 4.12, as the bidirectional method is exact

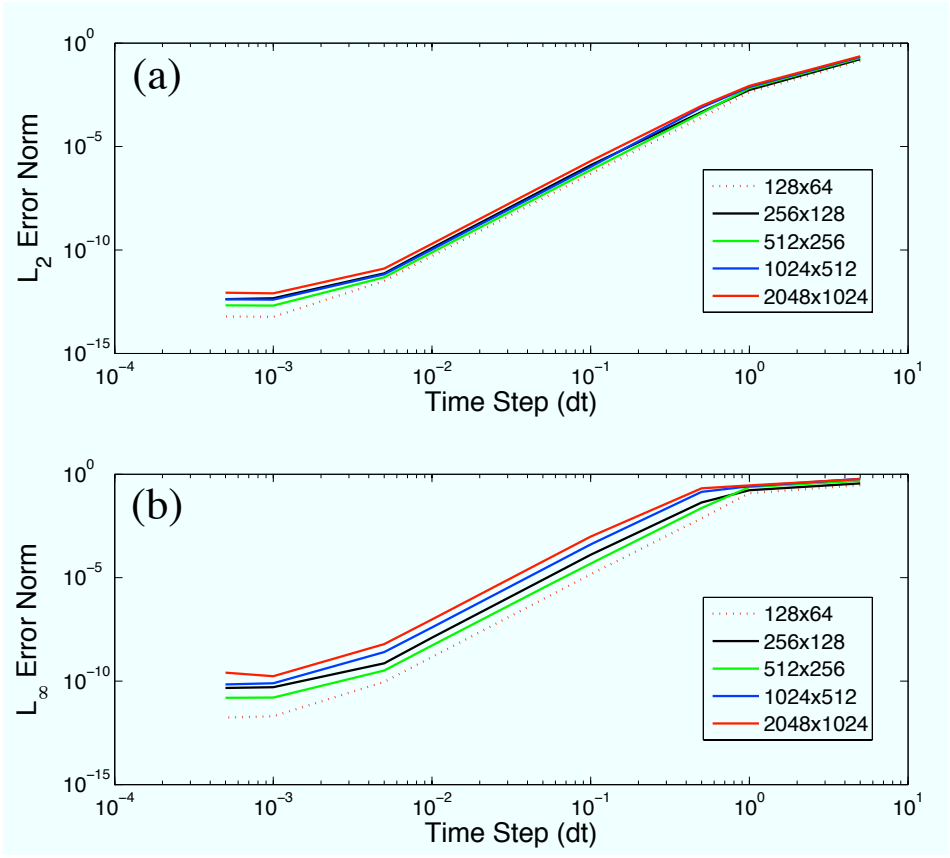


Figure 4.11: Convergence tests for $L_2$ and $L_\infty$ error of the FTLE field vs. integration step and grid spacing on double-gyre.

at these iterations. Bidirectional method (b) overcomes this increasing cost vs. iteration by using the flow map from the current iteration as the reference flow map at the next iteration. However, using an approximate flow map to compute the next approximation causes bidirectional method (b) to accumulate error more quickly than method (a). The unidirectional method is both the fastest and most accurate method in this comparison.

### 4.5.2 Computational resources

Again, consider a sequence of time-$T$ flow maps spaced $h$ apart, as might be required for an unsteady visualization. When there are many integration time-steps of size $\Delta t$ between each neighboring flow map, i.e. $\Delta t \ll h$, then the added cost of flow map composition becomes relatively small compared with the cost of integrating a time-$h$ flow map.

All methods take about the same amount of time to compute the first FTLE field in the sequence. For subsequent iterations, the standard method involves $(T/h) \times (h/\Delta t)$ integration steps for each new FTLE field, whereas the unidirectional method only requires $h/\Delta t$ integration steps, and bidirectional method (b) requires $2h/\Delta t$ integration steps. Assuming $\Delta t \ll h$, the speed-up of the unidirectional method

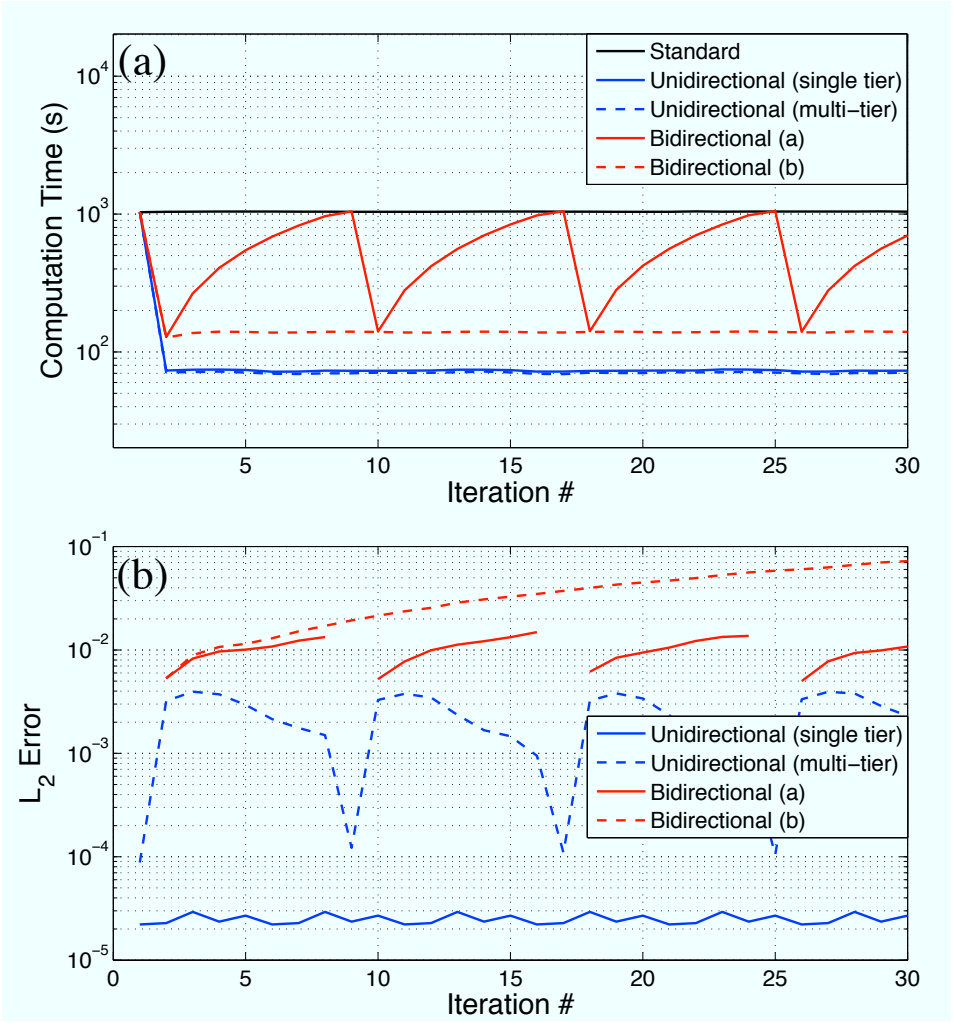


Figure 4.12: Comparison of methods for computing the FTLE field of the double gyre with resolution $1024 \times 512$. Each method is iterated to compute a sequence of 30 FTLE fields in time. (a) Computational time vs. Iteration, and (b) $L_2$ error vs. Iteration.

over the standard method will increase as the number of frames in the animation per flow map duration, $T$. In other words, as $\Delta t/h \to 0$, the computation of $\Phi_{t_0}^{t_0+T}$ using the unidirectional method is $T/h$ times faster than using the standard method, and twice as fast as the bidirectional method.

In the examples above, all intermediate flow maps were stored in memory until no longer useful for future computations. Regardless of any parameters of the FTLE field animation, the standard and bidirectional methods must store a fixed number of flow maps. The standard method stores the single flow map $\Phi_{t_0}^{t_0+T}$, while the bidirectional method stores three maps: $\Phi_{t_0}^{0}$, $\Phi_{0}^{T}$, and $\tilde{\Phi}_{t_0}^{t_0+T}$. The unidirectional method, however, stores every intermediate time-$h$ flow map $\Phi_{(k-1)h}^{kh}$, of which there are $T/h$. Therefore, the memory requirement of the unidirectional method scales linearly with the upper-bound on its speed-up, $T/h$.

The memory usage of the unidirectional method scales with the dimension of the flow $D$, the spatial resolution $R$, and the possible computational speed up of the method $S$, given by $T/h$:

$$\text{Memory (GB)} \sim S \times D \times R^D \tag{4.20}$$

$$= \frac{8 \text{ B/double}}{1024^3 \text{ B/GB}} \times \frac{T}{h} \times D \times R^D \tag{4.21}$$

For example, a series of two dimensional, high-definition ($1920 \times 1080$ resolution) FTLE fields may be computed using the unidirectional method with up to $100\times$ speed up using approximately 3.1 GB of RAM. A three dimensional FTLE field with resolution $512 \times 256 \times 64$ may be computed with up to $100\times$ speed up with approximately 19 GB of RAM.

In the double gyre and ABC flow examples, the velocity field is defined analytically, according to Eqns. (4.16) and (4.19). Thus, in these two examples, the velocity field is calculated analytically at every time, and no velocity fields need to be stored in data files. However, in the pitching plate example, velocity fields are obtained from data files that are the output of a direct numerical simulation. Because loading velocity fields from a hard disk is slow, it is important to minimize the number of file loads. In the pitching plate example, all of the velocity fields are loaded up-front and stored in memory throughout the computation. However, velocity fields are often too large to store them all in memory, for example in large 2D or 3D simulations, so that subsequent iterations of the methods require re-loading the same velocity field data from previous iterations. In practice, although loading data files is time consuming, it represents a fraction of the cost of particle integration.

## 4.6 Error analysis of flow map approximation

The aim of this section is to explain why the method of unidirectional composition is accurate while bidirectional composition is prone to large errors. Moreover, why are the errors in the bidirectional method found in regions of high FTLE of the opposite-time flow map, as illustrated in the third and fourth columns of Fig. 4.10?

For a given particle in a flow, larger finite-time Lyapunov exponent indicates greater stretching between neighboring particles and more sensitive dependence on

initial conditions. Thus, the trajectories of particles with large FTLE are more sensitive to errors in their initial conditions.

The set $\Sigma_\alpha(\Phi)$, defined as the set of points $\mathbf{x}$ with FTLE above a threshold value $\alpha$,

$$\Sigma_\alpha(\Phi) = \{\mathbf{x} \mid \sigma(\Phi;\mathbf{x}) > \alpha\}, \tag{4.22}$$

is the collection of points where error will magnify the most through the map $\Phi$. The flow map approximations above all involve composing intermediate flow maps,

$$\Phi_2 \circ \Phi_1, \tag{4.23}$$

so it is important to know what points flow into $\Sigma_\alpha(\Phi_2)$ through the map $\Phi_1$. In other words, we want to describe the set $\Phi_1^{-1}(\Sigma_\alpha(\Phi_2)) = \{\mathbf{x} \mid \Phi_1(\mathbf{x}) \in \Sigma_\alpha(\Phi_2)\}$, and this is the subject of Section 4.6.1.

If the flow map $\Phi_2$ is defined on a regular grid $X_0$, it is necessary to pass trajectories of $\Phi_1$ through the interpolated map $\mathcal{I}(\Phi_2|_{X_0})$. This is the source of error in the flow map approximations, and this error is significant when the trajectories of $\Phi_1$ pass into the set $\Sigma_\alpha(\Phi_2)$, where FTLE is large. Using a nearest neighbor interpolation, the interpolation error becomes particularly simple:

$$\Phi_2(\Phi_1(\mathbf{x})) \approx \mathcal{I}(\Phi_2|_{X_0})(\Phi_1(\mathbf{x})) = \Phi_2(\Phi_1(\mathbf{x}) + \epsilon) \tag{4.24}$$

where $\mathbf{x} \in X_0$, and $\epsilon$ is the difference between $\Phi_1(\mathbf{x})$ and its nearest neighbor in $X_0$. However, each approximate method has been tested using nearest neighbor, linear, and bicubic spline interpolations with no significant qualitative change in results. The propagation of interpolation error using unidirectional and bidirectional composition is the subject of Section 4.6.2.

### 4.6.1 Accumulation of particles

The main result of this section is that particles near the positive-time LCS (pLCS) flow into particles near the negative-time LCS (nLCS) in forward time, and vice-versa. This is consistent with the fact that pLCS and nLCS correspond to finite-time unstable and stable manifolds, respectively; it is observed in Figs. 4.13 and 4.14 for the pitching plate and double gyre examples.

Figure 4.13 shows particles in the set $\Sigma_{0.14}(\Phi_0^T)$, defined in Eq. (4.22), near the pLCS of the pitching plate example. As the particles convect downstream, they attract onto the nLCS. Compare this figure with the first and last panel of the second row of Figure 4.10 to see what the pLCS and nLCS look like for this example. Similarly, Fig. 4.14 shows points in $\Sigma_{0.3}(\Phi_0^{-T})$ near the nLCS of the double gyre example being integrated in negative time until they attract onto the pLCS. Compare this figure with the first and last panel of the first row of Fig. 4.10 to see the pLCS and nLCS of the double gyre.

The bottom panel of Fig. 4.14 is a zoom-in of the tangle of particles near a time-dependent saddle point at $T = -10$. A point $\mathbf{x}(t)$ is a time-dependent saddle if it is at the transverse intersection of the pLCS and the nLCS. It is numerically observed that these saddles mediate transport of particles near the pLCS into particles near the nLCS in positive time.

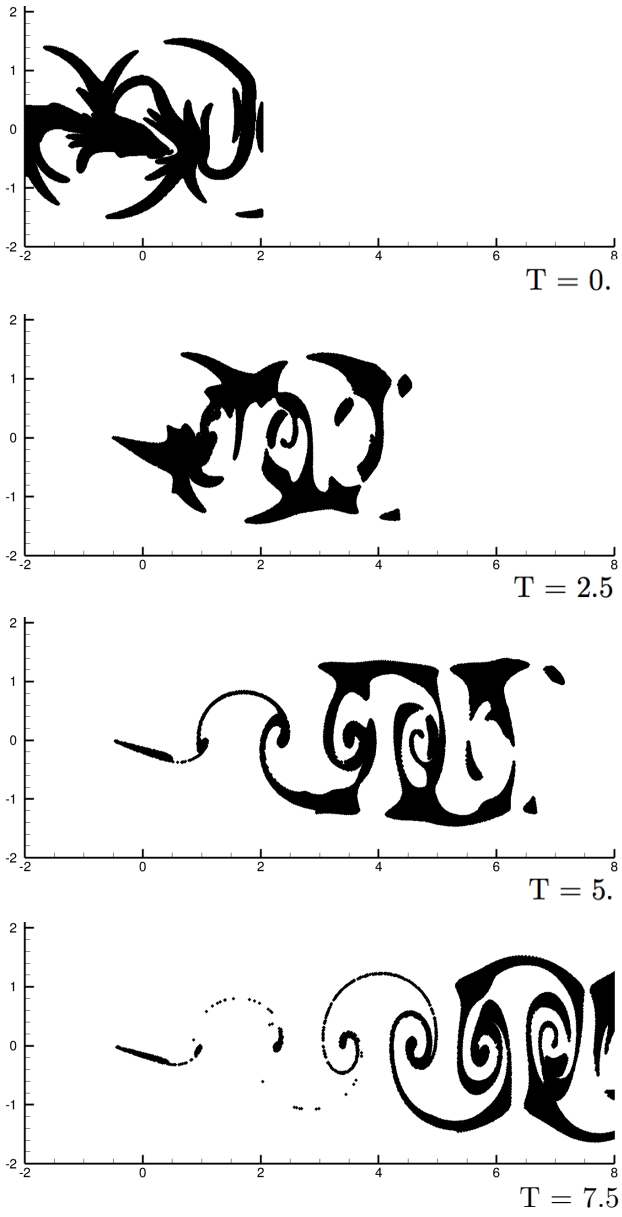


Figure 4.13: Particle trajectories of the set $\Sigma_{0.14}(\Phi_0^{15})$ for the pitching flat plate. Particles near the pLCS are integrated forward until they attract near the nLCS.

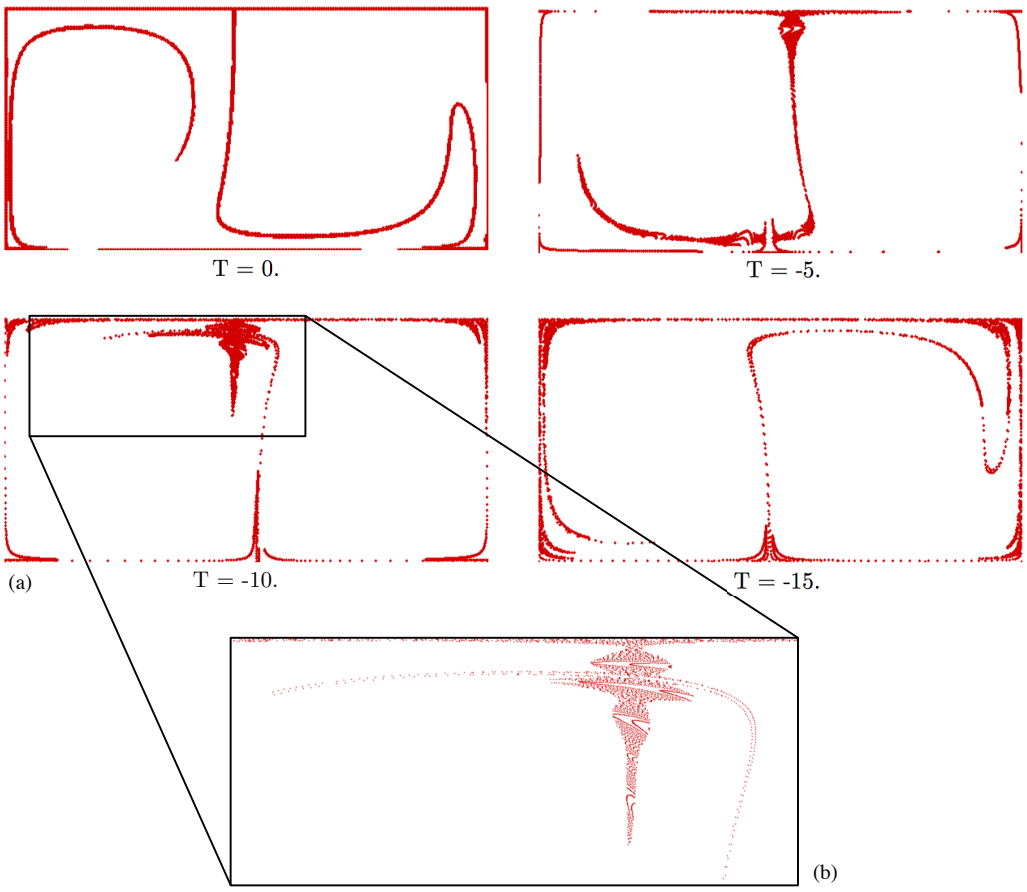


Figure 4.14: (top) Particle trajectories of the set $\Sigma_{0.3}(\Phi_0^{-15})$ for the double gyre. As particles on the nLCS are integrated backward they adhere to the pLCS. (bottom) The time-dependent saddle (intersection of pLCS and nLCS) at $T = -10$ is blown-up to show the heteroclinic tangle.

Further, suppose that $\mathbf{x}(t)$ persists as a time dependent saddle over a range of time $t \in (t_0 - T - \epsilon, t_0 + T + \epsilon)$, where $\epsilon > 0$ ensures uniform hyperbolicity. The positive and negative-time FTLE properties of this point establish an exponential dichotomy, which implies that $\mathbf{x}(t)$ is a time-dependent hyperbolic trajectory [127]. This trajectory now carries with it all of the regular theory about saddles, including Hartman-Grobman and Stable/Unstable Manifold Theorems. In particular, we may consider the pLCS (resp. nLCS) to be the time-dependent stable (resp. unstable) manifold of $\mathbf{x}(t)$.

Applying the Lambda lemma [44], it follows that a disk that intersects the pLCS transversely will attract arbitrarily $C^1$ close to a disk on the nLCS in positive-time, eventually. In the examples shown above, we observe a similar phenomena, namely, that in the neighborhood of a time-dependent saddle, the particles near the nLCS came from particles near the pLCS at an earlier time.

Similarly, it is possible to flow particles with large positive-time FTLE backward in time, and vice-versa, resulting in a set that resembles a positive-time LCS com-

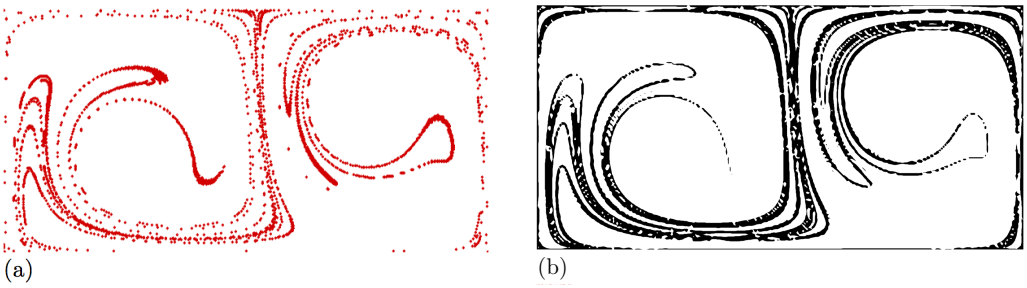


Figure 4.15: Particle trajectories of the set $\Sigma_{0.3}(\Phi_0^{-15})$ for the double gyre. Particles on the nLCS are flowed forward, shown in (a), resulting in a longer time nLCS, shown in (b).

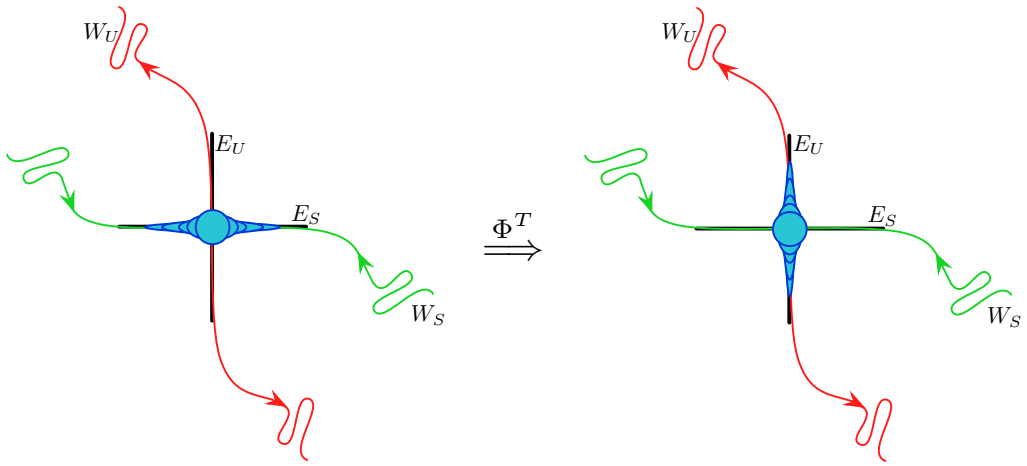


Figure 4.16: Schematic of time-dependent saddle point mediating the transport of material near the stable manifold, $W_S$, (left) into material near the unstable manifold, $W_U$, (right) after a time$-T$ map.

puted using a longer integration time. This is observed in Fig. 4.15, where particles in $\Sigma_{0.3}\left(\Phi_0^{-15}\right)$ are flowed forward along $\Phi_0^{15}$, resulting in a set that accumulates on the nLCS of the longer-time flow $\Phi_{15}^{-15}$.

A simplified schematic of the ideas above is shown in Figure 4.16.

### 4.6.2 Propagation of interpolation error

Consider the bidirectional composition of a positive-time flow map $\Phi^T$ with a negative-time flow map $\Phi^{-T}$, where error $\epsilon$ is introduced due to interpolation:

$$\begin{aligned}\Phi^T\left(\Phi^{-T}(\mathbf{x})+\epsilon\right) &\approx \Phi^T\left(\Phi^{-T}(\mathbf{x})\right)+\mathbf{D}\Phi^T\left(\Phi^{-T}(\mathbf{x})\right)\cdot\epsilon \\ &= \mathbf{x}+\mathbf{D}\Phi^T\left(\Phi^{-T}(\mathbf{x})\right)\cdot\epsilon \end{aligned} \tag{4.25}$$

The composition error is largest for points $\mathbf{x} \in X_0$ where $\mathbf{D}\Phi^T\left(\Phi^{-T}(\mathbf{x})\right)$ is large. From Eqns. (4.3) and (4.4), we have the following relationship:

$$\|\mathbf{D}\Phi^T(\mathbf{y})\| \geq e^{\alpha|T|} \quad \text{for} \quad \mathbf{y} \in \Sigma_\alpha(\Phi^T) \tag{4.26}$$

where $\|A\| = \max_{\mathbf{x}} \dfrac{\|A\mathbf{x}\|_2}{\|\mathbf{x}\|_2}$ is the maximum singular value of $A$. Thus, composition error is large at points $\mathbf{x}$, where $\mathbf{y} = \Phi^{-T}(\mathbf{x})$ is in the set $\Sigma_\alpha(\Phi^T)$, for large $\alpha$ and $T$.

Moreover, the results of the previous section indicate that points $\mathbf{x}$ satisfying $\Phi^{-T}(\mathbf{x}) \in \Sigma_\alpha(\Phi^T)$ originate in the set $\Sigma_\beta(\Phi^{-T})$ near the nLCS, in a neighborhood of a time-dependent saddle. Therefore, it is seen that the composition error will be largest at points $x \in \Sigma_\beta(\Phi^{-T})$, near the nLCS.

Now, consider the unidirectional composition of two positive-time flow maps, with interpolation error $\epsilon$:

$$\begin{aligned}\Phi^T\left(\Phi^T(\mathbf{x}) + \epsilon\right) &\approx \Phi^T\left(\Phi^T(\mathbf{x})\right) + \mathbf{D}\Phi^T\left(\Phi^T(\mathbf{x})\right) \cdot \epsilon \\ &= \Phi^{2T}(\mathbf{x}) + \mathbf{D}\Phi^T\left(\Phi^T(\mathbf{x})\right) \cdot \epsilon\end{aligned} \tag{4.27}$$

Here the error is largest for points $\mathbf{x} \in X_0$ where $\mathbf{D}\Phi^T\left(\Phi^T(\mathbf{x})\right)$ is large. Again, $\mathbf{D}\Phi^T(y)$ is large when $y \in \Sigma_\alpha(\Phi^T)$, for sufficiently large $\alpha$ and $T$.

In unidirectional composition, because the pLCS is repelling in positive time, points $\mathbf{x} \in X_0$ must be exactly in $\Phi^{-T}\left(\Sigma_\alpha(\Phi^T)\right)$, or else they will repel away from the regions where error is magnified. Similarly for bidirectional composition, because the pLCS is attracting in negative time, points will attract toward the regions where error magnifies. For this reason, the unidirectional method is robust to interpolation error, while the bidirectional method amplifies this error.

## 4.7 Summary of fast methods

A number of methods have been developed for the efficient computation of finite-time Lyapunov exponent (FTLE) fields in unsteady flows. In particular, the methods speed up the computation of a sequence of FTLE fields in time, used for frames of a movie, by approximating the particle flow map with information from neighboring times. The methods fall into two categories of flow map approximation based on composition of intermediate flow maps of the same time direction (unidirectional) or of both positive and negative-time directions (bidirectional). The main result is that the unidirectional method is both fast and accurate: the computational savings over the standard method are proportional to the number of FTLE fields being computed per time $T$. The unidirectional method provides one or two orders of magnitude computational savings over the standard method on the three example flows, as summarized in Table 4.2.

The bidirectional methods are also fast and use less memory than the unidirectional methods; however, bidirectional methods suffer from large errors that are concentrated along regions where the opposite-time FTLE field is large, in the vicinity of time-dependent saddle points. This coherent error was unexpected, but it is explained by dynamical systems theory. Particles close to the pLCS near a time-dependent saddle will map into particles close to the nLCS in positive time. This

result extends the relevance of Lagrangian coherent structure analysis to near identity maps in general.

The fast methods are implemented on three example velocity fields, chosen to represent typical fluid flows. The performance of each method is compared on the basis of computation time, accuracy and memory usage. The results of the method comparisons are summarized in Table 4.2 and Fig. 4.10. The unidirectional algorithm works well on 2D and 3D domains with either compact or spatially periodic domains. For open domains, as in the example of the pitching plate in a free stream velocity, the unidirectional method accurately computes the negative-time FTLE fields corresponding to the attracting set, or nLCS. However, error is introduced when computing the positive-time FTLE field, as particle trajectory information is lost downstream of the FTLE domain. This loss of information is not a problem when computing the nLCS because trajectory information upstream of the plate is well approximated using uniform flow. In experiments, however, velocity field data might only be available on a restricted domain, limiting the size of the FTLE domain. In this case, the unidirectional and standard methods will produce matching positive-time FTLE fields.

There are a number of future directions that might arise from this work. First, FTLE algorithms lend themselves to parallelization, so it is conceivable that with further optimization, it will be possible to obtain real-time FTLE visualizations for interesting problems. It would also be interesting to extend the above methods to incorporate adaptive mesh refinement (AMR) as well as complex domain geometries. Additionally, it is important to more precisely determine how and when particles near the pLCS flow into particles near the nLCS in positive-time.

# Chapter 5

# Unsteady aerodynamic models based on the Navier-Stokes Equations

This chapter develops the reduced order modeling framework that is used extensively in later chapters. Section 5.1 provides an overview of the models and clarifies the coordinate systems that are used throughout. Section 5.2 presents linear state-space models for the lift coefficient in response to pitching, plunging, and surging motion. Section 5.3 contains the algorithms used to construct these linear models from numerical or experimental data. System identification maneuvers are specially developed in Section 5.4 for either wind tunnel simulations or experiments.

The models in this chapter are obtained from the linearized Navier-Stokes equations, and they capture the viscous fluid dynamic forces that are important at low Reynolds number. The quasi-steady and added-mass forces are isolated in these models, and the reduced order modeling effort targets intermediate frequencies. This results in accurate models of low order. These reduced order models may be obtained from expensive high fidelity simulations and wind tunnel tests.

## 5.1 Overview

Aerodynamics involves the study of forces and moments on a body moving through a fluid. In particular, the unsteady Navier-Stokes equations describe a nonlinear dynamical system for the evolution of an unsteady fluid velocity field interacting with itself and with immersed bodies according to Newton's second law of motion. In addition, we assume incompressibility, and impose a boundary condition $u = u_B$ on the body surface. The input to this dynamical system is the motion of the immersed body, which enters as a time-varying boundary condition. Additionally, if we are interested in the unsteady *aerodynamic* forces and moments on the body, the output is a nonlinear function of the fluid velocity field. In particular, we seek unsteady aerodynamic models of the form:

$$\begin{aligned} \dot{\mathbf{x}} &= \mathbf{f}(\mathbf{x}, \mathbf{u}; \mu) \\ \mathbf{y} &= \mathbf{g}(\mathbf{x}, \mathbf{u}; \mu) \end{aligned} \tag{5.1}$$

where $\mathbf{x} \in \mathbb{R}^n$ contains relevant information about the aerodynamic state (vorticity or velocity field, angle of attack, amount of separation, etc.), $\mathbf{u} \in \mathbb{R}^p$ contains the inputs to the system (wing kinematics, actuators, etc.), $\mathbf{y} \in \mathbb{R}^q$ are the outputs of interest (forces, moments, pressure, etc.), and $\mu \in \mathbb{R}^k$ are the bifurcation parameters (Reynolds number Re, etc.). $\mathbf{f}$ is related to the nonlinear Navier-Stokes equations, for example as the discretized equations from a fluid solver, or the equations resulting from Galerkin projection onto a set of basis modes.

For a model of the unsteady lift given pitching motion, a general state $\mathbf{x}$ will include information about the fluid state $x$ (a vector containing either the vorticity $\omega$ or velocity $u$ at each grid point), as well as the angle of attack $\alpha$, and the rate $\dot{\alpha}$:

$$\dot{\mathbf{x}} \triangleq \frac{d}{dt}\begin{bmatrix} x \\ \alpha \\ \dot{\alpha} \end{bmatrix} = \begin{bmatrix} f_{\text{NS}}(x, \alpha, \dot{\alpha}, \ddot{\alpha}) \\ \dot{\alpha} \\ \ddot{\alpha} \end{bmatrix} \tag{5.2}$$

$$\begin{aligned} y &= g_{\text{lift}}(x, \alpha, \dot{\alpha}, \ddot{\alpha}) \\ &= g_\nu(x, \alpha, \dot{\alpha}) + g_\phi(\dot{\alpha}, \ddot{\alpha}) \end{aligned} \tag{5.3}$$

The output is split into the viscous forces $g_\nu$ and the added-mass forces $g_\phi$, which depend linearly on $\dot{\alpha}$ and $\ddot{\alpha}$. The input to Eq. (5.1) could also be vertical plunging motion $\ddot{h}$ or horizontal surging motion $\ddot{g}$, which will be considered in Section 5.2.2.

### 5.1.1 Coordinate systems

The coordinate system used throughout this chapter is chosen to be consistent with the notation used in Theodorsen's seminal paper [114]. This notation is still widely used in the unsteady aerodynamics community [78]. Unless explicitly stated, coordinates are referenced to an inertial *wind* frame where the wind velocity has a constant magnitude $U_\infty$ and is positive right and horizontal. The angle of attack $\alpha$ is the angle of inclination of the airfoil with respect to the wind velocity, and it follows a left-hand rule convention; motion in this direction is called *pitch*. The vertical position of the axis of rotation is given by $h$ and is positive downward; motion in this direction is called *plunge*. The horizontal position of the axis of rotation is given by $g$, and is positive left; motion in this direction is called *surge*. Therefore, the configuration of the airfoil is given uniquely by $(g, h, \alpha)$. This is different than the coordinate system typically used for flight dynamics, where $\alpha$ is the difference between the body $x$-axis angle ($\theta$) and the velocity vector angle ($\gamma$) [110]. However, aerodynamicists typically introduce the *effective* angle of attack $\alpha_e$, which takes into consideration the contribution of surge $g$ and plunge $h$ motion to the flight path angle. Therefore, $(g, h, \alpha, \alpha_e)$ are equivalent to $(-x, -y, -\theta, \alpha)$ from Chapter 3.

It will also be useful to consider the non-inertial *body* frame where coordinates $(\xi, \eta, \alpha)$ are referenced to the body: $\xi$ is motion parallel to the airfoil, $\eta$ is motion normal to the airfoil, and $\alpha$ is pitch motion. $\xi$ is called *slice* and $\eta$ is called *normal plunge*, distinguishing it from *vertical plunge* $h$. Note that the variables $g, \xi$, and $\eta$ and the names *slice* and *normal plunge* are not standard, but are introduced here.

Finally, the models in Eq. (5.5), (5.6), and (5.7) are constructed for pitching motion about a specific pitch axis location $p$, measured in downstream chord lengths from the leading edge. Thus, if $g = h = \text{constant}$, then $\theta = \alpha = \alpha_e$.

## 5.2 Linearized aerodynamic models

The models in this section are linearizations of Eqs. (5.1) about an equilibrium $\bar{\mathbf{x}}$. Translating $\bar{\mathbf{x}}$ to the origin, $\mathbf{x} = \mathbf{x} - \bar{\mathbf{x}}$, yields the standard state-space system:

$$\begin{aligned} \dot{\mathbf{x}} &= A\mathbf{x} + B\mathbf{u} \\ \mathbf{y} &= C\mathbf{x} + D\mathbf{u} \end{aligned} \tag{5.4}$$

where $A = \partial\mathbf{f}/\partial\mathbf{x}|_{\bar{\mathbf{x}}}$, $B = \partial\mathbf{f}/\partial\mathbf{u}|_{\bar{\mathbf{x}}}$, $C = \partial\mathbf{g}/\partial\mathbf{x}|_{\bar{\mathbf{x}}}$, and $D = \partial\mathbf{g}/\partial\mathbf{u}|_{\bar{\mathbf{x}}}$.

For the models below, the output is $\mathbf{y} = C_L$ where $C_L = 2L/\rho U_\infty^2 S$ is the non-dimensional lift coefficient; $L$ is lift, $\rho$ is density, $U_\infty$ is free-stream velocity, and $S$ is wing surface area. The input $\mathbf{u}$ will either be pitch $\ddot{\alpha}$ in Section 5.2.1, plunge $\ddot{h}$ or surge $\ddot{g}$ in Section 5.2.2, or some combination $\begin{bmatrix} \ddot{\alpha} & \ddot{h} & \ddot{g} \end{bmatrix}^T$ in Section 5.2.3.

### 5.2.1 Pitch models

Linearizing Eqs. (5.2) and (5.3) about an equilibrium $\bar{x}(\alpha_0)$ at a base angle of attack $\alpha_0 < \alpha_{\text{crit}}$ yields a model for the lift coefficient $C_L$ in response to pitch motion $\ddot{\alpha}$:

$$\begin{aligned} \frac{d}{dt}\begin{bmatrix} x \\ \alpha \\ \dot{\alpha} \end{bmatrix} &= \begin{bmatrix} A & B_1 & B_2 \\ 0 & 0 & 1 \\ 0 & 0 & 0 \end{bmatrix}\begin{bmatrix} x \\ \alpha \\ \dot{\alpha} \end{bmatrix} + \begin{bmatrix} B_3 \\ 0 \\ 1 \end{bmatrix}\ddot{\alpha} \\ C_L &= \begin{bmatrix} C & C_\alpha & C_{\dot{\alpha}} \end{bmatrix}\begin{bmatrix} x \\ \alpha \\ \dot{\alpha} \end{bmatrix} + C_{\ddot{\alpha}}\ddot{\alpha} \end{aligned} \tag{5.5}$$

where $A = \partial f_{\text{NS}}/\partial x$, $B_1 = \partial f_{\text{NS}}/\partial\alpha$, $B_2 = \partial f_{\text{NS}}/\partial\dot{\alpha}$, $B_2 = \partial f_{\text{NS}}/\partial\ddot{\alpha}$, $C = \partial g_\nu/\partial x$, $C_\alpha = \partial g_\nu/\partial\alpha$, $C_{\dot{\alpha}} = \partial(g_\nu + g_\phi)/\partial\dot{\alpha}$, and $C_{\ddot{\alpha}} = \partial g_\phi/\partial\ddot{\alpha}$. This model, and all pitch models that follow, are linearized about an equilibrium state $\bar{x}(\alpha_0)$ at a base angle of attack $\alpha_0$. The models in Eq. (5.6), (5.7), and (5.10) are developed for pitching about a specific pitch axis location $p$, measured in downstream chord lengths from the leading edge (e.g., $p = 0.0$ is the leading edge, and $p = 1.0$ is the trailing edge). Eq. (5.5) is consistent with Theodorsen's model in Eq. (6.18) with $B_3 = 0$.

The model in Eq. (5.5) is in a general form with no assumption made about the fluid state $x$. However, from Section 2.5, the flow responds instantaneously to pitch acceleration $\ddot{\alpha}$ with an unsteady (irrotational) potential flow, resulting in the added mass forces $C_{\dot{\alpha}}\dot{\alpha}$ and $C_{\ddot{\alpha}}\ddot{\alpha}$. Thus, if the fluid state $x$ represents vorticity, $B_3 = 0$, so that $\dot{\alpha}$ is the input to the transient fluid dynamics given by $(A, B, C)$ in Eq. (5.6).

$$\begin{aligned} \frac{d}{dt}\begin{bmatrix} x \\ \alpha \\ \dot{\alpha} \end{bmatrix} &= \begin{bmatrix} A & 0 & B \\ 0 & 0 & 1 \\ 0 & 0 & 0 \end{bmatrix}\begin{bmatrix} x \\ \alpha \\ \dot{\alpha} \end{bmatrix} + \begin{bmatrix} 0 \\ 0 \\ 1 \end{bmatrix}\ddot{\alpha} \\ y &= \begin{bmatrix} C & C_\alpha & C_{\dot{\alpha}} \end{bmatrix}\begin{bmatrix} x \\ \alpha \\ \dot{\alpha} \end{bmatrix} + C_{\ddot{\alpha}}\ddot{\alpha} \end{aligned} \tag{5.6}$$

The term $B_1$ has been set equal to 0 in Eq. (5.6). This is possible if $A$ is invertible by introducing the new state variable $\tilde{x} = x + A^{-1}B_1\alpha$. Thus, $A$ and $C$ are the same in Eqs. (5.5) and (5.6), and $B = B_2 + A^{-1}B_1$. The coefficient $C_\alpha$ in Eq. (5.6) is equal to $C_\alpha - CA^{-1}B_1$ in terms of Eq. (5.5). However, $CA^{-1}B_1$ is equal to zero.

Similarly, if the fluid state $x$ represents the velocity, then $B_3$ is nonzero, so that $\ddot{\alpha}$ is the input to the transient fluid dynamics given by $(A, B, C)$ in Eq. (5.7).

$$\begin{aligned} \frac{d}{dt}\begin{bmatrix} x \\ \alpha \\ \dot{\alpha} \end{bmatrix} &= \begin{bmatrix} A & 0 & 0 \\ 0 & 0 & 1 \\ 0 & 0 & 0 \end{bmatrix}\begin{bmatrix} x \\ \alpha \\ \dot{\alpha} \end{bmatrix} + \begin{bmatrix} B \\ 0 \\ 1 \end{bmatrix}\ddot{\alpha} \\ y &= \begin{bmatrix} C & C_\alpha & C_{\dot{\alpha}} \end{bmatrix}\begin{bmatrix} x \\ \alpha \\ \dot{\alpha} \end{bmatrix} + C_{\ddot{\alpha}}\ddot{\alpha} \end{aligned} \tag{5.7}$$

It is important to show how the models in Eq. (5.6) and Eq. (5.7) are related to each other and to the linearized model in Eq. (5.5). The primary difference between these models is in how the wing motion $(\alpha, \dot{\alpha}, \ddot{\alpha})$ enters into the $x$-dynamics. In particular, consider the system

$$\begin{aligned} \dot{x} &= Ax + Bu \\ y &= Cx \end{aligned} \quad \Longleftrightarrow \quad Y(s) = G(s)U(s) \tag{5.8}$$

where $G(s) = C(sI - A)^{-1}B$ is the transfer function relating the Laplace transformed input $U(s)$ and output $Y(s)$ signals. It is possible to construct an equivalent system $(\tilde{A}, \tilde{B}, \tilde{C}, \tilde{D})$ with input $\tilde{u} = \int u\,dt$, since $G(s)$ is strictly proper (i.e., $D = 0$). The new transfer function $\tilde{G}(s) = sG(s)$ is proper, and $\tilde{D} = -CA^{-1}B$ if $A$ is invertible.

Each of the models in Eqs. (5.5), (5.6), and (5.7) are useful in various contexts. This will be discussed in Section 5.2.4.

### 5.2.2 Plunge and surge models

Models for plunge and surge are closely related to the pitch models above, except that there is no steady-state force associated with a specific horizontal position $g$ or vertical position $h$; thus, there are no $C_g$ or $C_h$ coefficients in the model. Because $\ddot{g}$ and $\ddot{h}$ contribute to the rate of effective angle of attack, $\dot{\alpha}_e$, these generate vorticity and are considered to be the inputs to the transient dynamics $x$. A simple plunge model is given in Eq. (5.9).

$$\begin{aligned} \frac{d}{dt}\begin{bmatrix} x \\ \dot{h} \end{bmatrix} &= \begin{bmatrix} A & 0 \\ 0 & 0 \end{bmatrix}\begin{bmatrix} x \\ \dot{h} \end{bmatrix} + \begin{bmatrix} B \\ 1 \end{bmatrix}\ddot{h} \\ C_L &= \begin{bmatrix} C & C_{\dot{h}} \end{bmatrix}\begin{bmatrix} x \\ \dot{h} \end{bmatrix} + C_{\ddot{h}}\,\ddot{h} \end{aligned} \tag{5.9}$$

Surge is identical, with $g$ replacing $h$.

### 5.2.3 Combined pitch, plunge and surge models

It is possible to combine the pitch, plunge and surge models above. We may use either pitch formulation above (with either $\dot{\alpha}$ or $\ddot{\alpha}$ as input to the state $x$). Combining the pitch model in Eq. (5.7) with plunge and surge models in Eq. (5.9) yields the following multiple-input single-output (MISO) model:

$$\frac{d}{dt}\begin{bmatrix} x \\ \alpha \\ \dot{\alpha} \\ \dot{h} \\ \dot{g} \end{bmatrix} = \begin{bmatrix} A & 0 & 0 & 0 & 0 \\ 0 & 0 & 1 & 0 & 0 \\ 0 & 0 & 0 & 0 & 0 \\ 0 & 0 & 0 & 0 & 0 \\ 0 & 0 & 0 & 0 & 0 \end{bmatrix} \begin{bmatrix} x \\ \alpha \\ \dot{\alpha} \\ \dot{h} \\ \dot{g} \end{bmatrix} + \begin{bmatrix} B_1 & B_2 & B_3 \\ 0 & 0 & 0 \\ 1 & 0 & 0 \\ 0 & 1 & 0 \\ 0 & 0 & 1 \end{bmatrix} \begin{bmatrix} \ddot{\alpha} \\ \ddot{h} \\ \ddot{g} \end{bmatrix} \tag{5.10}$$

$$C_L = \begin{bmatrix} C & C_\alpha & C_{\dot{\alpha}} & C_{\dot{h}} & C_{\dot{g}} \end{bmatrix} \begin{bmatrix} x \\ \alpha \\ \dot{\alpha} \\ \dot{h} \\ \dot{g} \end{bmatrix} + \begin{bmatrix} C_{\ddot{\alpha}} & C_{\ddot{h}} & C_{\ddot{g}} \end{bmatrix} \begin{bmatrix} \ddot{\alpha} \\ \ddot{h} \\ \ddot{g} \end{bmatrix}$$

The model in Eq. (5.10) is linearized about a base angle of attack $\alpha_0$ and a *specific* pitch axis location $p$. However, it is possible to obtain a more general MISO model that is parameterized by the pitch axis location $p$. All pitch motions about a given pitch point $p$ may be considered a combination of pitch about the mid-chord (or any point of interest) and an induced plunge and surge motion. The magnitude of the induced plunge and surge motions at the middle-chord location are $a\mathcal{C}_0\ddot{\alpha}/2$ and $a\mathcal{S}_0\ddot{\alpha}/2$, respectively, where $a = -1 + 2p$, $\mathcal{C}_0 = \cos(\alpha_0)$, and $\mathcal{S}_0 = \sin(\alpha_0)$. Note that this is not an approximation but an exact kinematic transformation; this idea is used in Theodorsen's model in Chapter 6. The case of mid-chord pitching is particularly interesting, at least for a symmetric flat plate airfoil, because the added-mass forces proportional to $\ddot{\alpha}$ are zero. A model that is parameterized by the pitch axis location $p$, via $a = -1 + 2p$, is given in Eq. (5.11).

$$\frac{d}{dt}\begin{bmatrix} x \\ \alpha \\ \dot{\alpha} \\ \dot{h} \\ \dot{g} \end{bmatrix} = \begin{bmatrix} A & 0 & 0 & 0 & 0 \\ 0 & 0 & 1 & 0 & 0 \\ 0 & 0 & 0 & 0 & 0 \\ 0 & 0 & 0 & 0 & 0 \\ 0 & 0 & 0 & 0 & 0 \end{bmatrix} \begin{bmatrix} x \\ \alpha \\ \dot{\alpha} \\ \dot{h} \\ \dot{g} \end{bmatrix} + \begin{bmatrix} B_1 + a(\mathcal{C}_0 B_2 + \mathcal{S}_0 B_3)/2 & B_2 & B_3 \\ 0 & 0 & 0 \\ 1 & 0 & 0 \\ a\mathcal{C}_0/2 & 1 & 0 \\ a\mathcal{S}_0/2 & 0 & 1 \end{bmatrix} \begin{bmatrix} \ddot{\alpha} \\ \ddot{h} \\ \ddot{g} \end{bmatrix} \tag{5.11}$$

$$C_L = \begin{bmatrix} C & C_\alpha & C_{\dot{\alpha}} & C_{\dot{h}} & C_{\dot{g}} \end{bmatrix} \begin{bmatrix} x \\ \alpha \\ \dot{\alpha} \\ \dot{h} \\ \dot{g} \end{bmatrix} + \begin{bmatrix} C_{\ddot{\alpha}} + a(\mathcal{C}_0 C_{\ddot{h}} + \mathcal{S}_0 C_{\ddot{g}})/2 & C_{\ddot{h}} & C_{\ddot{g}} \end{bmatrix} \begin{bmatrix} \ddot{\alpha} \\ \ddot{h} \\ \ddot{g} \end{bmatrix}$$

Here, $(A, B_1, B_2, B_3C)$ are from the model in Eq. (5.10) for the case of pitch about the mid-chord. Alternatively, it is convenient to use body-frame coordinates $(\xi, \eta, \alpha)$, as discussed in Section 5.1.1. This results in the slightly simpler model in Eq. (5.12)

because at any base angle $\alpha_0$, the induced acceleration of the mid-chord point is entirely in the *normal plunge* direction $\eta$. In the case of $\alpha_0 = 0°$, the models in Eqs. (5.11) and (5.12) are equivalent. It is often the case that the dynamics in the $\xi$ or *slice* direction are negligible, so that this term may sometimes be removed.

$$\frac{d}{dt}\begin{bmatrix} x \\ \alpha \\ \dot{\alpha} \\ \dot{\eta} \\ \dot{\xi} \end{bmatrix} = \begin{bmatrix} A & 0 & 0 & 0 & 0 \\ 0 & 0 & 1 & 0 & 0 \\ 0 & 0 & 0 & 0 & 0 \\ 0 & 0 & 0 & 0 & 0 \\ 0 & 0 & 0 & 0 & 0 \end{bmatrix} \begin{bmatrix} x \\ \alpha \\ \dot{\alpha} \\ \dot{\eta} \\ \dot{\xi} \end{bmatrix} + \begin{bmatrix} B_1 + aB_2/2 & B_2 & B_3 \\ 0 & 0 & 0 \\ 1 & 0 & 0 \\ a/2 & 1 & 0 \\ 0 & 0 & 1 \end{bmatrix} \begin{bmatrix} \ddot{\alpha} \\ \ddot{\eta} \\ \ddot{\xi} \end{bmatrix} \tag{5.12}$$

$$C_L = \begin{bmatrix} C & C_\alpha & C_{\dot{\alpha}} & C_{\dot{\eta}} & C_{\dot{\xi}} \end{bmatrix} \begin{bmatrix} x \\ \alpha \\ \dot{\alpha} \\ \dot{\eta} \\ \dot{\xi} \end{bmatrix} + \begin{bmatrix} C_{\ddot{\alpha}} + aC_{\ddot{\eta}}/2 & C_{\ddot{\eta}} & C_{\ddot{\xi}} \end{bmatrix} \begin{bmatrix} \ddot{\alpha} \\ \ddot{\eta} \\ \ddot{\xi} \end{bmatrix}$$

### 5.2.4 Summary of models

The models developed in this section isolate the asymptotic low-frequency and high-frequency behavior due to the configuration variables (i.e., $C_\alpha$, $C_{\ddot{\alpha}}$, etc.) from the transient fluid dynamic effects, which are captured by the state $x$. Recall that the state $x$ is a large vector corresponding to either the velocity or vorticity at each grid point of the discrete Navier-Stokes equations, Eq. (5.1), and the transient dynamics will capture viscous effects that are neglected in the classical theory. This approach allows us to focus our reduced order modeling effort, detailed in the next section, to a narrow range of frequencies where the transient dynamics dominate.

Each of the pitch models in Eqs. (5.5), (5.6), and (5.7) may be useful, depending on the specific problem. The model in Eq. (5.5) is in a general form, and a variant is used to represent Theodorsen's model in state-space in Chapter 6. However, it is difficult to separate the effects of $\alpha$, $\dot{\alpha}$, and $\ddot{\alpha}$ on the $x$-dynamics using the system identification techniques in Sections 5.3 and 5.4. The models in Eqs. (5.6) and (5.7) are both well suited for models based on simulations, as demonstrated in Chapter 7, and each model has its relative strengths. For example, the algorithm in Section 5.3.2 for obtaining a reduced order model of the form in Eq (5.6) is simple and accurate. However, the model in Eq. (5.7) may be constructed using realistic input maneuvers with the observer/Kalman filter identification (OKID) method, as discussed in Section 5.3.4. This is particularly useful in Chapter 8 for models based on wind tunnel measurements.

The multiple input models in Eqs. (5.10), (5.11), and (5.12) have pitch dynamics of the form in Eq. (5.7), although they could equally well have been formulated using the pitch models in Eqs. (5.5) or (5.6). Although the models parameterized by pitch axis location, Eqs. (5.11) and (5.12), are quite general, it is often the case that a model about a single pitch axis is sufficient.

It is worth noting that the matrices $A, B_1, B_2, B_3$, and $C$ in Eqs. (5.5), (5.11), and (5.12) are not equal, although they are the same for Eqs. (5.10) and (5.11). Additionally, the matrices $A, B$, and $C$ in Eqs. (5.5), (5.6), (5.7), and (5.9) are not

necessarily equal to each other. The $A, B$, and $C$ matrices and the coefficients $C_{\dot{\alpha}}$ and $C_{\dot{\alpha}}$ in Eqs. (5.5), (5.6), (5.7), and (5.10) depend on the pitch axis location $p$. The matrix $A$ has dimension $n \times n$, the $B$ matrices have dimension $n \times 1$, and the matrix $C$ has dimension $1 \times n$, where $n$ is the dimension of the fluid state, $x \in \mathbb{R}^n$. Finally, the matrices and constants for every model in this chapter depend on the base angle of attack. $\alpha_0$.

## 5.3 Algorithms for obtaining linearized models

The algorithms in this Section provide a methodology for obtaining low-order models for Eqs. (5.6), and (5.7) from either numerical or experimental data. There are three basic algorithms that may be extended or modified as necessary. These methods are presented for the case where the input is pitch acceleration $\ddot{\alpha}$ and the output is the lift coefficient $C_L$. However, they may be generalized to include plunge and surge input motions, as well as drag and moment coefficient outputs.

In all of the models that follow, the quasi-steady and added-mass forces are identified first, guaranteeing correct behavior in the limit of low and high frequency motion. Then, the eigensystem realization algorithm (ERA) is used to identify the unsteady aerodynamics at intermediate frequencies due to the transient dynamics of the viscous fluid. This allows us to focus the reduced order modeling effort in the frequency range where the transient dynamics are important.

It may appear at first glance that it would be simplest to use the ERA/OKID method from Section 2.2 to identify a reduced order model for the entire model in Eq. (5.6) or Eq. (5.7). However, the structure of the model, with added-mass forces proportional to $\ddot{\alpha}$ and quasi-steady forces proportional to $\alpha$, makes it important to subtract these off before modeling the remaining transient dynamics with ERA. There are two reasons: First, the input should be $\ddot{\alpha}$ for the system to be proper, and identifying an ERA model with input $\ddot{\alpha}$ from OKID, without modification, yields an unstable system. Second, if OKID/ERA is applied assuming that the input is $\dot{\alpha}$, a large model order is required to approximate the derivative, $\ddot{\alpha}$, and the model will be inaccurate at high frequencies. This concept is illustrated on an example in Section 5.3.5.

### 5.3.1 General procedure for all methods

All of the algorithms below share some common features, and they are each based on an impulse response in either $\dot{\alpha}$ or $\ddot{\alpha}$, which corresponds to a step response in either $\alpha$ or $\dot{\alpha}$, respectively. The step response may be obtained directly or estimated from a frequency-rich input/output maneuver using the observer/Kalman filter identification (OKID) method. An overview of the OKID method is presented in Section 2.2.2.

The next step is to identify the quasi-steady and added-mass coefficients $C_\alpha, C_{\dot{\alpha}}$, and $C_{\ddot{\alpha}}$ from the impulse response in either $\dot{\alpha}$ or $\ddot{\alpha}$. After subtracting off these effects, the last step is to identify the remaining transient dynamics using the eigensystem realization algorithm (ERA), which is reviewed in Section 2.2.1. The transient portion $(A, B, C)$ of the model in Eqs. (5.6) and (5.7) is approximated by the ERA model $(A_r, B_r, C_r)$ of order $r \ll n = \dim(A)$; the input is either $\dot{\alpha}$ or $\ddot{\alpha}$, and the output is $C_L$. This splitting of quasi-steady, added-mass, and transient effects is

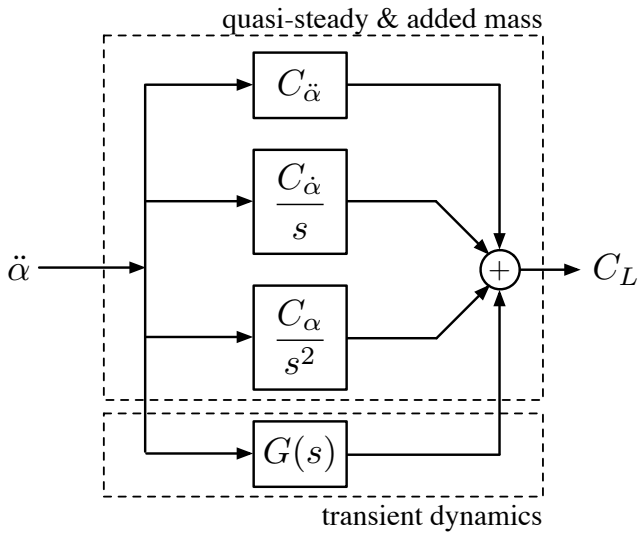


Figure 5.1: Schematic for transfer function of reduced order model (5.7) based on indicial response. $G(s) = C(sI - A)^{-1}B$ where $(A, B, C)$ are given in Eq. (5.7).

illustrated in Figure 5.1 for Eq. (5.7), where $G(s) = C(sI - A)^{-1}B$ is the transfer function for the transient dynamics. The general procedure is summarized as follows:

1. Obtain the impulse response in either $\dot{\alpha}$ or $\ddot{\alpha}$, possibly via OKID.
2. Determine the coefficients $C_{\alpha}$ and $C_{\ddot{\alpha}}$, which guarantee correct low frequency and high frequency behavior of the model, respectively.
3. Identify remaining dynamics by the eigensystem realization algorithm (ERA).

Identification of $C_{\alpha}$ and $C_{\ddot{\alpha}}$ is discussed in Section 5.3.2. Determining $C_{\dot{\alpha}}$ is an important step in Section 5.3.2, but is optional in the other algorithms. When $\ddot{\alpha}$ is the input to $(A, B, C)$, as in Eq. (5.7), the $C_{\dot{\alpha}}$ contribution is captured by $\lim_{s\to 0} C(sI - A)^{-1}B = -CA^{-1}B$.

Before providing details of each specific method, it is helpful to consider a typical step response for an unsteady aerodynamic system modeled by Eq. (5.6) or Eq. (5.7). The actual aerodynamic step responses used in later chapters have many temporal and spatial scales, due to the order of magnitude difference in various forces at different frequencies. Therefore, to make the individual features more apparent, we use a slower version of the step maneuver from Section 5.4.1 on a modified system with many of the same features as the aerodynamic systems we seek to model.

Figure 5.2 shows a sketch of a typical step response in $\alpha$ for a wing pitching about a point in front of the mid-chord. The top plot shows the lift coefficient history throughout the step, and the bottom three plots show the angle of attack and its derivatives throughout the maneuver. The step response is characterized by large added-mass forces during the step (1 and 2), followed by a transient lift (3), which decays to a steady-state value (4) after a large number of convective times. The added-mass forces are a combination of terms proportional to $\dot{\alpha}$ (B) and $\ddot{\alpha}$ (C), and may be written as $C_{\dot{\alpha}}\dot{\alpha} + C_{\ddot{\alpha}}\ddot{\alpha}$. The steady-state lift is given by

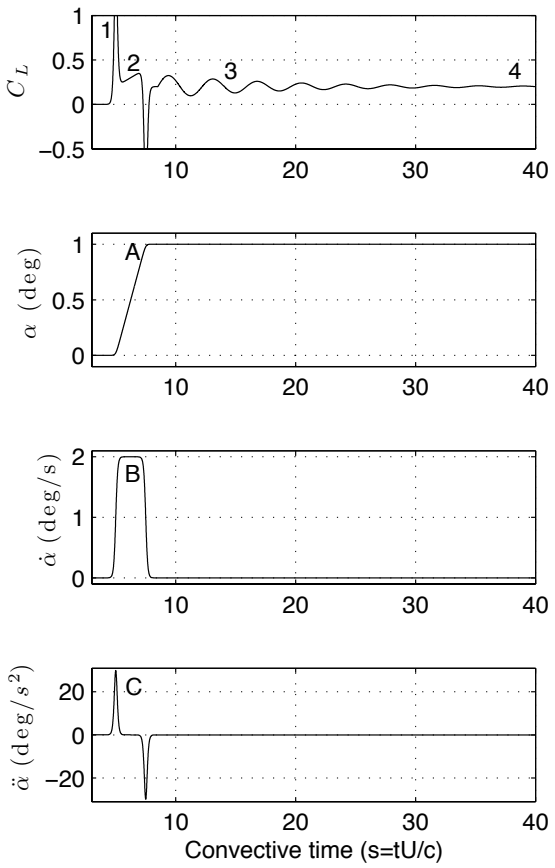


1. added-mass proportional to $\ddot{\alpha}$ (C)

2. added-mass proportional to $\dot{\alpha}$ (B)
+ quasi-steady proportional to $\alpha$ (A)

3. transient dynamics (G)
+ quasi-steady proportional to $\alpha$ (A)

4. quasi-steady proportional to $\alpha$ (A)

Figure 5.2: Aerodynamic response for step in angle of attack about the leading edge.

$C_\alpha\alpha$, where $C_\alpha$ is the lift coefficient slope. Finally, the transient lift in region (3) comes from unsteady fluid dynamic effects. The fluid dynamic transients include separation bubble dynamics and other boundary layer effects, which are observed in experiments and simulations. These transients are represented by $Cx$, where $x$ represents the generalized fluid dynamic state. This gives the following expression:

$$C_L(\alpha, \dot{\alpha}, \ddot{\alpha}, x) = C_\alpha\alpha + C_{\dot{\alpha}}\dot{\alpha} + C_{\ddot{\alpha}}\ddot{\alpha} + Cx. \tag{5.13}$$

The coefficient $C_\alpha$ in Eq. (5.13) is equal to the stability derivate $C_{L_\alpha}$, and the expression is generalized to include fluid dynamic transients via the state $x$. Because the transient dynamics arise from viscous fluid interactions, it is not possible to model them in terms of coefficient expansions of derivatives of the configuration variables.

For all of the methods that follow, let $\Delta t_f$ be the time step for the time-resolved measurements and $\Delta t_c$ be the time step for coarse sampling and for the resulting discrete-time model. Further, let $Y = \begin{bmatrix} Y_0 & Y_1 & \dots & Y_N \end{bmatrix}^T$ be a vertical vector of lift coefficient outputs $Y_k = C_L(k\Delta t_f)$ and $U = \begin{bmatrix} U_0 & U_1 & \dots & U_N \end{bmatrix}^T$ be a vertical vector of inputs $U_k = \ddot{\alpha}(k\Delta t_f)$ measured at times $k\Delta t_f$.

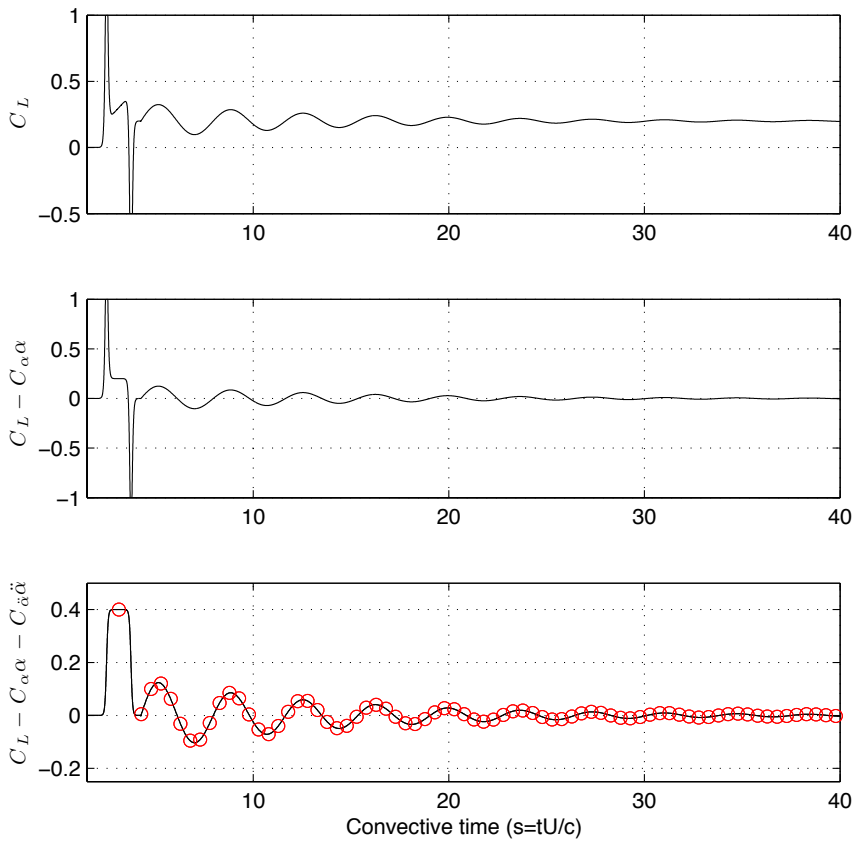


Figure 5.3: Illustration of method 1. (top) Lift coefficient in response to smoothed ramp-step in $\alpha$. (middle) Lift coefficient after subtracting $C_\alpha \alpha$ (low-frequency asymptote). (bottom) Lift coefficient after subtracting $C_\alpha \alpha + C_{\ddot{\alpha}} \ddot{\alpha}$ (low and high-frequency asymptotes). Circles indicate coarse sampling of time-resolved data.

### 5.3.2 Method 1: Model (5.6) from a ramped step response in $\alpha$

This method is based on the lift output in response to a step maneuver in $\alpha$ from $\alpha_0$ to $\alpha_0 + \Delta\alpha$. It is used primarily in Chapter 7 to identify models of the form in Eq. (5.6). The step maneuver described in Section 5.4.1 is a smoothed linear ramp function that may be viewed as a time-resolved, smoothed approximation to a discrete-time impulse in $\dot{\alpha}$ of magnitude $\Delta\alpha/\Delta t_c$, where $\Delta t_c$ is the duration of the step maneuver. In Chapter 7, $\Delta\alpha = 0.1^\circ$ and $\Delta t_c = 0.01$ convective time.

The lift slope $C_\alpha(\alpha_0)$ is approximated by $(Y_N - Y_0)/\Delta\alpha$, where $Y_N$ is the steady-state lift, measured many convective time intervals after the step, and $Y_0$ is the initial lift at a fixed angle $\alpha_0$ before the step. We subtract $C_\alpha \alpha(k\Delta t_f)$ from each $Y_k$.

The added-mass coefficient $C_{\ddot{\alpha}}$ may be solved for in the equation $Y \approx C_{\ddot{\alpha}} U$, which is approximately true during the step maneuver when $U$ is large. This amounts to finding a least squares fit for $Y$ in terms of $U$ by using the pseudoinverse: $C_{\ddot{\alpha}} = Y \backslash U \triangleq U^*(UU^*)^{-1}Y$. It is important to use only portions of $Y$ and $U$ restricted to the step maneuver. We may now subtract $C_{\ddot{\alpha}} U_k$ from each $Y_k$.

After subtracting $C_L^{\text{asymptotic}} \triangleq C_\alpha \alpha + C_{\ddot{\alpha}} \ddot{\alpha}$ from the step response, the remaining transient dynamics can be modeled using ERA. Recall from Section 2.2.1 that in order to determine a model using ERA, we require Markov parameters $\mathcal{H}_i$, which are the outputs $y_k$ from a discrete-time impulse response. It is possible to obtain $\mathcal{H}_i$ by sampling the signal with time step $\Delta t_c$ starting from the middle of the impulse, as shown in Figure 5.3. With this set of Markov parameters, it is possible to identify the remaining portion of the model corresponding to the terms $C_L^{\text{transient}} \triangleq C_{\dot{\alpha}} \dot{\alpha} + Cx$:

- $\mathcal{H}_0 = \Delta\alpha C_{\dot{\alpha}} / \Delta t_c$, (since the magnitude of the discrete pulse in $\dot{\alpha}$ is $\Delta\alpha / \Delta t_c$),
- $\{\mathcal{H}_j / \Delta\alpha \,|\, j \geq 1\} \;\rightarrow\; (A_r, B_r, C_r)$ using ERA (divide by $\Delta\alpha$ for unit step).

Finally, the resulting discrete-time model $(A_r, B_r, C_r)$ can be converted to a continuous-time model, since the dynamics at very high frequencies are dominated by added-mass terms.

As an aside, it is possible to refine the estimate for $C_{\ddot{\alpha}}$ by subtracting off $C_{\dot{\alpha}} \dot{\alpha}$ and correcting for the change in angle of attack during the step: $C_{\ddot{\alpha}} = \tilde{Y} \backslash U$ where $\tilde{Y} = \begin{bmatrix} \tilde{Y}_0 & \tilde{Y}_1 & \dots \tilde{Y}_S \end{bmatrix}^T$ and $\tilde{Y}_k = (Y_k - C_{\dot{\alpha}} \dot{\alpha}(k\Delta t_f)) / \cos(\alpha(k\Delta t_f))$. However, the effects of $C_\alpha \alpha$ and $C_{\dot{\alpha}} \dot{\alpha}$ are generally orders of magnitude smaller than the added-mass force $C_{\ddot{\alpha}} \ddot{\alpha}$ during the step, and may be neglected in practice.

### 5.3.3 Method 2: Model (5.7) from step response in $\alpha$

There are instances when it is useful to represent the aerodynamics with a model of the form in Eq. (5.7). For example, in Chapter 8, transient aeroelastic effects are not well modeled by Eq. (5.6), since the they are excited directly by $\ddot{\alpha}$. This method identifies models of the form in Eq. (5.7) from a step response in $\alpha$.

The first step is to identify the lift coefficient slope $C_\alpha$ and subtract $C_\alpha \alpha(k\Delta t_f)$ from each $Y_k$, as in Section 5.3.2. Next, the coefficient $C_{\dot{\alpha}}$ may be identified by sampling the measured lift during the middle of the impulse in $\dot{\alpha}$, when $\ddot{\alpha}$ is zero. To identify $C_{\ddot{\alpha}}$, the remaining signal is integrated to give the step response in $\dot{\alpha}$ (impulse response in $\ddot{\alpha}$), less the $C_\alpha$ and $C_{\dot{\alpha}}$ contributions. Sampling the remaining signal yields the Markov parameters $\mathcal{H}_i$, which are synthesized into $C_{\ddot{\alpha}}$ and a low-order, discrete-time model $(A_r, B_r, C_r)$ for the transient dynamics $(A, B, C)$ in Eq. (5.7):

- $\mathcal{H}_0 = \Delta\alpha C_{\ddot{\alpha}} / \Delta t_c$, (since the magnitude of the discrete pulse in $\ddot{\alpha}$ is $\Delta\alpha / \Delta t_c$),
- $\{\mathcal{H}_j / \Delta\alpha \,|\, j \geq 1\} \;\rightarrow\; (A_r, B_r, C_r)$ using ERA (divide by $\Delta\alpha$ for unit step).

This method is shown in Figure 5.4.

Note that there may be a steady-state value after integrating the signal, corresponding to $-CA^{-1}B$ in terms of the matrices in Eq. (5.6); this may either be removed and lumped in with $C_{\dot{\alpha}}$, or not. An alternative is to *not* identify and remove $C_{\dot{\alpha}}$ before integrating. Then, the steady-state value for the step in $\dot{\alpha}$ would all be lumped into $C_{\dot{\alpha}}$; in this case, it is important to remove the $C_{\dot{\alpha}} \dot{\alpha}(k\Delta t_f)$ from each $Y_k$ before using ERA.

To understand the method above, consider the Laplace transforms of the lift coefficient, $Y(s) = \mathcal{L}[C_L(t)]$, and angle of attack, $U(s) = \mathcal{L}[\alpha(t)]$. This results in the following transfer function representation of Eq. (5.7),

$$Y(s) = \left[ \frac{C_\alpha}{s^2} + \frac{C_{\dot{\alpha}}}{s} + C_{\ddot{\alpha}} + G(s) \right] s^2 U(s), \tag{5.14}$$

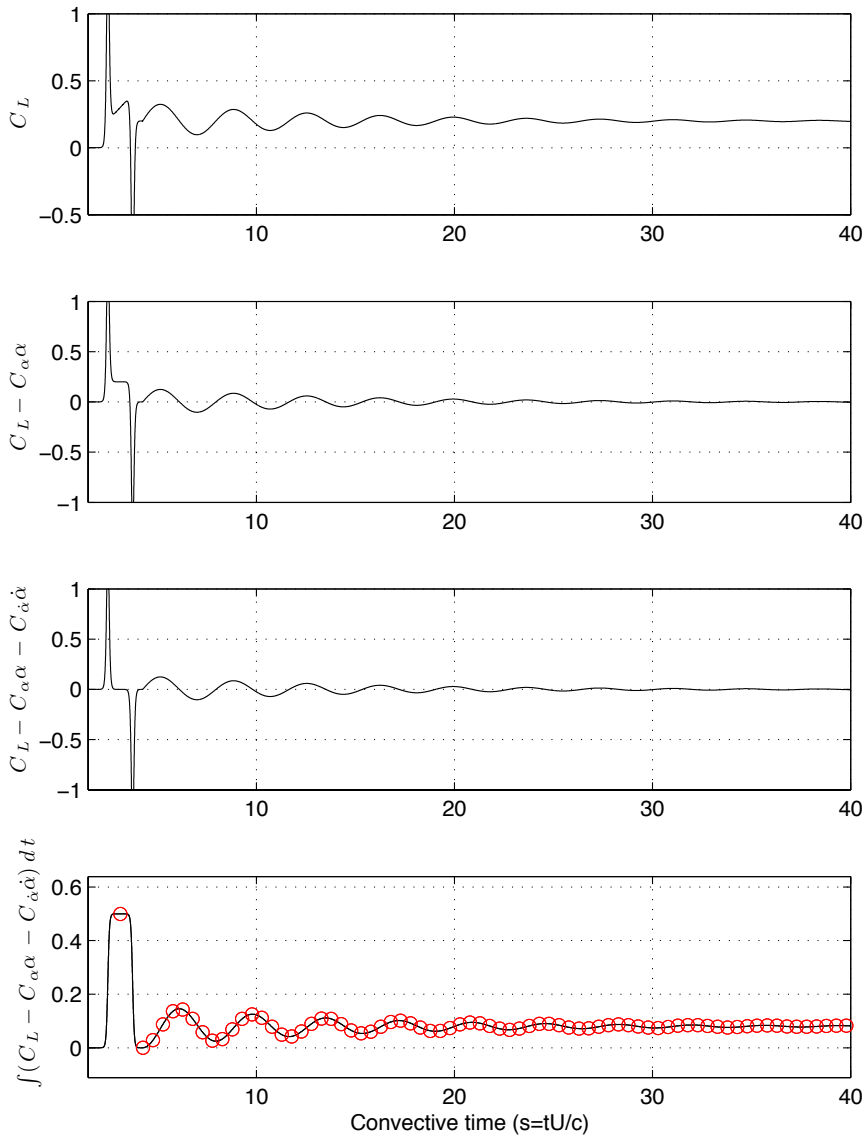


Figure 5.4: Illustration of method 2. (top) Lift coefficient in response to smoothed ramp-step in $\alpha$. (second) Lift coefficient after removing $C_\alpha\alpha$. (third) Lift coefficient after removing $C_\alpha\alpha + C_{\dot\alpha}\dot\alpha$. (bottom) Integrating third panel gives lift in response to ramp-step in $\dot\alpha$. Circles indicate coarse sampling of time-resolved data.

where $G(s) = C(sI - A)^{-1}B$, and $(A, B, C)$ are matrices from Eq. (5.7). $G(s)$ is a stable, strictly proper transfer function for the additional transient dynamics. The procedure is summarized as follows:

1. Given a unit step input in $\alpha$, $U(s) = 1/s$, the output signal is $Y(s) = \left[\frac{C_\alpha}{s^2} + \frac{C_{\dot\alpha}}{s} + C_{\ddot\alpha} + G(s)\right] s$
2. By the final value theorem, $C_\alpha$ is the steady state value, $\lim_{s\to 0} sY(s) = y(\infty)$
3. Subtract $C_\alpha$ from $y(t)$ and integrate, yielding $\tilde{y}(t) = \int_0^t [y(\tau) - C_\alpha]\, d\tau$. The corresponding signal is $\tilde{Y}(s) = \left[\frac{C_{\dot\alpha}}{s} + C_{\ddot\alpha} + G(s)\right]$
4. By the final value theorem, $C_{\dot\alpha}$ is the steady state value, $\lim_{s\to 0} s\tilde{Y}(s) = \tilde{y}(\infty)$.
5. Subtract $C_{\dot\alpha}$ from $\tilde{y}(t)$, leaving $\tilde{\tilde{y}}(t) \triangleq \tilde{y}(t) - C_{\dot\alpha} = \tilde{\tilde{Y}} = C_{\ddot\alpha} + G(s)$
6. Sample $\tilde{\tilde{y}}(t)$ to identify the Markov parameters.

This procedure is more involved than the method in Section 5.3.2, but it demonstrates the equivalence of Eq. (5.6) and Eq. (5.7).

### 5.3.4 Method 3: Model (5.7) from impulse response in $\ddot\alpha$ (OKID)

This method develops models of the form in Eq. (5.7) from realistic input/output maneuvers, such as those described in Section 5.4.2. In particular, the observer/Kalman filter identification (OKID) method from Section 2.2.2 is used to obtain the Markov parameters for the impulse response in $\ddot\alpha$ of the *linearized* system. From the impulse response, one may identify the parameters $C_\alpha, C_{\dot\alpha}$, and $C_{\ddot\alpha}$ as well as a low-dimension ERA model, $(A_r, B_r, C_r)$, using a technique similar to the method in Section 5.3.3. This method is used extensively in Chapter 8 to identify models based on wind tunnel measurements.

The OKID method provides Markov parameters for an impulse response in $\ddot\alpha$ given the input/output data for a frequency-rich maneuver, such as the maneuvers in Section 5.4.2. Typically the input/output pair used with OKID have been sampled from the time-resolve input motion $\ddot\alpha(t)$ and lift signal $C_L(t)$. The sample time $\Delta t_c$ is the desired coarse time step for the discrete-time model of the transient dynamics. For wind tunnel experiments, the time step $\Delta t_c = 0.1$ convective time units has been determined to be sufficiently small to capture the relevant frequencies for the transient dynamics. Higher frequency motions are dominated by added-mass forces, which are accurately captured by the coefficient $C_{\ddot\alpha}$ in the continuous-time model, Eq. (5.7).

Figure 5.5 illustrates the time-resolved impulse response in $\ddot\alpha$ for a linearized system of the form in Eq. (5.7). Because an impulse in $\ddot\alpha$ is a step in $\dot\alpha$ and a ramp in $\alpha$, there is a linear growth in the lift coefficient as the angle of attack increases linearly with time. Clearly it is not possible to obtain this *linear* impulse response from a step in $\dot\alpha$ in a real experiment, since the linear growth in $\alpha$ would quickly excite nonlinear phenomena; this is one motivation for the OKID method, which *estimates* the linear impulse response from a bounded maneuver in a region where the linear approximation is valid. The discrete-time Markov parameters $\mathcal{H}_i$ for the flat plate at Reynolds number 100 linearized about $\alpha_0 = 0^\circ$ are shown in Figure 7.14.

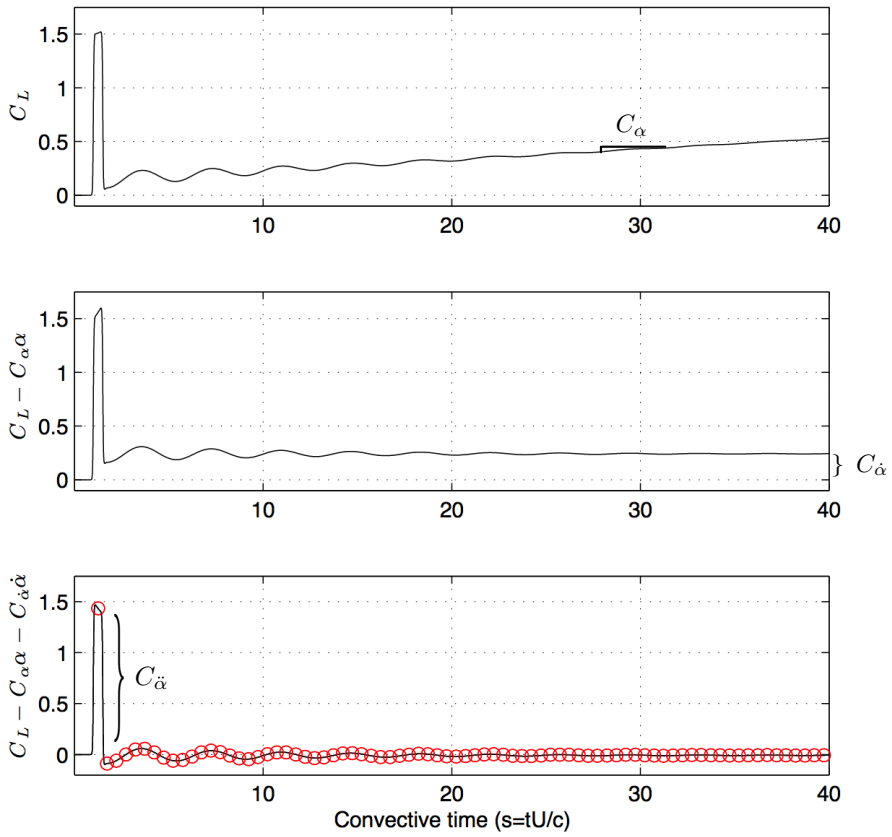


Figure 5.5: Illustration of method 3. (top) Lift coefficient in response to smoothed ramp-step in $\dot{\alpha}$. (middle) Lift coefficient after removing $C_\alpha\alpha$. (bottom) Lift coefficient after removing $C_\alpha\alpha + C_{\dot\alpha}\dot\alpha$. Circles indicate coarse sampling of data.

To identify a model of the form in Eq. (5.7), we must first identify the lift coefficient slope $C_\alpha$, which is the slope of the impulse response in Figure 5.5 after all transients have died out. After subtracting off $C_\alpha\alpha$, $C_{\dot\alpha}$ is the steady-state value (since this is a step in $\dot{\alpha}$). After these modifications, the first Markov parameter is $C_{\ddot\alpha}$, and the remaining parameters are passed to the ERA to obtain a low-dimensional, discrete-time model $(A_r, B_r, C_r)$ for the transient dynamics $(A, B, C)$ in Eq. (5.7).

### 5.3.5 Caution against incorrect use of ERA/OKID

One may be inclined to try and identify the entire model in Eq. (5.6) or Eq. (5.7) using the ERA directly on the Markov parameters from OKID. However, if one incorrectly applies the ERA to the impulse response in $\ddot{\alpha}$, shown in the top plot of Figure 5.5, the resulting model will be unstable, because of the linear growth in $C_L$. In addition, if one incorrectly applies OKID/ERA to an impulse in $\dot{\alpha}$ (i.e., to identify a model of the indicial response), the resulting model will not capture the correct added-mass forces. This is why it is important that the input to the system is $\ddot{\alpha}$, and the $C_\alpha$ and $C_{\ddot\alpha}$ terms must be identified and removed in advance of applying ERA.

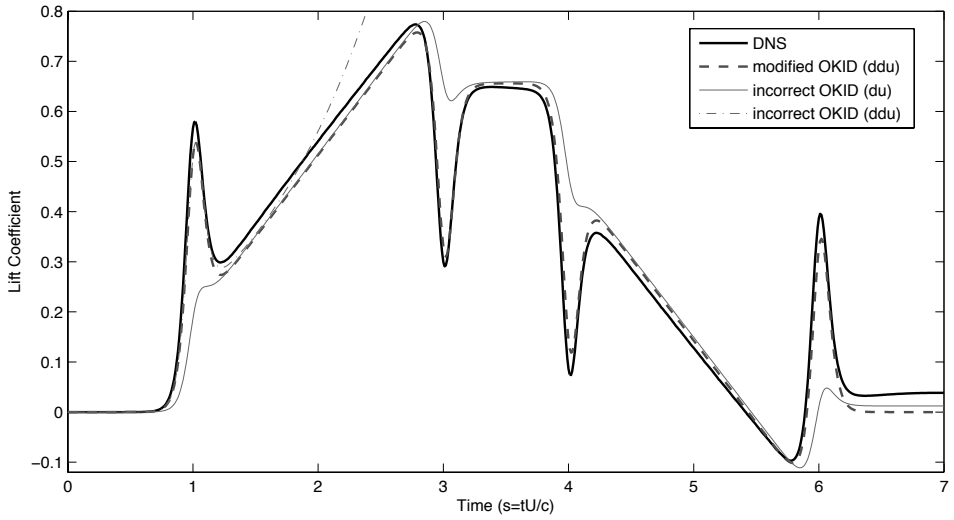


Figure 5.6: Example of correct and incorrect use of OKID/ERA to model the pitch-up, hold, pitch-down maneuver.

Examples of these systematic failures are shown in the the response to the canonical maneuver from Section 2.6 in Figure 5.6, and in the Bode plot in Figure 5.7. In these plots, the model based on the method in Section 5.3.4 is labeled "modified OKID (ddu)". The two incorrect uses of OKID/ERA are labeled "incorrect OKID". In Figure 5.7, "IR model" is the correct model based on the indicial response.

### 5.3.6 Identifying multi-input, multi-output models with ERA

It is possible to extend each of the methods above to identify models with multiple inputs and multiple outputs (MIMO), such as a model with both pitch and plunge inputs, as in Eq. (5.10). As with the single-input, single output (SISO) case, we start with individual impulse-response data for both pitch and plunge, possibly estimated using OKID. All of the steps remain identical for each step response, including pulling off the quasi-steady and added-mass coefficients, and formatting the remaining dynamics into a sampled discrete-time impulse. At the step where ERA is used to identify a model for the remaining dynamics, we construct a general Hankel matrix from the MIMO Markov parameters that have size outputs $\times$ inputs. The ERA algorithm will then identify the remaining dynamics as before. It is shown that MIMO models do not require a significant increase in model order.

### 5.3.7 Relationship to indicial response models

The algorithms in Sections 5.3.2 and 5.3.3 above are based on the step response in $\alpha$, which is also known as the indicial response. Therefore, the resulting low-order models for Eq. (5.6) and Eq. (5.7) may be viewed as reduced-order, state-space representations of the indicial response model in Eq. (2.6). It is possible to use the time-resolved step response from any of the above methods for the indicial response. It is important to include the $\ddot{\alpha}$ coefficient if using the method in Algorithm 1.

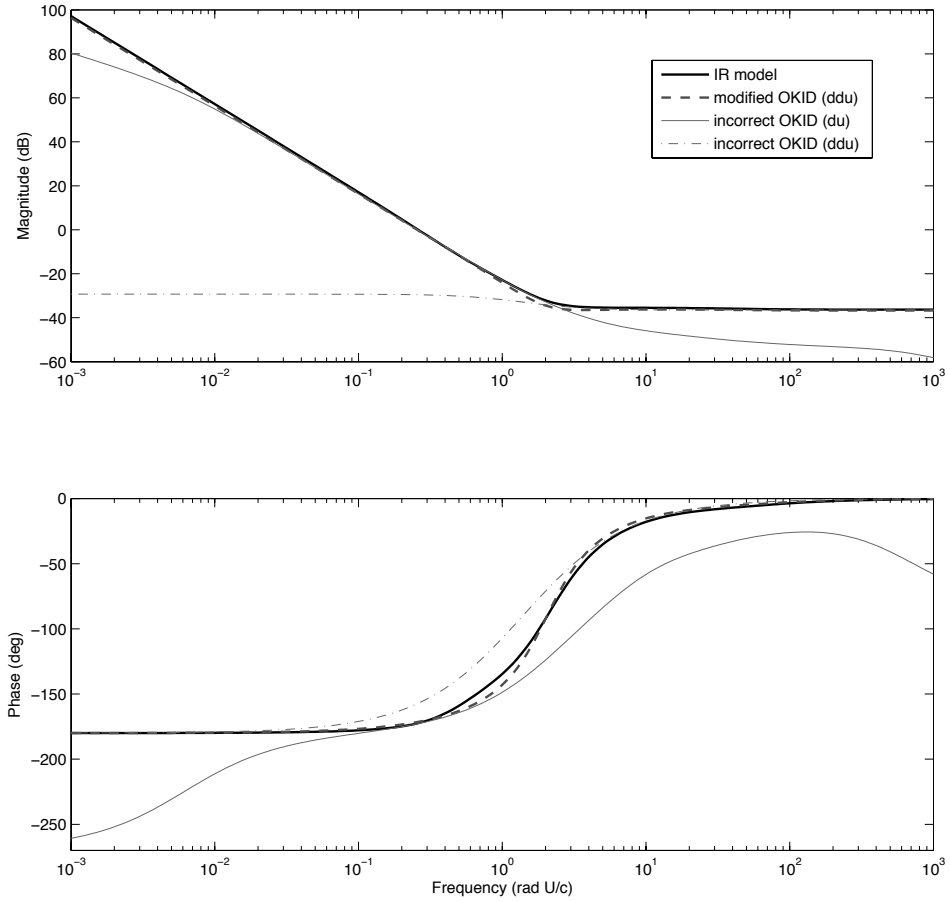


Figure 5.7: Bode plot of correct and incorrect use of OKID/ERA to model leading-edge pitch dynamics. Input is either $\dot{\alpha}$ or $\ddot{\alpha}$ and output is $C_L$.

## 5.4 System identification maneuvers

The maneuvers in this section are used in the algorithms in Section 5.3 to develop models of the form in Section 5.2 from either numerical or experimental data. The algorithms in Sections 5.3.2 and 5.3.3 rely on the step response of $\alpha$ (or $\dot{g}, \dot{h}$). Two smoothed step functions that are useful in simulations are discussed in Section 5.4.1. Section 5.4.2 presents a set of maneuvers that are used with the OKID method in Section 5.3.4 to obtain the impulse response in $\ddot{\alpha}$ (or $\ddot{g}, \ddot{h}$) from a more realistic input maneuver. The pseudo-random maneuvers in the second part of Section 5.4.2 are particularly useful for experiments, where it is important to have an aggressive maneuver that excites varies frequencies to overcome noisy measurements.

The measurements from a direct numerical simulation (DNS) of the Navier-Stokes (NS) equations or from a wind tunnel experiment are necessarily a discrete-time signal. Typically, a fine time step $\Delta t_f$ is required for the DNS to remain stable and for the discrete-time signal to approximate the continuous-time NS equations. The transient aerodynamic effects, however, are modeled as a discrete-time system with a coarse time step $\Delta t_c \gg \Delta t_f$. Therefore, we will command maneuvers defined

by a coarse discrete-time signal $u_k$, but simulate a corresponding smoothed discrete-time signal $\tilde{u}_j$ with time step $\Delta t_f$.

### 5.4.1 Smoothed step functions

For a number of reasons, an actual step response is non physical. First, it is impossible to command in experiments or simulations, because it would correspond to a body instantaneously dematerializing and then rematerializing it in another location. An alternative is to use a smoothed step maneuver and approach the limit as the maneuver becomes very rapid. As the maneuver becomes increasingly rapid, the added-mass forces begin to dominate; in fact, a good rule of thumb is to choose a maneuver rapid enough that the lift response for the duration of the maneuver is dominated by added-mass forces.

There are a number of choices for a smoothed step-up maneuver. In this thesis, results are based on a smoothed linear ramp-up maneuver, discussed in 5.4.1. It is also possible to use a sigmoidal step-up [11], discussed in 5.4.1.

The duration of the step maneuvers used for simulations in later chapters is $T = 0.01$ convective time units. The amplitude is either $\Delta\alpha = 0.1^\circ \approx 0.001745$ rad in the case of pitching or $\Delta\alpha = 0.0017451$ chord lengths per convection time in the case of vertical velocity, corresponding to $0.1^\circ$ change in effective angle of attack. This is sufficiently rapid for the added-mass forces to dominate for the duration of the maneuver. To obtain a model for plunging, we start with a step-up in vertical velocity, which is then differentiated in time, resulting in the corresponding step-up in vertical position.

#### Linear ramp maneuver

The linear ramp maneuver is based on the pitch-up, hold portion of a pitch-up, hold, pitch-down maneuver first introduced as a canonical pitching maneuver to compare and study various experiments, simulations and models [26, 79]. The equations for $u$ and $\dot{u}$ are given in Eq. (5.15). For a step in angle of attack, $u = \alpha$,

$$u(t) = \Delta\alpha \frac{G(t)}{\max G(t)}, \qquad \dot{u}(t) = \Delta\alpha \frac{\tanh(a(t-t_1)) - \tanh(a(t-t_2))}{\max G(t)} \tag{5.15}$$

where

$$G(t) = \log\left[\frac{\cosh(a(t-t_1))}{\cosh(-at_2)} \cdot \frac{\cosh(-a(t-t_2))}{\cosh(-at_1)}\right]. \tag{5.16}$$

The maneuver is shown in Figure 5.8. The start of the maneuver is $t = t_1$ and the duration of the ramp-up is $T = t_2 - t_1$. The parameter $a$ effects how gradual or abrupt the ramp acceleration is; this $a$ is different than the pitch axis parameter in Section 5.2. By choosing $a$ large, such as $a = 1000$, it is possible to obtain a maneuver where the $\ddot{u}$ acceleration effects are localized near time $t_1 = 0$ and $t_2 = T$, and the velocity $\dot{u}$ is constant throughout much of the maneuver. This yields an approximately piecewise linear ramp, with smooth transitions at $t_1 = 0$ and $t_2 = T$.

The linear ramp maneuver has a number of characteristics that make it a natural choice for the smoothed step maneuver. First, the boxy profile of the velocity $\dot{u}$ resembles the shape of a discrete-time impulse in $\dot{u}$ with time step $T$. Thus, it is

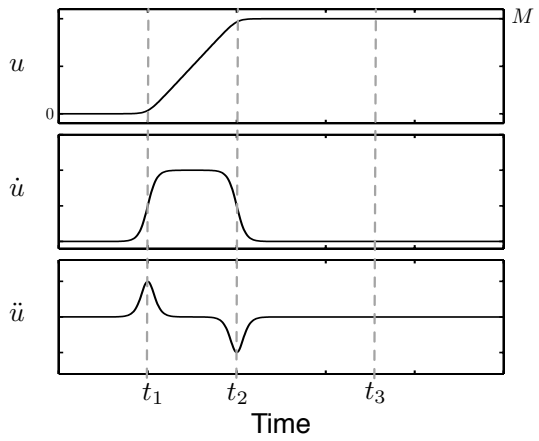


Figure 5.8: Linear ramp-step in $u$, approximating $\dot{u} = \Delta\alpha/\Delta t_c$ for $\Delta t_c = t_2 - t_2$.

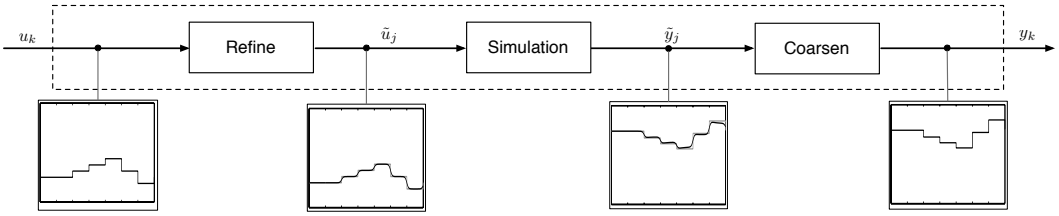


Figure 5.9: Diagram showing the discrete-time system arising from pitch-ramp step.

possible to run simulations with a fine time step $\Delta t_f$ that fully resolve the maneuver in time, and then down-sample to obtain a coarse discrete-time signal with sample time $\Delta t_c = T$. This is shown schematically in Figure 5.9.

**Sigmoidal step maneuver**

Alternatively, a sigmoidal step is given by Eqs. (5.17-5.18), shown in Figure 5.10.

$$u(t) = \frac{\Delta\alpha}{T}\frac{12}{\sqrt{\pi}}\exp\left[-\left(\frac{12}{T}(t - T/2)\right)^2\right] \tag{5.17}$$

$$\int_{-\infty}^{t} u(\tau)d\tau = \frac{\Delta\alpha}{2}\left[1 + \mathrm{erf}\left(\frac{12}{T}(t - T/2)\right)\right] \tag{5.18}$$

In the limit of infinitesimal variance, a Gaussian function will become a delta function. However, the fine resolution discrete-time system arising from this maneuver has large oscillations about the desired coarse resolution discrete-time signal, as seen in Figure 5.11. Moreover, the sigmoidal step poses difficulty in sampling the fine resolution output to obtain a coarse resolution output signal.

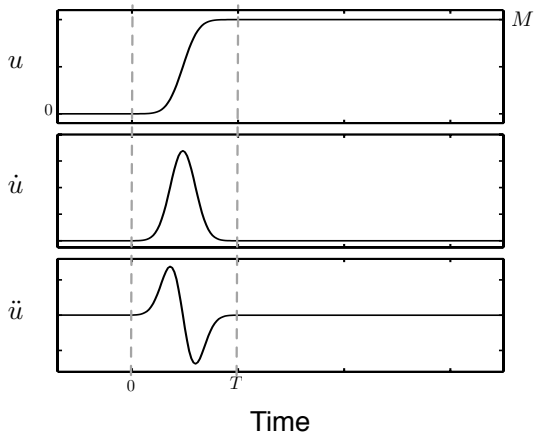


Figure 5.10: Sigmoidal step in $u$ arising from a Gaussian input to $\dot{u}$.

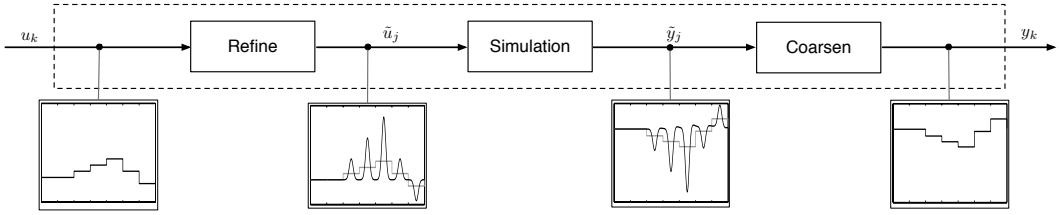


Figure 5.11: Diagram showing the discrete-time input $u_j$ (grey) and the resulting time-resolved signal $\tilde{u}_k$ (black) arising from sigmoidal step.

### 5.4.2 Maneuvers for OKID method

As discussed in Section 2.2.2, the observer/Kalman filter identification (OKID) algorithm is useful for obtaining the Markov parameters (impulse response parameters) from more realistic input/output data. For example, in an experiment, it may be difficult to obtain an impulse response in $\ddot{\alpha}$ because of the accompanying linear growth in $\alpha$. Therefore, it is desirable to use a realistic maneuver with bounded $\alpha$ and estimate what the impulse response would be for the linearized system. Because we are interested in identifying models of the form in Eq. (5.7) with $\ddot{\alpha}$ as the input, it is important that the maneuvers have rich frequency content in $\ddot{\alpha}$ to excite a large range of unsteady flow phenomena.

#### Gaussian white noise in $\ddot{\alpha}$

A good choice for a maneuver is to use a Gaussian white noise process as the input to $\ddot{\alpha}$, since this maneuver is rich in frequency content. The wing kinematics are shown in the first three subplots in Figure 5.12, and the lift coefficient response is plotted in the fourth subplot. The sample time for the white noise process is $\Delta t_c = 0.1$ convective time.

This maneuver is primarily used with simulations, since the lift effect from various parts of the maneuver are subtle and may be swamped by noise in an experiment.

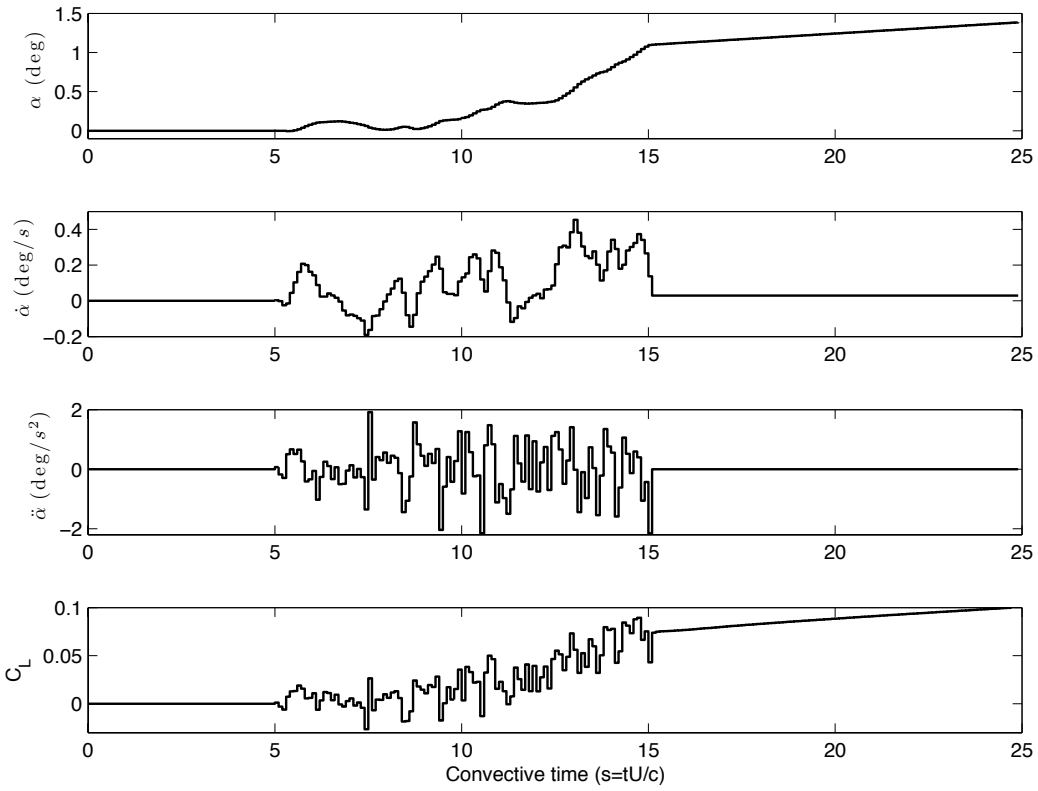


Figure 5.12: System ID maneuver used with OKID to produce Markov parameters for impulse in $\ddot{\alpha}$. Random input to $\ddot{\alpha}$ is chosen because of rich frequency content.

### Pseudo-random pulse train

The system identification (ID) maneuver for the wind tunnel experiments in Chapter 8 was chosen with a number of criteria in mind. Because the input to the model is $\ddot{\alpha}$, we ultimately need a maneuver with rich $\ddot{\alpha}$ content. Also, because we are identifying various stability derivatives, we need the contribution from individual changes in $\ddot{\alpha}$ to be distinguishable in the measured lift force. Finally, because the experimental measurements have noise, we require the system ID maneuver to be sufficiently aggressive so that the change in force is measurable in response to the maneuver.

The maneuver is constructed as a pseudo-random sequence of ramp-up, hold and ramp-down, hold maneuvers, related to the canonical maneuvers in Eldredge *et al.*[26, 79]. The equations for $u$ and $\dot{u}$ for a single pitch-up, hold are given in Eq. (5.15), with $u = \alpha$. The building block for our maneuver is shown in Figure 5.8.

The duration of the ramp $\tau_r = t_2 - t_1$ and hold $\tau_h = t_3 - t_2$ are bounded Gaussian white noise processes. Similarly, the step amplitude $\Delta\alpha$ is sampled from a normal distribution, with the constraint that the maneuver amplitude never exceeds $\pm 10°$. A maneuver of this type is attractive for a number of reasons. First, the signal $\ddot{\alpha}$ consists of pseudo-randomly spaced pulses at the beginning and end of each ramp. The result is that the large added-mass forces are similarly spaced

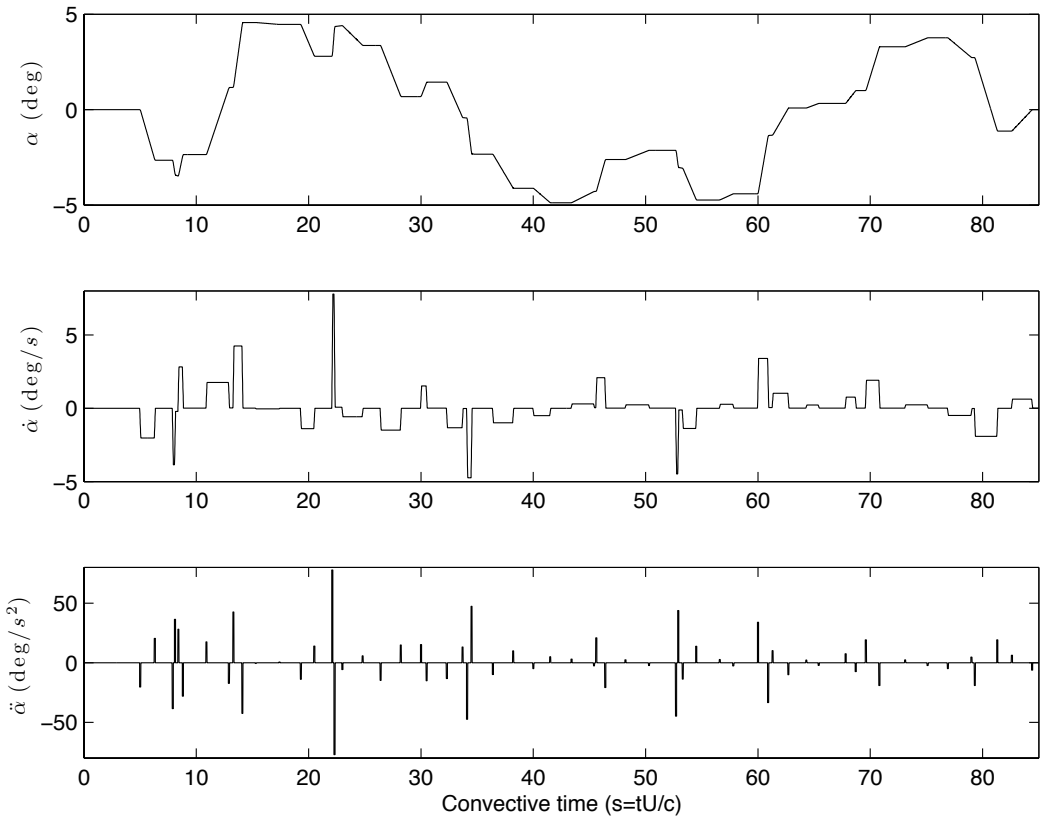


Figure 5.13: Aggressive maneuver for identifying pitch dynamics.

pulses. Additionally, having a pseudo-random train of pulses in $\ddot{\alpha}$ is ideal for the OKID method. Finally, having large aggressive ramp-up and ramp-down maneuvers will result in forces large enough to measure.

Similarly, a pseudo-random maneuver is generated for plunging motion. Because there is no steady-state lift associated with a fixed vertical position $h$, unlike the case of pitching, it is unnecessary for the maneuver to sample different vertical positions during the hold periods.

## 5.5 Summary

We have presented a general form of the unsteady aerodynamic model, and its linearization for the cases of pure pitch, pure plunge, and combined pitch plunge. In addition, we have presented three distinct computational algorithms for obtaining such a linearization, which are used extensively in later chapters. These algorithms produce reduced order models using system identification maneuvers developed for direct numerical simulations and wind tunnel experiments.

The models in this chapter have a number of advantages. It is shown that the models are reduced order representations of the linearized Navier-Stokes equations, and they may be viewed as low-order, state-space realizations of the corresponding indicial response model. The models may be obtained from a variety of sources,

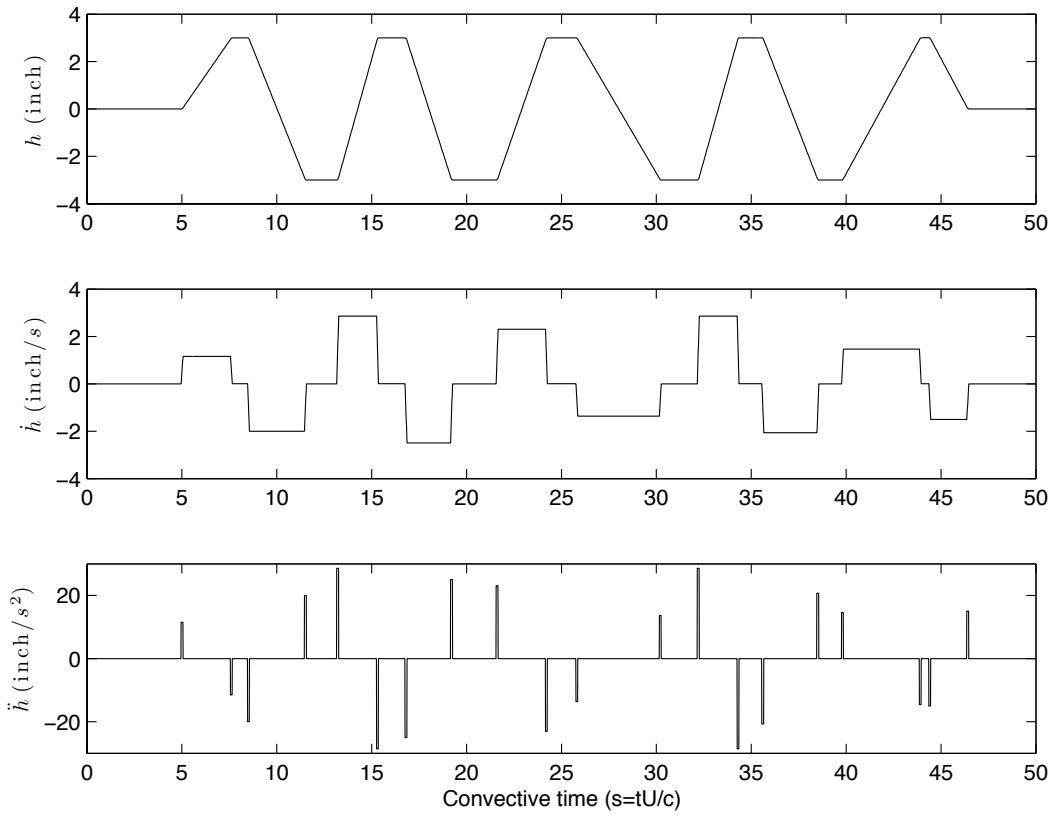


Figure 5.14: Aggressive maneuver for identifying plunge dynamics.

including analytical expressions, direct numerical simulations, and wind tunnel experiments; therefore, they capture the transient fluid dynamic forces of the real viscous flow. There are a number of features that are inspired by Theodorsen's model, including pitch-axis parameterization. In addition, the low and high frequency asymptotes are isolated from the transient dynamics. This means that the reduced order modeling is targeted to the intermediate frequencies where the transient fluid dynamic effects are important, so that the model is more accurate at a lower order.

The algorithms in this chapter are designed to be flexible, yielding model realizations from either step-response data or pseudo-random-input data. A number of maneuvers have been specifically developed for use with these algorithms. These maneuvers excite the unsteady aerodynamic system over a range of frequencies so that the asymptotic effects may be isolated from the transient dynamics.

Although the models in this chapter have been derived for pitch and plunge inputs and lift coefficient output, the methods are sufficiently general to include additional inputs, such as surge motion, as well as additional outputs, such as drag and moment coefficients. The models have been developed in a coordinate system that is especially convenient for aerodynamics, where the translational motion of the wing is in reference to the center of rotation. This is consistent with the notation used in Theodorsen's work, which is used extensively in the field.

# Chapter 6

# Classical unsteady models of Wagner and Theodorsen

This chapter addresses state-space realizations for the classical unsteady models of Wagner [125] and Theodorsen [114]. After a brief overview, the models of Theodorsen and Wagner are presented in Section 6.2, with an emphasis on the underlying assumptions and physical interpretations. In Section 6.3 a number of assumptions are relaxed, and Theodorsen's model is cast in a general form that allows for the introduction of empirically determined quasi-steady and added-mass coefficients as well as an empirical Theodorsen function. These terms may be determined empirically from simulations or experiments, as is demonstrated on numerical data for a flat plate at low Reynolds number, $\mathrm{Re} = 100$. Next, a low-dimensional, state-space realization is developed in Section 6.4 that is useful for either the classical Theodorsen model or the empirical model. The resulting models are parameterized by pitch axis location and have physically meaningful states that isolate the effect of added-mass and quasi-steady forces, as well as the effect of the wake. State-space realizations for Wagner's model are briefly discussed in Section 6.5 for completeness. Although Theodorsen's model includes the effect of an aileron and also describes moment calculations, we consider only the lift coefficient output for pitch and plunge motion.

## 6.1 Overview

Among the wide range of unsteady aerodynamic models in the literature [60], the classical models of Wagner [125] and Theodorsen [114] remain widely used and provide a benchmark for the linear models that proceed them. Theodorsen's model is particularly attractive for a number of reasons. Foremost, the model is derived from first principles using clear assumptions. The resulting model is broken down into physically meaningful components, including the added-mass and quasi-steady contributions as well as the effect of the wake, captured by Theodorsen's transfer function. It is then clear how the model changes as certain assumptions are relaxed. Additionally, the model is parameterized by the pitch center $p$. Finally, the model is already extensively used, which carries its own inherent value.

Theodorsen's lift model was developed in 1935 to explain flutter induced instability that occurs in aircraft at high velocity. The theory is based on incompressible,

inviscid assumptions, and the resulting model is expressed in the frequency domain. This formulation limits the usefulness of Theodorsen's model, both for predicting the lift response in the time-domain, as well as for designing modern control laws [23, 22, 121, 61]. In addition, the inviscid assumption becomes less accurate for flows at low Reynolds number, which are characterized by a thick, laminar boundary layer [9]. Unsteady aerodynamics at low Reynolds number is of particular recent interest to understand insect and bird flight [5, 123] as well as to develop advanced controllers for high performance micro-aerial vehicles [131, 78].

We address both of these issues in this chapter. First, we develop an empirical generalization to Theodorsen's model, extending the model to various geometries and Reynolds numbers. In particular, empirical models from simulations or experiments [12, 14] are cast into the form of Theodorsen's model using empirical added-mass and quasi-steady lift coefficients, as well as an empirical Theodorsen function. The method of obtaining an empirical Theodorsen model is demonstrated for a flat plate pitching at low Reynolds number, $\mathrm{Re} = 100$.

Next, state-space representations are developed for either the classical Theodorsen model or the empirical model. These state-space models are ideal because they fit naturally into existing flight models, and they are useful for the design of optimal controllers. The models developed in this section are constructed to isolate the effect of added-mass and quasi-steady forces, as well as the effect of the wake, as in Theodorsen's original model. In addition, the models maintain the original pitch-axis parameterization. It is important to note that although Theodorsen's model includes the effect of an aileron and also describes moment calculations, we consider only the lift coefficient output for pitch and plunge motion.

### 6.1.1 Previous work on representation of Theodorsen's model

The literature contains a number of rational function approximations to Theodorsen's transfer function [48, 122, 121, 8], Eq. (6.3), and Wagner's indicial response function [48, 50, 30, 23, 121], many of which are based on Padé approximation. Breuker *et al.* [8] and Dinyavari and Friedmann [22] constructed state-space realizations for Theodorsen's transfer function, and Leishman and Nguyen [61] used R. T. Jones's approximation to derive a state-space realization for the circulatory lift. Edwards [25] derived a state-space realization for the coupled aeroelastic equations, which he used to construct a linear-quadratic-regulator for flutter suppression.

Peters *et al.* [86, 85, 84] developed a general potential flow theory in state-space based on the Glauert expansion of inflow states, of which Theodorsen's model is a special case. However, Peters's model requires eight states for close agreement with Theodorsen's model, while the other approximations require between two and four states. With the exception of Peters, none of the above references develop state-space models for the full unsteady model, Eq. (6.2), including added-mass forces.

## 6.2 Model statement

This background review is based closely on material in Leishman [60]. A thorough derivation and review of Theodorsen's theory may be found in Bisplinghoff and Ashley [6] and Newman [75]. Theodorsen and Wagner both make the assumptions

of a 2D flat plate airfoil in an inviscid, incompressible flow. Moreover, the motion of the airfoil is assumed to be infinitesimal in amplitude, resulting in a planar wake.

### 6.2.1 Theodorsen's model

Theodorsen's model is an unsteady extension of the quasi-steady thin airfoil theory. Thin airfoil theory assumes that the vertical center of mass $h$ and angle of attack $\alpha$ motion of the airfoil is relatively slow and small, so that the flow field locally equilibrates to the motion. Thus, $\dot{h}$ and $\dot{\alpha}$ effects manifest as a varying local angle of attack along the airfoil, which may be integrated into an effective angle of attack for the entire airfoil. This results in a quasi-steady expression for the lift coefficient:

$$C_L = 2\pi\left(\alpha + \dot{h} + \frac{1}{2}\dot{\alpha}\left(\frac{1}{2} - a\right)\right) = 2\pi\alpha_e \tag{6.1}$$

Lengths are nondimensionalized by the chord length $c$ and time is nondimensionalized by $c/U_\infty$, where $U_\infty$ is the free stream velocity. $a$ is the pitch axis location with respect to the 1/2-chord (e.g., pitching about the leading edge corresponds to $a = -1$, whereas the trailing edge is $a = 1$).

For rapid maneuvers, it is necessary to include added-mass terms to account for the reaction force due to the mass of fluid that is accelerated by the airfoil. Additionally, one must account for the induced vorticity on the airfoil due to the effect of the wake. Theodorsen's model, Eq. (6.2), includes these added-mass forces and multiplies the circulatory lift from thin airfoil theory by a transfer function $C(s)$ to account for lift attenuation by the wake vorticity.

$$C_L = \underbrace{\frac{\pi}{2}\left[\ddot{h} + \dot{\alpha} - \frac{a}{2}\ddot{\alpha}\right]}_{\text{Added-Mass}} + \underbrace{2\pi\left[\alpha + \dot{h} + \frac{1}{2}\dot{\alpha}\left(\frac{1}{2} - a\right)\right]}_{\text{Circulatory}} C(s) \tag{6.2}$$

Each of the $C_L$, $\alpha$, and $h$ terms, and their derivatives, are expressed in the frequency domain, and depend on the Laplace variable $s$.

Theodorsen's transfer function $C(s)$ is given by Eq. (6.3) and is expressed in terms of Hankel functions $H_\nu^{(2)} = J_\nu - iY_\nu$, where $J_\nu$ and $Y_\nu$ are Bessel functions of the first and second kind, respectively:

$$C(s) = \frac{H_1^{(2)}(-is/2)}{H_1^{(2)}(-is/2) + iH_0^{(2)}(-is/2)} \tag{6.3}$$

Note that Theodorsen's function $C(s)$ is a complex valued function expressed in terms of the Laplace variable $s$. Historically, $C$ is expressed in terms of the reduced frequency $k$, which is frequency nondimensionalized by half chord; however, in the remainder of the thesis, we present models nondimensionalized by full chord, so for consistency, we nondimensionalize by the full chord here. When $s = 2ik$, $C(s)$ gives the amplitude and phase of the response to a sinusoidal input with reduced frequency $k$.

Figure 6.1 shows the frequency response of Theodorsen's model, Eq. (6.2). The input motion is $\ddot{h}$ for the case of plunging and $\ddot{\alpha}$ for the case of pitching, and the output is lift coefficient $C_L$. The magnitude plot(top) shows the ratio of output

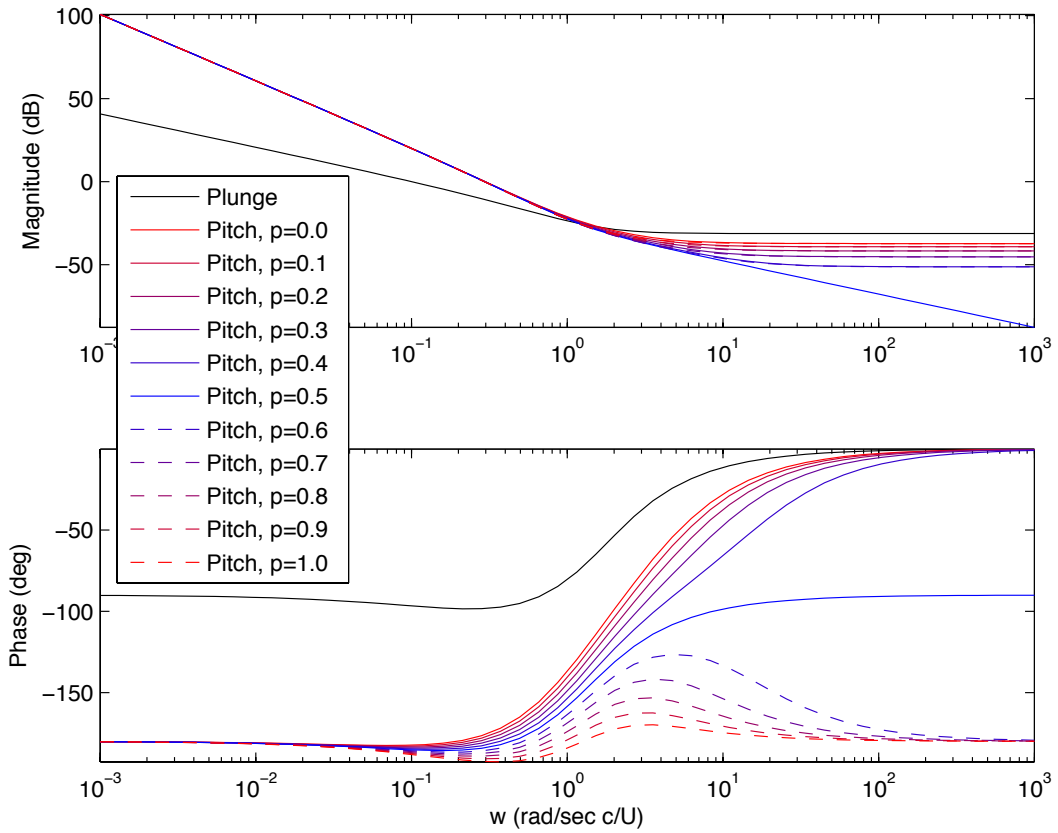


Figure 6.1: Frequency response of Theodorsen's model, Eq. (6.2). Input is $\ddot{h}$ for plunging motion and $\ddot{\alpha}$ for pitching motion about various locations $p$ along the chord. The output is lift coefficient $C_L$.

magnitude ($C_L$) to input magnitude ($\ddot{\alpha}$ or $\ddot{h}$) in decibels (dB) for sinusoidal forcing at various fixed frequencies. Similarly, the phase plot (bottom) shows the phase difference of the output and input signal in degrees. Theodorsen's model for pitching motion is parameterized by $a = -1 + 2p$, where $p$ is the pitch axis location measured in positive chord lengths $c$ from the leading edge.

The frequency response in Figure 6.1 undergoes a qualitative change as the pitch point is moved aft of the mid-chord, after which the effect of added-mass terms on high frequency motions becomes negative; i.e., the phase approaches $-180°$ for large frequency. To understand this, it helps to analyze how the poles and zeros of the system change as pitch point is varied. Using the transfer function representation Eq. (6.8) derived in the next section, it is clear that the pitch point $a$ only enters the numerator, meaning that the poles are the same regardless of pitch center. Figure 6.2 shows how the zeros move as the pitch axis varies. In particular, as the pitch axis moves aft of the mid-chord, the branch of real zeros exits at negative infinity and re-enters at positive infinity. The appearance of a zero in the right half plane makes the system non-minimum phase. A direct result is that given a positive step in angle of attack, the lift initially moves in the negative direction, because of

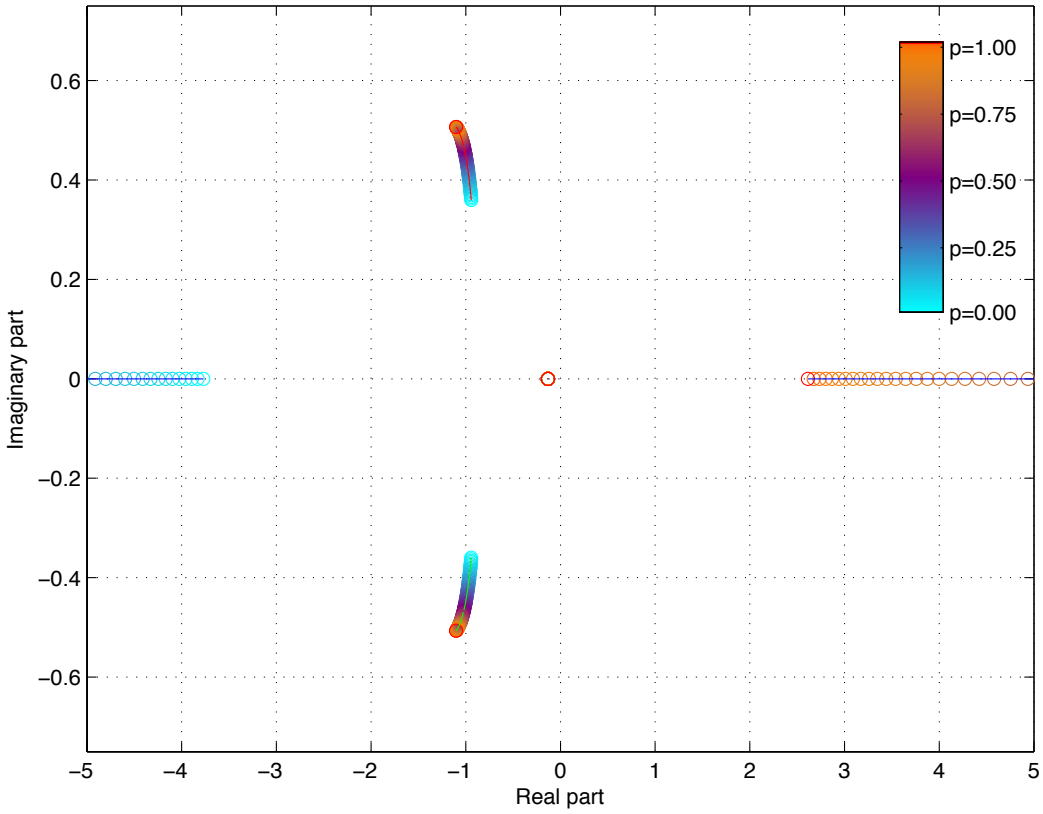


Figure 6.2: Zeros of Theodorsen's lift model as pitch axis moves from the leading edge ($p = 0$) to the trailing edge ($p = 1$). The zero at $s \approx -4$ moves to negative infinity as $p \to 0.5$ and reappears at positive infinity for $p > 0.5$.

negative added-mass forces, before the circulatory forces have a chance to catch up and the system relaxes to a positive steady state.

### 6.2.2 Wagner's model

Wagner's model is similar to Theodorsen's, except that it is formulated in the time domain, making it useful for arbitrary input maneuvers. The model rests on a similar set of fundamental assumptions, including a planar wake, inviscid, incompressible flow, and infinitesimal motion. The formulation is based on convolution with the indicial (step) response function $\phi(t)$, where $t$ is time dimensionless time. At time $t = 0$ the aerodynamic center is at the mid-chord, and it shifts to the 1/4 chord for all future time $t > 0$. The lift due to the step is then written as

$$C_L^\delta = \frac{\pi}{2}\delta(t) + 2\pi\alpha\phi(t) \tag{6.4}$$

The first term is the added-mass for a step in angle of attack about the mid-chord. The circulatory terms for an arbitrary maneuver $\alpha(t)$ are given by

$$C_L^{\text{circ}} = 2\pi \left( \alpha(0)\phi(t) + \int_0^t \dot{\alpha}(\sigma)\phi(t-\sigma)\, d\sigma \right) = 2\pi\alpha_e(t) \tag{6.5}$$

where $\alpha_e(t)$ is the effective angle of attack due to the induced circulation from the wake history. Wagner originally expressed the indicial response in terms of time nondimensionalized by half-chord, and he used the variable $s$ (for semi-chords); however, we use $t$ so that the dimensionless time is not confused with the Laplace variable $s$ that is used throughout.

### 6.2.3 Relationship between Wagner's and Theodorsen's functions

It was noted early on by Garrick [30] and R.T. Jones [48] that Theodorsen's transfer function and Wagner's indicial response function are related by a Laplace transform pair:

$$C(s) = s \int_0^\infty \phi(t) e^{-st}\, dt \tag{6.6}$$

There are a number of approximations to Theodorsen's transfer function $C(s)$, shown in Table 6.2, and to Wagner's indicial response function $\phi(t)$, shown in Table 6.1. Figure 6.3 shows a comparison between the exact Theodorsen function in Eq. 6.2 and the R.T. Jones approximation for $C(s)$ and $\phi(t)$ from Tables 6.2 and 6.1. These will be useful in Section 6.4 for obtaining state-space realizations.

## 6.3 Generalized Theodorsen model

It is possible to generalize Theodorsen's model by replacing the coefficients $\pi/2$ and $2\pi$, which are obtained using linearized potential flow theory, with generalized coefficients $C_1$ and $C_2$. The new coefficients may be obtained empirically, either through simulation or experiment, at a given Reynolds number and wing geometry. This will yield better performance in the limit of low and high frequency motions. Additionally, it is possible to use an empirically determined function $\hat{C}(s)$, which plays the same role as Theodorsen's $C(s)$. Eq. (6.2) becomes:

$$C_L = C_1 \left[ \ddot{h} + \dot{\alpha} - \frac{a}{2}\ddot{\alpha} \right] + C_2 \left[ \alpha + \dot{h} + \frac{1}{2}\dot{\alpha}\left( \frac{1}{2} - a \right) \right] \hat{C}(s). \tag{6.7}$$

We now take the Laplace transform, $\mathcal{L}$, of both sides to obtain a transfer function. For the case of pitch, $u = \ddot{\alpha}$,

$$\frac{\mathcal{L}\left[C_L\right]}{\mathcal{L}\left[\ddot{\alpha}\right]} = C_1 \left( \frac{1}{s} - \frac{a}{2} \right) + C_2 \left[ \frac{1}{s^2} + \frac{1}{2s}\left( \frac{1}{2} - a \right) \right] \hat{C}(s) \tag{6.8}$$

where $s$ is the Laplace variable, which is twice the reduced frequency if $c = U_\infty = 1$. The transfer function $1/s$ corresponds to integration in the time domain. Equation (6.8) is represented schematically in Figure 6.4.

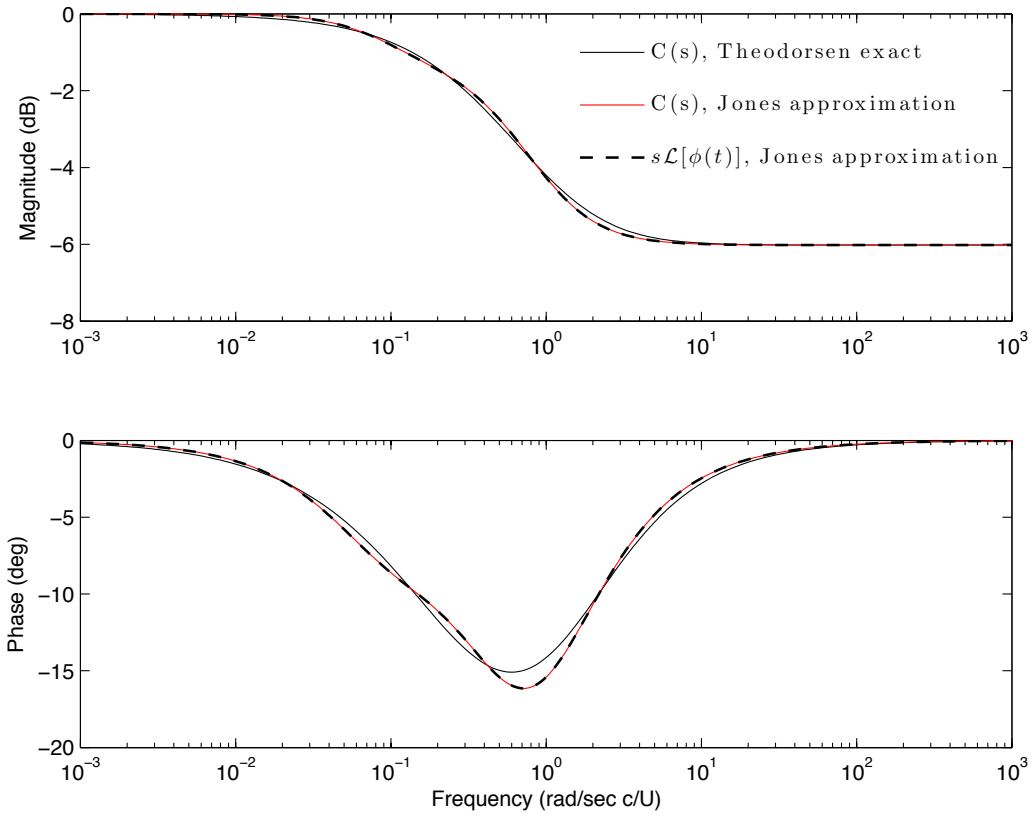


Figure 6.3: Theodorsen's transfer function $C(s)$ (black) and the R.T. Jones approximation for $C(s)$ (red) and $\phi(t)$ (black dash), respectively. Input is quasi-steady lift coefficient, and output is circulatory lift coefficient attenuated by the wake.

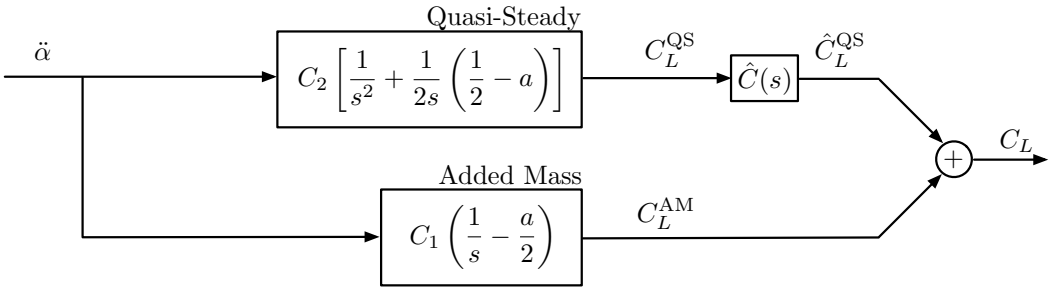


Figure 6.4: Empirical Theodorsen's model, Eq. (6.8), for a pitching airfoil.

| | Approximate indicial response, $\phi(t)$ |
|---|---|
| R.T. Jones [48] | $\phi(t) \approx 1.0 - 0.165e^{-0.091t} - 0.335e^{-0.6t}$ |
| W.P. Jones [50] | $\phi(t) \approx 1.0 - 0.165e^{-0.082t} - 0.335e^{-0.64t}$ |
| Garrick [30] | $\phi(t) \approx \dfrac{t+1}{t+2}$ |
| Venkatesan et al. [121] | $\phi(t) \approx 1.0 - 0.309e^{-0.193t} - 0.191e^{-0.991t}$ |
| Venkatesan et al. [121] | $\phi(t) \approx 1.0 - 0.203e^{-0.144t} - 0.236e^{-0.501t}$ $-0.06e^{-1.6t}$ |

Table 6.1: Approximations for Wagner's indicial response function $\phi(t)$. Time $t$ is nondimensionalized by chord $c$; in references, time $t' = 2t$ is used.

The case of plunging, $u = \ddot{h}$, has a simpler transfer function:

$$\frac{\mathcal{L}\left[C_L\right]}{\mathcal{L}\left[\ddot{h}\right]} = C_1 + \frac{C_2}{s}\hat{C}(s)$$

These transfer functions will be used to construct state-space representations in the next section.

### 6.3.1 Determining coefficients $C_1$ and $C_2$

Theodorsen's function $C(s)$ is 1 at low frequencies and 1/2 at high frequencies. It is convenient to decompose $C(s) = 1 - C'(s)$, resulting in the following pitch model:

$$C_L = \underbrace{-\frac{a}{2}C_1}_{C_{\ddot{\alpha}}}\ddot{\alpha} + \underbrace{\left[C_1 + \frac{C_2}{2}\left(\frac{1}{2} - a\right)\right]}_{C_{\dot{\alpha}}}\dot{\alpha} + \underbrace{C_2}_{C_\alpha}\alpha - \underbrace{C_2 C'(s)\left[\alpha + \frac{1}{2}\dot{\alpha}\left(\frac{1}{2} - a\right)\right]}_{\text{transient dynamics}} \tag{6.9}$$

Equating the coefficient of the $\ddot{\alpha}$ and $\alpha$ terms in Eqs. (5.13) and (6.9) yields expressions for the coefficients in terms of stability derivatives, $C_1 = -2C_{\ddot{\alpha}}/a$ and $C_2 = C_\alpha$, which may be determined empirically using methods in Chapter 5. There are a number of ways to model the additional transient dynamics. The simplest ap-

| | Approximate transfer function, $C(s)$ |
|---|---|
| R.T. Jones [48] | $C(s) \approx \dfrac{0.5s^2 + 0.5616s + 0.0546}{s^2 + 0.691s + 0.0546}$ |
| Vepa [122] | $C(s) \approx \dfrac{0.5s^2 + 1.5s + 0.75}{s^2 + 2.5s + 0.75}$ |
| Vepa [122] | $C(s) \approx \dfrac{0.5s^3 + 3.5s^2 + 5.425s + 1.875}{s^3 + 6.5s^2 + 8.5s + 1.875}$ |
| Venkatesan *et al.* [121] | $C(s) \approx \dfrac{0.5(s + 0.270)(s + 1.302)}{(s + 0.193)(s + 0.911)}$ |
| Venkatesan *et al.* [121] | $C(s) \approx \dfrac{0.5(s + 0.176)(s + 0.74)(s + 1.844)}{(s + 0.144)(s + 0.522)(s + 1.60)}$ |
| Breuker *et al.* [8] | $C(s) \approx \dfrac{0.5177s^2 + 0.5504s + 0.06404}{s^2 + 0.6828s + 0.06328}$ |
| Modified from [8] | $C(s) \approx \dfrac{0.5s^2 + 0.547s + 0.06328}{s^2 + 0.6828s + 0.06328}$ |

Table 6.2: Approximate Theodorsen's transfer function $C(s)$, where $s = 2ik$.

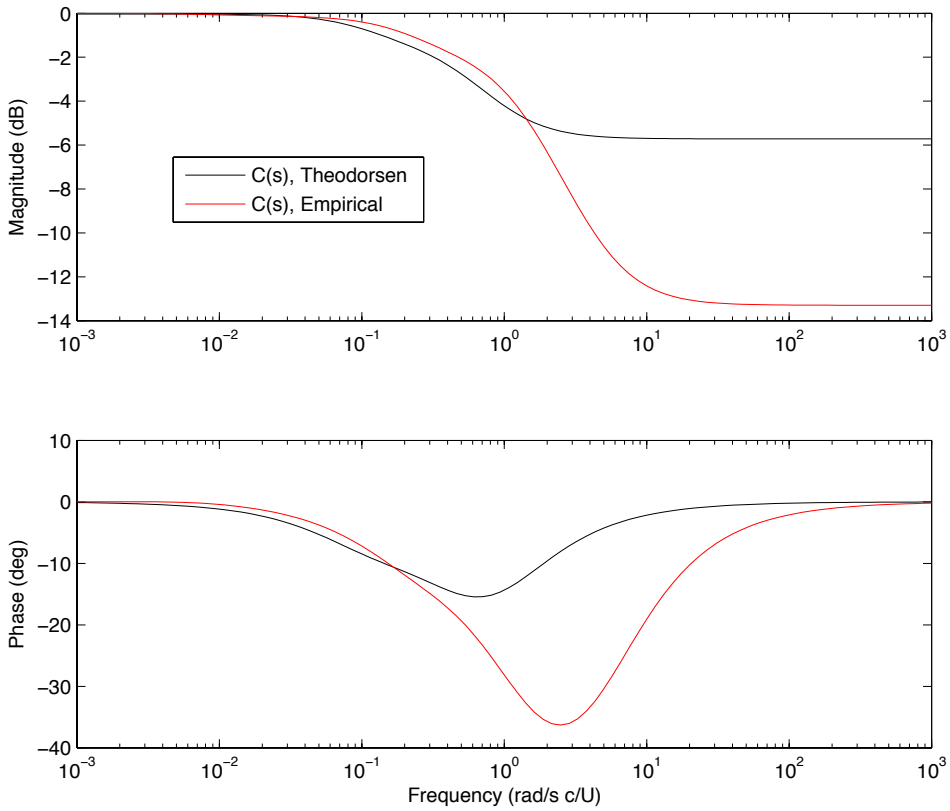


Figure 6.5: Theodorsen's function $C(s)$ from theory (black) and empirical $\hat{C}(s)$ for a flat plate pitching at the leading edge, $p = 0.0$, at Re $= 100$ (red). The input is quasi-steady lift and the output is circulatory lift attenuated by the wake.

proach is to use the analytic Theodorsen function $C(s)$; in this case, the empirically determined $C_1$ and $C_2$ still guarantee the correct high and low frequency behavior. For better performance at intermediate frequencies, it is possible to obtain an empirically determined Theodorsen function $\hat{C}(s)$, as discussed in the next section.

### 6.3.2 Empirical Theodorsen function $\hat{C}(s)$

Starting with an accurate state-space model for a given Reynolds number and geometry, for example based on the methods from Chapter 5, it is possible to determine an empirical Theodorsen function, $\hat{C}(s)$. Starting with a transfer function model $G(s)$ from $\ddot{\alpha}$ to $C_L$ it is possible to solve for $\hat{C}(s)$ in Eq. (6.8) by first subtracting off the added-mass terms and then dividing through by the quasi-steady terms:

$$\hat{C}(s) = \frac{G(s) - C_1\left(1/s - a/2\right)}{C_2\left[1/s^2 + 1/2s\left(1/2 - a\right)\right]} \tag{6.10}$$

This is demonstrated in Figure 6.5 for a model of a plate pitching about the leading-edge at Re $= 100$. The empirical model has order $r = 2$; the resulting lift coefficient model is shown in Figure 6.6.

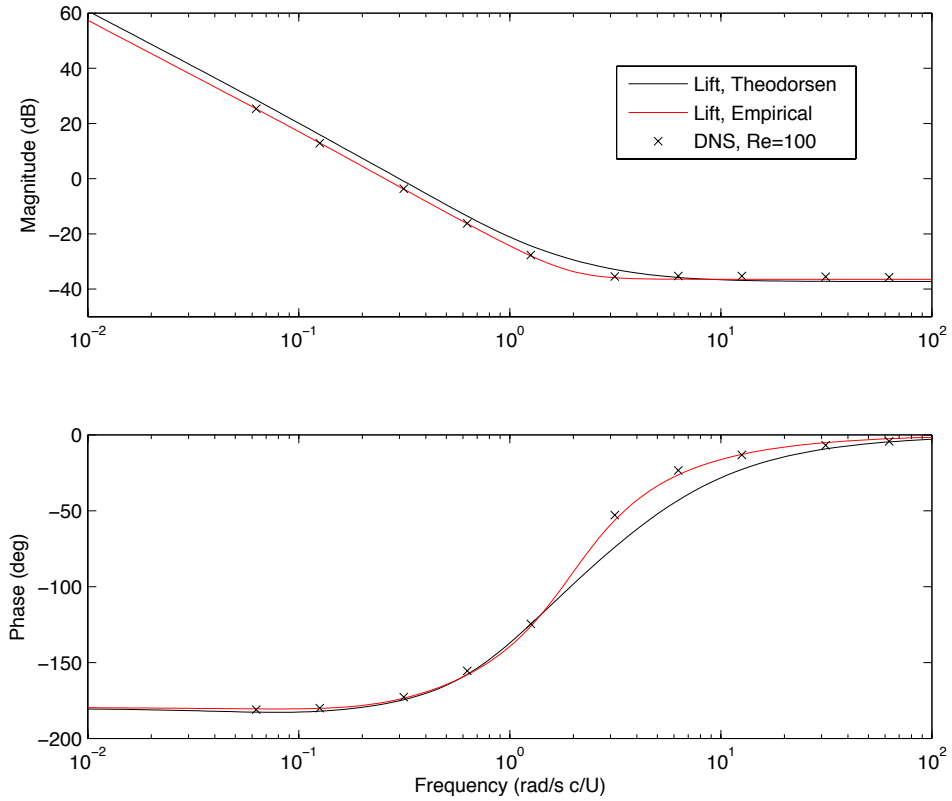


Figure 6.6: Theodorsen's lift model (black) and empirical lift model for a flat plate pitching at the leading edge, $p = 0.0$, at Re $= 100$ (red). Direct numerical simulations ($\times$) are included for validation. The input is $\ddot{\alpha}$ and the output is lift coefficient.

Based on inviscid theory, one would expect that the empirical Theodorsen function $\hat{C}(s)$ is the same regardless of pitch center. This is not the case for a flat plate pitching at Re$= 100$, as seen in Figure 6.7. In a viscous fluid, angle of attack and plunge motions have different effects on the wake, thus, two different $C(s)$ for pitch and plunge.

## 6.4 State-space realizations for Theodorsen's model

Starting with Theodorsen's model, Eq. (6.2), or the empirical model, Eq. (6.8), we construct a state-space representation of the form:

$$\begin{aligned} \dot{x} &= Ax + Bu \\ y &= Cx + Du \end{aligned} \qquad \Longleftrightarrow \qquad \begin{bmatrix} \dot{x} \\ y \end{bmatrix} = \left[\begin{array}{c|c} A & B \\ \hline C & D \end{array}\right] \begin{bmatrix} x \\ u \end{bmatrix} \tag{6.11}$$

$u \in \mathbb{R}^q$ is the input, $y \in \mathbb{R}^p$ is the output, and $x \in \mathbb{R}^n$ is the state; the matrix notation is shorthand. These representations are constructed to retain the favorable properties of Theodorsen's model. The model is parameterized by the pitch-axis location, and the added-mass and quasi-steady forces are isolated from the effect of the wake. Moreover, the states of the model are physically meaningful quantities.

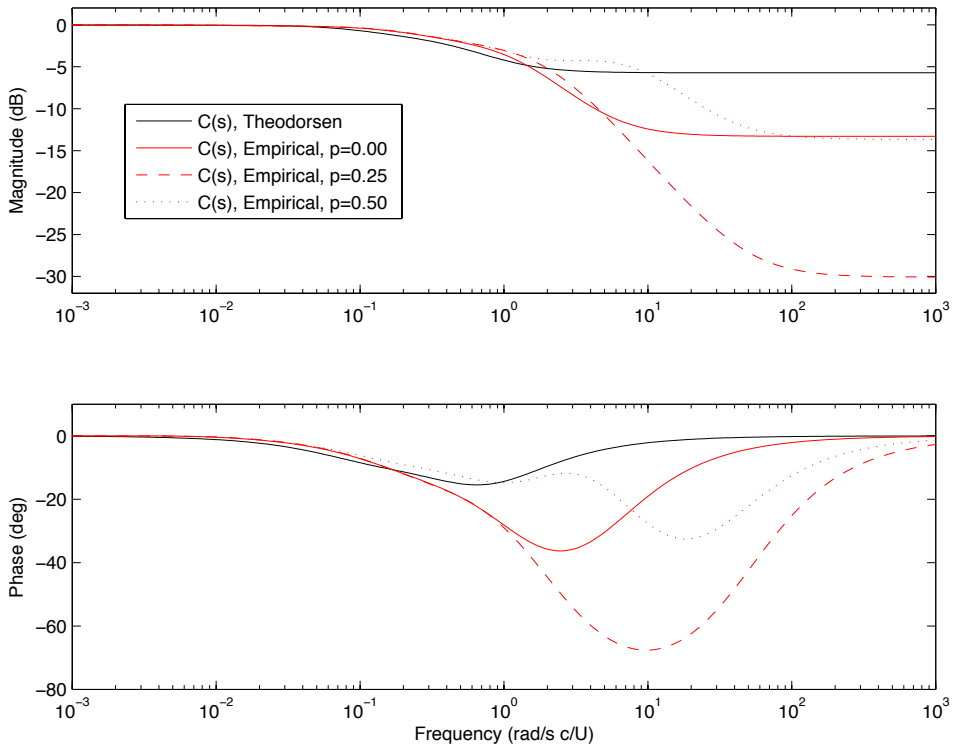


Figure 6.7: Theodorsen's transfer function $C(s)$ from theory (black) and empirical $\hat{C}(s)$ for a flat plate pitching about various locations at $\mathrm{Re} = 100$ (red). The input is quasi-steady lift and the output is circulatory lift attenuated by the wake.

Consider state-space realizations for the quasi-steady (QS) and Theodorsen transfer function $C(s)$ blocks in Figure 6.4:

$$\text{Quasi-steady:} \qquad \begin{aligned} \dot{x} &= Ax + Bu \\ y &= Cx \end{aligned} \tag{6.12}$$

$$\text{Theodorsen:} \qquad \begin{aligned} \dot{\tilde{x}} &= \tilde{A}\tilde{x} + \tilde{B}\tilde{u} \\ \tilde{y} &= \tilde{C}\tilde{x} + \tilde{D}\tilde{u} \end{aligned} \tag{6.13}$$

The output of the quasi-steady model is the input to Theodorsen's transfer function, $y = \tilde{u}$, resulting in:

$$\begin{aligned} \frac{d}{dt}\begin{bmatrix}\tilde{x}\\ x\end{bmatrix} &= \begin{bmatrix}\tilde{A} & \tilde{B}C\\ 0 & A\end{bmatrix}\begin{bmatrix}\tilde{x}\\ x\end{bmatrix} + \begin{bmatrix}0\\ B\end{bmatrix}u \\ \tilde{y} &= \begin{bmatrix}\tilde{C} & \tilde{D}C\end{bmatrix}\begin{bmatrix}\tilde{x}\\ x\end{bmatrix} \end{aligned} \quad \Longleftrightarrow \quad \left[\begin{array}{cc|c} \tilde{A} & \tilde{B}C & 0 \\ 0 & A & B \\ \hline \tilde{C} & \tilde{D}C & 0 \end{array}\right] \tag{6.14}$$

Note that $C$ is the output matrix for the quasi-steady model, not Theodorsen's transfer function, $C(s)$. State-space realizations $(\tilde{A}, \tilde{B}, \tilde{C}, \tilde{D})$ for Theodorsen's function will be presented in Section 6.4.4.

### 6.4.1 Pure pitch model

For the case of pure pitching motion, $u = \ddot{\alpha}$, the quasi-steady transfer function from Eq. (6.8) is given by

$$\mathrm{QS}(s) = C_2 \left[ s^{-2} + s^{-1}(1 - 2a)/4 \right] \tag{6.15}$$

A state-space realization for Eq. (6.15) may be constructed by introducing a state, $\mathbf{x} = \begin{bmatrix} \alpha & \dot{\alpha} \end{bmatrix}^T$, input $u = \ddot{\alpha}$, and output $y = C_L^{\mathrm{QS}}$:

$$\begin{gathered} \frac{d}{dt} \begin{bmatrix} \alpha \\ \dot{\alpha} \end{bmatrix} = \begin{bmatrix} 0 & 1 \\ 0 & 0 \end{bmatrix} \begin{bmatrix} \alpha \\ \dot{\alpha} \end{bmatrix} + \begin{bmatrix} 0 \\ 1 \end{bmatrix} \ddot{\alpha} \\ C_L^{\mathrm{QS}} = \begin{bmatrix} C_2 & C_2 \left( \frac{1}{2} - a \right) /2 \end{bmatrix} \begin{bmatrix} \alpha \\ \dot{\alpha} \end{bmatrix} \end{gathered} \tag{6.16}$$

The quasi-steady lift coefficient, $C_L^{\mathrm{QS}}$, depends on $\alpha$ and $\dot{\alpha}$, which comprise the state, $\mathbf{x}$. The added-mass transfer function is $\mathrm{AM}(s) = C_1 \left[ s^{-1} - a/2 \right]$. With state $x = \dot{\alpha}$, input $u = \ddot{\alpha}$, and output $y = C_L^{\mathrm{AM}}$, a state-space realization for the added-mass portion is:

$$\begin{gathered} \frac{d}{dt} \dot{\alpha} = 0 \cdot \dot{\alpha} + 1 \cdot \ddot{\alpha} \\ C_L^{\mathrm{AM}} = C_1 \cdot \dot{\alpha} - C_1 \frac{a}{2} \cdot \ddot{\alpha} \end{gathered} \tag{6.17}$$

Both the quasi-steady and added-mass models share a state $\dot{\alpha}$, so we may represent the total lift in a compact model:

$$\begin{gathered} \frac{d}{dt} \begin{bmatrix} \tilde{x} \\ \alpha \\ \dot{\alpha} \end{bmatrix} = \begin{bmatrix} \tilde{A} & \tilde{B}C_2 & \tilde{B}C_2 \left( \frac{1}{2} - a \right) /2 \\ 0 & 0 & 1 \\ 0 & 0 & 0 \end{bmatrix} \begin{bmatrix} \tilde{x} \\ \alpha \\ \dot{\alpha} \end{bmatrix} + \begin{bmatrix} 0 \\ 0 \\ 1 \end{bmatrix} \ddot{\alpha} \\ C_L = \begin{bmatrix} \tilde{C} & \tilde{D}C_2 & C_1 + \tilde{D}C_2 \left( \frac{1}{2} - a \right) /2 \end{bmatrix} \begin{bmatrix} \tilde{x} \\ \alpha \\ \dot{\alpha} \end{bmatrix} - C_1 \frac{a}{2} \ddot{\alpha} \end{gathered} \tag{6.18}$$

In this model, we have combined the quasi-steady model in Eq. (6.16) with the model of Theodorsen's function in Eq. (6.13) according to the formula in Eq. (6.14), and we have included the additional added-mass forces from Eq. (6.17). Note that the model in Eq. (6.18) has the same form as the model in Eq. (5.5) with $B_3 = 0$.

### 6.4.2 Pure plunge model

For plunge, $u = \ddot{h}$, the quasi-steady transfer function is $\mathrm{QS}(s) = C_2 s^{-1}$ and the added-mass is $C_1 \ddot{h}$. This results in the following combined model

$$\begin{aligned} \frac{d}{dt}\begin{bmatrix}\tilde{x}\\ \dot{h}\end{bmatrix} &= \begin{bmatrix}\tilde{A} & \tilde{B}C_2\\ 0 & 0\end{bmatrix}\begin{bmatrix}\tilde{x}\\ \dot{h}\end{bmatrix} + \begin{bmatrix}0\\ 1\end{bmatrix}\ddot{h} \\ C_L &= \begin{bmatrix}\tilde{C} & \tilde{D}C_2\end{bmatrix}\begin{bmatrix}\tilde{x}\\ \dot{h}\end{bmatrix} + C_1\ddot{h} \end{aligned} \tag{6.19}$$

This model is simpler than the corresponding pitch model because there is no dependence on the vertical height, $h$, only on its derivatives.

### 6.4.3 Combined pitch and plunge model

For combined pitch and plunge, $u = \begin{bmatrix}\ddot{h} & \ddot{\alpha}\end{bmatrix}^T$, the model is:

$$\begin{aligned} \frac{d}{dt}\begin{bmatrix}\tilde{x}\\ \dot{h}\\ \alpha\\ \dot{\alpha}\end{bmatrix} &= \begin{bmatrix}\tilde{A} & \tilde{B}C_2 & \tilde{B}C_2 & \tilde{B}C_2(1-2a)/2\\ 0 & 0 & 0 & 0\\ 0 & 0 & 0 & 1\\ 0 & 0 & 0 & 0\end{bmatrix}\begin{bmatrix}\tilde{x}\\ \dot{h}\\ \alpha\\ \dot{\alpha}\end{bmatrix} + \begin{bmatrix}0 & 0\\ 1 & 0\\ 0 & 0\\ 0 & 1\end{bmatrix}\begin{bmatrix}\ddot{h}\\ \ddot{\alpha}\end{bmatrix} \\ C_L &= \begin{bmatrix}\tilde{C} & \tilde{D}C_2 & \tilde{D}C_2 & C_1 + \tilde{D}C_2(1-2a)/2\end{bmatrix}\begin{bmatrix}\tilde{x}\\ \dot{h}\\ \alpha\\ \dot{\alpha}\end{bmatrix} + \begin{bmatrix}C_1 & -C_1 a/2\end{bmatrix}\begin{bmatrix}\ddot{h}\\ \ddot{\alpha}\end{bmatrix} \end{aligned} \tag{6.20}$$

This realization is not minimal, since the state $\begin{bmatrix}0 & 1 & -1 & 0\end{bmatrix}^T$ is unobservable. This is consistent with the fact that in Theodorsen's framework, $\dot{h}$ contributes to an effective angle of attack after proper nondimensionalization. It is possible to construct a minimal realization by introducing the state variable $\alpha_e = \alpha + \dot{h}$.

$$\begin{aligned} \frac{d}{dt}\begin{bmatrix}\tilde{x}\\ \alpha_e\\ \dot{\alpha}\end{bmatrix} &= \begin{bmatrix}\tilde{A} & \tilde{B}C_2 & \tilde{B}C_2(1-2a)/2\\ 0 & 0 & 1\\ 0 & 0 & 0\end{bmatrix}\begin{bmatrix}\tilde{x}\\ \alpha_e\\ \dot{\alpha}\end{bmatrix} + \begin{bmatrix}0 & 0\\ 1 & 0\\ 0 & 1\end{bmatrix}\begin{bmatrix}\ddot{h}\\ \ddot{\alpha}\end{bmatrix} \\ C_L &= \begin{bmatrix}\tilde{C} & \tilde{D}C_2 & C_1 + \tilde{D}C_2(1-2a)/2\end{bmatrix}\begin{bmatrix}\tilde{x}\\ \alpha_e\\ \dot{\alpha}\end{bmatrix} + \begin{bmatrix}C_1 & -C_1 a/2\end{bmatrix}\begin{bmatrix}\ddot{h}\\ \ddot{\alpha}\end{bmatrix} \end{aligned} \tag{6.21}$$

This representation is particularly attractive because the pitch and plunge models share the same dynamics, $\tilde{A}$, resulting in a compact model.

### 6.4.4 State-space realizations for Theodorsen's function $C(s)$

To obtain the $\tilde{A}, \tilde{B}, \tilde{C}$, and $\tilde{D}$ from Eq. (6.13), there are a number of rational approximations to Theodorsen's function $C(s)$, Eq. (6.3), including the approximation by

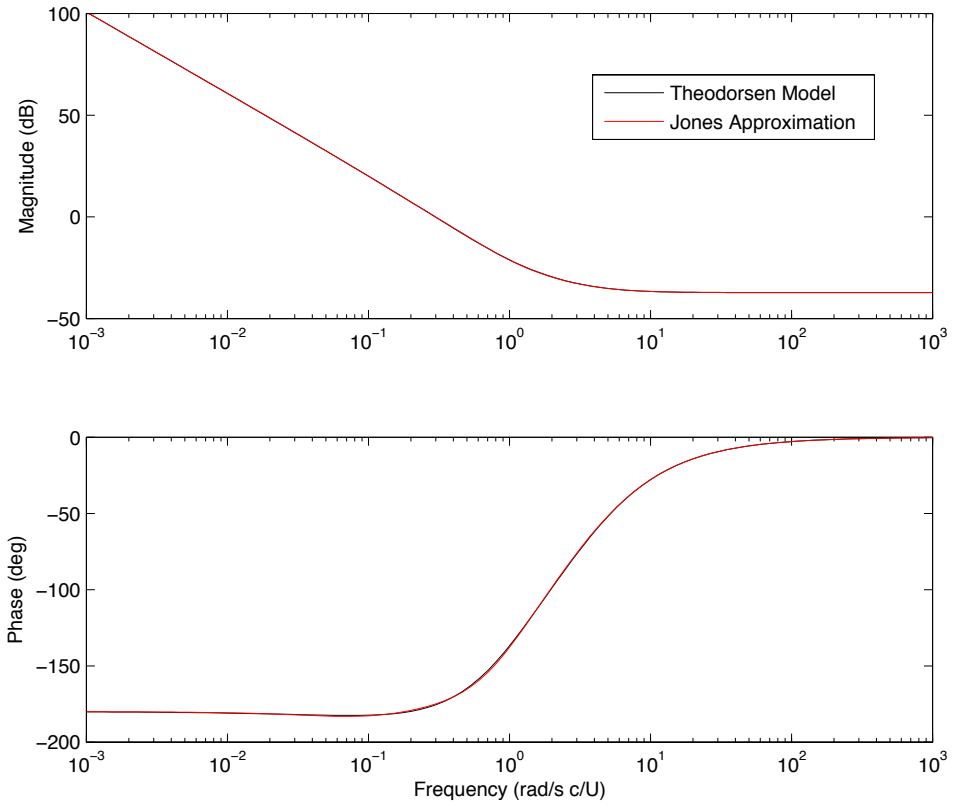


Figure 6.8: Frequency response for pitching about leading-edge, $p = 0.0$, Eq. (6.2), with $\ddot{\alpha}$ as input and $C_L$ as output. Exact model (black) and state-space model based on Jones approximation (red).

Jones [48] and a Padé approximation [8]. For each of these transfer functions, given in Table 6.2, it is possible to obtain a state-space realization in controller canonical form. These realizations are presented in Table 6.3. Note, we have converted the reduced frequency $k$ to the Laplace variable $s = 2ik$. The resulting model agrees very well with the exact model as seen in the frequency response in Figure 6.8.

## 6.5 State-space realization for Wagner's model

This section is included for completeness, although realizations based on R.T. Jones's approximation [48, 49] have been previously developed [22, 61].

The Laplace transform of the indicial response function $\phi$ is the transfer function from $\dot{\alpha}$ to the circulatory lift coefficient $C_L^{\text{circ}}$. Garrick's approximation from Table 6.1 is a simple expression, but it does not have a simple Laplace transform. The other two expressions in Table 6.1 have the form $\phi(t) = 1 - a_1 e^{-b_1 t} - a_2 e^{-b_2 t}$. The Laplace transform has the form:

$$\mathcal{L}\phi(s) = \frac{1}{s} - \frac{a_1}{s + b_1} - \frac{a_2}{s + b_2} \tag{6.22}$$

| Approximation | $\left[\begin{array}{c\|c} \tilde{A} & \tilde{B} \\ \hline \tilde{C} & \tilde{D} \end{array}\right]$, State-space realization of $C(s)$ |
|---|---|
| R.T. Jones [48] | $\left[\begin{array}{cc\|c} -0.691 & -0.0546 & 1 \\ 1 & 0 & 0 \\ \hline 0.2161 & .0273 & 0.5 \end{array}\right]$ |
| Vepa [122] | $\left[\begin{array}{cc\|c} -2.5 & -0.75 & 1 \\ 1 & 0 & 0 \\ \hline 0.25 & 0.375 & 0.5 \end{array}\right]$ |
| Vepa [122] | $\left[\begin{array}{ccc\|c} -6.5 & -8.5 & -1.875 & 1 \\ 1 & 0 & 0 & 0 \\ 0 & 1 & 0 & 0 \\ \hline 0.25 & 1.175 & 0.9375 & 0.5 \end{array}\right]$ |
| Venkatesan [121] | $\left[\begin{array}{cc\|c} -1.104 & -0.1758 & 1 \\ 1 & 0 & 0 \\ \hline 0.234 & 0.08786 & 0.5 \end{array}\right]$ |
| Venkatesan [121] | $\left[\begin{array}{ccc\|c} -2.266 & -1.141 & -0.1203 & 1 \\ 1 & 0 & 0 & 0 \\ 0 & 1 & 0 & 0 \\ \hline 0.247 & 0.3393 & 0.05995 & 0.5 \end{array}\right]$ |
| Breuker *et al.* [8] | $\left[\begin{array}{cc\|c} -0.6828 & -0.06328 & 1 \\ 1 & 0 & 0 \\ \hline 0.1969 & 0.03028 & 0.5177 \end{array}\right]$ |
| Modified from [8] | $\left[\begin{array}{cc\|c} -0.6828 & -0.06328 & 1 \\ 1 & 0 & 0 \\ \hline 0.2056 & 0.03164 & 0.5 \end{array}\right]$ |

Table 6.3: State-space realizations for approximate $C(s)$.

| Approximation | $\left[\begin{array}{c\|c} \tilde{A} & \tilde{B} \\ \hline \tilde{C} & \tilde{D} \end{array}\right]$, State-space realization of $\phi(s)$ |
|---|---|
| R.T. Jones [48] | $\left[\begin{array}{ccc\|c} -0.691 & -0.0546 & 0 & 1 \\ 1 & 0 & 0 & 0 \\ 0 & 1 & 0 & 0 \\ \hline 0.5 & 0.5615 & 0.0546 & 0 \end{array}\right]$ |
| W. P. Jones [50] | $\left[\begin{array}{ccc\|c} -0.722 & -0.0525 & 0 & 1 \\ 1 & 0 & 0 & 0 \\ 0 & 1 & 0 & 0 \\ \hline 0.5 & 0.5889 & 0.0525 & 0 \end{array}\right]$ |
| Venkatesan [121] | $\left[\begin{array}{ccc\|c} -1.184 & -0.1913 & 0 & 1 \\ 1 & 0 & 0 & 0 \\ 0 & 1 & 0 & 0 \\ \hline 0.5 & 0.8409 & 0.1913 & 0 \end{array}\right]$ |
| Venkatesan [121] | $\left[\begin{array}{cccc\|c} -2.245 & -1.104 & -0.1154 & 0 & 1 \\ 1 & 0 & 0 & 0 & 0 \\ 0 & 1 & 0 & 0 & 0 \\ 0 & 0 & 1 & 0 & 0 \\ \hline 0.501 & 1.368 & 0.8827 & 0.1154 & 0 \end{array}\right]$ |

Table 6.4: State-space realizations for approximate $\phi(s)$.

This yields the state-space realizations with input $\dot{\alpha}$ and output $C_L^{\text{circ}}$ in Table 6.4.

Because of the equivalence of Wagner's function $\phi(t)$ and Theodorsen's transfer function $C(s)$, it is not necessary to develop an explicit state-space realization for Wagner's full unsteady model. Wagner's model imposes the additional constraints that at $t = 0$ the aerodynamic center is at the mid-chord, and it shifts to the quarter-chord for all time after. The aerodynamic center is located at the mid-chord at $t = 0$ to simplify the added-mass forces, since the term proportional to $\ddot{\alpha}$ disappears when pitching at the mid-chord.

## 6.6 Summary

In this chapter, a generalized Theodorsen model is developed and cast into a low-dimensional, state-space representation. Using a number of approximations for Theodorsen's transfer function $C(s)$ [48, 8], it is possible to obtain a rational trans-

fer function and corresponding minimal state-space representation for Theodorsen's lift model, given by Eq. (6.18) for pure pitch, Eq. (6.19) for pure plunge, and Eq. (6.21) for combined pitch and plunge. These models retain the positive attributes of Theodorsen's model, in that they are parameterized by pitch axis and have physically meaningful states that isolate the effect of quasi-steady and added-mass forces, as well as the effect of the wake.

Additionally, a method is presented to obtain empirical added-mass and quasi-steady coefficients, $C_1$ and $C_2$, as well as an empirical Theodorsen function, $\hat{C}(s)$, using either simulations or experiments. This guarantees agreement of the model in the limit of high and low frequency motions, as well as in between. The method of obtaining an empirically determined Theodorsen's model has been demonstrated for a flat plate pitching at low Reynolds number, $\mathrm{Re} = 100$. The numerical example presented indicates that at low Reynolds number, the effect of the wake is not the same for each pitch center. Understanding the variation in the empirical $\hat{C}(s)$ with pitch axis location may be an important avenue of future research.

Finally, Wagner's model is included for completeness. In addition to a direct comparison with Theodorsen's model, a state-space realization is presented for Wagner's indicial response function, $\phi(t)$. However, because of the additional constraints on Wagner's model, as well as the equivalence of Wagner's function, $\phi$, and Theodorsen's function, $C$, via Laplace transform, this work has focused on developing state-space representations of Theodorsen's model.

# Chapter 7

# Models of a flat plate airfoil at Re = 100 from direct numerical simulations

In this chapter, the modeling techniques from Chapter 5 are applied to develop linear, reduced-order models for the unsteady lift coefficient on a flat plate airfoil at low Reynolds number, Re= 100. The inputs to the model are pitch and plunge motion ($\ddot{\alpha}$ and $\ddot{h}$, respectively), and the output is the lift coefficient $C_L$. The results are based on direct numerical simulations, the details of which are described in Chapter 3. The flat plate airfoil has a thickness equal to 1% of the chord length.

The majority of the models in this chapter are of the form in Eq. (5.6) and are constructed from a time-resolved step response using the algorithm in Section 5.3.2. In the case of pitching, the step maneuver in Figure 5.8 is used with a step magnitude of 0.1°. For the case of plunging, the vertical velocity undergoes a step to a velocity of $\dot{h} = 0.001745$ chords per convection time, which corresponds to a step in effective angle of attack of 0.1°. The step duration in both cases is 0.01 convective time.

These models may be considered to be low-order, state-space representations of an indicial (step) response model from Section 2.1.2. However, models constructed using algorithms in Sections 5.3.3 and 5.3.4 of the form in Eq. (5.7) are also investigated, and it is shown that models based on the algorithm in Section 5.3.3 are nearly equivalent to those based on Section 5.3.2. Additionally, models for plunging motion take the form in Eq. (5.9), and are constructed using a modified version of the algorithm in Section 5.3.3. Finally, multiple-input, single-output (MISO) models are developed with both pitch and plunge inputs and take the form in Eq. (5.10). A major result of this section is that MISO models do not require a higher-order ERA model to capture the transient dynamics.

This chapter is organized into models linearized at zero angle of attack, $\alpha_0 = 0°$, and models linearized at non-zero angles of attack up to the critical bifurcation angle, after which the flow is characterized by periodic vortex shedding and is inherently nonlinear. All models are compared with the indicial response model, as well as direct numerical simulation (DNS) and the Theodorsen model for a number of maneuvers. Small amplitude sinusoidal maneuvers are compared in Bode plots. Additionally, models are used to re-compute the time-resolved step response data that was used for the indicial response model. Finally, the models are compared on

a moderate amplitude pitch/plunge maneuver with 10° amplitude motion in both angle-of-attack and effective angle-of-attack based on plunging velocity.

## 7.1 Models linearized at $\alpha_0 = 0°$

At zero angle of attack, step response simulations are obtained for a flat plate pitching about various points (leading edge, quarter chord, and middle chord) and plunging vertically. The lift coefficient history from the step response simulations are synthesized into models of the form in Eqs. (5.6) and (5.9) with ERA models $(A_r, B_r, C_r)$ for the transient dynamics of order $r = 7$. Additionally, a multiple-input model is obtained using Eq. (5.10) that combines plunging with pitching about various points. For the multiple-input case of combined pitch and plunge, the ERA model still has order $r = 7$. It is shown in Figure 7.1 that a model of order $r = 5$ (red) is sufficient for accurate Bode plots at low angle of attack. However, as we shall see in Figure 7.13, a model of order $r = 7$ is required to capture a subtle flow feature that develops into a vortex shedding mode at larger angle of attack.

### 7.1.1 Small amplitude motions

The reduced-order models presented are based on step-response simulations with a small step magnitude; $\Delta\alpha = 0.1°$ in the case of pitching motion, and $\Delta\alpha = 0.1°$ effective angle of attack ($\dot{h} = 0.00175$) in the case of plunging motion. Therefore, it is natural to compare the models with DNS for small amplitude motions. The response of each model (ERA model, indicial response, Theodorsen, and DNS) are computed for sinusoidal inputs $u(t) = \Delta\alpha \sin(\omega t)$ with $\Delta\alpha = 1°$ for pitch ($u = \alpha$), and $\Delta\alpha = 0.01$ for plunge ($u = h$). The input to the models in Eq. (5.6) and Eq. (5.7) is $\ddot{u} = -\Delta\alpha\omega^2 \sin(\omega t)$, so the Bode plot is a frequency response from input $\ddot{u}$ to $C_L$.

Figures 7.2, 7.4, and 7.6 show the Bode plots comparing the reduced-order model (5.6), indicial response (2.6), Theodorsen's model (6.21), and DNS for pitching about the quarter-chord and middle-chord and plunging, respectively. It is important to gain a physical intuition for the frequency response (i.e., Bode) plots and how they relate to the aerodynamic response. The low-frequency asymptote in each Bode plot corresponds to the quasi-steady case when the lift coefficient depends only on the angle of attack in the case of pitch, or effective angle of attack in the case of plunge. For pitching motion, the low-frequency asymptote in the magnitude plot has a slope of $-40$ dB/decade, consistent with the fact that $\alpha$ is obtained by integrating the input $\ddot{\alpha}$ twice. In the case of plunge, the low-frequency asymptote has a slope of $-20$ dB/decade, since the effective angle of attack is related to $\dot{h}$, which is the integral of the input $\ddot{h}$. In all instances, the low-frequency asymptote of the model is lower than that of Theodorsen's model because Theodorsen's model uses the ideal $2\pi$ lift slope, which over-predicts the true lift slope at Re$=$ 100. The high-frequency asymptote in the Bode magnitude plots corresponds to the case when there are large accelerations and the lift coefficient is strongly influenced by added-mass forces. In the case of pitch about the quarter-chord and plunge motion, there are added-mass forces directly proportional to the inputs ($\ddot{\alpha}$ and $\ddot{h}$), so that the Bode plot has zero slope at high frequencies. There are no added-mass forces proportional to $\ddot{\alpha}$ in the case of mid-chord pitching, but there are forces proportional to $\dot{\alpha}$, so the Bode plot

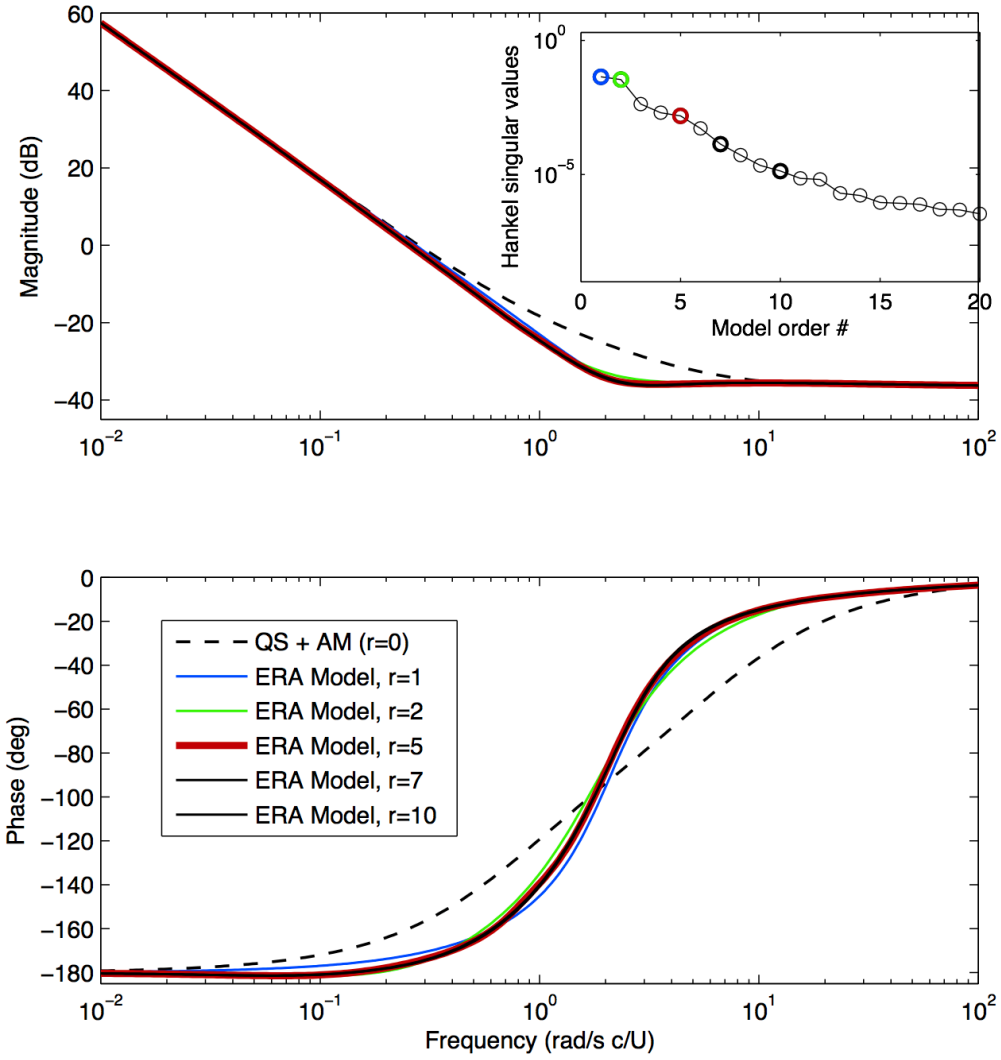


Figure 7.1: Frequency response (Bode plot) for reduced-order models with pitching at leading edge. Various order ERA models are shown. The model input is $\ddot{\alpha}$, and the output is $C_L$.

has a slope of $-20$ dB/decade at high frequencies. This information is also reflected in the Bode phase plot. Notice that the phase at low-frequency starts at $-180^\circ$ for the pitching models, which is consistent with the fact that the angle of attack is the second integral of the input (twice integrating a sinusoid results in another negative sinusoid, hence the $-180^\circ$ phase).

Many of these properties are also reflected in the step-response data, shown in Figures 7.3, 7.5, and 7.7. For example, it is seen in Figure 7.3 that there are added-mass forces directly proportional to $\ddot{\alpha}$, unlike the step-response in Figure 7.5, where the added-mass forces are proportional to $\dot{\alpha}$. Even though the added-mass in the plunge maneuver resemble those in the mid-chord pitching case, the maneuver is slightly different (step in $\dot{h}$ rather than $h$).

In all of the Bode plots and step response plots, the low-order ERA models (single-input, single-output as well as the multi-input, single-output) accurately reproduce the frequency response of the direct numerical simulations. Moreover, the ERA model is nearly identical to the indicial response model, as they are both based on the same numerical step response. Theodorsen's model consistently over predicts the quasi-steady lift slope, and is not as accurate in capturing the phase. As is mentioned in Chapter 6, it is possible to *hand-tune* Theodorsen's model to the correct lift curve slope, but this does not improve the phase at moderate frequencies.

### 7.1.2 Large amplitude motions

The model in Eq. (5.6) has shown excellent agreement with the indicial response model, Eq. (2.6), and DNS for small-amplitude maneuvers, and so it is natural to investigate maneuvers with a larger amplitude. Because both the reduced-order model and the indicial response method are linear, they should continue to agree with each other for large amplitude motions. However, the actual flow physics is nonlinear, and so comparison with DNS on a larger maneuver will provide a more challenging test case for the models, and indicate whether the flow is linear enough for these models to be valid. Additionally, comparison with a simplified model based on quasi-steady and added-mass forces will highlight the advantages of the reduced-order model; this simplified model may be considered to be the same as Eq. (5.6) with no ERA component for the additional transient dynamics (i.e., set $C = 0$).

The large amplitude motion is a combined pitch/plunge maneuver based on the canonical pitch-up, hold, pitch-down maneuver [26, 79] that is discussed in Section 2.6. The pitching portion of the maneuver consists of a pitch-up, hold, pitch-down about the leading edge with a maximum angle of $10^\circ$. The plunging portion of the maneuver consists of a step-down in vertical position that is the negative integral of the step-up, hold, step-down maneuver, and is chosen to have a maximum effective angle of attack based on vertical velocity of $10^\circ$. This specific maneuver is chosen because of its relationship to the canonical test case as well as its physical significance as a perching maneuver. The motion is given by the following

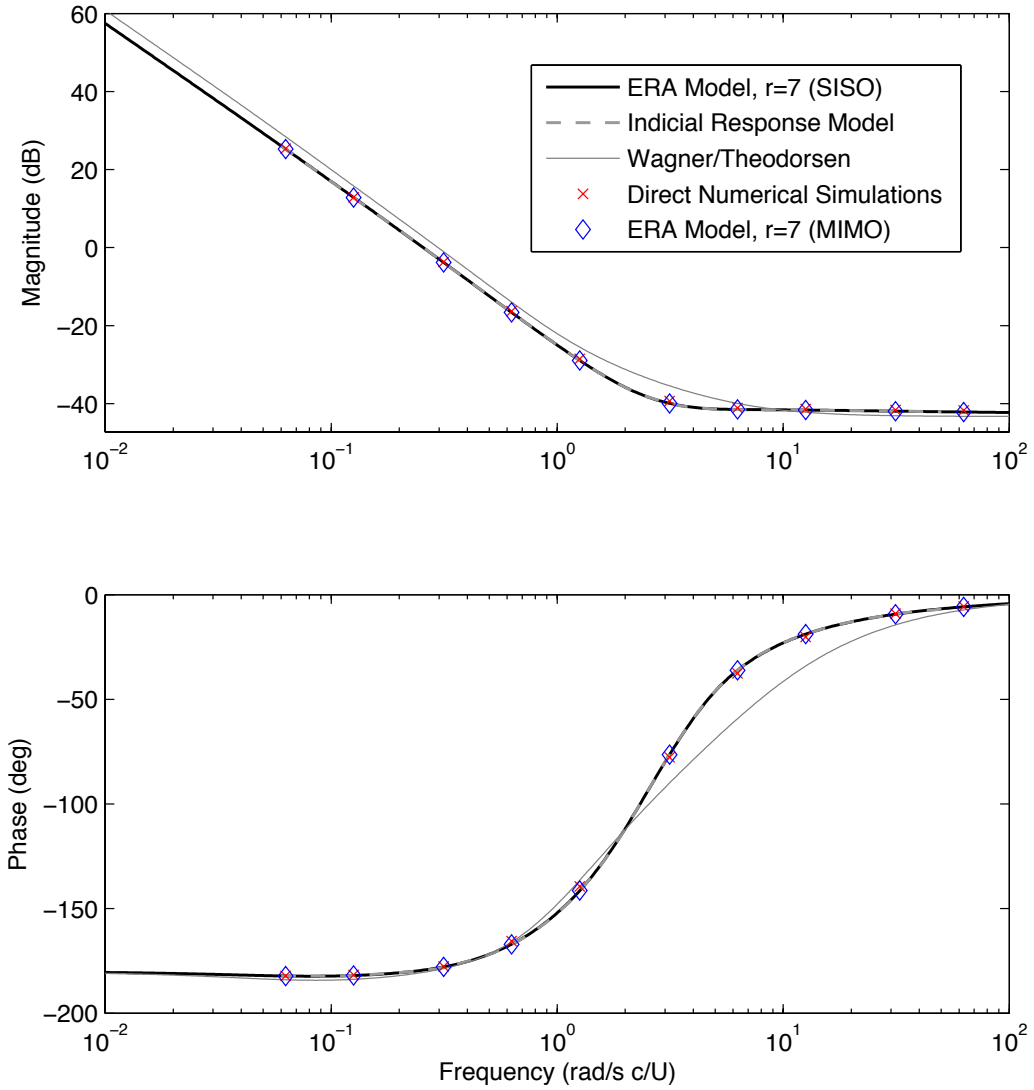


Figure 7.2: Frequency response of reduced order model (5.6) (7-mode ERA), indicial response, Theodorsen and DNS for pitching at quarter chord. Multiple-input ERA model (5.10) for pitch/plunge agrees well (diamond). Input is $\ddot{\alpha}$ and output is $C_L$.

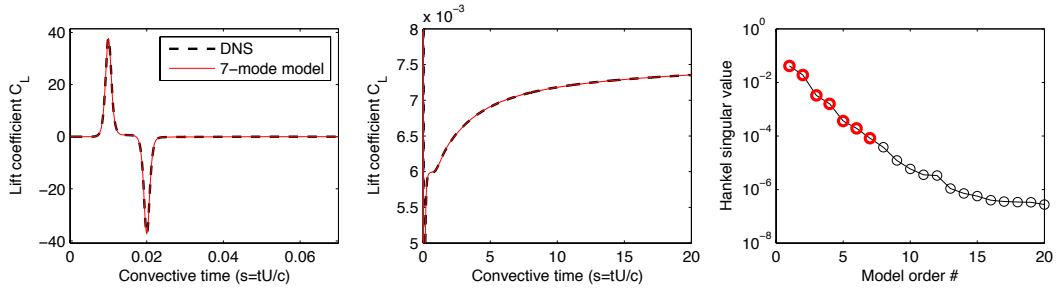


Figure 7.3: Step-response (left, middle) and Hankel singular values (right) for 0.1° pitch-up about the quarter chord. DNS is compared with a 7-mode ERA model.

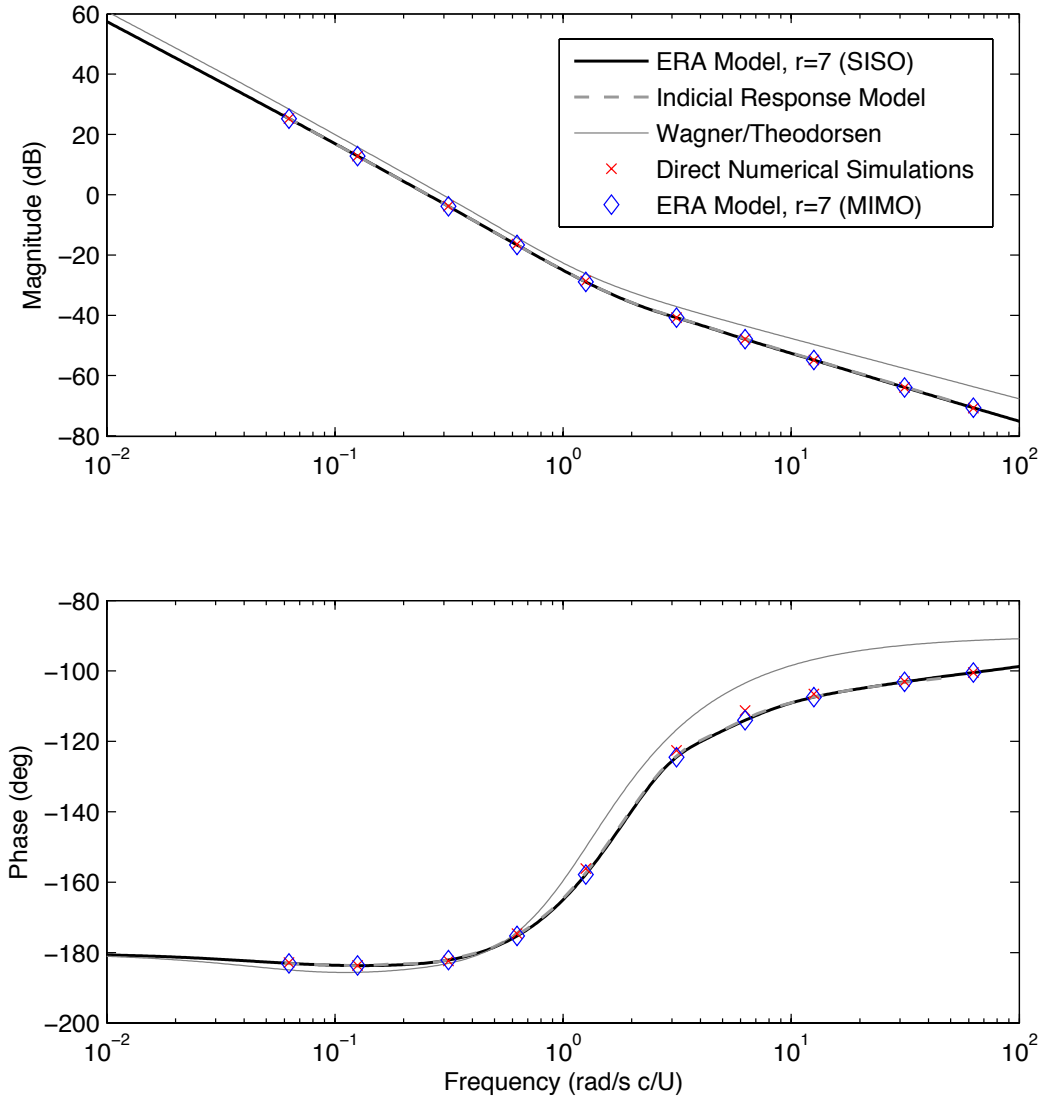


Figure 7.4: Frequency response of reduced order model (5.6) (7-mode ERA), indicial response, Theodorsen and DNS for pitching at mid chord. Multiple-input ERA model (5.10) for pitch/plunge agrees well (diamond). Input is $\ddot{\alpha}$ and output is $C_L$.

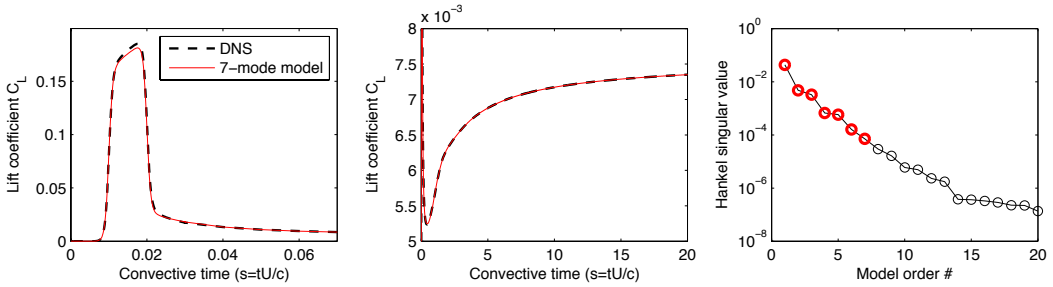


Figure 7.5: Step response (left, middle) and Hankel singular values (right) for 0.1° pitch-up about the mid chord. DNS is compared with a 7-mode ERA model.

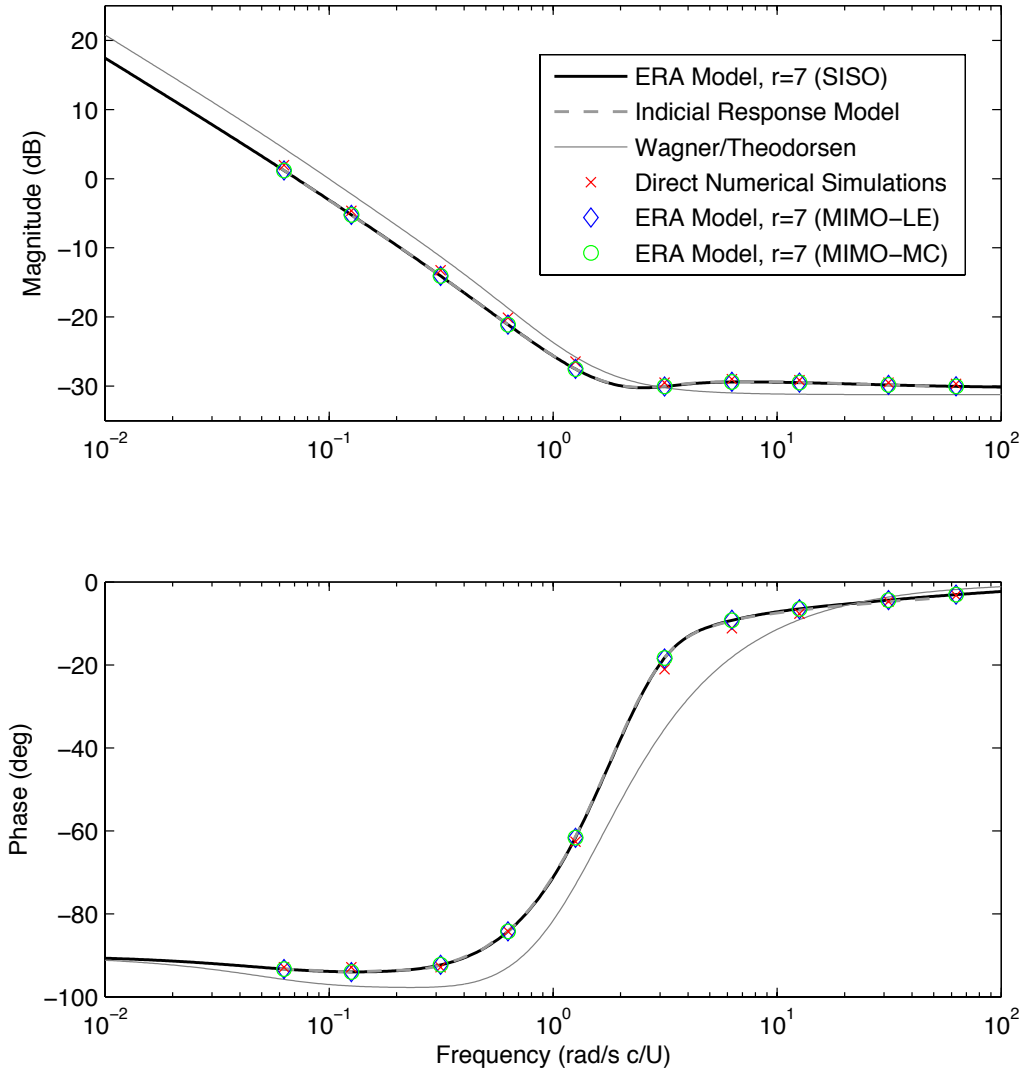


Figure 7.6: Frequency response of reduced order model (5.9) (7- mode ERA), indicial response, Theodorsen and DNS for plunging. Multiple-input ERA model (5.10) for pitch/plunge agrees well (LE - diamond, MC - circle). Input is $\ddot{h}$ and output is $C_L$.

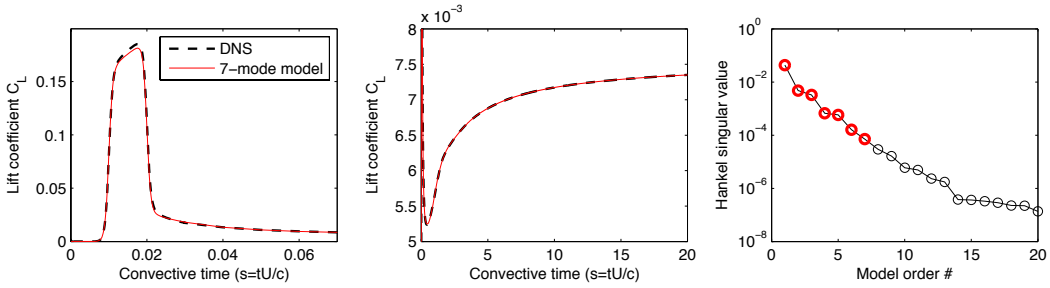


Figure 7.7: Step response (left, middle) and Hankel singular values (right) in plunge velocity with $\alpha_e = 0.1^\circ$ . DNS is compared with a 7-mode ERA model.

| | IBPM Simulation | Convolution | ERA Model |
|---|---|---|---|
| Time (s) | $2.55 \times 10^3$ | $2.13 \times 10^{-2}$ | $3.48 \times 10^{-3}$ |

Table 7.1: Computational time of each method.

expressions:

$$G_\alpha(t) = \log\left[\frac{\cosh(a(t-t_1))\cosh(a(t-t_4))}{\cosh(a(t-t_2))\cosh(a(t-t_3))}\right], \quad \alpha(t) = \alpha_{\max}\frac{G_\alpha(t)}{\max(G_\alpha(t))}; \tag{7.1}$$

$$G_h(t) = \log\left[\frac{\cosh(b(t-t_1))\cosh(b(t-t_4))}{\cosh(b(t-t_2))\cosh(b(t-t_3))}\right], \quad h(t) = \int_0^t \dot{h}_{\max}\frac{G_h(\tau)}{\max(G_h(\tau))}\,d\tau, \tag{7.2}$$

where $a = b = 11$, $\alpha_{\max} = 10^\circ$ and $\dot{h}_{\max} = -0.1745$, which corresponds to $\alpha_e = 10^\circ$. For the pitching motion, $t_1 = 1, t_2 = 3, t_3 = 4, t_4 = 6$, and for the plunging motion, $t_1 = 2, t_2 = 4, t_3 = 5, t_4 = 7$.

Figure 7.8 shows the performance of each model on the combined pitch/plunge maneuver. The top plot is the maneuver itself, and the bottom plot shows the lift coefficient of each model throughout the maneuver. There is excellent agreement between the indicial response model and the reduced-order model (5.6). Additionally, the multiple-input model (5.10) with ERA order $r = 7$ agrees well with the sum of two individual models for pitching and plunging, each with ERA order $r = 7$. Finally, the close agreement with DNS shows that the indicial response model, and its reduced-order counterpart, outperform the Theodorsen's model.

The computational time of the three accurate methods (DNS, convolution Eq.(2.6), and the ERA model Eq. (5.6)) are provided in Table 7.1. The ERA model is about 6 times faster than the indicial response model and on the order of $10^6$ times faster than the direct simulation. The computation time required for the DNS, ERA models, and the convolution integral scale linearly with the time of the maneuver.

### 7.1.3 Model parameterized by pitch point

As was mentioned in Section 5.2.2 in Eq. (5.11), it is possible to construct a multiple-input model for pitch and plunge that is parameterized by pitch axis location $p$. In particular, pitching about any point may be considered equivalent to pitching about the mid-chord with an additional plunging motion superimposed. Therefore, having identified models for pitching at the mid-chord and plunging, it is possible to reconstruct the model for pitch about the leading-edge and quarter-chord based on a linear combination of these two models. The agreement is nearly exact, as shown in Figure 7.9. This is also consistent with the pitch-point parameterization in Theodorsen's model in Eq. (6.2).

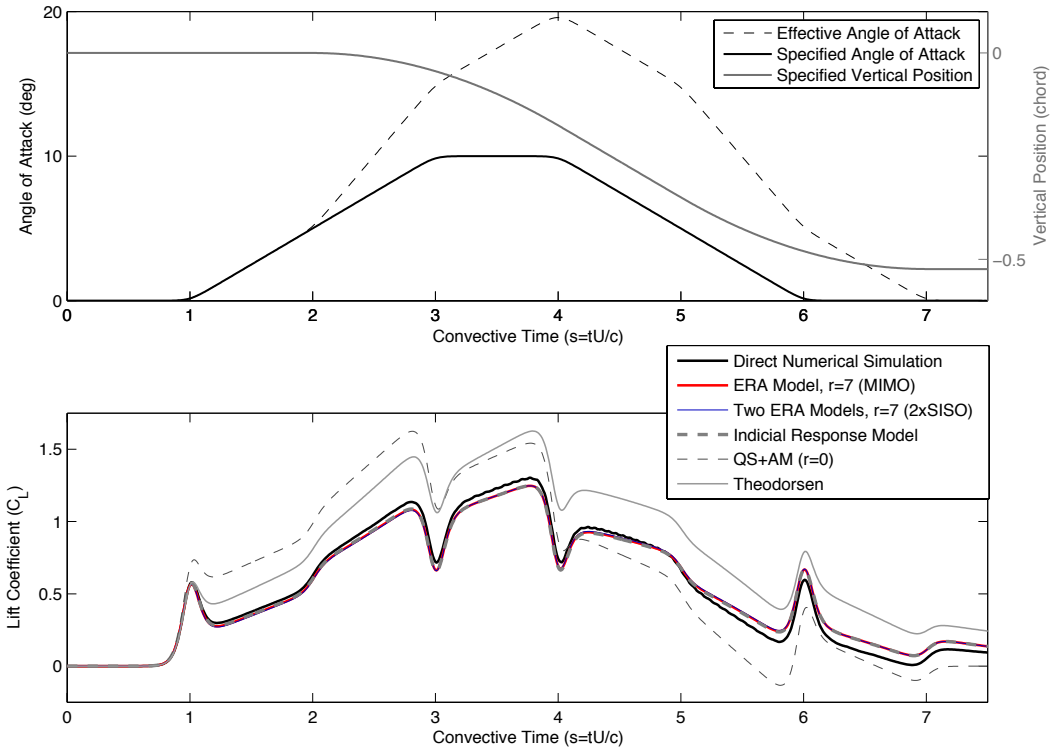


Figure 7.8: Combined pitch/plunge maneuver. (top) The angle-of-attack and vertical center of mass motions. (bottom) Lift coefficient response is shown for DNS, indicial response, reduced-order model (multiple-input system (5.10) with $r = 7$ and sum of two single-input systems for pitch (5.6) and plunge (5.9), each with $r = 7$), quasi-steady plus added-mass, and Theodorsen.

## 7.2 Models linearized at large angles, $\alpha_0 \in [0°, \alpha_{\mathbf{crit}})$

As the plate's angle of attack is increased, the flow physics becomes significantly more involved. In particular, increasing the angle of attack results in an adverse pressure gradient on the upper surface. This increasingly adverse pressure gradient thickens the upper boundary layer until the flow reverses, resulting in a stable, attached separation bubble. At a critical angle of attack, $\alpha_{\text{crit}}$, the separation bubble bursts, resulting in periodic, laminar vortex shedding. This progression is shown in Figures 1.3 and 3.1

This section presents linearized models for a flat plate at various nonzero angle of attack up to the critical angle, $\alpha_{\text{crit}}$, at which a Hopf bifurcation occurs. These cases provide a more challenging demonstration of our modeling procedure, because the fluid dynamic interactions are increasingly complicated at larger angle of attack. All models in this section are computed for pitch about the leading edge.

### 7.2.1 Frequency domain analysis

Using the method discussed in Chapter 5, we have computed reduced order models linearized at $\alpha_0 \in [0°, 27°]$. Figure 7.10 shows the frequency response of models

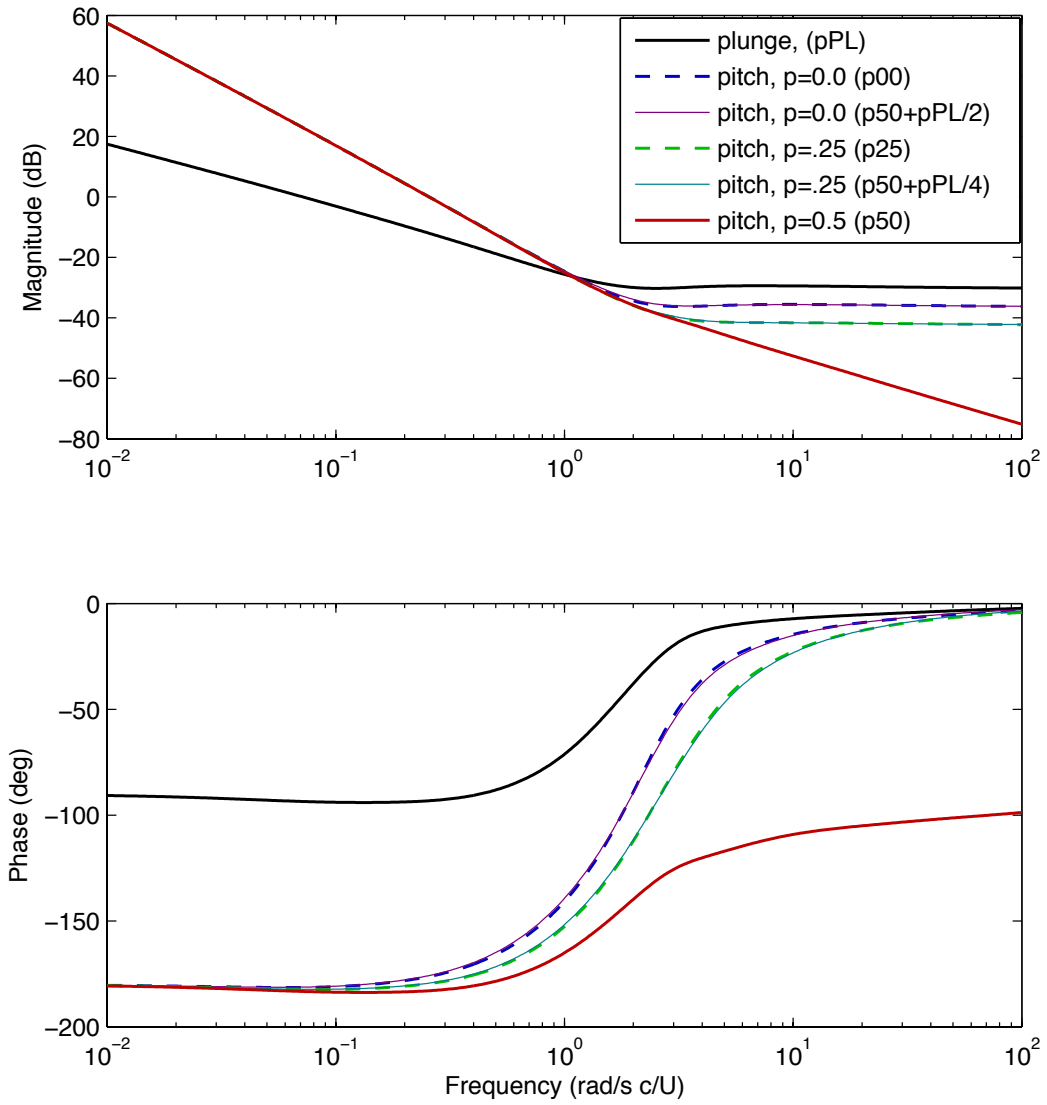


Figure 7.9: Bode plot illustrating that pitch about leading-edge and quarter-chord points is linear combination of pitching about the middle-chord and plunging motion. ERA model order is $r = 7$. The model input is either $\ddot{\alpha}$ or $\ddot{h}$, and the output is $C_L$.

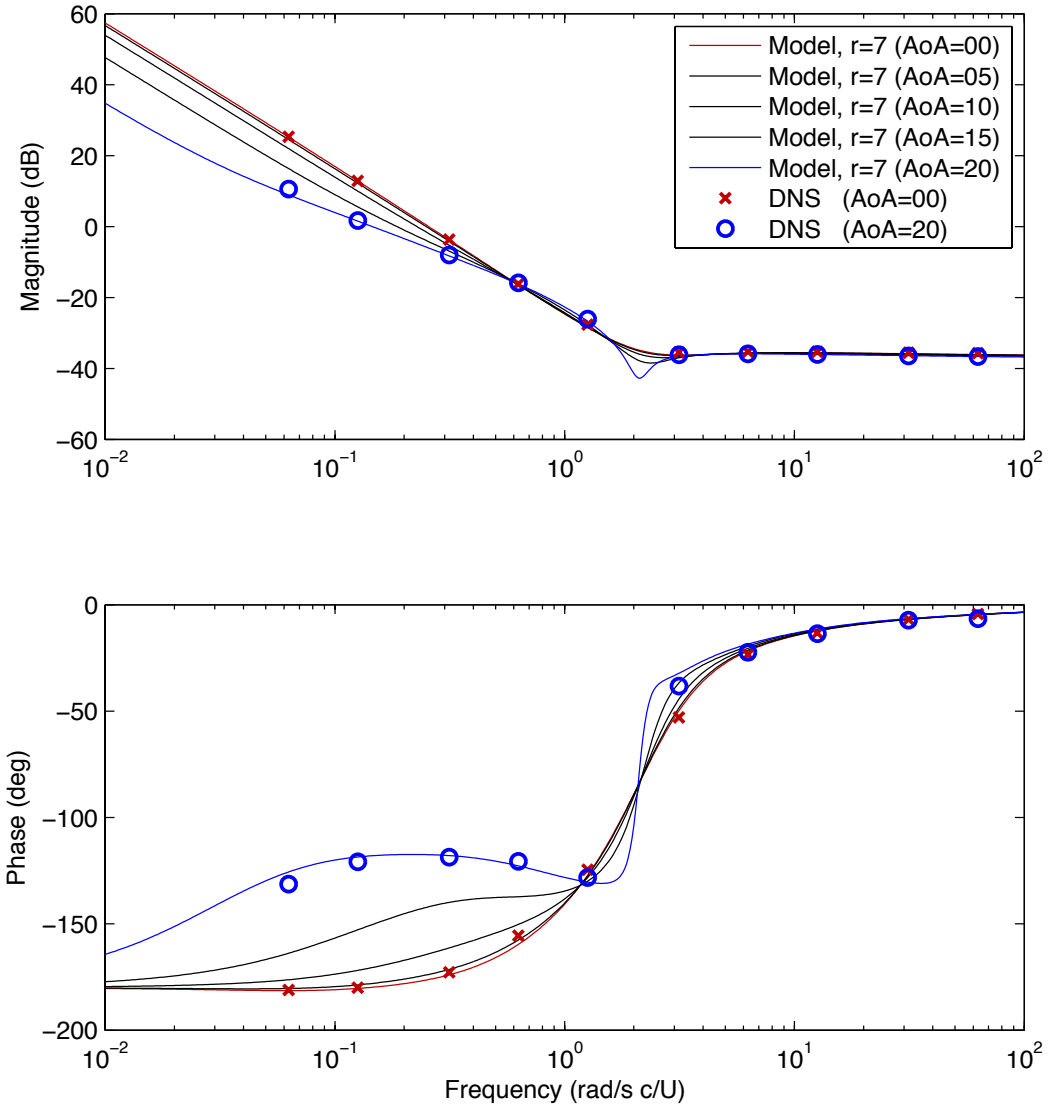


Figure 7.10: Frequency response of models linearized at various angles from $\alpha_0 = 0°$ to $\alpha_0 = 20°$. Results from direct numerical simulation linearized at $\alpha_0 = 0°$ and $\alpha_0 = 20°$ are included for comparison. The model input is $\ddot{\alpha}$, and the output is $C_L$.

linearized at various $\alpha_0$, and the corresponding data from DNS for $\alpha_0 = 0°$ and $\alpha_0 = 20°$. As seen in Figure 1.3, the lift slope decreases for increasing angle of attack, so it is not surprising that the low frequency magnitude in the Bode plot decreases for increasing angle of attack. Additionally, we see that at larger angle of attack the phase converges to $-180°$ at lower frequencies, indicating that solutions take longer to reach equilibrium in the time domain. This is consistent with the fact that for larger angle of attack the system is closer to instability, and a pair of eigenvalues of the system are moving closer to the imaginary axis, effecting the time-scale of relaxation [1].

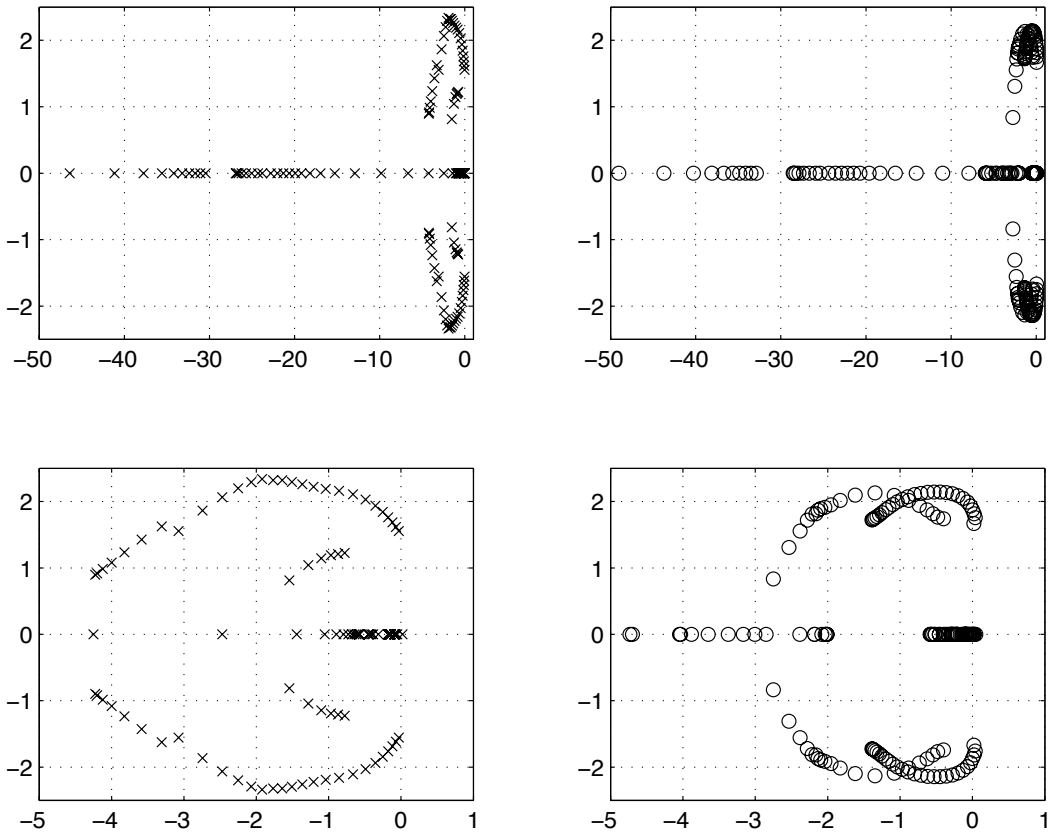


Figure 7.11: Poles (left) and zeros (right) of models for pitch about the leading edge, linearized at various angle of attack, from $\alpha = 0°$ to $\alpha = 27°$. (bottom) zoom in.

To see this more clearly, we plot the poles and zeros of the models for $\alpha_0 \in [0°, 27°]$, shown in Figure 7.11. The model given by Eq. (5.6) always has two poles at the origin because the input $\ddot{\alpha}$ must be integrated twice to obtain the states $\dot{\alpha}$ and $\alpha$. Because we use an ERA model of order $r = 7$ for the transient dynamics, there are seven additional branches of poles, as indicated in the plot. Similarly, there are nine branches of zeros.

The most striking feature of Figure 7.11 is that as angle of attack increases, a pair of poles and a pair of zeros march towards the imaginary axis. This explains the longer relaxation times (convergence of Bode plots to $-180°$ at successively lower frequencies). It also indicates that the models are capturing the dynamics as the system approaches a Hopf bifurcation. It is also interesting to note that there is a second set of poles and zeros that branch from the real axis and march toward the imaginary axis for increasing angle of attack. This is consistent with the fact that at larger angle of attack, there is more complicated limit cycle behavior. It is not surprising that the flow may undergo several Hopf bifurcations as angle of attack or Reynolds number is increased [95].

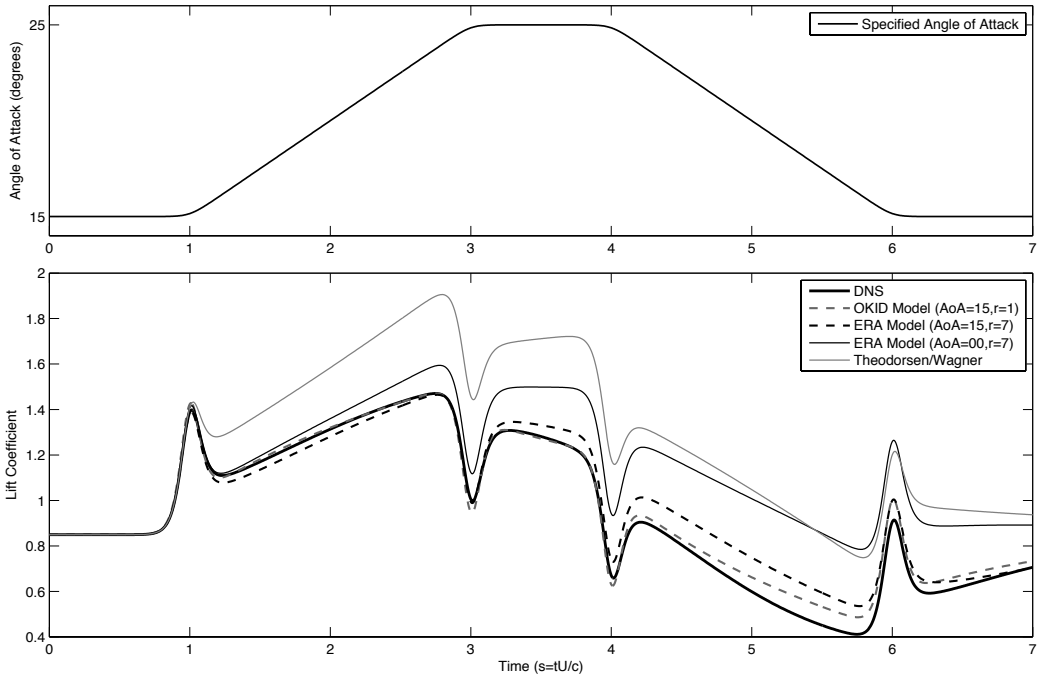


Figure 7.12: Figure showing improved performance of models linearized at $\alpha_0 = 15°$ over models linearized at $\alpha_0 = 0°$ for a pitch maneuver from 15° to 25° and back.

### 7.2.2 Time domain analysis

The large amplitude pitch-up, hold, pitch-down maneuver from Eq. (7.1) is used again, at an angle of attack starting at 15° and reaching a maximum angle of 25°; the pitch point is the leading edge. This specific maneuver is beneficial because it involves large added-mass forces and leading-edge separation.

The comparison of various reduced-order models with DNS is shown in Figure 7.12. The Theodorsen/Wagner analytical model is included for a baseline comparison. Perhaps the most striking feature of this comparison is the nearly perfect agreement of the OKID-based model with the DNS. Interestingly, the order of the transient dynamics portion of the model is $r = 1$ for the OKID-based model and $r = 7$ for the model from Eq. (5.6). Next, we notice that both models linearized about $\alpha_0 = 15°$ outperform the model linearized at $\alpha_0 = 0°$. Although this is not surprising, it is a validation of this approach. In addition to being closer in magnitude to the DNS curve, the models linearized at $\alpha_0 = 15°$ also have the correct negative slope during the "hold" portion of the maneuver, which is characteristic at larger angles of attack as seen in Figure 2.5. Finally, we see that even the indicial response based model linearized at $\alpha_0 = 0°$ outperforms the Theodorsen/Wagner model, which is also linearized at $\alpha_0 = 0°$.

Additionally, it is interesting to see the step-response simulations for the various base angles from $\alpha_0 = 0°$ to $\alpha_0 = 27°$ in Figure 7.13. The lift coefficient at the base angle is subtracted, and we are only plotting the transient dynamics after the step, so added-mass is omitted. Notice that between one and five convective times,

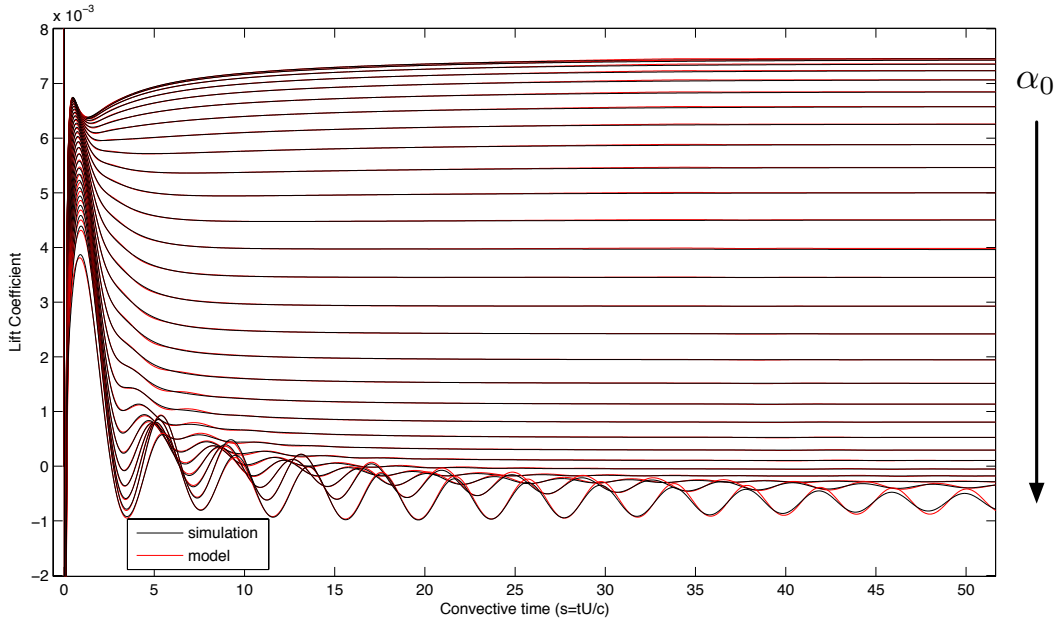


Figure 7.13: Simulations and model prediction for small step of $\Delta\alpha = 0.1°$ from a reference angle $\alpha_0$ to $\alpha_0 + \Delta\alpha$ for $\alpha_0 \in [0°, 27°]$. The initial lift coefficient $C_L(\alpha_0)$ is subtracted out, and $\alpha$ increases with the arrow. ERA model order is $r = 7$.

there is a dip in the lift coefficient followed by a rise to steady state. A 7-mode ERA model is required to capture this feature accurately at $\alpha_0 = 0°$. Interestingly, a 7-mode model is also required to accurately capture the frequency and decay rate of the oscillations in the large angle of attack cases.

## 7.3 OKID for system identification

An example maneuver that is used with OKID is shown in Figure 5.12. The maneuver consists of Gaussian white noise in $\ddot{\alpha}$. The input to the OKID method would be the pair $(\ddot{\alpha}, C_L)$, and the output of the method are the Markov parameters $\mathcal{H}_i$ for the impulse response in $\ddot{\alpha}$. OKID is reviewed in Section 2.2.2.

The impulse response parameters obtained from the maneuver in Figure 5.12 are shown in Figure 7.14 for a base angle of $\alpha_0 = 0°$. The first parameter corresponds to the added-mass term $C_{\ddot{\alpha}}$ in our state-space model (5.7). Because an impulse in $\ddot{\alpha}$ is a ramp in $\alpha$, we see a linear increase in $\mathcal{H}_i$, and the slope is the lift slope $C_\alpha$ Subtracting off $C_\alpha\alpha$, the Markov parameters decay to a non-zero value corresponding to $C_{\dot{\alpha}}$, since an impulse in $\ddot{\alpha}$ is a step in $\dot{\alpha}$. Finally, after subtracting off each stability derivative, a low order representation of the remaining transient response is obtained using the ERA, as discussed in Section 5.3.4. It is important to note that without subtracting off $C_\alpha\alpha$, the resulting ERA model is unstable. This system is used as an example to demonstrate the correct procedure for using OKID in Section 5.3.5.

For the sake of clarity, we have omitted the reduced-order models based on OKID in most of the figures. However, the general trends are also captured by the OKID-based models. Figure 7.15 shows a comparison of the models (5.6) and (5.7)

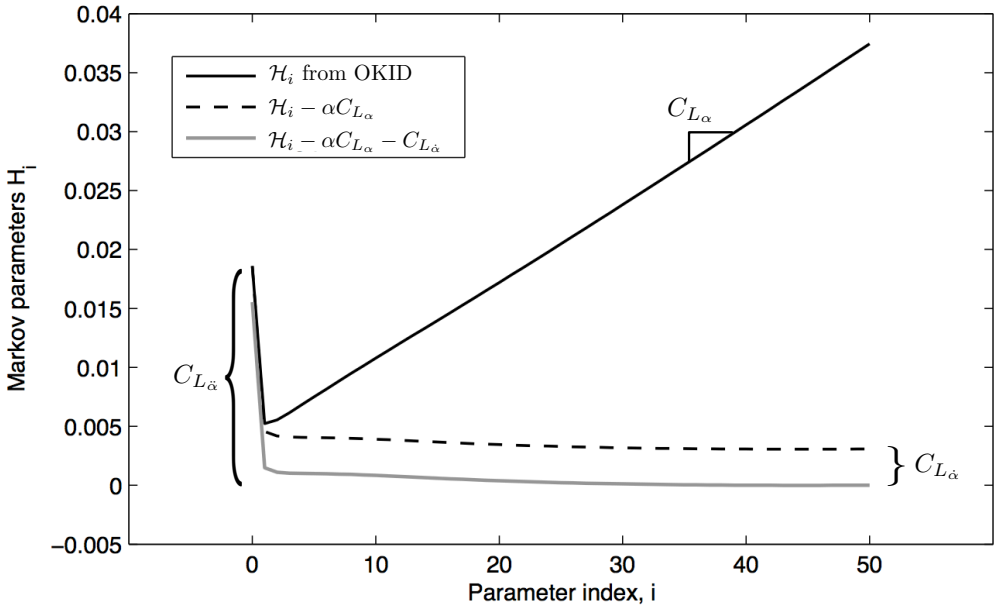


Figure 7.14: Markov parameters from OKID with $(\ddot{\alpha}, C_L)$ as input/output pair.

based on the three algorithms in Section 5.3 linearized at $\alpha_0 = 0°$ and $\alpha_0 = 15°$. The frequency response from DNS is included for comparison.

## 7.4 Summary of Re = 100 results

In this chapter, a number of models have been developed for the pitching and plunging motion of a flat plate airfoil at Re = 100. The modeling procedures in Chapter 5 have been compared against direct numerical simulations as well as the indicial response model, Eq. (2.6), and Theodorsen's model, Eq. (6.2). The low-dimensional models match both the indicial response model and DNS for a range of maneuvers, pitch points, and base angle of attack.

There are a number of results. First, the reduced-order models match the indicial response model and direct numerical simulation (DNS) for small amplitude motions over a range of frequencies and base angle of attack $\alpha_0$, as shown in Figures 7.2, 7.4, 7.6, and 7.10. The reduced-order model and indicial response model both agree with direct numerical simulations (DNS) for a moderate amplitude combined pitch/plunge maneuver, as shown in Figures 7.8 and 7.12. They both outperform Theodorsen's model as well as the model based on quasi-steady and added-mass forces. Finally, a multiple-input model capturing both pitch and plunge dynamics performs as well as individual models without an increase in the order of the ERA model.

The modeling techniques are applied to study motion at various angles of attack up to the critical angle, at which point the Hopf bifurcation occurs. It is shown in Figures 7.10 and 7.12 that a model linearized at a given base angle $\alpha_0$ will outperform other linear models for a maneuver in the neighborhood of $\alpha_0$. Finally, Figures 7.11

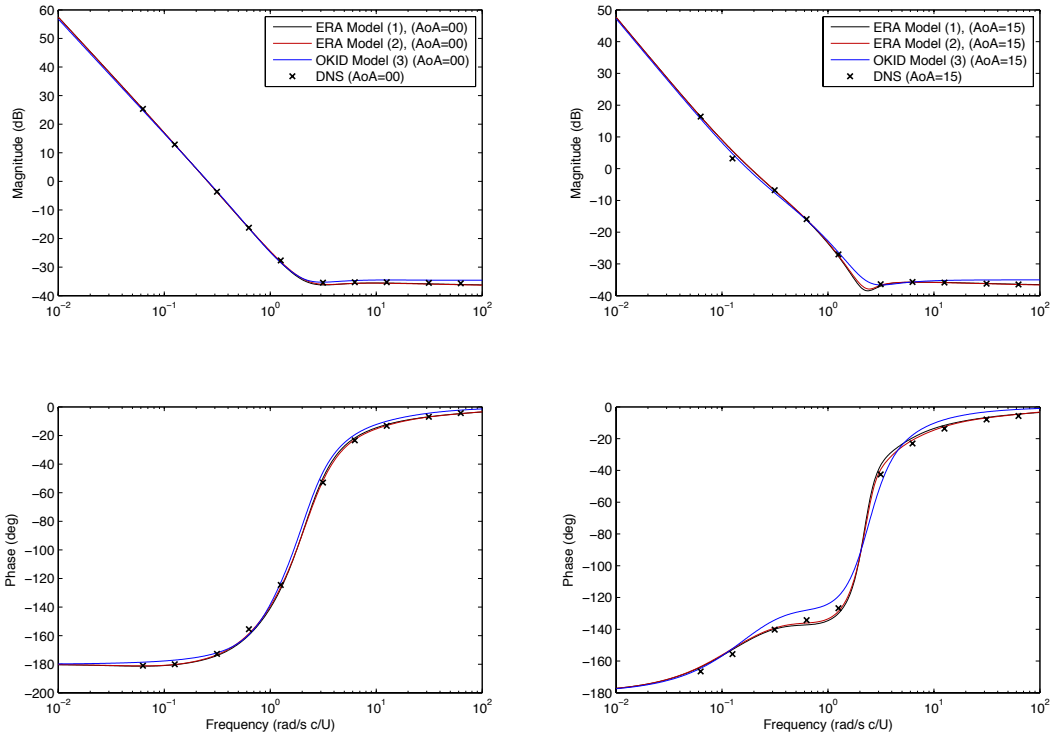


Figure 7.15: Bode plot of models of leading edge pitch generated using algorithms $1, 2$ and $3$ from Section 5.3. Models are based at $\alpha_0 = 0°$ (left) and $\alpha_0 = 15°$ (right). The model input is $\ddot{\alpha}$, and the output is $C_L$.

and 7.13 demonstrate that the linear models capture the relevant dynamics as the angle of attack is increased and the system approaches the Hopf bifurcation.

# Chapter 8

# Models of a NACA 0006 airfoil at $\mathbf{Re} = 65,000$ from wind tunnel experiments

In this chapter, unsteady aerodynamic models are developed for a NACA 0006 airfoil at Reynolds number $65,000$ based on wind tunnel experiments. Pitch and plunge models of the form in Eqs. (5.7) and (5.9) are constructed using the OKID/ERA method described in Section 5.3.4. The family of system identification maneuvers in the second part of Section 5.4.2 was developed specifically to extract relevant unsteady information from phase averaged wind tunnel measurements. Two sets of experimental results are presented, each involving pitching and plunging motion about $\alpha_0 = 0^\circ$ and $\alpha_0 = 10^\circ$. It is shown that the low-order models identified from experiments are more accurate than Theodorsen's model for all maneuvers, especially those based at larger base angle of attack. This work was done in collaboration with Professor David Williams at the Illinois Institute of Technology in the Andrew Fejer Unsteady Flow Wind Tunnel.

Section 8.1 provides details about the wind tunnel experiment, as well as the system identification maneuvers and the modeling procedure. Section 8.2 contains the first set of results including maneuvers and models for pitching about $\alpha_0 = 0^\circ$ and $\alpha_0 = 10^\circ$ and for pure plunge; models in this section are based on the actual measured position of the airfoil. Section 8.3 contains the second set of results after modifications were made to improve the accuracy of wind tunnel measurements and reduce aeroelastic effects and noise. The input to the models in Section 8.2 is either the measured angle of attack or measured plunge position, so these models capture purely aerodynamic and aeroelastic effects. Conversely, the input to the models in Section 8.3 is the commanded angle of attack and plunge position, resulting in models that include the actuator dynamics and associated time-delays. The second set of models may be more relevant for designing feedback control experiments. All results include comparison with Theodorsen's model.

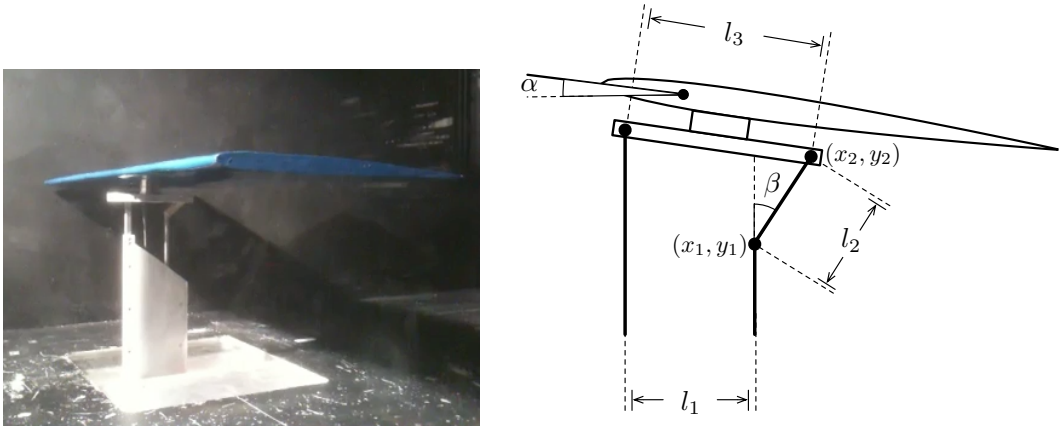


Figure 8.1: (left) NACA 0006 model in wind tunnel. (right) Schematic of hinge apparatus connecting pushrods to platform.

## 8.1 Experimental Methods

### 8.1.1 Wind Tunnel Experiment

The following experimental data was collected in the Andrew Fejer Unsteady Flow Wind Tunnel at the Illinois Institute of Technology. The dimensions of the wind tunnel test section are 0.6m $\times$ 0.6m $\times$ 3.5m.

The model is a NACA 0006 airfoil, shown in Figure 8.1, with a chord length of 0.246 m and span of 0.598 m. The free stream velocity is 4.00 m/s, which results in a Reynolds number of approximately $65,000$ and a convective time of 0.0615 seconds. In all pitching experiments the pitch point is $p = 0.11$, or 11% chord.

Forces and moments are measured using the 6-axis ATI Nano25 force transducer for the results in Section 8.2 and the more sensitive Nano17 force transducer for Section 8.3. The free stream velocity is measured using a Pitot tube with a Validyne DP-103 pressure transducer. The model is actuated using two Copley servo tubes connected to individual pushrods, allowing for a full range of pitch and plunge motions. The position of these pushrods is measured using linear potentiometers in Section 8.2; however, they were removed before the results in Section 8.3 to prevent stick-slip friction. This explains the different model input in each results section.

Because the force transducer moves with the body, forces are measured in the body-fixed frame of the airfoil. Therefore, we rotate the normal ($N$) and parallel ($P$) forces in the $z$- and $x$- directions into the lift ($L$) and drag ($D$) forces relative to the free stream velocity according to the following:

$$\begin{bmatrix} L \\ D \end{bmatrix} = \begin{bmatrix} \cos(\alpha) & -\sin(\alpha) \\ \sin(\alpha) & \cos(\alpha) \end{bmatrix} \begin{bmatrix} N \\ P \end{bmatrix} \tag{8.1}$$

The pushrods are connected to the airfoil and force balance via a platform with a hinge constraint, as shown in Figure 8.1. It is then possible to command an angle of attack $\alpha$ by varying the relative displacement of the two pushrods. For the

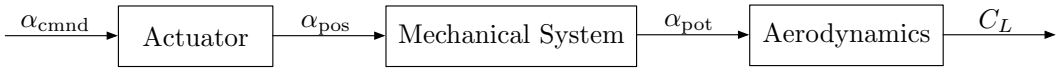


Figure 8.2: Schematic of signals in wind tunnel experiment.

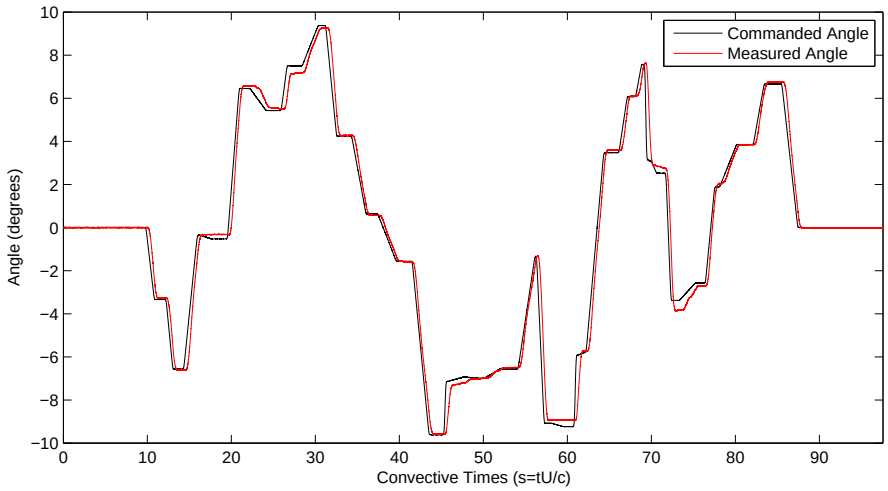


Figure 8.3: Pitch maneuver; Command angle is $\alpha_{\text{cmnd}}$, and measured angle is $\alpha_{\text{pot}}$.

pitching experiments below, the front pushrod is held fixed, and the height of the rear pushrod $y_1$ is varied to vary $\alpha$. The vertical displacement $y_1$ may be solve for a given $\alpha$, and vice versa, using the following relationship:

$$(l_3 \cos(\alpha) - l_1)^2 + (-l_3 \sin(\alpha) - y_1)^2 - l_2^2 = 0 \tag{8.2}$$

where $l_1 = 2.1$", $l_2 = 1.25$", and $l_3 = 3$" for the setup in Figure 8.1.

Finally, the inertia of the model, sting and pushrods introduces time lags, so the measured angle is not exactly the same as the commanded angle. Additionally, the Copley servo tube controller has its own PID dynamics. Figure 8.2 is a schematic of the signals, and Figure 8.3 shows the commanded angle $\alpha_{\text{cmnd}}$ and measured angle $\alpha_{\text{pot}}$ for a particular maneuver. In Section 8.2 the model input is the angle of attack as measured by the potentiometer $\alpha_{\text{pot}}$, so that the model captures the aerodynamics without the actuator or mechanical system. In Section 8.3, the model input is the commanded angle of attack $\alpha_{\text{cmnd}}$, so that the models include the effect of the actuator and the mechanical apparatus.

### 8.1.2 Modeling Procedure

The methods in Chapter 5 are used to develop pitch models of the form in Eq. (5.7) and plunge models of the form in Eq. (5.9). In particular, the observer/Kalman filter identification (OKID) method from Sections 2.2.2 and 5.3.4 is used with experimental measurements. For this method to produce accurate models, the input maneuver must excite the unsteady aerodynamics across a full range of relevant

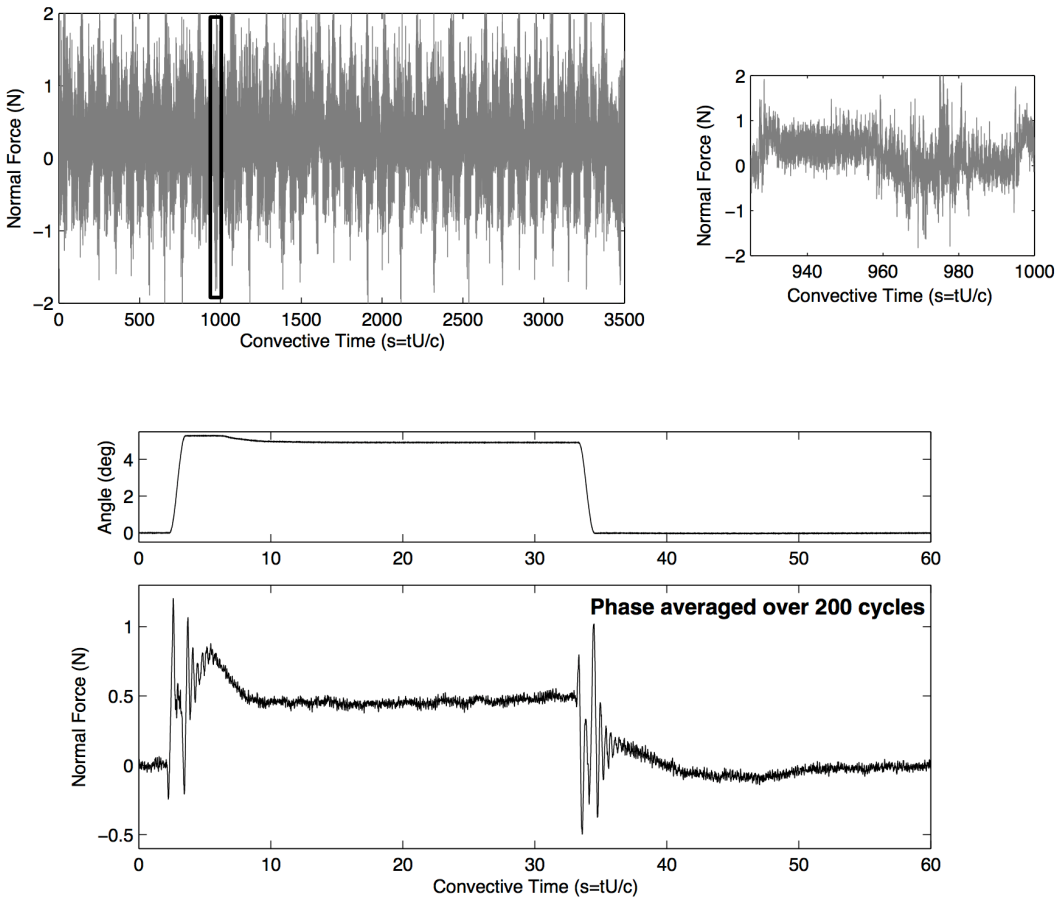


Figure 8.4: Phase averaged force measurement for 5 degree step-up, step-down.

frequencies. The pseudo-random maneuvers shown in Figures 5.13 and 5.14 are developed specifically for the pitch and plunge maneuvers in this experiment. The maneuvers are sufficiently aggressive to overcome noise in the force measurements, and they are generated by a train of distinct impulses in the input variable.

### 8.1.3 Phase Averaged Force Measurements

The force measurements are inherently noisy, and, therefore, we phase average over a number of cycles. This means that we collect data from a number of identical runs, and average the results to reduce the noise. The top of Figure 8.4 shows the noisy force measurements, and the bottom shows the phase averaged force.

Before phase averaging, we use a 6-th order Butterworth low-pass filter at 2500 Hz. In addition, we coarsen the data by averaging the measurements inside each interval $[k\Delta t, (k+1)\Delta t)$, where $\Delta t = 0.1$ convective time unit, or 0.00615 seconds. Using this coarsened data as an input to the OKID method results in a discrete-time model with time-step $\Delta t$. Because the added-mass force appears as a feed-through term, it is possible to convert this to a continuous time system without loss of accuracy at high frequencies. This step is also important to ensure that the angular acceleration $\ddot{\alpha}$, as computed by finite differencing, is not too noisy.

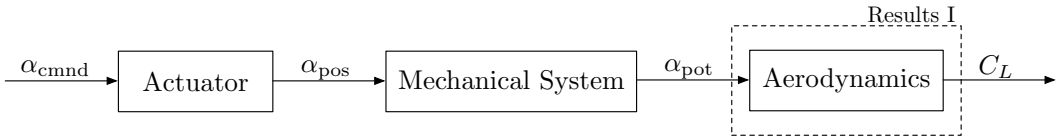


Figure 8.5: Schematic of models in Section 8.2.

## 8.2 Results I: Models based on measured position

In this section, experimental data and reduced order models are presented based on the system ID maneuvers discussed in Section 5.4.2. The input to these models is the angle of attack measured by the potentiometer, $\alpha_{\text{pot}}$, as shown in Figure 8.5. For the case of pitching about $\alpha_0 = 0°$ and $\alpha_0 = 10°$, three pseudo-random maneuvers are used to identify the reduced order models. For every maneuver, force and positions measurements are taken for 100 identical instances of the maneuver and phase averaged. After phase averaging the data, the measured force and angle of attack measurements are discretized with $\Delta t = 0.1$ convective time unit, as discussed in Section 8.1.3.

### 8.2.1 Pitching, $\alpha_0 = 0°$

Figure 8.6 shows the measured angle of attack and lift coefficient for one of the pseudo-random test maneuvers, maneuver B. The black curve is the measured force, the red curve is the low-order model (5.7), and the green curve is Theodorsen's model (6.2). Although Theodorsen's model predicts the quasi-steady lift, it does not adequately capture the large added-mass forces.

The modeling procedure is repeated with similar results for three pseudo-random maneuvers, A, B, and C. It is possible to combine the measured response for each of the three maneuvers and obtain a model based on the concatenated signal. Each of the maneuvers has amplitude roughly $\pm 5°$. The models obtained using each system ID maneuver accurately reproduce the measured force for each of the other test maneuvers, as seen in Figure 8.7.

The Bode plots of each of the reduced order models based on the three system ID maneuvers, as well as the concatenated maneuver, is shown in Figure 8.8. All three models have similar asymptotes, corresponding to the low-frequency quasi-steady limit and high-frequency added-mass limit. In all of the models, there is a prominent resonance at around 12 rad/s·c/U. In dimensional units, this corresponds to a frequency around 30 Hz. It appears that this resonant peak is the result of dynamics in the mechanical system and is not aerodynamic in nature. Similar ringing can be seen in Figure 8.4 after the fast step-up and step-down maneuver.

Finally, the impulse response parameters identified using the OKID method are shown in Figure 8.9. In contrast to Figure 7.14, the added-mass forces are not all lumped into the first Markov parameter (equal to $C_{\ddot{\alpha}}$), but are rather spread out over the first few parameters. The mechanical ringing can be seen clearly in the impulse response parameters, which contributes to the phase bump in the Bode plot around 5 rad/s c/U. This bump is captured by the transient dynamics, since it is not entirely governed by the $C_{\ddot{\alpha}}$ term as in the case of theory and DNS.

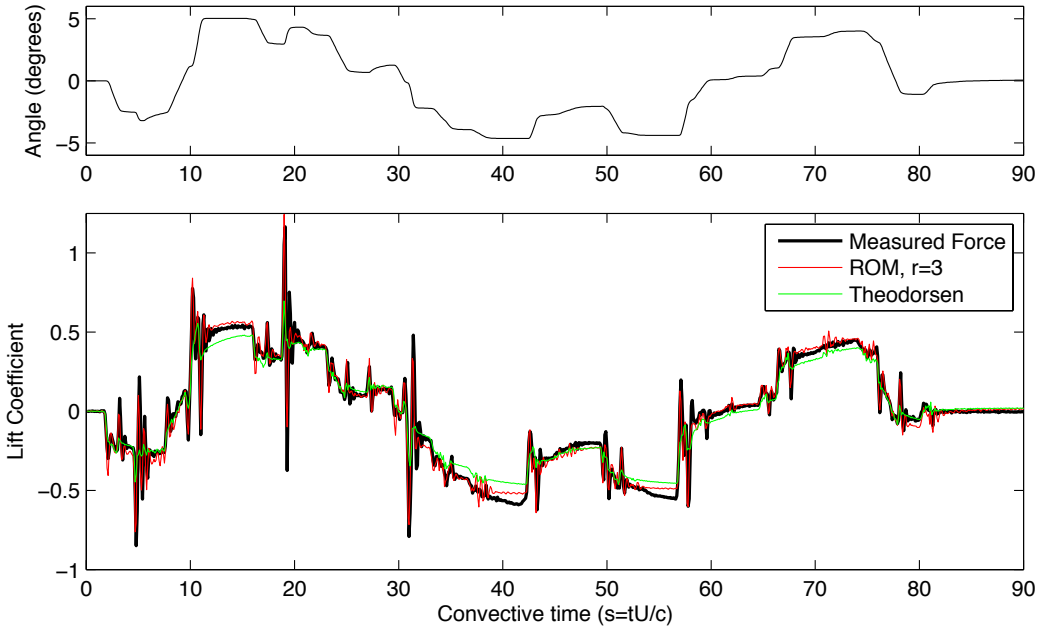


Figure 8.6: Measured force compared with models (bottom) for pseudo-random maneuver B centered at $\alpha_0 = 0°$ (top). A reduced order model (5.7) for transient dynamics of order $r = 3$ outperforms Theodorsen's model.

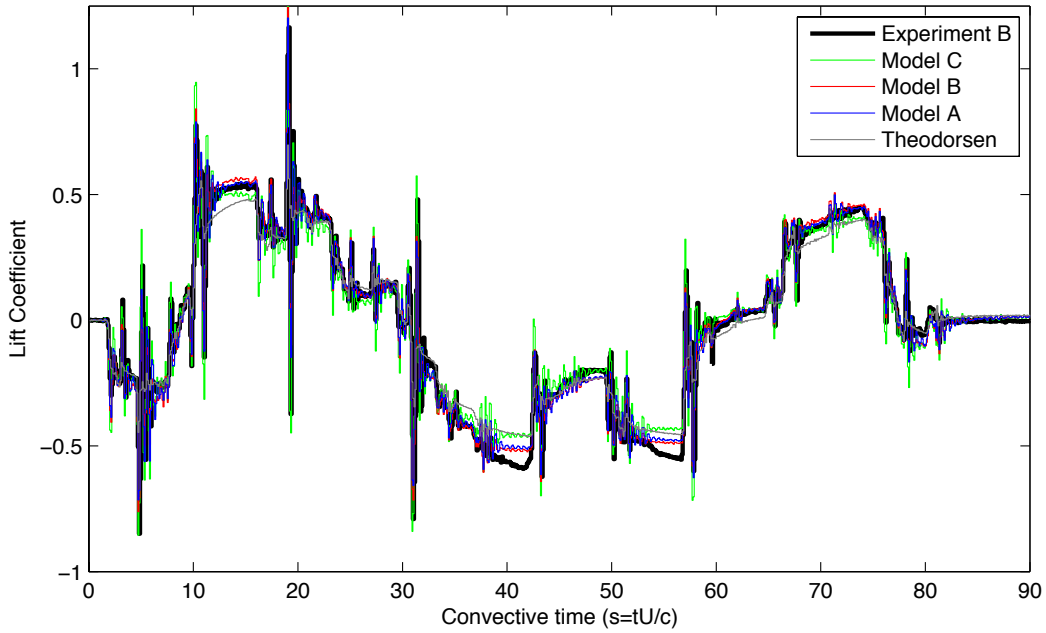


Figure 8.7: Performance of each reduced order model obtained on separate system ID maneuvers, applied to maneuver B.

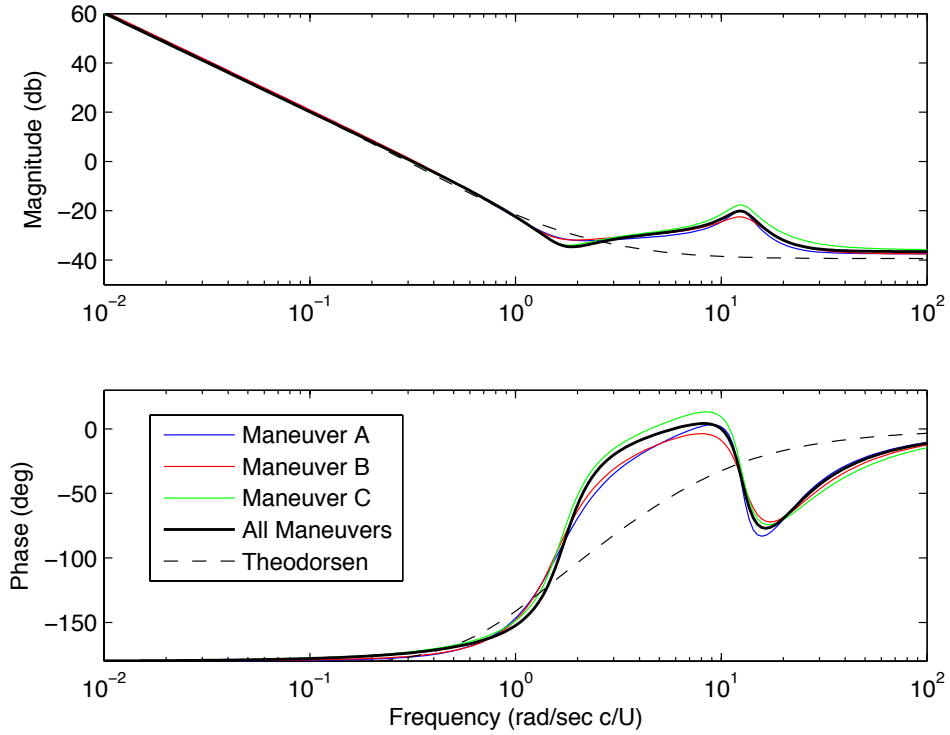


Figure 8.8: Bode plots of the reduced order models obtained using each of the three system ID maneuvers, and concatenated maneuver at base angle of attack $\alpha_0 = 0°$. The model input is $\ddot{\alpha}$, and the output is $C_L$.

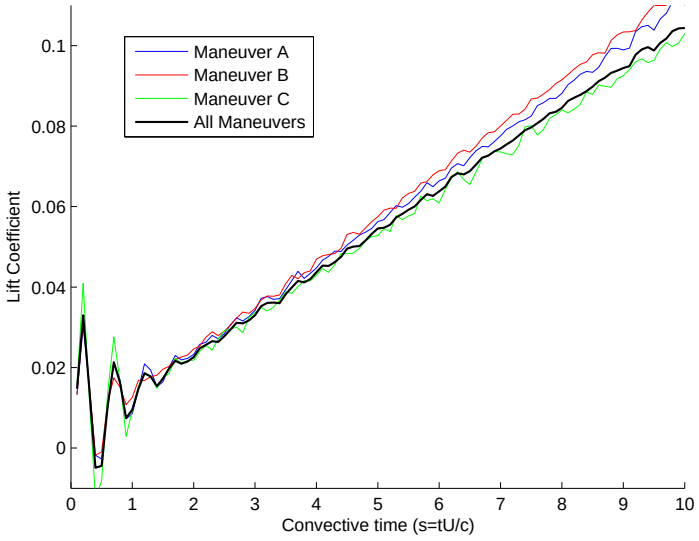


Figure 8.9: Impulse response in $\ddot{\alpha}$ identified using OKID, for system ID maneuvers based around $\alpha_0 = 0°$.

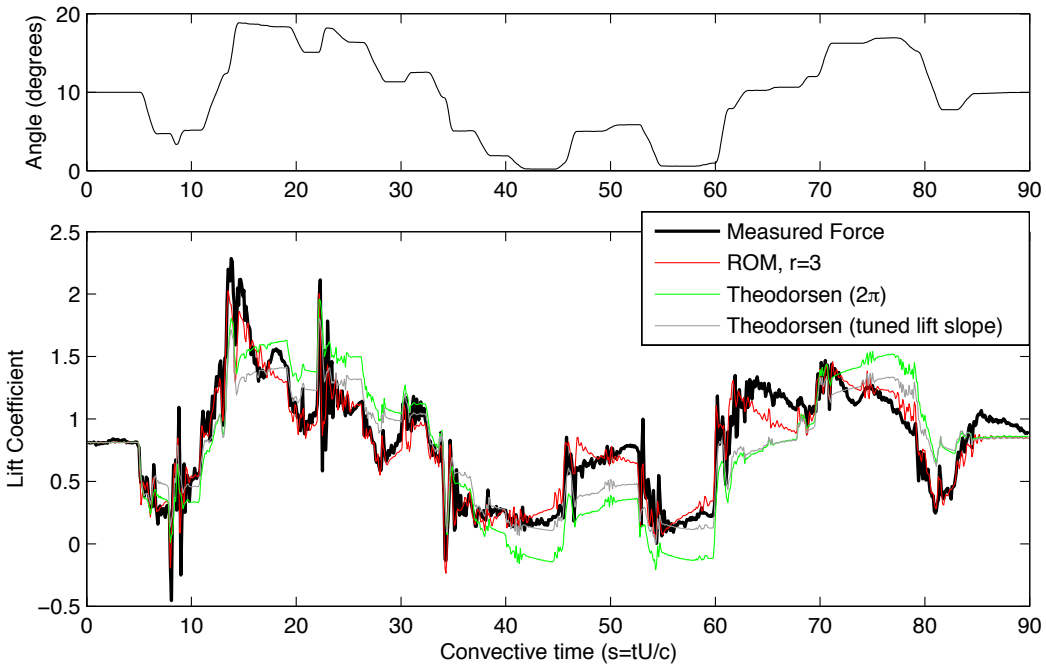


Figure 8.10: Measured force compared with models (bottom) for pseudo-random maneuver B centered at $\alpha_0 = 10^\circ$ (top). A reduced order model with transient dynamics of order $r = 3$ outperforms Theodorsen's model.

### 8.2.2 Pitching, $\alpha_0 = 10^\circ$

Here, the system identification maneuvers are repeated for a new base angle of $\alpha_0 = 10^\circ$. In these experiments, the pitching amplitude is $\pm 10^\circ$, which is twice as large as in the previous section. The $2\pi$ lift slope predicted by Theodorsen is not exact for this airfoil and Reynolds number, and so there is a steady-state error between Theodorsen's predicted lift at $\alpha_0 = 10^\circ$ and the measured lift at $\alpha_0 = 10^\circ$. This error is subtracted off in the plots.

Figure 8.10 shows the measured response for maneuver B, along with the model prediction. The agreement of the model in Eq. (5.7) is not as close as in the $\alpha_0 = 0^\circ$ case, which is most likely due to nonlinear flow effects that are not modeled. However, the model significantly outperforms Theodorsen's model.

The Theodorsen model has relatively poor quasi-steady performance, which is due to the fact that the lift slope decreases significantly for larger angles of attack. This is seen in the decreased slope in the impulse response parameters in Figure 8.12 as well as in the low frequency asymptote in the Bode plot in Figure 8.11. It is possible to tune Theodorsen's model with the correct lift slope, and this is also plotted. Again, there is a prominent resonant peak at around 30 Hz corresponding to mechanical ringing. This can be seen in the Bode plot in Figure 8.11 as well as the impulse response parameters in Figure 8.12.

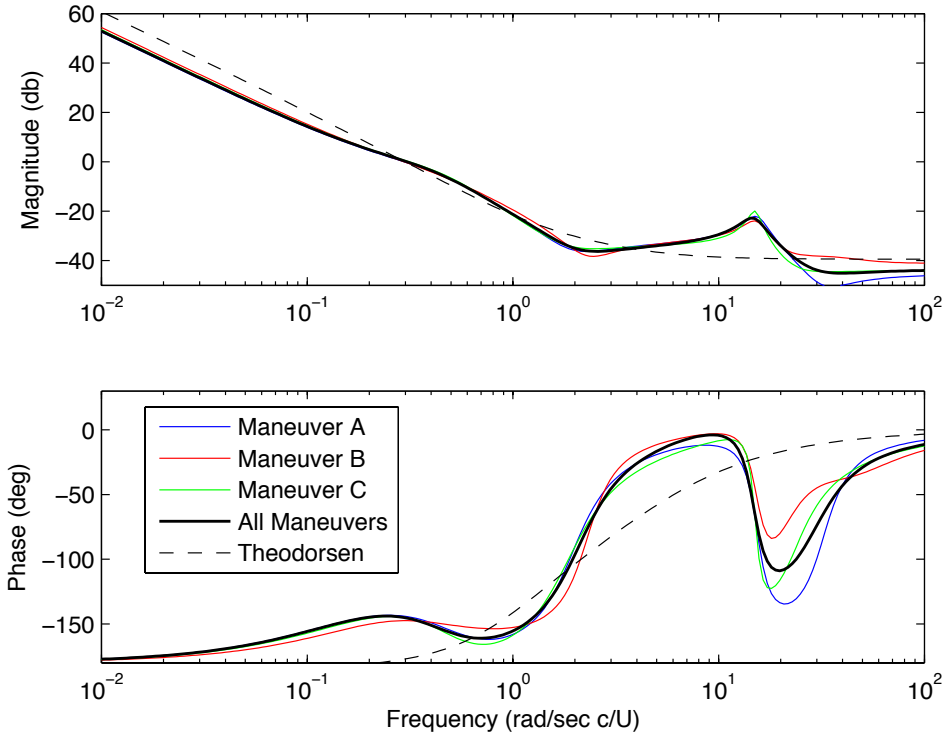


Figure 8.11: Bode plots of the models obtained using each of the three system ID maneuvers, and concatenated maneuver at base angle of attack $\alpha_0 = 10°$. The model input is $\ddot{\alpha}$, and the output is $C_L$.

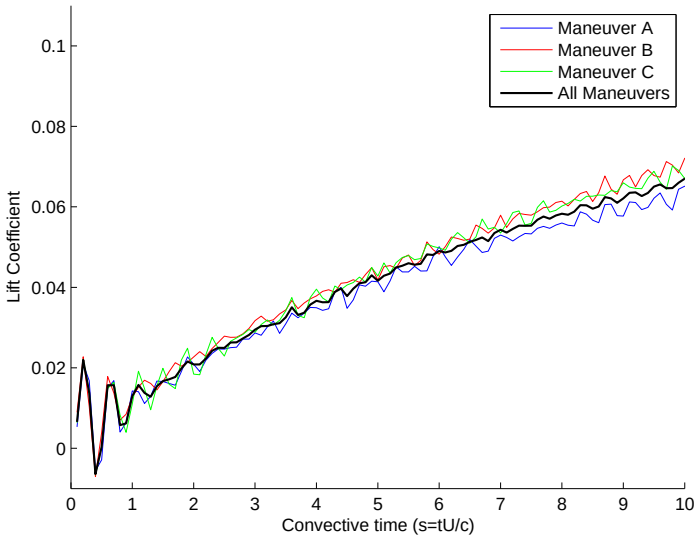


Figure 8.12: Impulse response in $\ddot{\alpha}$ from OKID. Maneuvers are based around a nonzero angle of attack, $\alpha_0 = 10°$.

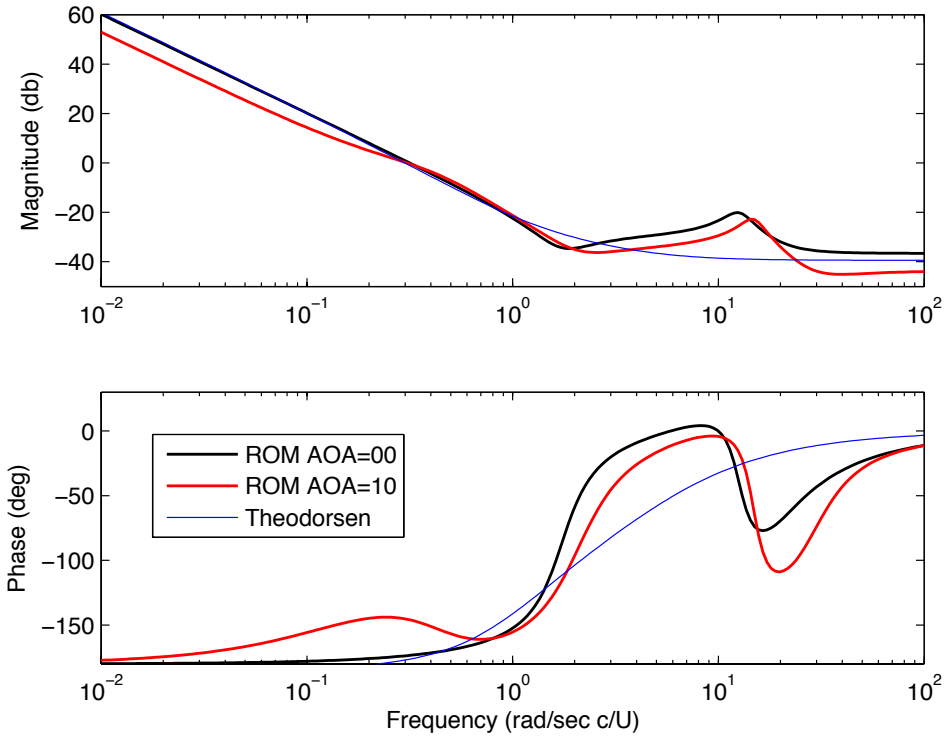


Figure 8.13: Comparison of Bode plots of models based at $\alpha_0 = 0°$ and $\alpha_0 = 10°$. The model input is $\ddot{\alpha}$, and the output is $C_L$.

### 8.2.3 Comparison of Model at $\alpha_0 = 0$ and $\alpha_0 = 10$

Figure 8.13 shows the Bode plots of the pitch models linearized at $\alpha_0 = 0°$ and $\alpha_0 = 10°$. The model based at $\alpha_0 = 10°$ takes longer to reach steady state, as illustrated by the convergence of low-frequency asymptotes at lower frequencies. Additionally, this model has a smaller magnitude at the low frequency asymptote, indicating that the airfoil has partially stalled. Both of these effects are observed when comparing similar models at Reynolds number 100, for example in Figure 7.10.

It also appears that the resonant peak is somewhat attenuated at the larger angle of attack. This may be the result of an aerodynamic *cushioning* effect from the partially separated flow.

### 8.2.4 Model for Plunging

Figure 8.14 shows the model obtained for the case of pure plunge. The system ID maneuver is essentially the same as in the pitching case, except both servo tube controllers are sent the same signal, resulting in plunge motion. Figure 8.15 shows the frequency response for the pure plunge model. Again, there is a resonance at around 30 Hz. It is observed in Figure 8.14 that the lift response is dominated by added-mass and ringing; this motivates the separate system identification maneuver for plunge in the next section.

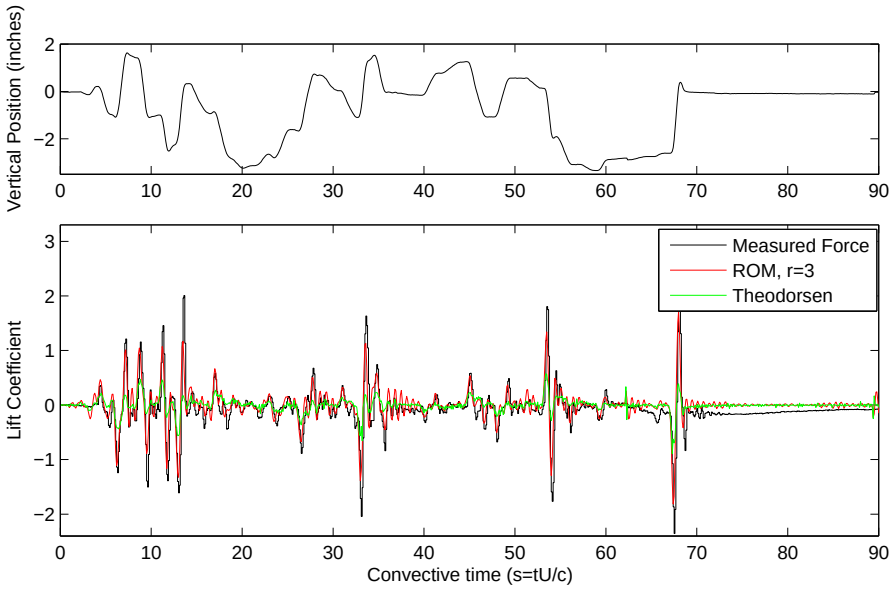


Figure 8.14: Measured force and model prediction for plunge maneuver using reduced order model with transient dynamics of order $r = 3$.

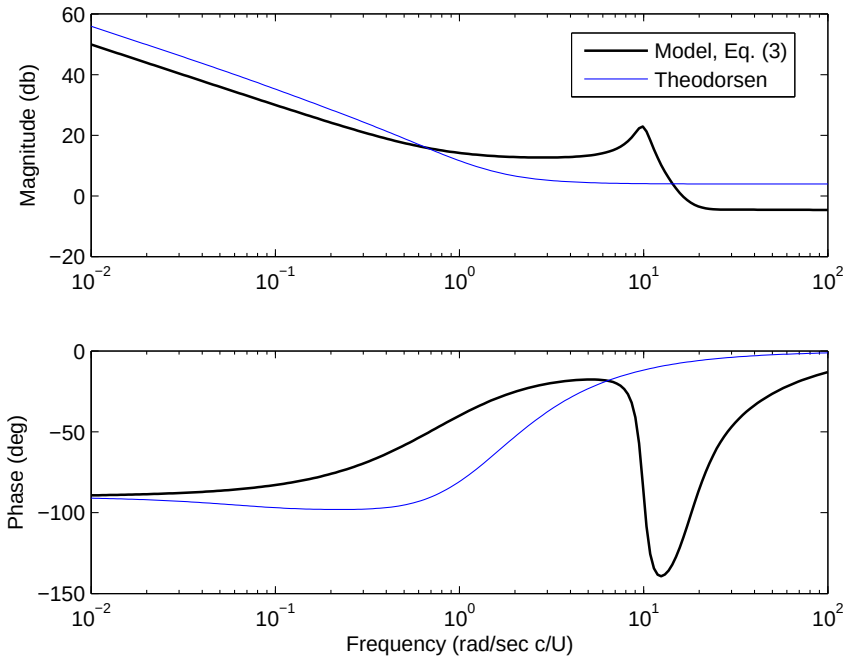


Figure 8.15: Bode plot of the model, Eq. (5.9), and Theodorsen's model for plunge. The input is $\ddot{h}$, and the output is $C_L$.

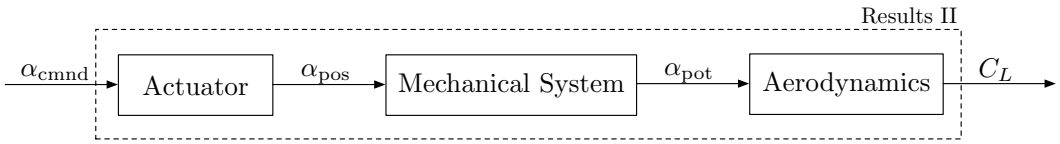


Figure 8.16: Schematic of models in Section 8.3.

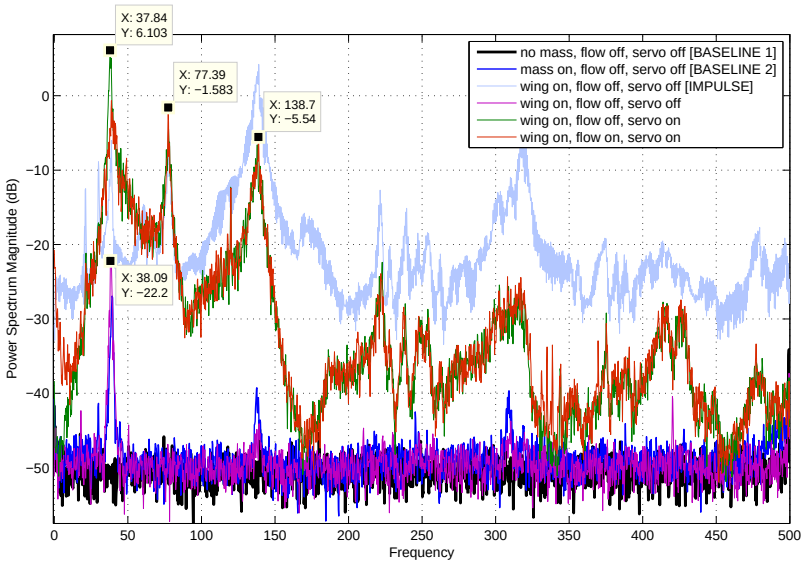


Figure 8.17: Mechanical resonances involved in the wind tunnel experiment.

## 8.3 Results II: Models based on commanded position

After identifying significant mechanical ringing and aeroelastic effects in the results from Section 8.2, efforts were made to rebuild the structural supports and retune the PID controller for the servo motor to reduce sources of noise and vibration. In addition, a more sensitive Nano17 force transducer is used to measure forces, so that less aggressive maneuvers may be accurately measured. Finally, the linear potentiometers were modified to reduce stick-slip, at the cost of accuracy in $\alpha_{\text{pot}}$. Thus, the input to models in this section is the commanded position, so that the actuator is included in the plant model. This is shown in Figure 8.16.

The Nano17 transducer has less sensor noise than the Nano25, so fewer samples are required for phase averaging. Pitch maneuvers in this section the same as the one in Figure 8.6. A new plunge maneuver is developed, shown in Figure 5.14.

### 8.3.1 Mechanical ringing

In the models from Section 8.2, there is a significant resonance due to mechanical vibrations. Therefore, it is important to characterize more accurately and systematically the mechanical resonances involved in the system.

| | Error (Theodorsen) | Error (ERA Model) | Markov parameters | Model order |
|---|---|---|---|---|
| Pitch, $\alpha_0 = 0°$ | 0.0604 | 0.0331 | 100 | 7 |
| Pitch, $\alpha_0 = 5°$ | 0.0752 | 0.0430 | 50 | 5 |
| Pitch, $\alpha_0 = 10°$ | 0.1279 | 0.0629 | 150 | 5 |
| Plunge, $\alpha_0 = 0°$ | 0.1414 | 0.0701 | 100 | 5 |
| Plunge, $\alpha_0 = 10°$ | 0.2028 | 0.0991 | 100 | 5 |

Table 8.1: Comparison of Theodorsen and ERA model error with wind tunnel measurements for pitch and plunge maneuvers. Error is quantified by computing the standard deviation of the error signal (measurement minus model).

| Markov parameters | 100 | 100 | 100 | 100 |
|---|---|---|---|---|
| Model order | 7 | 7 | 7 | 7 |
| Time delay ($\Delta t$) | 1 | 2 | 3 | 4 |
| Error (ERA Model) | $0.0359^1$ | $0.0331^2$ | $0.0331^3$ | $0.0727^4$ |

Table 8.2: Effect of time delay on model error. $\Delta t = 0.1$ convective time units.

Figure 8.17 shows the power spectrum of the normal force measurement for a number of control experiments to determine the source and frequency of the mechanical resonance. In one case, the bottom of the actuator assembly is struck with a rubber mallet, resulting in a strong resonance at 77 Hz and at 139 Hz. When power is fed to the servo motor controller, a significant resonant peak at 38 Hz develops, regardless of whether or not the wind tunnel fan is on. It is likely that the resonance peak at 38 Hz is a result of the internal PID dynamics of the servo motor controller, partially explaining the peaks in the Bode plots at nearby frequencies.

### 8.3.2 Model benchmarks

The results of Sections 8.3.3 and 8.3.4 are summarized here. Table 8.1 shows the error between the measured data and both Theodorsen's model and the identified model from OKID/ERA. The error is measured by integrating the square of the difference between each model and the measured data for a given maneuver. In all of the cases, the error in the ERA model is about half of the error in Theodorsen's model. It is also interesting to note that the error increases as the base angle of attack $\alpha_0$ increases. This is reasonable, since the flow becomes increasingly nonlinear for increasing angle of attack.

The inherent time delay between command signal and measured force is identified by choosing the time delay that minimizes the model error. The results are shown in Table 8.2. Recall from Section 8.1.3 that the coarse sample time is $\Delta t = 0.1$ convective time. Since the error is the same for a time delay of $2\Delta t$ and $3\Delta t$, it helps to use other indicators, such as the frequency response or how closely the peaks in $\ddot{\alpha}$ line up with the added-mass peaks in the force measurement. Based on these comparisons, it was determined that the time-delay is $3\Delta t$ (0.3 convective times).

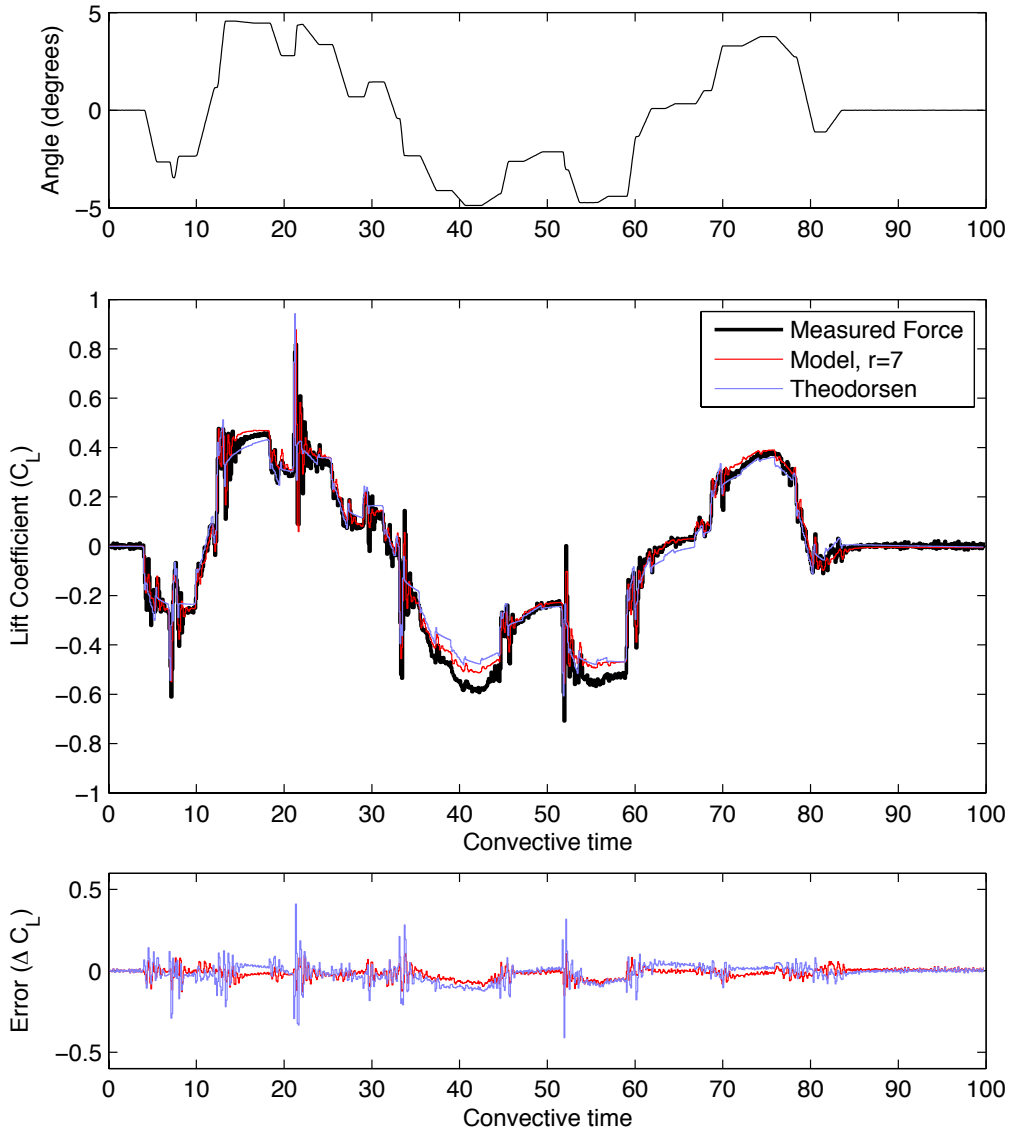


Figure 8.18: Experimental and modeled lift for pitch about a base angle $\alpha_0 = 0°$.

### 8.3.3 Pitching experiments

The pitching experiments from Section 8.2 are repeated with the more sensitive Nano17 force transducer. Figure 8.18 shows the measured and modeled response linearized at $\alpha_0 = 0°$. Both models, Eq. (5.7) and Theodorsen's model, appear to closely match the measured force; however, from Table 8.1, Theodorsen's model has nearly twice the error as the ERA model. It is reassuring that Theodorsen's model is accurate at $\alpha_0 = 0°$, since this speaks to the accuracy of the experiments after efforts were made to clean up the measurements and reduce ringing.

Figure 8.19 shows the same pitch maneuver performed at a base angle of $\alpha_0 = 10°$. For this maneuver, Theodorsen's model is significantly less accurate than in

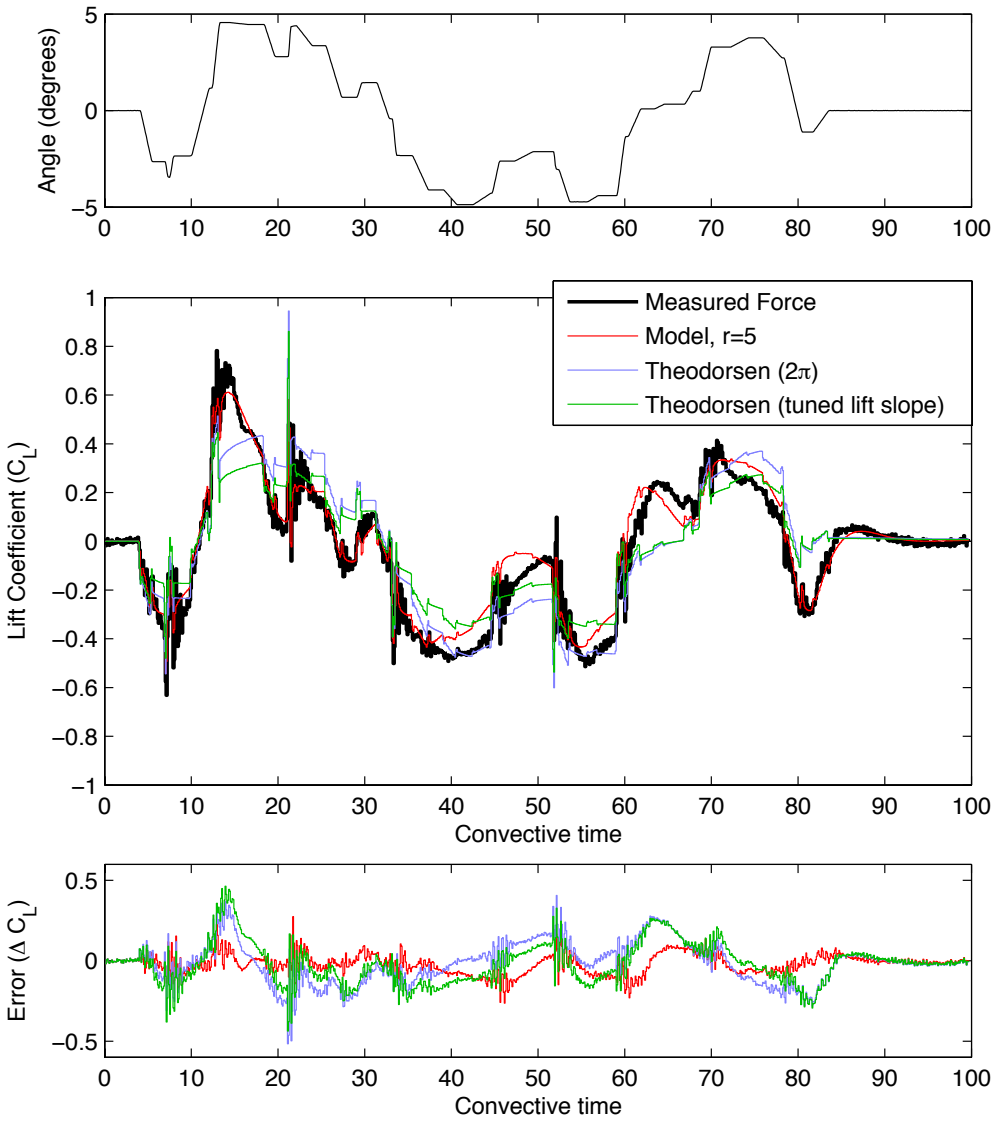


Figure 8.19: Experimental and modeled lift for pitch about a base angle $\alpha_0 = 10°$.

the $\alpha_0 = 0°$ case. This is not entirely surprising, considering that the flow physics is increasingly nonlinear for larger angle of attack.

Figure 8.20 compares the Bode plots of the ERA models at $\alpha_0 = 0°$ and $\alpha_0 = 10°$ and Theodorsen's model. The model linearized at $\alpha_0 = 10°$ converges to the low-frequency asymptote at a lower frequency than the $\alpha_0 = 0°$ model, and the magnitude is smaller at low frequencies, consistent with the shallower lift coefficient slope. Additionally, since the new models include the effect of the actuator and mechanical system, there is a strong new mechanical resonance at 30 rad/s c/U, which corresponds to about 76 Hz. The model at $\alpha_0 = 10°$ does not have a prominent resonance at 10 rad/s c/U (38 Hz), unlike the model based at $\alpha_0 = 0°$. It appears that the aerodynamic damping has almost entirely eliminated this resonance.

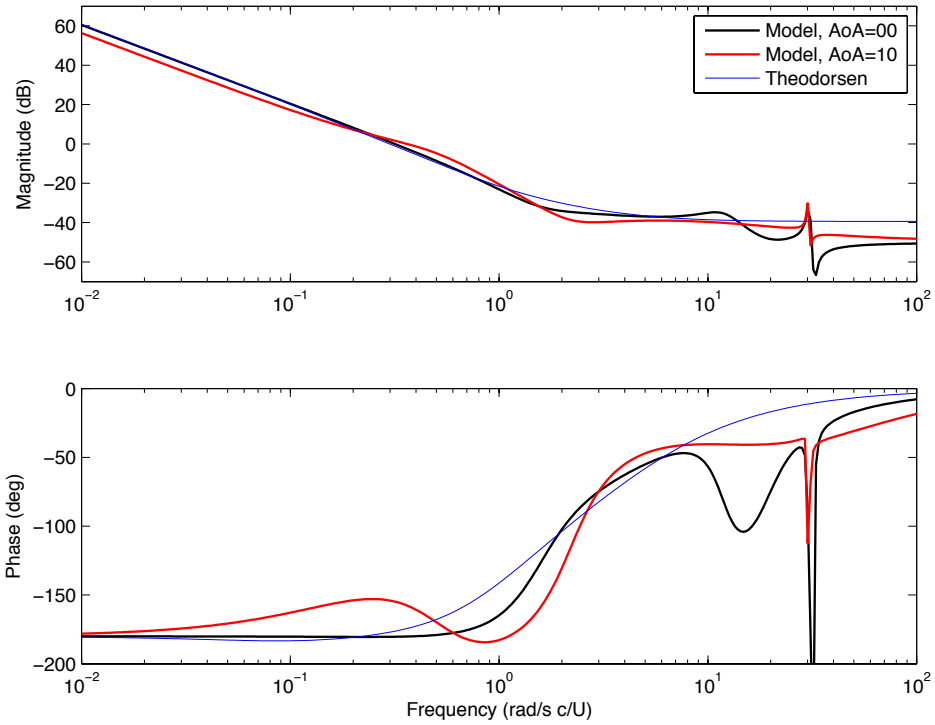


Figure 8.20: Bode plots of pitch models at $\alpha_0 = 0°$ and $\alpha_0 = 10°$. The model input is $\ddot{\alpha}$, and the output is $C_L$.

### 8.3.4 Plunge experiments

The new plunge maneuver in Figure 5.14 is modified from the plunge maneuver used in Section 8.2.4. Since there is no $C_h$ term in the plunge model (5.9), it is unnecessary to have the "hold" portions of the maneuver at different heights. Therefore, the new maneuver accelerates into linear ramps of different vertical velocity until a maximum or minimum height has been reached, after which the height is held for a time and then the direction is reversed. The different vertical velocities correspond to different *effective* angle of attack.

Figure 8.21 shows the results for plunging about $\alpha_0 = 0°$ and Figure 8.22 shows the results for plunging about $\alpha_0 = 10°$. At $\alpha_0 = 0°$ Theodorsen's model is quite accurate, capturing the qualitative behavior. At $\alpha_0 = 10°$, however, it is clear that Theodorsen's model is failing to predict the regions of constant vertical velocity, which correspond to a constant effective angle of attack. In fact, during these effective angle of attack holds, Theodorsen's model rises to a steady state that is larger in magnitude, while the actual lift decreases from a large initial lift. Although the ERA model does a better job capturing this phenomena, it is clear from the error signal that both models systematically underpredict the lift at the beginning of these hold periods.

Figure 8.23 shows a comparison of the Bode plots for the plunge models linearized at $\alpha_0 = 0°$ and $\alpha_0 = 10°$.

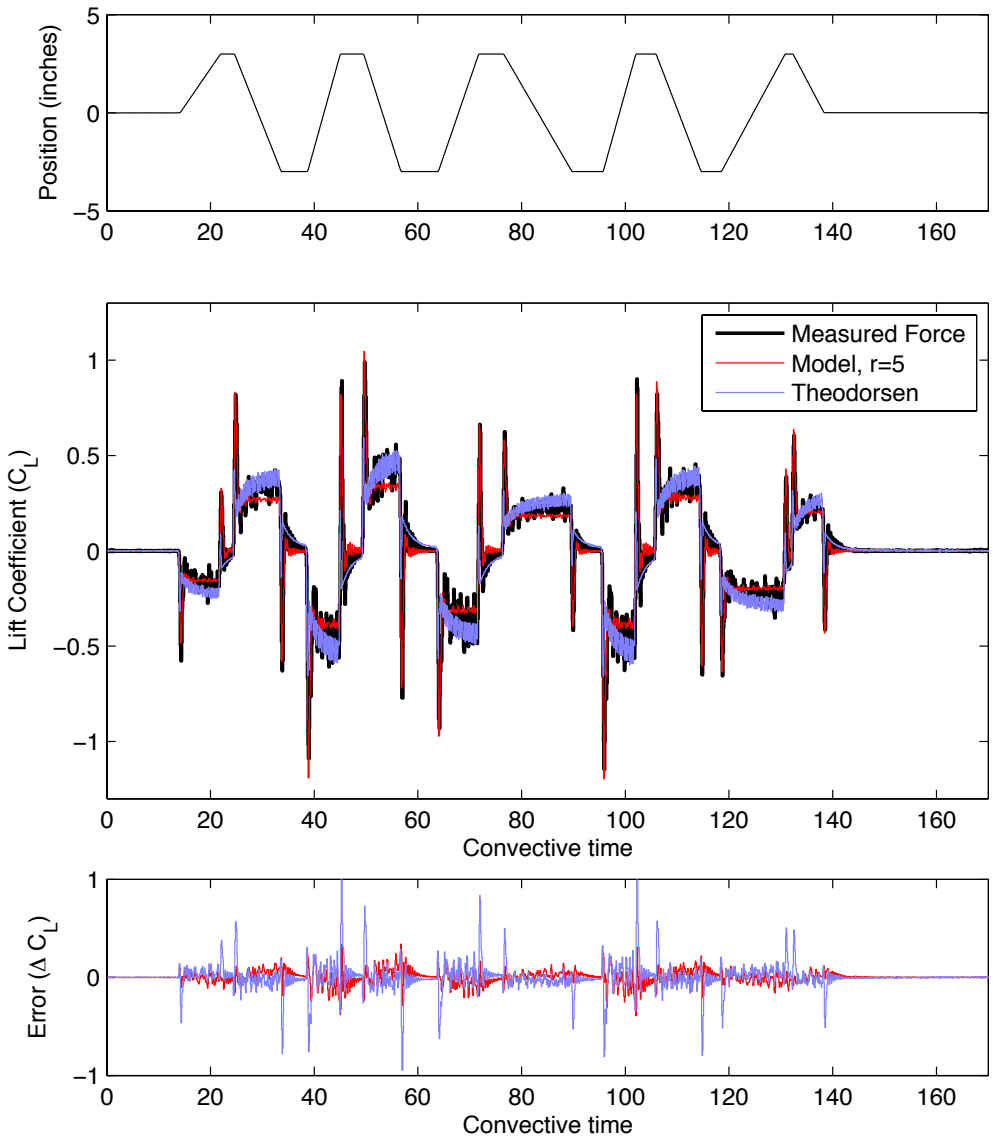


Figure 8.21: Experimental and modeled lift for plunge about a base angle $\alpha_0 = 0°$.

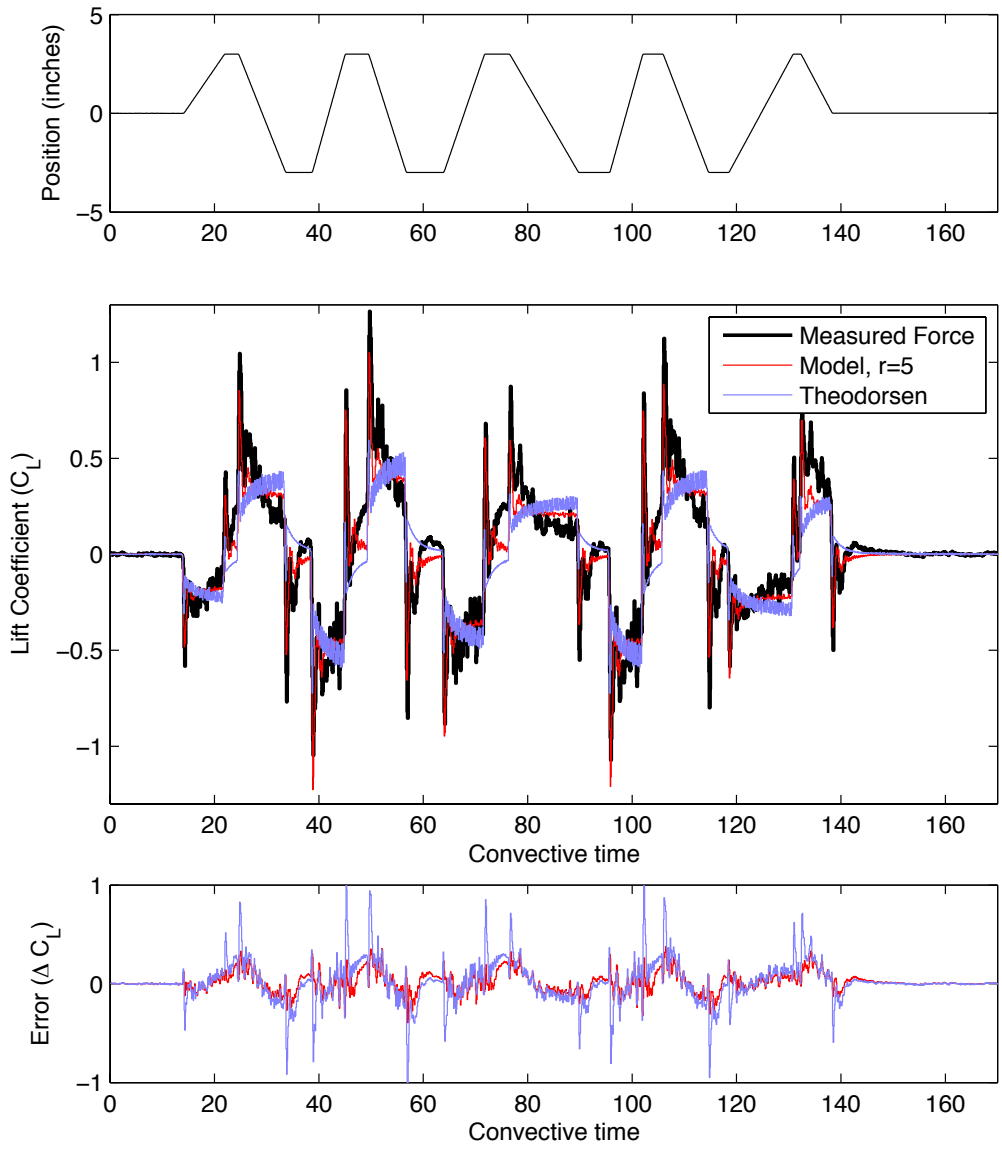


Figure 8.22: Experimental and modeled lift for plunge about a base angle $\alpha_0 = 10°$.

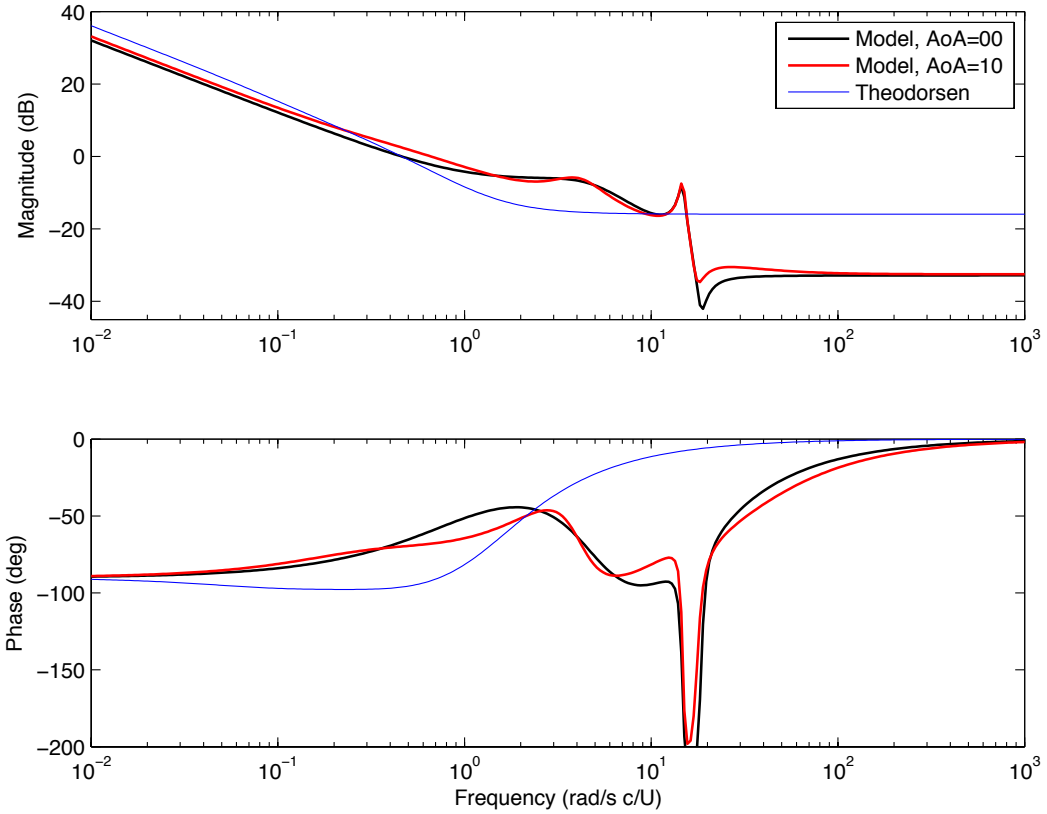


Figure 8.23: Bode plots for plunge models based at $\alpha_0 = 0°$ and $\alpha_0 = 10°$. The model input is $\ddot{h}$, and the output is $C_L$.

## 8.4 Discussion about experimental results

The modeling procedures from Chapter 5 have been applied to develop low-dimensional models for the unsteady aerodynamic force on a NACA 0006 airfoil from wind tunnel measurements. The wind tunnel is a more challenging test case with the addition of plant disturbances and sensor noise. Additionally, the experiment is performed at a moderate Reynolds number, Re $= 65,000$, with a three-dimensional wing with rounded leading edge, providing a more realistic model of a micro aerial vehicle. The issue of plant disturbance and sensor noise motivates the aggressive maneuvers used in this chapter, which excite strong unsteady aerodynamic responses across a range of relevant frequencies. These maneuvers are used in conjunction with the algorithm in Section 5.3.4, based on OKID, to construct pitch models (5.7) and plunge models (5.9).

The results in this chapter are based on two separate sets of experimental data. The models identified from the first set of data exhibit a strong resonant peak at around 30 Hz, which is caused by oscillations in the servo tube controllers exciting a mechanical resonance in the system. This discovery led to a redesigned experiment, and a cleaner second set of data. In both sets of results, at $\alpha_0 = 0°$ and $\alpha_0 = 10°$, our reduced order model outperforms Theodorsen's model. At larger base angle of attack, $\alpha_0 = 10°$, the difference with Theodorsen is more pronounced. However,

at $\alpha_0 = 10^\circ$ the total error is larger in both models than in the $\alpha_0 = 0^\circ$ case, presumably because of nonlinear flow effects that are not modeled. The fact that the low-order model captures the additional mechanical effects indicates that these methods may be applied more generally to problems in aeroelasticity. It is also noted that there is an aerodynamic cushioning effect at $\alpha_0 = 10^\circ$, whereby the mechanical resonance is attenuated and occurs at a slightly higher frequency.

The models in this chapter follow similar trends to those from Chapter 7. For example, at larger base angle of attack, the model takes longer to equilibrate to steady state, as reflected in the convergence to the quasi-steady asymptote at a lower frequency. Additionally, at $\alpha_0 = 0^\circ$, the data and models exhibit a transient rise to their steady-state values given a step in effective angle of attack, while at $\alpha_0 = 10^\circ$, the data and models exhibit a transient decay to their steady-state values from a larger initial value. It is believed that in the experimental data this is due to the formation and convection of a leading edge vortex, as is the case in simulations. The qualitative agreement with simulations suggests that the experimental flow field is still dominated by large fluid coherent structures.

# Chapter 9

# Conclusions

In this thesis, there are three major contributions toward advancing the state of the art of unsteady aerodynamic modeling at low Reynolds number. First, I have developed an efficient and accurate linear modeling framework, consisting of reduced order models, algorithms, and system identification maneuvers that may be applied to data from high fidelity simulations and experiments. Next, I have applied these techniques to obtain low-order models for the unsteady aerodynamics at low Reynolds number using data from direct numerical simulations and wind tunnel experiments. Finally, I have developed two computational tools that dramatically improve our ability to compute and visualize fully resolved direct numerical simulations. These three points are addressed in the following sections, along with suggestions for future work in this field.

## 9.1 Linear modeling framework and procedure

A main result of this work is the development of a set of general unsteady aerodynamic models in Section 5.2. Moreover, a number of algorithms and maneuvers for system identification have been developed to construct these reduced order aerodynamic models, either from simulations or from experimental data.

These models are directly inspired by the classical models of Wagner [125] and Theodorsen [114], but they have been significantly extended and modernized for use with current control design and analysis techniques. In particular, the models may be viewed as state-space realizations of the accurate indicial response models obtained from direct numerical simulations and wind tunnel measurements. These models, therefore, capture the transient, viscous fluid dynamic effects that are not captured by inviscid theories.

Additionally, the models have explicit terms for the quasi-steady lift coefficient slope and added-mass forces, which is reminiscent of Theodorsen's model. Identifying these terms separately has two positive outcomes. First, the model is guaranteed to have the correct behavior in the limit of low and high frequency motion. Second, the subsequent reduced order modeling effort is focused at the intermediate frequencies where the transient fluid dynamic effects are important. The resulting models are, thus, both accurate and efficient. Moreover, the models developed are parameterized by the pitch axis location, as is Theodorsen's model.

## 9.2 Unsteady model results at low Reynolds numbers

In Chapter 6 the models of Wagner and Theodorsen are cast into a modern state-space framework, and they conform to the general aerodynamic model presented in Eq. (5.5). In Chapter 7, linear models are developed for direct numerical simulations of a pitching and plunging flat plate at Reynolds number of $\mathrm{Re} = 100$. It is shown that for a relatively low order model, $r = 7$, the unsteady aerodynamic effects are well captured for all angles of attack up to the Hopf bifurcation angle. Moreover, the identified linear models are more accurate than Theodorsen's model, because they include viscous boundary layer effects. In Chapter 8, the modeling procedure is applied to characterize the unsteady aerodynamics of a NACA 0006 airfoil at Reynolds number $65,000$ in a wind tunnel experiment at the Illinois Institute of Technology. In addition to providing a real-world validation of these methods, it is interesting to note that the modeling procedure from Chapter 5 is sufficiently general to capture aeroelastic effects, as well as the actuator dynamics in the experiment.

The models obtained in Chapters 7 and 8 provide quantifiable insights into the physics of laminar separation that characterize flows at low Reynolds number. In both the simulated results and the wind tunnel measurements, the resulting models exhibit similar trends as the angle of attack is increased. The quasi-steady limit is pushed to lower frequencies at larger base angle of attack, consistent with the fact that a pair of imaginary eigenvalues moves toward the imaginary axis in the low-order models. In addition, at large angle of attack, we see an attenuation of the fluid-structure resonance, due to the cushioning effect of the separated boundary layer.

Also, based on the model in Eq. (5.11), at a given angle of attack, all of the models for pitch about various points and plunge have the same poles. The differences are explained by the changing zeros. This is consistent with Theodorsen's framework.

## 9.3 Development of computational tools for unsteady fluid dynamics

Two computational tools for simulating and visualizing unsteady fluid dynamics have been improved upon as a result of this work. First, the immersed boundary projection method was extended to simulate the Navier-Stokes equations in the body-fixed frame of an airfoil. This provides an order of magnitude computational improvement over the previous method for the case of a moving airfoil. In addition, it is possible to simulate large amplitude wing motions that would have previously left the domain.

Second, a number of methods are developed that improve the computation of finite-time Lyapunov exponents (FTLE), which are useful for characterizing unsteady fluid coherent structures and understanding unsteady flow mechanisms. The new methods are orders of magnitude faster than the standard algorithm. In [9], we used the FTLE field to understand how the classical model of Theodorsen breaks down for large amplitude pitching and plunging motion with large reduced frequency and Strouhal number.

## 9.4 Future directions

There are a number of extensions and open problems related to this work. A few promising directions include:

- **$\mathcal{H}_2$ and $\mathcal{H}_\infty$ optimal control based on models**– It is of particular interest to use the models developed in this thesis for control. The low-dimensional, state-space form of these models will be ideal for use with modern control techniques. Comparison of control methods based on Theodorsen's model and the more accurate models in this thesis would provide a valuable performance metric. In particular, it will be interesting to compare the controllers developed for models at zero angle of attack, $\alpha_0 = 0°$, where Theodorsen's model is most accurate, with controllers at larger angle of attack, where the appearance of right half plane zeros make the control problem more challenging.

  A preliminary control objective is to maintain a constant lift coefficient (or track a reference lift) using pitch angle control while rejecting gust disturbances; vertical gust will be modeled by a plunge acceleration. It will then be interesting to investigate the coupled flight dynamic/aerodynamic control problem of trajectory tracking. The design of flight controllers for small MAVs will be particularly interesting when the flight dynamic and aerodynamic timescales are comparable.

- **Nonlinear aerodynamic models**– Developing nonlinear models based on the methods and models in this thesis will be a challenging and worthwhile endeavor. In particular, extending the modeling techniques to the unstable equilibria and stable periodic orbits for post-critical angle of attack will provide valuable information about the form of the nonlinearity in the model. The goal would be to develop a single model that yields the models from this thesis, when linearized, and is more accurate for large amplitude maneuvers when nonlinear effects are excited.

- **Generalize for full 3D flight**– The analysis in this thesis has concerned modeling the unsteady lift coefficient for longitudinal wing motions. It is a straightforward, though technically involved, generalization of the methods in this thesis to obtain models from general kinematic inputs in three dimensions, $TSE(3)$, to all force and moment outputs. This will extend the scope of these methods to include improved flight simulators and six degree-of-freedom flight control.

# Bibliography


[1] S. Ahuja and C. W. Rowley. Feedback control of unstable steady states of flow past a flat plate using reduced-order estimators. *Journal of Fluid Mechanics*, 645:447–478, 2010.

[2] S. Ahuja, C. W. Rowley, I. G. Kevrekidis, M. Wei, T. Colonius, and G. Tadmor. Low-dimensional models for control of leading-edge vortices: Equilibria and linearized models. AIAA Paper 2007-709, 45th Aerospace Sciences Meeting, January 2007.

[3] D. Amsallem, J. Cortial, and C. Farhat. Towards real-time computational-fluid-dynamics-based aeroelastic computations using a database of reduced-order information. *AIAA Journal*, 48(9):2029–2037, 2010.

[4] S. Bagheri, L. Brandt, and D. S. Henningson. Input-output analysis, model reduction and control of the flat-plate boundary layer. *Journal of Fluid Mechanics*, 620:263–298, 2009.

[5] J. Birch and M. Dickinson. Spanwise flow and the attachment of the leading-edge vortex on insect wings. *Nature*, 412:729–733, 2001.

[6] R. L. Bisplinghoff and H. Ashley. *Principles of Aeroelasticity*. John Wiley & Sons, Inc., Hoboken, New Jersey, 1962.

[7] C. E. Brennen. A review of added mass and fluid inertial forces. Technical Report CR 82.010, Naval Civil Engineering Laboratory, 1982.

[8] R. D. Breuker, M. Abdalla, A. Milanese, and P. Marzocca. Optimal control of aeroelastic systems using synthetic jet actuators. AIAA Paper 2008-1726, 49th Structures, Structural Dynamics, and Materials Conference, April 2008.

[9] S. L. Brunton and C. W. Rowley. Modeling the unsteady aerodynamic forces on small-scale wings. AIAA Paper 2009-1127, 47th Aerospace Sciences Meeting, January 2009.

[10] S. L. Brunton and C. W. Rowley. Fast computation of FTLE fields for unsteady flows: a comparison of methods. *Chaos*, 20:017503, 2010.

[11] S. L. Brunton and C. W. Rowley. Unsteady aerodynamic models for agile flight at low Reynolds numbers. AIAA Paper 2010-552, 48th Aerospace Sciences Meeting, January 2010.

[12] S. L. Brunton and C. W. Rowley. Low-dimensional state-space representations for classical unsteady aerodynamic models. AIAA Paper 2011-476, 49th Aerospace Sciences Meeting, January 2011.

[13] S. L. Brunton, C. W. Rowley, K. Taira, T. Colonius, J. Collins, and D. R. Williams. Unsteady aerodynamic forces on small-scale wings: experiments, simulations and models. AIAA Paper 2008-520, 46th Aerospace Sciences Meeting, January 2008.

[14] S. L. Brunton, C. W. Rowley, and D. R. Williams. Linear unsteady aerodynamic models from wind tunnel measurements. AIAA Paper 2011-3581, 41st Fluid Dynamics Conference, June 2011.

[15] J. Buchholz and A. J. Smits. The wake structure and thrust performance of a rigid, low-aspect-ratio pitching panel. *Journal of Fluid Mechanics*, 603:331–365, 2008.

[16] L. Caracoglia. Influence of uncertainty in selected aerodynamic and structural parameters on the buffeting response of long-space bridges. *Journal of Wind Engineering and Industrial Aerodynamics*, 96:327–344, 2008.

[17] C. W. Chen, J. K. Huang, M. Phan, and J. N. Juang. Integrated system-identification and state estimation for control of flexible space structures. *Journal of Guidance, Control and Dynamics*, 15(1):88–95, 1992.

[18] K. K. Chen, T. Colonius, and K. Taira. The leading-edge vortex and quasi-steady vortex shedding on an accelerating plate. *Physics of Fluids*, 22:033601, 2010.

[19] T. Colonius and K. Taira. A fast immersed boundary method using a nullspace approach and multi-domain far-field boundary conditions. *Computer Methods in Applied Mechanics and Engineering*, 197:2131–2146, 2008.

[20] C. Costa. Aerodynamic admittance functions and buffeting forces for bridges via indicial functions. *Journal of Fluids and Structures*, 23:413–428, 2007.

[21] C. Costa and C. Borri. Application of indicial functions in bridge deck aeroelasticity. *Journal of Wind Engineering and Industrial Aerodynamics*, 94:859–881, 2006.

[22] M. A. H. Dinyavari and P. P. Friedmann. Application of time-domain unsteady aerodynamics to rotary-wing aeroelasticity. *AIAA Journal*, 24(9):1424–1432, 1986.

[23] E. H. Dowell. A simple method for converting frequency-domain aerodynamics to the time domain. Technical Memorandum 81844, NASA, 1980.

[24] E. H. Dowell, K. C. Hall, and M. C. Romanowski. Eigenmode analysis in unsteady aerodynamics: Reduced-order models. *Applied Mechanics Reviews*, 50(6):371–386, 1997.

[25] J. W. Edwards, J. V. Breakwell, and A. E. B. Jr. Active flutter control using generalized unsteady aerodynamic theory. *Journal of Guidance and Control*, 1:32–40, 1978.

[26] J. D. Eldredge, C. Wang, and M. V. OL. A computational study of a canonical pitch-up, pitch-down wing maneuver. AIAA Paper 2009-3687, 39th Fluid Dynamics Conference, June 2009.

[27] B. Etkin. *Dynamics of Atmospheric Flight*. John Wiley & Sons, Inc., Hoboken, New Jersey, 1972.

[28] E. Franco, D. N. Pekarek, J. Peng, and J. O. Dabiri. Geometry of unsteady fluid transport during fluid-structure interactions. *Journal of Fluid Mechanics*, 589:125–145, 2007.

[29] D. Fransos and L. Bruno. Determination of the aeroelastic transfer functions for streamlined bodies by means of a Navier-Stokes solver. *Mathematical and Computer Modelling*, 43:506–529, 2006.

[30] I. E. Garrick. On some reciprocal relations in the theory of nonstationary flows. Technical Report 629, NACA, 1938.

[31] C. Garth, F. Gerhardt, X. Trichoche, and H. Hagen. Efficient computation and visualization of coherent structures in fluid flow applications. *IEEE Transactions on Visulization and Computer Graphics*, 13(6):1464–1471, 2007.

[32] C. Garth, A. Wiebel, X. Trichoche, K. Joy, and G. Scheuermann. Lagrangian visualization of flow-embedded surface structures. *Computer Graphics Forum*, 27(3):1007–1014, 2008.

[33] P. Gold and M. Karpel. Reduced-size aeroservoelastic modeling and limit-cycle-oscillation simulations with structurally nonlinear actuators. *Journal of Aircraft*, 45(2):471–477, 2008.

[34] M. Goman and A. Khrabrov. State-space representation of aerodynamic characteristics of an aircraft at high angles of attack. *Journal of Aircraft*, 31(5):1109–1115, 1994.

[35] N. E. Goodzeit. *System and disturbance identification for adaptive disturbance-rejection control*. PhD thesis, Princeton University, 1998.

[36] M. A. Green. *Analysis of Bio-Inspired Propulsors*. PhD thesis, Princeton University, 2009.

[37] M. A. Green, C. W. Rowley, and G. Haller. Detection of Lagrangian coherent structures in 3d turbulence. *Journal of Fluid Mechanics*, 572:111–120, 2007.

[38] M. A. Green, C. W. Rowley, and A. J. Smits. The unsteady three-dimensional wake produced by a trapezoidal pitching panel. *Journal of Fluid Mechanics*, 685:117–145, 2011.

[39] M. A. Green and A. J. Smits. Effects of three-dimensionality on thrust production by a pitching panel. *Journal of Fluid Mechanics*, 615:211–220, 2008.

[40] G. Haller. Distinguished material surfaces and coherent structures in three-dimensional fluid flows. *Physica D*, 149:248–277, 2001.

[41] G. Haller. Lagrangian coherent structures from approximate velocity data. *Physics of Fluids*, 14(6):1851–1861, June 2002.

[42] G. Haller. An objective definition of a vortex. *Journal of Fluid Mechanics*, 525:1–26, 2005.

[43] B. L. Ho and R. E. Kalman. Effective construction of linear state-variable models from input/output data. In *Proceedings of the 3rd Annual Allerton Conference on Circuit and System Theory*, pages 449–459, 1965.

[44] P. Holmes and J. Guckenheimer. *Nonlinear oscillations, dynamical systems, and bifurcations of vector fields*, volume 42 of *Applied Mathematical Sciences*. Springer-Verlag, Berlin, Heidelberg, 1983.

[45] P. Holmes, J. L. Lumley, and G. Berkooz. *Turbulence, coherent structures, dynamical systems and symmetry*. Cambridge Monographs in Mechanics. Cambridge University Press, Cambridge, England, 1996.

[46] M. Ilak and C. W. Rowley. Modeling of transitional channel flow using balanced proper orthogonal decomposition. *Physics of Fluids*, 20:034103, 2008.

[47] S. J. Illingworth, A. S. Morgans, and C. W. Rowley. Feedback control of flow resonances using balanced reduced-order models. *Journal of Sound and Vibration*, 330(8):1567–1581, 2010.

[48] R. T. Jones. Operational treatment of the non-uniform lift theory in airplane dynamics. Technical Note 667, NASA, 1938.

[49] R. T. Jones. The unsteady lift of a wing of finite aspect ratio. Technical Report 681, NACA, 1940.

[50] W. P. Jones. Aerodynamic forces on wings in nonuniform motion. R & M 2117, ARC, 1945.

[51] J. N. Juang. *Applied System Identification*. Prentice Hall PTR, Upper Saddle River, New Jersey, 1994.

[52] J. N. Juang and R. S. Pappa. An eigensystem realization algorithm for modal parameter identification and model reduction. *Journal of Guidance, Control and Dynamics*, 8(5):620–627, 1985.

[53] J. N. Juang, M. Phan, L. G. Horta, and R. W. Longman. Identification of observer/Kalman filter Markov parameters: Theory and experiments. Technical Memorandum 104069, NASA, 1991.

[54] S. M. Kaplan, A. Altman, and M. Ol. Wake vorticity measurements for low aspect ratio wings at low Reynolds number. *Journal of Aircraft*, 44(1):241–251, 2007.

[55] J. Kim and T. R. Bewley. A linear systems approach to flow control. *Annual Review of Fluid Mechanics*, 39:383–417, 2007.

[56] R. Krechetnikov, J. E. Marsden, and H. M. Nagib. A low-dimensional model of separation bubbles. *Physica D*, 238:1152–1160, 2009.

[57] J. G. Leishman. Indicial lift approximations for two-dimensional subsonic flow as obtained from oscillatory measurements. *Journal of Aircraft*, 30(3):340–351, 1993.

[58] J. G. Leishman. Unsteady lift of a flapped airfoil by indicial concepts. *Journal of Aircraft*, 31(2):288–297, 1994.

[59] J. G. Leishman. Subsonic unsteady aerodynamics caused by gusts using the indicial method. *Journal of Aircraft*, 33(5):869–879, 1996.

[60] J. G. Leishman. *Principles of Helicopter Aerodynamics*. Cambridge University Press, Cambridge, England, 2 edition, 2006.

[61] J. G. Leishman and K. Q. Nguyen. A state-space representation of unsteady aerodynamic behavior. *AIAA Journal*, 28(5):836–845, 1990.

[62] F. Lekien. *Time-dependent dynamical systems and geophysical flows*. PhD thesis, California Institute of Technology, 2003.

[63] F. Lekien, C. Coulliette, A. J. Mariano, E. H. Ryan, L. K. Shay, G. Haller, and J. E. Marsden. Pollution release tied to invariant manifolds: a case study for the coast of Florida. *Physica D*, 210:1–20, 2005.

[64] F. Lekien, S. C. Shadden, and J. E. Marsden. Lagrangian coherent structures in n-dimensional systems. *Journal of Mathematical Physics*, 48:065404, 2007.

[65] D. J. Lesieutre, P. H. Reisenthel, and M. F. E. Dillenius. A practical approach for calculating aerodynamic indicial functions with a Navier-Stokes solver. AIAA Paper 94-0059, 32nd Aerospace Sciences Meeting, January 1994.

[66] G. Liger-Belair, R. Marchal, B. Robillard, T. Dambrouck, A. Maujean, M. Vignes-Adler, and P. Jeandet. On the velocity of expanding spherical gas bubbles rising in line in supersaturated hydroalcoholic solutions: Application to bubble trains in carbonated beverages. *Langmuir*, 16:1889–1895, 2000.

[67] D. Lipinski, B. Cardwell, and K. Mohseni. A Lagrangian analysis of a two-dimensional airfoil with vortex shedding. *Journal of Physics A: Mathematical and Theoretical*, 41:344011, 2008.

[68] Z. Ma, S. Ahuja, and C. W. Rowley. Reduced order models for control of fluids using the eigensystem realization algorithm. *Theoretical and Computational Fluid Dynamics*, 25(1):233–247, 2011.

[69] J. Magill, M. Bachmann, and G. Rixon. Dynamic stall control using a model-based observer. *Journal of Aircraft*, 40(2):355–362, 2003.

[70] P. Marzocca, L. Librescu, and W. A. Silva. Aeroelastic response and flutter of swept aircraft wings. *AIAA Journal*, 40(5):801–812, 2002.

[71] P. Marzocca, L. Librescu, and W. A. Silva. Aeroelastic response of nonlinear wing sections using a functional series technique. *AIAA Journal*, 40(5):813–824, 2002.

[72] M. Meyer and H. G. Matthies. State-space representation of instationary two-dimensional airfoil aerodynamics. *Journal of Wind Engineering and Industrial Aerodynamics*, 92:263–274, 2004.

[73] M. Mor and E. Livne. Minimum-state unsteady aerodynamics for aeroservoelastic configuration shape optimization of flight vehicles. *AIAA Journal*, 43(11):2299–2308, 2005.

[74] S. M. Murman. A reduced-frequency approach for calculating dynamic derivatives. AIAA Paper 2005-0074, 43rd Aerospace Sciences Meeting, January 2005.

[75] J. Newman. *Marine Hydrodynamics*. The MIT Press, Cambridge, Massachusetts, 1977.

[76] B. R. Noack, K. Afanasiev, M. Morzynski, G. Tadmor, and F. Thiele. A hierarchy of low-dimensional models for the transient and post-transient cylinder wake. *Journal of Fluid Mechanics*, 497:335–363, 2003.

[77] M. Ol, B. R. McAuliffe, E. S. Hanff, U. Scholz, and C. Kahler. Comparison of laminar separation bubble measurements on a low Reynolds number airfoil in three facilities. AIAA Paper 2005-5149, 35th Fluid Dynamics Conference, June 2005.

[78] M. V. OL. Unsteady low Reynolds number aerodynamics for micro air vehicles (mavs). Technical Report 2010-3013, Air Force Research Laboratory, 2010.

[79] M. V. OL, A. Altman, J. D. Eldredge, D. J. Garmann, and Y. Lian. Résumé of the AIAA FDTC low Reynolds number discussion group's canaonical cases. AIAA Paper 2010-1085, 48th Aerospace Sciences Meeting, January 2010.

[80] K. Padberg, T. Hauff, F. Jenko, and O. Junge. Lagrangian structures and transport in turbulent magnetized plasmas. *New Journal of Physics*, 9:400, 2007.

[81] R. Palacios, J. Murua, and R. Cook. Structural and aerodynamic models in nonlinear flight dynamics of very flexible aircraft. *AIAA Journal*, 48(11):2648–2659, 2010.

[82] A. Pelletier and T. J. Mueller. Low Reynolds number aerodynamics of low-aspect-ratio, thin/flat/cambered-plate wings. *Journal of Aircraft*, 37(5):825–832, 2000.

[83] J. Peng and J. O. Dabiri. The 'upstream wake' of swimming and flying animals and its correlation with propulsive efficiency. *The Journal of Experimental Biology*, 211:2669–2677, 2008.

[84] D. A. Peters. Two-dimensional incompressible unsteady airfoil theory– an overview. *Journal of Fluids and Structures*, 24:295–312, 2008.

[85] D. A. Peters, M. che A. Hsieh, and A. Torrero. A state-space airloads theory for flexible airfoils. *Journal of the American Helicopter Society*, 52:329–342, 2007.

[86] D. A. Peters, S. Karunamoorthy, and W.-M. Cao. Finite state induced flow models part 1: Two-dimensional thin airfoil. *Journal of Aircraft*, 32(2):313–322, 1995.

[87] M. Phan, L. G. Horta, J. N. Juang, and R. W. Longman. Linear system identification via an asymptotically stable observer. *Journal of Optimization Theory and Applications*, 79:59–86, 1993.

[88] M. Phan, J. N. Juang, and R. W. Longman. Identification of linear-multivariable systems by identification of observers with assigned real eigenvalues. *The Journal of the Astronautical Sciences*, 40(2):261–279, 1992.

[89] R. J. Prazenica, P. H. Reisenthel, A. J. Kurdila, and M. J. Brenner. Volterra kernel extrapolation for modeling nonlinear aeroelastic systems at novel flight conditions. *Journal of Aircraft*, 44(1):149–162, 2007.

[90] Z. Qin, P. Marzocca, and L. Librescu. Aeroelastic instability and response of advanced aircraft wings at subsonic flight speeds. *Aerospace Science and Technology*, 6(3):195–208, 2002.

[91] P. H. Reisenthel. Development of a nonlinear indicial model for maneuvering fighter aircraft. AIAA Paper 1996-0896, 34th Aerospace Sciences Meeting, January 1996.

[92] P. H. Reisenthel and D. Nixon. Application of indicial theory to the prediction of unsteady separation. AIAA Paper 91-1742, 10th Computational Fluid Dynamics Conference, June 1991.

[93] A. D. Ronch, D. Vallespin, M. Ghoreyshi, and K. J. Badcock. Evaluation of dynamic derivatives using computational fluid dynamics. *AIAA Journal*, 50(2):470–484, 2011.

[94] C. W. Rowley. Model reduction for fluids using balanced proper orthogonal decomposition. *International Journal of Bifurcation and Chaos*, 15(3):997–1013, 2005.

[95] D. Ruelle and F. Takens. On the nature of turbulence. *Communications in Mathematical Physics*, 20:167–192, 1971.

[96] F. Sadlo and R. Peikert. Efficient visualization of Lagrangian coherent structures by filtered amr ridge extraction. *IEEE Transactions on Visulization and Computer Graphics*, 13(6):1456–1463, 2007.

[97] H. Salman, J. S. Hesthaven, T. Warburton, and G. Haller. Predicting transport by Lagrangian coherent structures with a high-order method. *Theoretical and Computational Fluid Dynamics*, 21:39–58, 2007.

[98] L. Salvatori and P. Spinelli. Effects of structural nonlinearity and along-span wind coherence on suspension bridge aerodynamics: Some numerical simulation results. *Journal of Wind Engineering and Industrial Aerodynamics*, 94:415–430, 2006.

[99] S. P. Sane. The aerodynamics of insect flight. *The Journal of Experimental Biology*, 206(23):4191–4208, 2003.

[100] H. T. Schlichting and E. A. Truckenbrodt. *Aerodynamics of the Aeroplane*. McGraw Hill Higher Education, New York, New York, 1979.

[101] S. C. Shadden, K. Katija, M. Rosenfeld, J. E. Marsden, and J. O. Dabiri. Transport and stirring induced by vortex formation. *Journal of Fluid Mechanics*, 593:315–331, 2007.

[102] S. C. Shadden, F. Lekien, and J. E. Marsden. Definition and properties of Lagrangian coherent structures from finite-time Lyapunov exponents in two-dimensional aperiodic flows. *Physica D*, 212:271–304, 2005.

[103] K. Shi, H. P. Seidel, H. Theisel, T. Weinkauf, and H. C. Hege. Visualizing transport structures of time-dependent flow fields. *IEEE Computer Graphics and Applications*, pages 24–36, September/October 2008.

[104] C. shun Yih. *Fluid Mechanics: A concise introduction to the theory*. McGraw Hill, New York, New York, 1969.

[105] W. A. Silva. Simultaneous excitation of multiple-input/multiple-output cfd-based unsteady aerodynamic systems. *Journal of Aircraft*, 45(4):1267–1274, 2008.

[106] W. A. Silva and R. E. Bartels. Development of reduced-order models for aeroelastic analysis and flutter prediction using the CFL3Dv6.0 code. *Journal of Fluids and Structures*, 19:729–745, 2004.

[107] R. Singh and J. D. Baeder. Direct calculation of three-dimensional indicial lift response using computational fluid dynamics. *Journal of Aircraft*, 34(4):465–471, 1997.

[108] J. Sitaraman and J. D. Baeder. Computational-fluid-dynamics-based enhanced indicial aerodynamic models. *Journal of Aircraft*, 41(4):798–810, 2004.

[109] A. Smith. *Vortex models for the control of stall*. PhD thesis, Boston University, 2005.

[110] R. F. Stengel. *Flight Dynamics*. Princeton University Press, Princeton, New Jersey, 2004.

[111] K. Taira and T. Colonius. The immersed boundary method: a projection approach. *Journal of Computational Physics*, 225(2):2118–2137, 2007.

[112] K. Taira and T. Colonius. Effect of tip vortices in low-Reynolds-number post-stall flow control. *AIAA Journal*, 47(3):749–756, 2008.

[113] K. Taira and T. Colonius. Three-dimensional flows around low-aspect-ratio flat-plate wings at low Reynolds numbers. *Journal of Fluid Mechanics*, 623:187–207, 2009.

[114] T. Theodorsen. General theory of aerodynamic instability and the mechanism of flutter. Technical Report 496, NACA, 1935.

[115] M. Tobak. On the use of the indicial function concept in the analysis of unsteady motions of wings and wing-tail combinations. Report 1188, NACA, 1954.

[116] M. Tobak, G. T. Chapman, and L. B. Schiff. Mathematical modeling of aerodynamic characteristics in flight dynamics. Technical Memorandum 85880, NASA, 1984.

[117] M. Tobak and L. B. Schiff. On the formulation of the aerodynamic characteristics in aircraft dynamics. Technical Report R-456, NASA, 1976.

[118] K. V. Truong and M. Tobak. Indicial response approach derived from Navier-Stokes equations. part 1: Time-invariant equilibrium state. Technical Memorandum 102856, NASA, 1990.

[119] F. Ubertini. Prevention of suspension bridge flutter using multiple tuned mass dampers. *Wind and Structures*, 13(3):235–256, 2010.

[120] J. Valasek and W. Chen. Observer/Kalman filter identification for online system identification of aircraft. *Journal of Guidance, Control and Dynamics*, 26(2):347–353, 2003.

[121] C. Venkatesan and P. P. Friedmann. A new approach to finite state modelling of unsteady aerodynamics. *AIAA Journal*, 24(12):1889–1897, 1986.

[122] R. Vepa. Finite state modeling of aeroelastic systems. Contractor Report 2779, NASA, 1977.

[123] J. J. Videler, E. J. Samhuis, and G. D. E. Povel. Leading-edge vortex lifts swifts. *Science*, 306:1960–1962, 2004.

[124] T. von Karman and W. R. Sears. Airfoil theory for non-uniform motion. *J. Aeronautical Sciences*, 5(10):379–390, 1938.

[125] H. Wagner. Über die Entstehung des dynamischen Auftriebes von Tragflügeln. *Zeitschrift für Angewandte Mathematic und Mechanik*, 5(1):17–35, 1925.

[126] Z. J. Wang. Dissecting insect flight. *Annual Review of Fluid Mechanics*, 37:183–210, 2005.

[127] S. Wiggins. *Introduction to applied nonlinear dynamical systems and chaos*. Texts in Applied Mathematics. Springer, Berlin, Heidelberg, 2000.

[128] K. Willcox and J. Peraire. Balanced model reduction via the proper orthogonal decomposition. *AIAA Journal*, 40(11):2323–2330, 2002.

[129] D. R. Williams, J. Collins, C. Jankhot, T. Colonius, and G. Tadmor. Control of flow structure on a semi-circular planform wing. AIAA Paper 2008-597, 46th Aerospace Sciences Meeting, January 2008.

[130] M. M. Wilson, J. Peng, J. O. Dabiri, and J. D. Eldgredge. Lagrangian coherent structures in low Reynolds number swimming. *Journal of Physics: Condensed Matter*, 21(20):204105, 2009.

[131] R. Zbikowski. On aerodynamic modelling of an insect-like flapping wing in hover for micro air vehicles. *Philosophical Transactions of the Royal Society A*, 360:273–290, 2002.